Experimental characterization of laminated ferromagnetic materials for calculation of pulse width modulation induced iron losses in electrical machines

Sirotić, Igor

University of Zagreb

FACULTY OF ELECTRICAL ENGINEERING AND COMPUTING

Igor Sirotić

EXPERIMENTAL CHARACTERIZATION OF LAMINATED FERROMAGNETIC MATERIALS FOR CALCULATION OF PULSE WIDTH MODULATION INDUCED IRON LOSSES IN ELECTRICAL MACHINES

DOCTORAL THESIS

Zagreb, 2023

University of Zagreb

FACULTY OF ELECTRICAL ENGINEERING AND COMPUTING

Igor Sirotić

EXPERIMENTAL CHARACTERIZATION OF LAMINATED FERROMAGNETIC MATERIALS FOR CALCULATION OF PULSE WIDTH MODULATION INDUCED IRON LOSSES IN ELECTRICAL MACHINES

DOCTORAL THESIS

Supervisor: Prof. Stjepan Stipetić, PhD
Zagreb, 2023

Sveučilište u Zagrebu
FAKULTET ELEKTROTEHNIKE I RAČUNARSTVA

Igor Sirotić

EKSPERIMENTALNA KARAKTERIZACIJA LAMELIRANIH FEROMAGNETSKIH MATERIJALA ZA IZRAČUN GUBITAKA U ŽELJEZU ELEKTRIČNIH STROJEVA UZROKOVANIH MODULACIJOM ŠIRINE IMPULSA NAPONA

DOKTORSKI RAD

Mentor: Prof. dr. sc. Stjepan Stipetić
Zagreb, 2023.

Doktorski rad izrađen je na Sveučilištu u Zagrebu Fakultetu elektrotehnike i računarstva, na Zavodu za elektrostrojarstvo i automatizaciju

Mentor: Prof. dr. sc. Stjepan Stipetić

Doktorski rad ima:207stranica

Doktorski rad br.: _____

About supervisor

Stjepan Stipetić is a professor at University of Zagreb, Faculty of Electrical Engineering and Computing, Department of Electric Machines, Drives and Automation. He graduated from the same Department in 2008 under the supervision of prof. Ivan Gašparac and received PhD degree in 2014 under the supervision of prof. Damir Žarko. In the period from 2008 to 2014, he worked as a junior researcher and postdoc, then in 2015 and 2016 he worked in France as a Marie Curie Fellow on the EU FP7 project ADEPT. In 2017, he returned to FER as an assistant professor, since 2019 he has worked as an associate professor and since 2023 as professor.

Scientific interest of professor Stjepan Stipetić includes design, modelling, testing and optimizing electrical machines and electrical drives. Stjepan Stipetić is the principal researcher on the scientific project Synchronous reluctance generators for micro hydropower plants, financed by the Croatian Science Foundation. During his tenure, Stjepan Stipetić was involved as a researcher in several national and international scientific projects and was a principal researcher or researcher in numerous industrial projects with domestic and foreign companies. He is the author of many papers published in international journals and on international conferences, of which over 15 papers in category A journals and over 30 papers in the proceedings of international conferences. He reviewed over 150 papers in high ranked scientific journals and on scientific conferences. He supervised more than twenty undergraduate and graduate students. He is a member of the HRO CIGRÉ, IEEE and EDZ professional associations.

O mentoru

Stjepan Stipetić redoviti je profesor na Sveučilištu u Zagrebu, Fakultetu elektrotehnike i računarstva, na Zavodu za elektrostrojarstvo i automatizaciju. Na istom Zavodu diplomirao je 2008. godine pod mentorstvom prof. dr. sc. Ivana Gašparca, a doktorirao 2014. godine pod mentorstvom prof. dr. sc. Damira Žarka. U razdoblju od 2008. do 2014. radio je kao znanstveni novak i poslijedoktorand, zatim se u 2015. i 2016. usavršavao u Francuskoj kao stipendist na EU FP7 projektu ADEPT iz zaklade Marie Curie. 2017. godine se vraća na FER u zvanju docenta, od 2019. godine je u zvanju izvanrednog profesora, a od 2023. u zvanju redovitog profesora.

Znanstveni interes prof. dr. sc. Stjepana Stipetića obuhvaća projektiranje, modeliranje, ispitivanje i optimiranje električnih strojeva i elektromotornih pogona. Stjepan Stipetić je voditelj znanstvenog projekta Sinkroni reluktantni generatori za mikro hidroelektrane, financiranog od Hrvatske zaklade za znanost. Tijekom svojeg radnog staža Stjepan Stipetić je bio uključen kao istraživač u više nacionalnih i međunarodnih znanstvenih projekata te je bio voditelj ili suradnik na brojnim stručnim projektima s domaćim i inozemnim poduzećima. Autor je većeg broja radova objavljenih u međunarodnim časopisima i međunarodnim konferencijama, od toga preko 15 radova u časopisima A kategorije i preko 30 radova u zbornicima međunarodnih skupova. Recenzirao je preko 150 radova u visokorangiranim znanstvenim časopisima i na znanstvenim skupovima. Mentorirao je više od dvadeset studenata na preddiplomskom i diplomskom studiju. Član je udruge HRO CIGRÉ, IEEE i EDZ.

Acknowledgements

I would like to express my sincere gratitude to Prof. Stjepan Stipetić for agreeing to be my mentor and supervisor, and for introducing me to the fascinating and rich field of scientific research. His experience, support and patience were invaluable in shaping the outcomes of this dissertation and greatly facilitated the challenges I faced on my journey from admission to the PhD programme to its successful completion.

I would also like to thank Marinko Kovačić, who played an important role in guiding my research and provided invaluable help in developing the measurement setup that was crucial for this study.

I am very grateful to the entire faculty of the Department of Electrical Machines, Drives and Automation for their unfailing support, insightful discussions, valuable advice and assistance throughout the entire process of preparing this thesis.

I would like to express my appreciation to Alan Miletić and his colleagues from the Končar Electrical Engineering Institute for granting me access to their laboratory for testing magnetic materials.

I extend my thanks to my colleagues Petar Mostarac and Marko Jurčević from the Department of Electrical Engineering Fundamentals and Measurements for their assistance in performing certain measurements.

I would like to thank the members of the committee, Prof. Damir Žarko, Prof. Andrea Cavagnino and Assistant Prof. Zlatko Hanić, for their thorough analysis of my work, valuable feedback and numerous insightful suggestions for future research.

Finally, I am deeply grateful to my family, whose selfless support and boundless understanding have made the completion of this work possible. Their constant encouragement and faith in me have been an source of motivation throughout this journey.

Abstract

The use of inverter-fed electrical machines in industry and even in the small consumer market is prevalent today. With the transition from sinusoidal AC supply to PWM-generated supply, the losses in the entire electrical powertrain increase. The magnetic circuit is also affected by PWM-generated excitation, which is manifested by the occurrence of relatively small remagnetization cycles along the main one: total iron losses increase. Soft magnetic materials are an essential component of any electrical device, and accurate loss data is therefore essential for design purposes. However, data on magnetic materials is still only available for sinusoidal excitation, and there is no generally accepted method for accounting for PWM-induced losses at the design stage.

For this purpose, the measurement setup was built and measurements were performed on cores with different geometrical parameters. The effect of the voltage generated by the PWM was analyzed and compared with the results obtained in other research papers which served as validation of the proposed setup. DC bias measurements were performed and data were collected in the form of 3D loss maps. Two methods for calculating the contribution of PWM-induced losses to the total losses AC were proposed and an corresponding algorithms were developed. The obtained 3D loss maps were used as magnetic material data, and the results of calculations using the methods were compared with the results of the performed AC measurements, which served as reference data. The results of the calculations agree well with the measurements.

Keywords: Experimental characterization of ferromagnetic materials, PWM effects on iron losses, Calculation of the contribution of PWM-induced losses, High-power single winding measurement setup for material characterization, Ring core, DC bias

Eksperimentalna karakterizacija lameliranih feromagnetskih materijala za izračun gubitaka u željezu električnih strojeva uzrokovanih modulacijom širine impulsa napona

Prošireni sažetak

Prema nedavno objavljenim podacima, 46% proizvedene električne energije u svijetu koristi se za električne motore. Kada se ograničimo samo na industriju, postotak postaje još veći: otprilike 65% električne energije u industriji koristi se za električne motore. Razvoj tehnologije, posebice prekidačkih elemenata energetske elektronike, i korištenje pretvarača omogućili su učinkovito i jednostavno upravljanje izmjeničnim strojevima. Daljnji razvoj i poboljšanje dizajna pretvarača, kao i razvoj drugih tehnologija i materijala poput trajnih magneta, omogućili su i primjenu novih vrsta strojeva koji do nedavno nisu bili u širokoj primjeni, poput sinkronih strojeva s trajnim magnetima ili sinkronih reluktantnih strojeva. Sve to dovelo je do prevladavajuće upotrebe strojeva s promjenjivom brzinom vrtnje. Osim toga, električni generatori u modernim elektranama na obnovljivu energiju, poput mikro i malih hidroelektrana te vjetroelektrana, su gotovo isključivo povezani na elektroenergetski sustav putem pretvarača napona i frekvencije. Konačno, razvojem automobilske industrije i industrije malih električnih vozila, dalje se povećava uporaba strojeva napajanih putem pretvarača, koji se tako sve više pojavljuju i na tržištu malog potrošača. Uz brojne prednosti i potrebu za korištenjem takvih upravljivih pogona, prijelaz sa sinusnog napajanja na napajanje generirano širinsko-impulsnom modulacijom (*eng.* PWM) povećava gubitke u cijelom pogonskom sustavu električnog stroja.

Meki magnetski materijali neizostavan su dio svakog električnog stroja koji se koristi za elektromehaničku pretvorbu energije. Imaju važan zadatak usmjeravanja i oblikovanja magnetskog toka koji služi kao spona između mehaničke i električne energije. Stoga, gubici u željezu imaju važnu ulogu u dizajnu električnog stroja, ne samo u vidu predviđanja performansi, već i u projektiranju sustava hlađenja. Točna predikcija gubitaka u željezu može biti ključna u automobilskoj industriji i industriji drugih električnih vozila gdje određene dimenzije, masa, volumen, toplinska učinkovitost itd.

imaju važnu ulogu u konačnom dizajnu. Precizni podaci o gubicima feromagnetskih materijala su stoga ključni za projektante električnih strojeva.

Napajanje generirano PWM-om utječe i na magnetski krug električnih strojeva, što se očituje povećanjem gubitaka u željezu. Glavni uzrok povećanju gubitaka zbog PWM-a su izobličeni strujni i naponskih valni oblici u usporedbi sa sinusnom pobudom. U magnetskim materijalima to se očituje pojavom relativno malih ciklusa remagnetizacije tijekom glavnog ciklusa, pa čak i stvaranjem malih petlji duž glavne petlje histereze u određenim slučajevima. To na kraju dovodi do povećanja ukupne površine omeđene glavnom petljom histereze, a površina malih petlji, ako postoje, dodaje se površini glavne petlje. Budući da je površina petlje histereze proporcionalna gubicima u željezu, to dovodi do povećanja gubitaka.

Podaci o feromagnetskim materijalima dostupni su u tehničkim listovima proizvođača ili u bazama podataka pripremljenima prema međunarodnim standardima za karakterizaciju materijala, ali samo u uvjetima sinusne pobude. Projektanti električnih strojeva još uvijek nemaju opće prihvaćenu metodu za uključivanje gubitaka uzrokovanih PWM-om tijekom faze projektiranja. Različite moguće kombinacije parametara pretvarača, s međusobnim nelinearnim učincima na gubitke, kao i fizička ograničenja za odvajanje porijekla gubitaka u materijalu, vjerojatno su glavni razlozi zbog kojih općeniti pristup još uvijek nije dostupan.

Ovo istraživanje motivirano je nedostatkom korisnih objavljenih mjerenih podataka za lamelirane magnetske materijale. Mjerenje gubitaka u željezu na sustavu s prstenastom jezgrom može poslužiti kao vrijedan alat za proučavanje svojstava gubitaka u željezu ne-orijentiranih mekih magnetskih materijala pri visokim frekvencijama pobude i uvjetima promjenljivog istosmjernog magnetskog polja.

U sklopu ovog istraživanja predložen je inovativni mjerni postav i metodologija koja omogućuje dobivanje korisnih mjernih podataka o gubicima u materijalu u obliku višedimenzionalnih interpolacijskih mapa, koristeći kao uzorak magnetsku jezgru jednostavne geometrije. Mjerni postav je izrađen i provedena su mjerenja gubitaka u uvjetima promjenljivog istosmjernog magnetskog toka. Rezultati mjerenja strukturirani su u obliku trodimenzionalnih mapa gubitaka, a na temelju tih mapa predložene su dvije metode za izračunavanje gubitaka u željezu uzrokovanih PWM-om. Valjanost predloženih metoda potvrđena je usporedbom s rezultatima mjerenja provedenim u uvjetima izmjenične sinusne pobude.

Disertacija je podijeljena na devet poglavlja:

Poglavlje 1 - U ovom poglavlju govori se o važnoj ulozi električnih motora u vidu potrošnje električne energije i energetske učinkovitosti. Govori se i o poteškoćama vezane uz korištenje pretvarača napona i frekvencije kao izvora napajanje i na koji način to utječe na projektiranje stroja. Isto je ujedno i usko vezano uz motiv ovog istraživanja o kojem se skupa s fokusom i ciljem istraživanja govori na kraju poglavlja.

Poglavlje 2 - U ovom poglavlju govori se o osnovama elektromehaničke pretvorbe energije s naglaskom na ulogu feromagnetskih materijala u pretvorbi. Definiraju se osnovne karakteristike feromagnetskih materijala i daje se detaljniji uvid u temeljni mehanizam nastanka gubitaka u željezu. Posebno se analizira utjecaj napajanja generiranog PWM-om na gubitke u željezu, i to u ovisnosti o sljedećim parametrima pretvarača: sklopna frekvencija, dubina modulacije, napon istosmjernog međukruga i vrsta modulacije. Zasebno se proučava i utjecaj promjene istosmjernog magnetskog toka u jezgri na doprinos gubitaka PWM-a ukupnim gubicima. Slijedi osnovni pregled metoda za izračunavanje gubitaka u feromagnetskim materijalima, koje su podijeljene u tri skupine prema načelu izračuna gubitaka: metode temeljene na Steinmetzovoj jednadžbi, metode temeljene na odvajanju gubitaka i metode temeljene na matematičkim modelima histereze. Na kraju poglavlja definira se način određivanja magnetske indukcije u lameliranim jezgrama korištenjem sekundarnog mjernog svitka.

Poglavlje 3 - U trećem poglavlju predstavljen je inovativni mjerni postav za provođenje mjerenja u svrhu analize utjecaja PWM-a na gubitke u željezu i karakterizacije materijala sa svrhom izračuna doprinosa gubitaka uzrokovanih PWM-om ukupnim gubicima u željezu. Mjerni postav se sastoji od upravljivog istosmejrnog (DC) izvora koji se koristi za napajanje istosmjernog međukruga izmjenjivača, jednofaznog izmjenjivača s MOSFET sklopkama baziranim na silicij-karbid tehnologiji, prstenaste jezgre s jednim uzbudnim namotom i jednim namotom za određivanje magnetskog toka u jezgri, upravljačkog, mjernog i akvizicijskog sustava. Detaljno se razrađuje svaka komponenta postava i analizira se utjecaj pojedinih komponenti na rezultate mjerenja odnosno proračuna gubitaka. Posebno se razmatra utjecaj strujnog senzora odnosno utjecaj kašnjenja kojeg on uvodi u mjerni akvizicijski sustav, kao i utjecaj izvedbe uzbudnog i mjernog namota na jezgri. Na kraju, predstavljene su prstenaste jezgre korištene u mjerenjima ovog istraživanja.

Poglavlje 4 - U poglavlju 4 predstavljena je metodologija mjerenja. Predloženi i izrađeni mjerni postav u ovom istraživačkom radu koristi se za provođenje tri glavna tipa mjerenja: mjerenja za određivanje krivulje magnetiziranja, mjerenja za određivanje utjecaja parametara napajanja PWM-generiranog napona na gubitke u željezu (AC mjerenja) i mjerenja za prikupljanje podataka u svrhu karakterizacije feromagnetskog materijala u ovisnosti o istosmjernoj vrijednosti magnetskog toka u jezgri i specifičnim parametrima valovitosti magnetskog toka (DC mjerenja).

Krivulju magnetizacije potrebno je odrediti kako bi se utvrdila veza između jačine magnetskog polja H i magnetske indukcije B. Vrijednost magnetske indukcije B bit će ključna kasnije u analizi rezultata proračuna doprinosa PWM-a ukupnim gubicima.

Za evaluaciju gubitaka u jezgri uzrokovanih PWM-om, implementiran je način rada koji se koristi za generiranje PWM napona dobivenog korištenjem različitih parametara izmjenjivača (sklopna frekvencija, dubina modulacije, napon istosmjernog međukruga, vrsta modulacije). Ovaj način rada omogućuje određivanje utjecaja pojedinačnog parametra PWM napajanja neovisno o ostalim parametrima. Također, rezultati AC mjerenja služe i u svrhu validacije predloženog mjernog postava, budući da se rezultati mogu lako usporediti s rezultatima drugih istraživačkih radova.

Implementiran je i DC način mjerenja koji se koristi za istovremeno generiranje istosmjernog magnetskog toka u jezgri i valovitosti magnetske indukcije. Promjenom sklopne frekvencije izmjenjivača, vrijednosti napona DC međukruga i radnog ciklusa sklopki izmjenjivača mijenjaju se vrijednosti istosmjerne magnetizacije (B_{bias}), valovitosti magnetske indukcije (ΔB) i brzine promjene magnetske indukcije u vremenu ($\frac{\mathrm{d}B}{\mathrm{d}t}$). Na taj se način u jezgri mogu postići remagnetizacijski ciklusi koji odgovaraju malim remagnetizacijskim ciklusima koji se uobičajeno pojavljuju prilikom AC pobuda i PWM generiranog napajanja. Izvođenjem DC mjerenja za širok raspon parametara dobivaju se podaci o gubicima u željezu koji se mogu prikazati kao višedimenzionalno polje specifičnih vrijednosti gubitaka za različite vrijednosti parametara B_{bias}, ΔB i $\frac{\mathrm{d}B}{\mathrm{d}t}$.

Poglavlje 5 - U petom poglavlju prezentirani su rezultati provedenih mjerenja određivanja krivulje magnetiziranja, određivanja utjecaja parametara izmjenjivača na gubitke u željezu i određivanja utjecaja parametara ΔB i $\frac{\mathrm{d}B}{\mathrm{d}t}$ na gubitke u željezu u uvjetima promjenjive istosmjerne magnetizacije jezgre B_{bias}. Za obje vrste mjerenja, AC i DC mjerenje, analizirani su utjecaji svakog pojedinog parametara na gubitke. Dodatno, dana je i usporedba rezultata mjerenja za sve tri korištene prstenaste jezgre koji pokazuju kako geometrijski parametri prstenastih jezgara utječu na nastale gubitke o čemu je potrebno

voditi računa prilikom standardizacije mjerenja i mjernog postava za karakterizaciju materijala.

Poglavlje 6 - U ovom poglavlju predlaže se metoda *3DLMB* za proračun doprinosa gubitaka uzrokovanih PWM-om ukupnim gubicima u željezu. Metoda se temelji na usporedbi malih petlji nastalih uslijed izmjenične pobude na jezgri i malih petlji dobivenih DC mjerenjem. Male petlje nastale uslijed AC pobude potrebno je prikupiti provođenjem simulacija na modelu jezgre ili stroja, a DC male petlje je potrebno odrediti mjerenjem na prstenastoj jezgri. Usporedbom parametara AC i DC malih petlji može se izračunati doprinos gubitaka uzrokovanih PWM-om.

Opisuje se postupak izrade 3D mape gubitaka u ovisnosti o parametrima B_{bias}, ΔB i $\frac{\mathrm{d}B}{\mathrm{d}t}$ i raspravlja se detaljnije o utjecajima PWM-a na gubitke u željezu s naglaskom na onaj dio koji se direktno tiče predložene metode.

U sklopu metode predložena su dva različita pristupa *MLL* i *TACL* pristup koji se razlikuju po načinu na koji se prikupljaju podaci o malim petljama iz nekog valnog oblika indukcije: u *MLL* pristupu podaci o malim petljama se prikupljaju iz signala magnetske indukcije koji sadrži osnovni harmonik i superponiranu valovitost uzrokovanu PWM generiranim napajanjem dok se u *TACL* pristupu podaci prikupljaju samo iz valnog oblika valovitosti magnetske indukcije odnosno s izbačenim osnovnim harmonikom i harmonicima nižeg frekvencijskog spektra. Ovisno o pristupu, proračun gubitaka daje rezultat doprinosa isključivo malih petlji (*MLL* pristup) odnosno ukupni doprinos PWM-a gubicima (*TACL* pristup).

Male petlje nastale uslijed izmjenične pobude i u uvjetima promjenjivog prvog harmonika razlikuju se po svojim parametrima od malih petlji dobivenih DC mjerenjima gdje se za vrijeme remagnetizacijskog ciklusa vrijednost B_{bias} ne mijenja. Zbog toga dolazi do razlike u oblicima malih petlji nastalih u uvjetima AC i DC mjerenja, a s obzirom na to da se predložena metoda temelji na njihovoj usporedbi, to utječe na točnost određivanja gubitaka. Najveći utjecaj na točnost određivanja gubitaka ima parametar $\frac{\mathrm{d}B}{\mathrm{d}t}$ te se u poglavlju predlaže nekoliko načina izračuna ekvivalentnog vrijednosti tog parametra kako bi se minimizirao utjecaj asimetričnosti malih petlji nastalih u uvjetima AC pobude i omogućila što bolja usporedba s petljama dobivenim DC mjerenjima.

Poglavlje 7 - S obzirom na to da su tijekom istraživanja postojale naznake da će biti poteškoća u određivanju valnog oblika magnetske indukcije B u dostupnim simulacijskim paketima, u ovom poglavlju predlaže se metoda *3DLMH* koja za razliku od metode *3DLMB* parametre malih petlji veže uz jakost magnetskog polja H, a ne uz magnetsku indukciju B. Sva mjerenja koja su provedena u sklopu istraživanja koncipirana su tako da prikupljaju podatke o malim petljama u ovisnosti o magnetskoj indukciji B, a nova mjerenja zbog vremenskih ograničenja nije bilo moguće provesti. Stoga se u ovom poglavlju bavi razvojem algoritma preslikavanja rezultata mjerenja prikupljenih u obliku parametara malih petlji vezanih uz B na parametre malih petlji vezanih uz H. Potvrđeno je kako predloženi algoritam preslikavanja postiže zadovoljavajuće rezultate.

Poglavlje 8 - U ovom poglavlju prezentirani su rezultati proračuna gubitaka korištenjem metoda *3DLMB* i *3DLMH*. Za metodu *3DLMB* prikazani su rezultati oba predložena pristupa *MLL* i *TACL*. Za *MLL* pristup prikazani su rezultati proračuna za jezgru C1a, dok su za *TACL* pristup prikazani rezultati za sve tri korištene prstenaste jezgre. Za *TACL* pristup analiziran je i utjecaj određivanja ekvivalentnog $\frac{\mathrm{d}B}{\mathrm{d}t}$ parametra na proračun gubitaka. Pokazalo se kako korištenje ekvivalentnog $\frac{\mathrm{d}B}{\mathrm{d}t}$ parametra temeljenog na omjeru površina prvog i drugog dijela male petlje daje najbolje rezultate, ali i kako aproksimacija korištenjem empirijskog parametra k_e za proračun ekvivalentnog $\frac{\mathrm{d}B}{\mathrm{d}t}$ također daje zadovoljavajuće rezultate. Svi dobiveni rezultati proračuna doprinosa gubitaka uzrokovanih PWM-om uspoređeni su s mjerenjima: greška u proračunu nalazi se unutar raspona od $\pm 5\%$ za jezgru C1a i $\pm 10\%$ za jezgre C2a i C3.

Na početku istraživanja postavljene su dvije pretpostavke: (i) korištenjem nelinearnog dinamičnog modela pretvarača i stroja temeljenog na mapama ulančanog toka i struja može se odrediti valni oblik struje pretvarača za svaku radnu točku stroja i (ii) strujno-pobuđena simulacija na modelu električnog stroja u simulacijskom paketu temeljenom na metodi konačnih elemenata rezultirat će valnim oblikom indukcije za svaki trokutić mreže modela. Te dvije pretpostavke su potvrđene za prstenaste jezgre, ali nisu potvrđene za električne strojeve. Očekivano je da će jednako vrijediti i za električne strojeve, ali to još predstoji eksperimentalno potvrditi.

U električnim strojevima očekuju se dodatne specifičnosti kao što su pojava harmonika niskog frekvencijskog spektra i rotacija vektora magnetske indukcije u jarmu statora. Te je specifičnosti potrebno uzeti u obzir prilikom implementacije predloženih metoda za proračun gubitaka. Uz uvjet da je sklopna frekvencija dovoljno veća od

frekvencije harmonika niskog frekvencijskog spektra, očekuje se kako će utjecaj harmonika niskog spektra samo utjecati na vrijednost istosmjerne magnetizacije u jezgri pri kojoj nastaje mali remagnetizacijski ciklus. Nadalje, s obzirom na to da je frekvencija valovitosti indukcije značajno veća od frekvencije rotacije vektora magnetske indukcije u statoru, očekuje se kako ta specifičnost vezana uz električne strojeve neće imati značajniji utjecaj na rezultate proračuna gubitaka predloženom metodom. Međutim, navedeno predstoji eksperimentalno provjeriti.

Poglavlje 9 - Poglavlje 9 čini zaključak.

Napajanje generirano PWM-om ima značajan utjecaj na povećanje gubitaka u željezu u električnim strojevima, stoga je točna estimacija doprinosa gubitaka uzrokovanih PWM-om u fazi projektiranja od velike važnosti. Za tu je svrhu potrebna precizna karakterizacija magnetskih materijala koja je do sada dostupna samo u uvjetima sinusne pobude i ne postoji standardizirana, opće prihvaćena metoda za uzimanje u obzir efekata uzrokovanih PWM-om u fazi projektiranja.

U sklopu istraživanja, izrađen je mjerni postav za provođenje mjerenja na mekim magnetskim materijalima koji omogućava: (i) analizu različitih učinaka PWM-a na gubitke u željezu (AC mjerenje) i (ii) prikupljanje podataka za karakterizaciju materijala u obliku parametara malih petlji B_{bias}, ΔB i $\frac{\mathrm{d}B}{\mathrm{d}t}$ (DC mjerenje). Mjerni postav izrađen je sa samo jednim uzbudnim namotom, pri čemu izmjenjivač služi kao izvor napajanja i izmjeničnog i istosmjernog napona što čini ovaj postav inovativnim.

Predložene su dvije metode za izračun doprinosa gubitaka uzrokovanih PWM-om ukupnim AC gubicima, obje temeljene na 3D mapama i usporedbi parametara malih petlji između malih petlji dobivenih AC pobudom i malih petlji dobivenih DC mjerenjem. Metoda *3DLMB* koristi valni oblik magnetske indukcije B za definiranje malih petlji, dok metoda *3DLMH* koristi valni oblik jakosti magnetskog polja H za istu svrhu. Metode su evaluirane usporedbom gubitaka dobivenih kao rezultat AC mjerenja s gubicima izračunatim korištenjem predloženih metoda. Razlika između izračuna i mjerenja varira ovisno o metodi, sklopnoj frekvenciji i vrijednostima parametra B_{1hpk}, ali pogreška se općenito kreće u rasponu od $\pm 5\%$ za referentnu jezgru C1a i u rasponu od $\pm 10\%$ za jezgre C2a i C3, što se smatra zadovoljavajućim za proračun gubitaka.

Iako su rezultati AC mjerenja korišteni u ovom istraživanju za evaluaciju predloženih metoda, korištenje tih metoda namijenjeno je za izračun doprinosa gubitaka

uzrokovanih PWM-om u fazi projektiranja električnih strojeva. Stoga se podaci o malim petljama formiranim u uvjetima AC pobude trebaju dobiti korištenjem modela električnog stroja i alata za simulaciju, dok se samo DC mjerenja trebaju izvršiti na prstenastoj jezgri izrađenoj od feromagnetskog materijala namijenjenog za izgradnju stroja. Preliminarni simulacijski eksperimenti provedeni su na modelu C1a jezgre kako bi se potvrdilo da se podaci o malim petljama mogu dobiti korištenjem simulacijskih alata. Međutim, primjenjivost predloženih metoda na jezgre složenijih geometrija i složenije magnetske krugove, poput onih koji se nalaze u električnim strojevima, još je uvijek potrebno eksperimentalno provjeriti.

Predlaže se provedba sljedećih daljnjih istraživanja vezanih uz fenomen gubitaka uzrokovanih PWM-om i moguću opću karakterizaciju feromagnetskih materijala:

1. Istraživanje veze između geometrijskih i konstrukcijskih parametara jezgre i gubitaka, te provedba analize moguće kvantifikacije tih veza.

2. Istraživanje ostalih mogućih definicija i izračuna ekvivalentnog parametra $\frac{\mathrm{d}B}{\mathrm{d}t}$ asimetričnih i nezatvorenih malih petlji, kao i provedba analize odnosa određenih empirijskih parametara i različitih vrsta feromagnetskih materijala.

3. Istraživanje mogućnosti generiranja 3D mape gubitaka temeljene na parametrima malih petlji ΔH, $\frac{\mathrm{d}H}{\mathrm{d}t}$i H_{bias}, kao i korištenja takve mape za izračun gubitaka metodom *3DLMH*.

Ključne riječi: Eksperimentalna karakterizacija feromagnetskih materijala, utjecaj PWM-a na gubitke u željezu, izračun doprinosa gubitaka uzrokovanih PWM-om, mjerni postav velike snage s jednim uzbudnim namotom za karakterizaciju materijala, prstenasta jezgra, istosmjerna magnetizacija (DC bias)

Contents

Chapter 1

Introduction

According to the recently published data, 46% of the total electricity consumption in the world is used by electric motors [1]. When the scope is limited to the industrial environment only, the percentage becomes even larger: about 65% of the electricity consumed in industry is used by electric motors [2,3]. The development of technology, especially the switching elements of power electronics, and the use of power converters have made it possible to control AC machines efficiently and easily without significantly affecting their rated characteristics. Further developments and improvements in converter design, as well as the development of other technologies and materials such as permanent magnets, have enabled the further development and application of machine types that were not widely used until recently, such as synchronous machines with permanent magnets or synchronous reluctance machines. All this has led to the present situation, namely the prevalent use of variable speed drives in industrial applications. In addition, electrical generators in modern renewable energy applications, such as micro and small hydropower applications, and wind power applications, are almost exclusively grid-connected through active front-end power converters. Finally, with the development of the automotive industry and the industry for other small electric vehicles, the use of inverter-fed machines has further increased and reached the small consumer market. In addition to numerous advantages and necessities of the use of converters, however, the transition from the sinusoidal AC voltage supply to the PWM voltage supply increases the losses in the entire electrical powertrain.

Soft magnetic materials are an essential part of any electrical device used for electromechanical energy conversion. They have the important task of concentrating and shaping the magnetic flux responsible for the transfer between mechanical and electrical energy or between electrical energies of different parameters. Therefore, iron losses play an important role in the design of the electrical machine, not only for predicting

the performance of the machine, but also for the design of the cooling system. Correct prediction of iron losses can be crucial for automotive applications, other electric vehicles or any other application where specific dimensions, mass, volume, thermal performance, etc. have an important role in the overall design. Accurate loss data for ferromagnetic materials is therefore essential for electrical machine designers.

The magnetic circuit of electrical machines is also affected by PWM-generated excitation, leading to an increase in iron losses [4–8]. The general cause of the increase in losses due to PWM is the distortion of the current and voltage waveforms compared to sinusoidal excitation. In magnetic materials, this is manifested by the occurrence of relatively small remagnetization cycles during the main cycle and even by the possible formation of small loops along the main hysteresis loop. This eventually leads to an increase in the total area bounded by the main hysteresis loop, and the area of the small loops, if any, is added to the main loop area. Since the area of the hysteresis loop is proportional to the iron losses, this leads to its increase.

Data on ferromagnetic materials are available in manufacturers' data sheets or in database collections prepared according to international standards for material characterization. Measurement setups and methods are proposed using Epstein frame specimens, single sheet testers, or ring core specimens to obtain loss data, but all under sinusoidal excitation. Therefore, a widely accepted and proven model for predicting PWM-induced iron losses is needed and of paramount importance. However, electrical machine designers still do not have a generally accepted method for accounting for PWM-induced losses during the design phase. Various possible combinations of inverter parameters, with mutual nonlinear effects on the losses as well as the physical limitations to separate the origin of the losses in the material are possibly the main reasons why a general approach is still not available.

This research was motivated by the lack of useful published measurement data for laminated steel materials. A ring core iron loss measurement system can serve as a valuable tool for studying the iron loss properties of non-oriented soft magnetic materials (e.g., silicon iron laminated steel) for high excitation frequencies and even varying DC bias fields [9–12]. Assuming that the DC bus voltage, modulation depth and switching frequency of the inverter are known for each operating point of a given electrical machine, it is possible to calculate the current ripple using a non-linear dynamic machine model based on flux-current maps. Once the current ripple is calculated, a current-driven transient FEA analysis can be performed, resulting in a detailed field solution over the entire geometry and serving as input for the loss calculation.

In this thesis, a novel measurement setup and methodology is proposed that allows useful measurement data to be obtained in the form of multi-dimensional gridded interpolating maps, using simple core geometry. The proposed measurement setup was built and DC bias measurements were performed resulting in data in the form of 3D loss maps. Based on these maps, two methods for calculating PWM-induced losses are proposed, which are evaluated by comparison with the results of measurements performed under AC excitation.

This thesis is structurally divided into 9 chapters:

1. Chapter1- contains an introduction, defines the problem and the research motivation and objectives.

2. Chapter2- gives an insight into the theoretical basis of the magnetic properties of materials, the magnetization process, the origin and measurement of iron losses and how these are influenced by an excitation voltage generated with pulse width modulation.

3. Chapter3- presents the novel measurement setup and discuses in detail on its components and how they affect the setup and measurement results .

4. Chapter4- is focused on the details of how to perform the measurements and calculations. It describes the measurement methodology for the AC measurement mode, including the determination of the normal magnetization curve and the iron losses, as well as for the DC bias measurement mode, which is used to gather the data for the creation of the 3D loss map.

5. Chapter5- presents the results of the AC and DC bias measurements and discusses how the core losses are affected by the PWM-generated power supply, DC bias and specific parameters of the minor loops as well as the core geometry and temperature change.

6. Chapter6- proposes a method for calculating PWM-induced losses based on the use of the created 3D loss map and the comparison between the minor loop parameters obtained from the AC simulation results and DC bias measurements. Details are presented on the creation of the 3D loss map, the definition of the minor loop parameters and the challenges in determining them, and minor loop comparison issues. Finally, an algorithm for applying the method is described.

7. Chapter7- describes another method that is based on the same principles and requires less computational data for its application, but is limited to certain core geometries.

8. Chapter8- summarizes the results and a discussion of the results obtained on the basis of the proposed methods for loss calculation. The evaluation of the proposed methods can be found at the end of the chapter.

9. Chapter9- concludes the dissertation and provides suggestions for future research steps and directions.

Chapter 2

Magnetic properties of material

Electromechanical energy conversion occurs through the medium of a magnetic field that serves as a coupling between the electrical and mechanical systems. The energy transferred from one system to another is temporarily stored in the magnetic field, and this is the fundamental mechanism by which energy is converted from one form to another. The development of magnetic flux in the core depends largely on the core material. Therefore, the magnetic properties of the materials used for core assembly are of great importance to the designers of electrical machines.

Soft magnetic materials play a crucial role in modern civilization as they concentrate and shape magnetic flux in electrical devices. These materials are named so because of their correlation between mechanical softness and ease of magnetization reversal. The most important characteristics desired include high saturation flux density, high permeability, low coercivity, and low core losses [13]. Each of the characteristics, in its own way, provides a measure of the efficiency of a magnetic material [14]. There is no magnetic material that combines the best of all properties, and electrical machine designers must make trade-offs between two or more key properties. In addition, other properties such as thermal and structural stability, stress sensitivity of magnetic parameters, mechanical properties and machinability, and thermal conductivity must be considered [15]. The final acceptance of a material in applications results from a cost-benefit evaluation of all these properties and accurate information on the magnetic properties of the material can help the machine designer address this problem.

The process of magnetization in these materials is characterized by complexity, which is reflected in the multiple manifestations of hysteresis [15]. This appears as the macroscopic result of a complicated combination of microscopic processes centred on the existence of magnetic domains, leading to collective rearrangements of magnetic moments under a changing magnetic field.

2.1 Magnetization of ferromagnetic materials

It can be assumed that every magnetized material contains a large number of elementary dipoles. These dipoles result from orbiting of the electrons around the nuclei or from their own rotation, i.e. the spin [16]. When a material is completely demagnetized, the average magnetic moment is balanced and the resulting magnetization equals zero. However, when an external magnetic field is applied, the dipole moments are reoriented either by the expansion and contraction of different domains or by the rotation of the magnetization within these domains. As a result, the dipole moments amplify the applied field, leading to an increase in the magnetic field called magnetization M.

Under the influence of an applied field, magnetic material becomes magnetized, and the degree of its magnetism depends on the strength of the applied field. The relationship between the magnetic field strength H and the flux density B in a vacuum is given by the following equation:

$$B = \mu_0 H \tag{2.1}$$

where μ_0 is the permeability of the vacuum. For any material other than free space, however, this relation is defined as [15–18]:

$$B = \mu_0(H + M) = \mu_0 H + J \tag{2.2}$$

where M stands for magnetization and J for magnetic polarization[1]. In this relation, the component $\mu_0 H$ represents the contribution from the external source, while $\mu_0 M$ represents the internal contribution from a magnetized material and J represents the corresponding increase in flux density [16].

The ratio of B and H can be defined as follows:

$$\frac{B}{H} = \mu_0 \left(1 + \frac{M}{H}\right) = \mu_0(1 + \chi) = \mu_0 \mu_\mathrm{r} = \mu \tag{2.3}$$

where χ stand for susceptibility, dimensionless ratio of M and H, μ_r for relative permeability of the material, and μ absolute permeability.

Theoretically, the relative permeability μ_r could be the best factor to describe the

[1] The quantities B, H, M and J are vector quantities. However, for the purposes of this thesis, the relative directions of the vectors are implied and they are therefore usually written in scalar form.

properties of magnetic materials, because it gives direct information about the relationship between two important material parameters: the flux density B and the magnetic field strength H. In practise, however, the situation is much more complex because the relationship between B and H is not linear and the permeability depends on the shape of the material and the direction of magnetization [16,17]. Therefore, although permeability is a very useful factor from a physical point of view, in engineering applications it is more useful to use the magnetization curve to describe the magnetization process. The curve that represents this relationship is called the initial B-H curve or the initial magnetization curve.

There are several ways to measure direct magnetic flux in a material, but most require the installation of a probe. This is extremely impractical when testing a large number of samples and different sample types and sizes. To overcome this problem, the magnetic flux can be increased incrementally in steps of any size to ensure a change in magnetic flux between every two steps. This change in magnetic flux can then be determined using a secondary winding wound around the sample and a suitable measuring instrument. In this way, however, the measurement uncertainty increases for each additional point of higher flux density, since it is the sum of the measurement uncertainties of all previously determined points. For this reason, it is more common to determine instead the normal magnetization curve (also called the commutation curve), which is the locus of the peaks of the normal hysteresis loops when the peak value of the cyclic magnetic field is varied (Figure2.1a). The normal magnetization curve coincides almost perfectly with the initial magnetization curve.

The shape of the hysteresis loop is defined by a phase shift of the waveforms of magnetic field strength and flux density and their higher harmonic content. It is a measure of the delay of a response to a given excitation. The phase shift between B and H waveforms changes in relation to the peak (maximum) value of the of the fundamental $B_{1\mathrm{hpk}}$, so that it decreases with the increase of $B_{1\mathrm{hpk}}$ value. Looking at the standard shape of the hysteresis loop, this can be seen by observing its width: The loop is widest where the phase shift is largest. As the material approaches saturation, the phase shift tends to zero, which can also be seen in the shape of the hysteresis loop, where the ascending and descending branches of the loop appear to coincide perfectly.

As long as there is a phase shift between B and H, the hysteresis loop has its peak points of B and H at different positions (Figure2.1b), and a single peak point of the hysteresis loop must be determined to find the normal magnetization curve. Since the initial $B-H$ curve to which the normal magnetization curve is to be aligned is

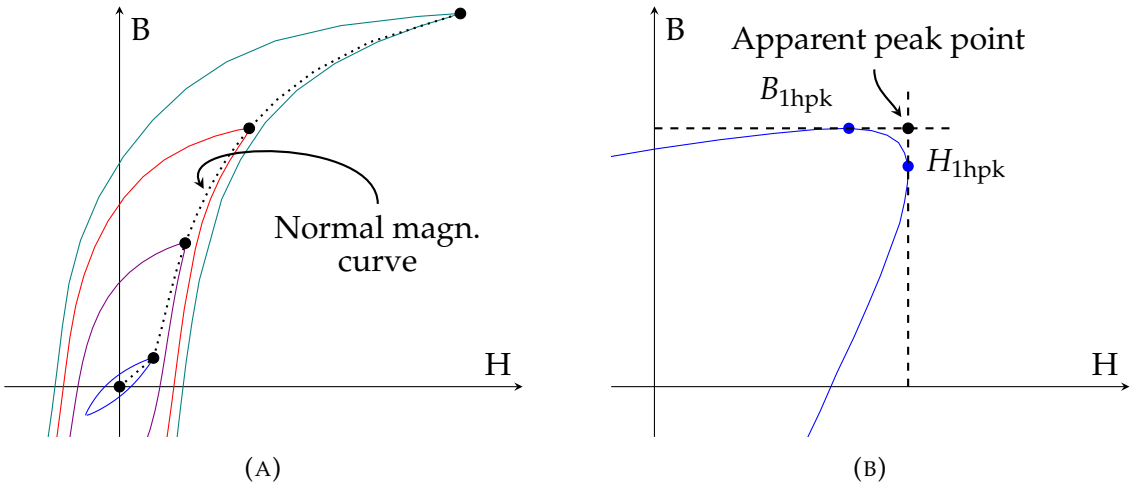

FIGURE 2.1: Determination of the normal magnetization curve in principle: (A) connection of the peaks of the $B - H$ loop for different values of B and H, respectively, yields the normal magnetization curve, (B) determination of the apparent peak point of the hysteresis loop based on the phase shift between B and H.

determined based on the DC current and magnetic field strength, one should determine what would be the value of B for a DC value of H equal to the peak value of the fundamental waveform of H, i.e. H_{1hpk}. The approach used in this thesis was to define the apparent peak point as (H_{1hpk}, B_{1hpk}). The actual achieved value of B may even be slightly higher than B_{1hpk} for a given value of H_{1hpk}, but this could not be determined with certainty within the scope of this thesis, so no further research was conducted on this topic.

Using the apparent peak point instead of the actual point on the hysteresis loop, e.g., where B_{1hpk} or H_{1hpk} is located, does not significantly affect the results of the total core loss calculation or the PWM contribution to the losses. This is especially true if the B_{1hpk} value is above the knee point of the normal magnetization curve. However, it affects the determined normal magnetization curve for lower flux densities, especially below 0.1 T. There, the difference with and without taking this effect into account can account for a difference in B value of up to 20% (according to measurements performed in this thesis). Above flux densities of 0.5 T, the influence of this effect is negligible.

The final values of B_{1hpk} and H_{1hpk} are determined as the average of the positive and negative peak values along a single main cycle to minimize the effects of the different magnetization capabilities in different directions of the soft magnetic material.

2.2 Core loss

In other than special circumstances, the magnetic structure of a ferromagnetic material is characterized by microscopic regions called magnetic domains [13]. The distribution of the magnetic field within each domain is essentially uniform, both in magnitude and direction, but the total magnetization vector differs between adjacent domains. The transition regions between the two are called Bloch walls. The Bloch wall represents a part of the ferromagnetic material in which the magnetic moment of electrons gradually changes between the orientations of adjacent domains (Figure2.2).

In the absence of the external field, ferromagnetic material remains magnetically neutral, i.e., the total magnetization vectors of the domains are equal or close to zero. However, when the ferromagnetic material is placed in an external magnetic field, the Bloch walls begin to move and the domains whose magnetization vectors are more aligned with the external field increase at the expense of the domains with less aligned magnetization vectors. The movement of the Bloch walls is the main mechanism to achieve global magnetization of the material at lower flux density values. Since the magnetization does not change uniformly through the material but in a highly localized manner, the magnetization change is spatially discrete, and due to impurities and imperfections in the material, the movement of the domain walls is disturbed, and rapid movements of the domain walls, called Barkhausen jumps, occur [20]. Such discontinuous and spatially non-uniform wall motion is responsible for hysteresis of the ferromagnetic material, even when the material is observed in a quasi-static state [13]. Domain wall motion is predominant at low flux density values, but magnetic domain rotation also occurs and has a predominant effect as the material approaches saturation [21]. Both mechanisms cause eddy currents that are strongest near the moving domain

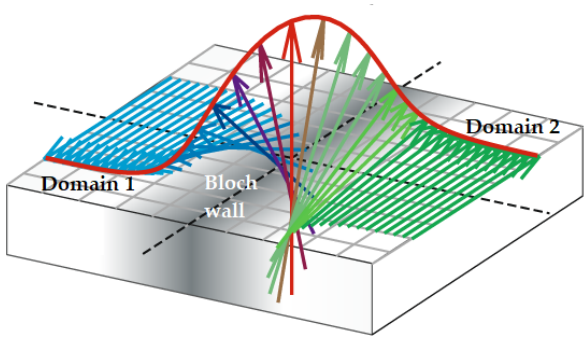

FIGURE 2.2: Representation of the Bloch wall between ferromagnetic material domains [19].

walls, which resist the change in magnetic field in the material and dissipate the energy as heat [17].

Hysteresis is the representation of the nonlinear relationship between magnetic field strength H and flux density B. All important properties of soft magnetic materials, i.e., saturation flux density value, coercivity, magnetic permeability, and core loss, can be represented with the hysteresis loop of the material, which is why it is often used for material analysis and characterization. The energy that needs to be provided for re-magnetization of the core over one full cycle of the alternating voltage is proportional to the core volume and hysteresis loop area:

$$E = \int_c e_{\text{induced}}(t) i(t) \mathrm{d}t = \int_c \frac{\mathrm{d}\Psi}{\mathrm{d}t} H \frac{\ell}{N} \mathrm{d}t = \int_c \frac{NS\mathrm{d}B}{\mathrm{d}t} H \frac{\ell}{N} \mathrm{d}t$$
$$= S\ell \int_c H \mathrm{d}B = V \int_c H \mathrm{d}B \quad (2.4)$$

It is thus apparent that the loss per cycle per unit volume of core is just the area enclosed by the dynamic $B - H$ loop. Dynamic hysteresis loop shape and area depend on the flux linkage and current waveforms and frequency. The larger the frequency, the wider the hysteresis loop will be.

2.2.1 Basic operating principle of PWM

Before proceeding further, the basic operating principle of generating the output voltage by means of PWM must be explained and basic terms on this subject introduced. For this purpose, a sinusoidal modulation is introduced. The principle of generating the PWM output voltage is based on the comparison between the control or reference signal, which in this case is a sine wave, and the carrier signal, which is a triangular wave (Subigure2.3a). The ratio of the amplitudes of the control and carrier signals, called the modulation depth m_a, is used to control the amplitude of the fundamental of the output voltage. As long as $m_a < 1$, the amplitude of the fundamental of the output voltage is linearly proportional to m_a. The frequency of the triangular wave determines the switching frequency of the inverter, while the frequency of the control wave determines the frequency of the fundamental of the output voltage.

The carrier signal and two control signals obtained with different values of m_a are shown in subfigure2.3a. The results of the comparison between the control signal and the triangular signal are shown in subfigures2.3band2.3c, one for each value of m_a. The result of the comparison is a series of pulses with variable width. The number

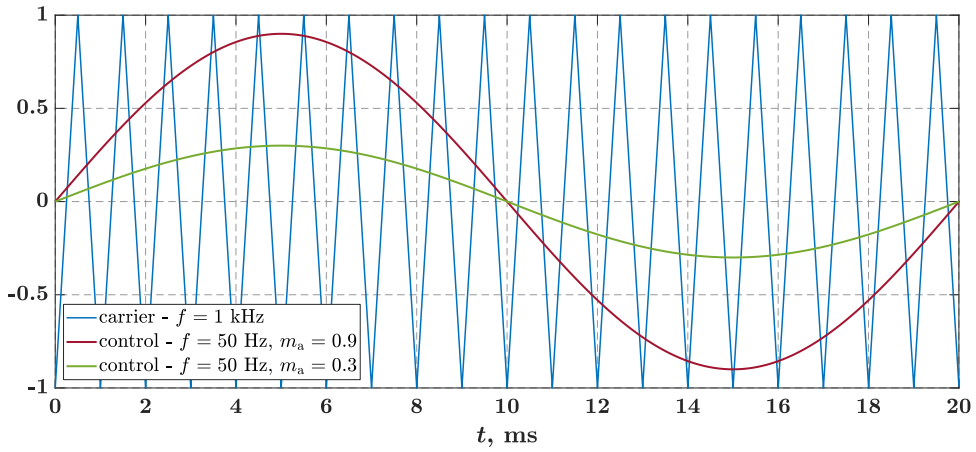

(A) The carrier and control signals

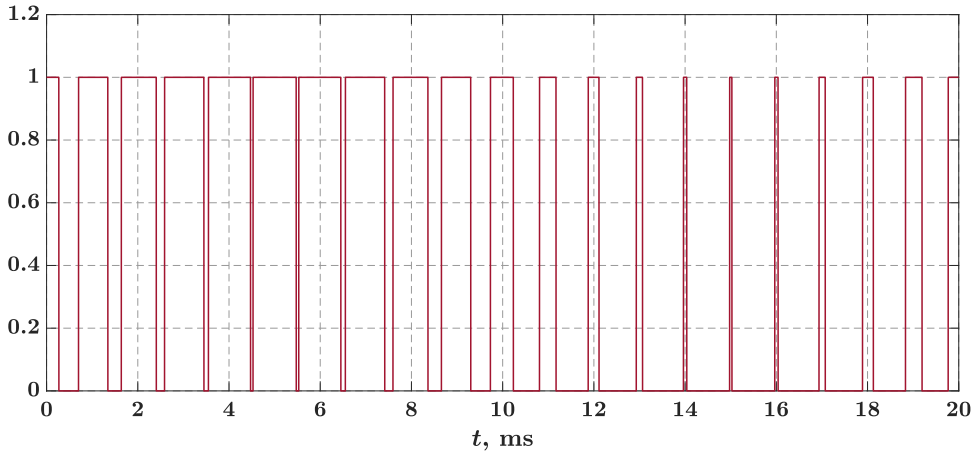

(B) Comparison result for $m_a = 0.9$

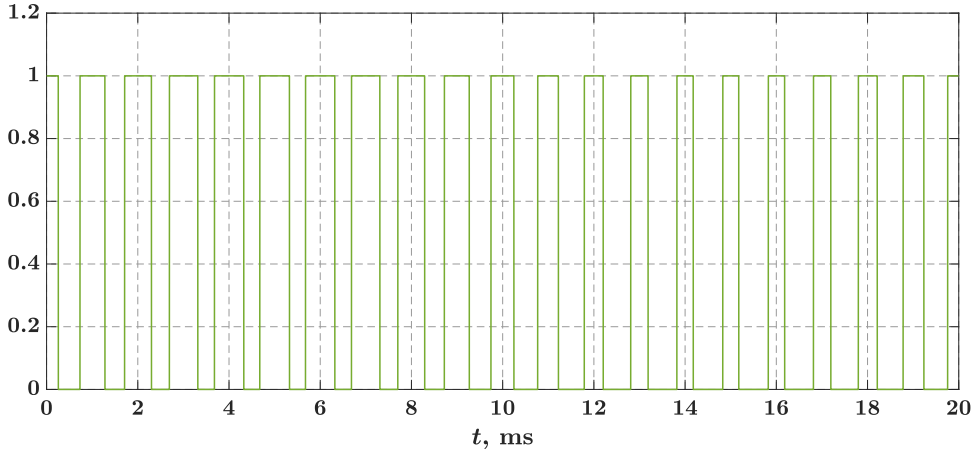

(C) Comparison result for $m_a = 0.3$

FIGURE 2.3: The carrier and control signals for two different values of modulation depth m_a and sinusoidal PWM modulation, as well as the results of the comparison between the carrier and control signals.

of pulses is fixed and related to the frequency of the triangular wave, i.e. the inverter switching frequency, and the width of the pulses changes along the single period of the control wave and depending on the value of m_a. These pulses are then indirectly used as signals to control the inverter switches, producing a PWM-generated sinusoidal voltage.

The ratio between the pulse width and the duration of the switching cycle is defined as the duty cycle of the inverter switches. This parameter determines how much time of a single switching cycle one of the inverter switches of a single inverter branch is in the ***on*** state and the other is in the ***off*** state. An example of how the duty cycle values change with the width of the pulses is shown in figure2.4, where the first quarter of the comparison between the carrier and control signals is shown for $m_a = 0.9$.

Two types of modulation are discussed throughout the thesis: unipolar and bipolar modulation. Figure2.5illustrates the principle of sinusoidal bipolar pulse-width modulation which is to control the output voltage with only two fixed values, namely $+U_{DC}$ and $-U_{DC}$. When the instantaneous value of the sine reference is larger than the triangular carrier, the output is at U_{DC} and when the reference is less than the carrier, the output is at $-U_{DC}$. This version of PWM is bipolar because the output alternates between plus and minus the DC supply voltage. In a unipolar modulation switching scheme (Figure2.6), two control signals are compared with the carrier signal, one of which has the opposite polarity to the other. In this way, two sets of pulses are obtained, the difference of which determines the final output voltage set of the pulses. The output

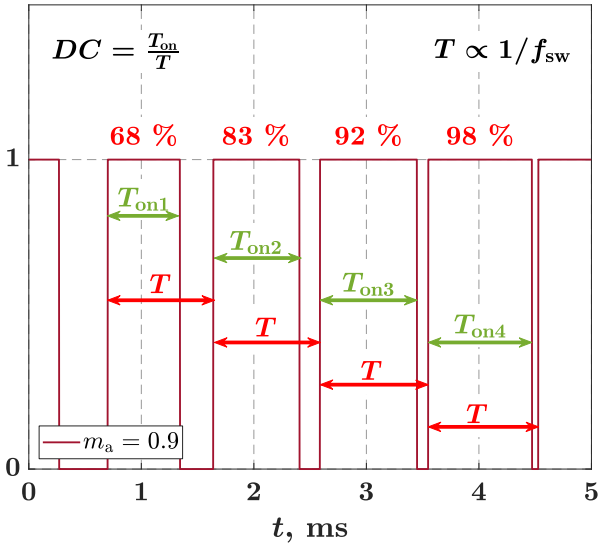

FIGURE 2.4: The duty cycle values of the series of PWM generated pulses.

voltage is controlled by PWM pulses with three different fixed values, which are $+U_{\mathrm{DC}}$, 0 and $-U_{\mathrm{DC}}$ value. In this way, there is never an opposite polarity of the pulse voltage along the main cycle loop for a single phase inverter and simple core geometries.

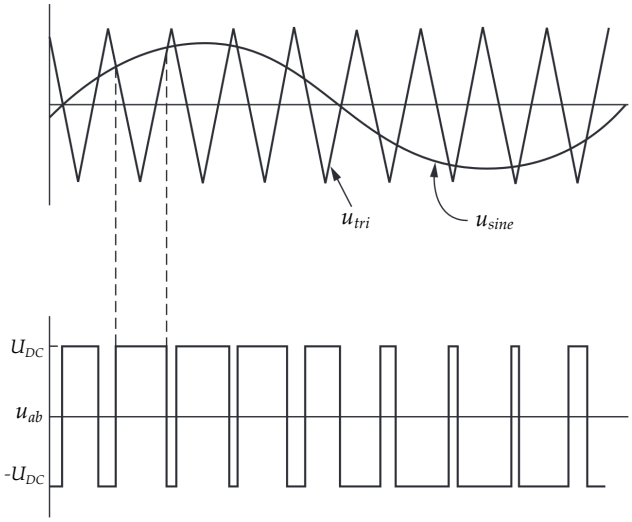

FIGURE 2.5: The principle of sinusoidal bipolar pulse-width modulation. U_{DC} is the DC link voltage, and u_{ab} is the output voltage of the inverter [22].

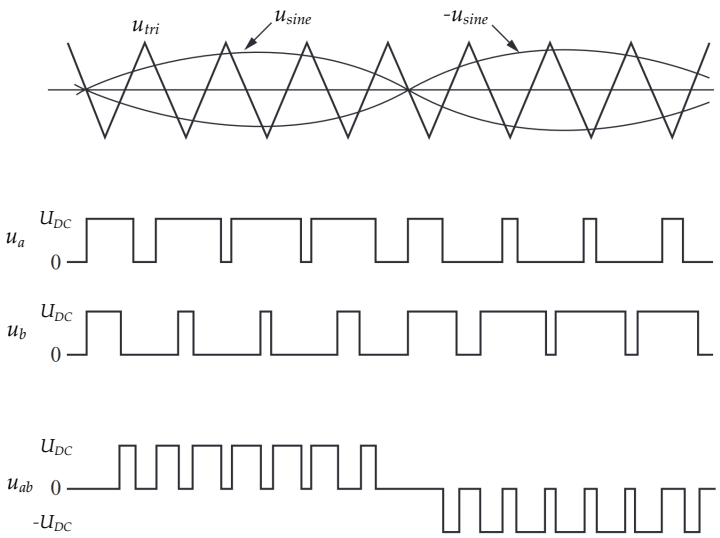

FIGURE 2.6: The principle of sinusoidal unipolar pulse-width modulation. U_{DC} is the DC link voltage, u_{a} and u_{b} are the bridge voltages of the ***a*** and ***b*** branches of the inverter and u_{ab} is the output voltage of the inverter [22].

2.2.2 PWM effect on core losses

When a PWM-generated sinusoidal voltage is used as excitation, the excitation voltage and current are significantly distorted compared to a sinusoidal voltage. The high-frequency ripple is superimposed on the low-frequency waveform, as shown in Figure 2.7for excitation current and flux linkage waveforms [2]. Such excitation leads to changes in the magnetic conditions of the core, which can be seen by the change in the hysteresis loop: small remagnetization cycles occur at the PWM switching points, which in some cases form additional small loops called minor loops (Subfigure2.7c). Depending on the inverter power supply parameters and duty cycle values, the number, size, and shape of the minor loops change, and in some cases they are absent: for example, when the unipolar modulation type is used or at low duty cycle values. The effects of the small remagnetization cycles can then still be observed by deformation and widening of the main cycle loop (Figure2.8). Regardless of the case, small remagnetization cycles lead to an enlargement of the total area bounded by the hysteresis loop, i.e. core power loss is increased [23–25].

Figure2.7clearly shows the difference in the waveforms of the current and flux linkage, which are the result of the voltage generated by PWM at two different switching frequencies: 4 kHz and 40 kHz. The higher the switching frequency of the inverter, the more switching instances occur during the single fundamental cycle, so that the number of small remagnetizations in a single main cycle is greater, i.e. determined by the ratio $f_{\mathrm{sw}}/f_{1\mathrm{h}}$. Although the frequency of the ripple increases and the number of small cycles increases, the peak-to-peak value of the ripple decreases [7], [26] and so does the total contribution of the small cycles to the losses. Subfigure2.8ashows a detailed view of two overlayed hysteresis loops, both obtained with the same parameters except the switching frequency, namely $f_{\mathrm{sw}} = 2$ kHz and $f_{\mathrm{sw}} = 8$ kHz, respectively. It can be observed that a part of the red loop area is not included in the blue hysteresis loop, resulting in a reduction of the total blue loop area, i.e., a reduction of the losses. One can also observe that the loop at $f_{\mathrm{sw}} = 8$ kHz is slightly narrower than that at $f_{\mathrm{sw}} = 2$ kHz. If switching frequency is increased further to $f_{\mathrm{sw}} = 40$ kHz, the trend is confirmed (Subfigure2.8b). The loop area asymptotically approaches the area obtained with

[2]For a basic evaluation of the effects of PWM on core losses, this section presents waveforms obtained through measurements with the proposed measurement setup used in this research. For a better understanding of the presented waveforms, the reader is referred to the chapter3and in particular to the block shematics of the measurement setup presented in the figure3.1.

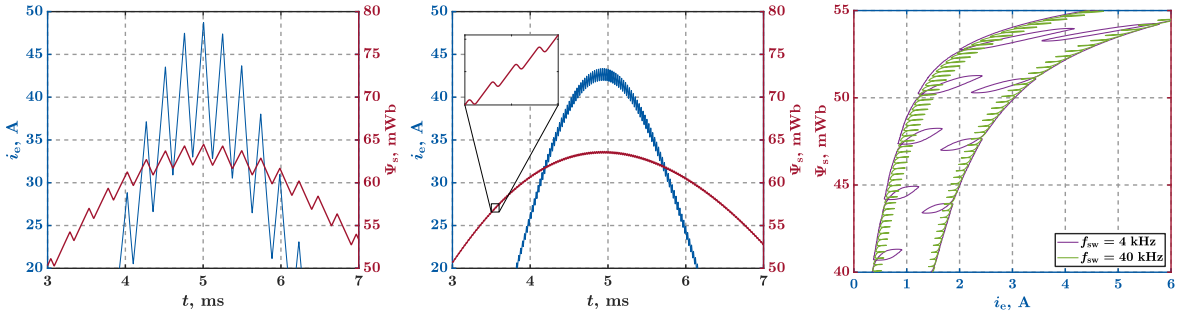

(A) $f_{sw} = 4$ kHz (B) $f_{sw} = 40$ kHz (C) Part of hysteresis loops

FIGURE 2.7: Detailed view of the core magnetization current and flux linkage waveforms. The power supply is generated with $U_{DC} = 100$ V, $m_a = 1$, $f_{1h} = 50$ Hz and bipolar PWM modulation at two different switching frequencies: $f_{sw} = 4$ kHz and $f_{sw} = 40$ kHz. The subfigure (C) shows the corresponding hysteresis loops for both cases.

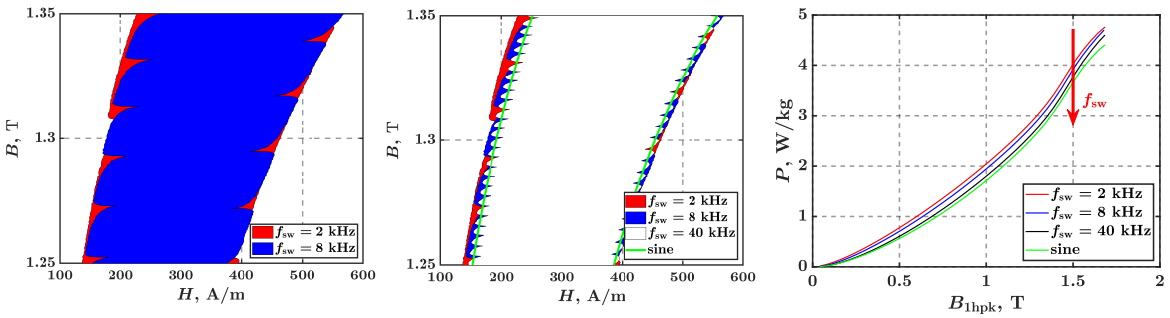

(A) Hysteresis loops detail (B) Hysteresis loops detail (C) Power loss curves

FIGURE 2.8: Effect of switching frequency on number of remagnetization cycles, total area of hysteresis loop, and contribution of PWM-generated power supply to total losses AC, shown for inverter supply parameters: $U_{DC} = 100$ V, $m_a \in [0, 1]$, $f_{1h} = 50$ Hz, unipolar modulation.

pure sinusoidal voltage excitation at the same fundamental frequency, which is also confirmed by observing the power loss curves for all cases in subfigure2.8c.

In contrast to unipolar modulation, the bipolar modulation type causes minor loop formation for most switching cycles [27]. The rest remains mostly the same: the number of minor loops is in relation to the ratio f_{sw}/f_{1h}, the area bounded by the minor loop decreases with the switching frequency, and the width of the main hysteresis loop also becomes narrower as the excitation approaches sinusoidal shape (Figure2.9). The area of minor loops is greatest at and around the knee of the material's magnetization curve, where the ratio of flux linkage to current ripple has the greatest influence on the formation of minor loops. For example, when a material is highly saturated, ΔH of the

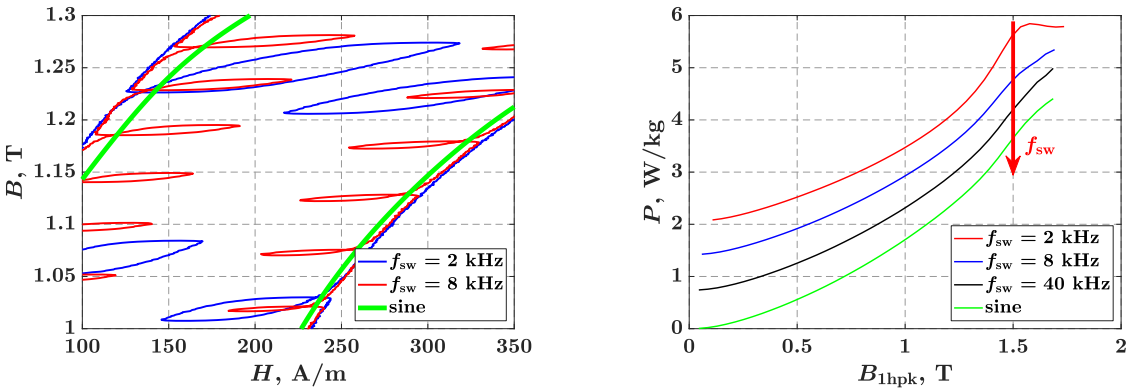

(A) Hysteresis loops detail

(B) Power loss curves

FIGURE 2.9: Effect of switching frequency on number of remagnetization cycles, total area of hysteresis loop, and contribution of PWM-generated power supply to total AC losses, shown for inverter supply parameters: $U_{\mathrm{DC}} = 100$ V, $m_{\mathrm{a}} \in [0,1]$, $f_{1\mathrm{h}} = 50$ Hz, bipolar modulation.

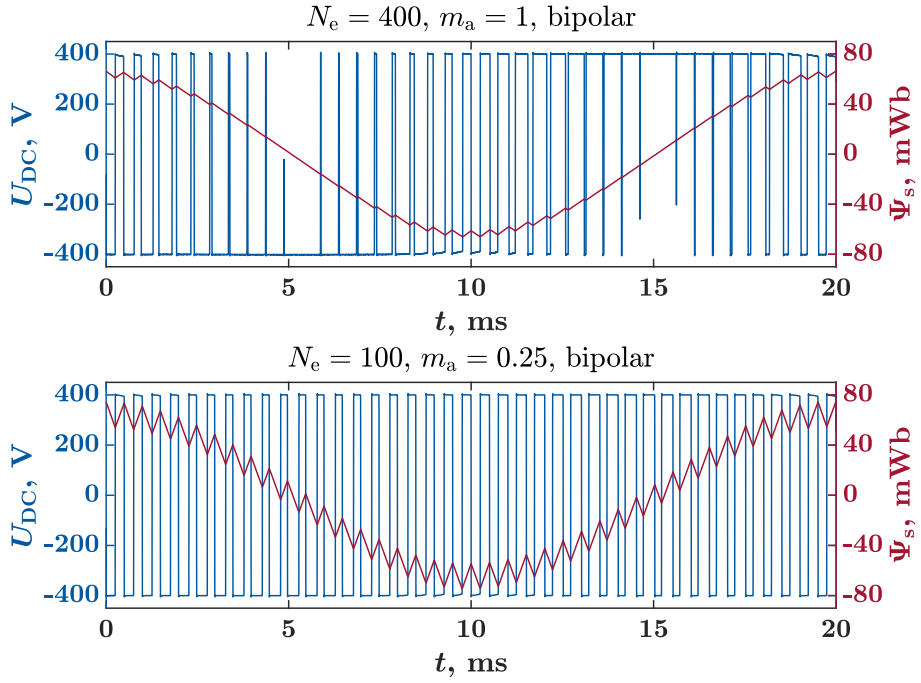

FIGURE 2.10: Comparison of PWM-generated supply voltage waveforms and corresponding flux linkages obtained with different modulation depth values. DC link voltage remains unchanged while N_{e} changes to ensure equal magnetic conditions with respect to low-frequency excitation components.

loop is large, but ΔB is small. Although the current ripple is high and the minor loop has a large width, it is very flattened because the core is saturated, so such minor loop does not contribute much to the increase in total power loss.

The modulation depth m_a, which determines the duty cycle of the inverter switches, can have a large effect on losses because it, in conjunction with the DC link voltage and winding parameters, determines the peak-to-peak ripple of the excitation waveforms. For example, for a constant DC link voltage, the same magnetic conditions in the core can be achieved with different numbers of excitation winding turns N_e and modulation depth values (same magnetic conditions here refers to the same conditions with respect to the low harmonic components: fundamental and near the fundamental). The comparison of the excitation voltage pulses and the resulting flux linkage for two different combinations of N_e and m_a is shown in figure2.10. It can be clearly seen how the peak-to-peak ripple changes significantly between the two cases, leading to a change in the size of the minor loops and consequently a change in the losses [28], [29].

In summary, a PWM-generated power supply leads to an increase in iron losses compared to a pure sinusoidal AC supply. DC link voltage, switching frequency, modulation type, and modulation depth are the inverter parameters that have an effect on iron losses [27].

2.2.3 DC bias influence on minor loop formation

The PWM switching frequency is typically much higher than the fundamental frequency, which means that the small remagnetization cycles occur under the condition of a practically unchanged fundamental field, so that it can be considered as a constant DC bias field [10]. Depending on the difference between the switching frequency and the fundamental frequency, the number of small remagnetization cycles during the main cycle is defined. Each of the small cycles takes place at a different value of the fundamental field. For this reason, it is necessary to investigate the influence of DC bias on forming of minor loops.

It was shown in [30–34] that the current state of magnetization of the core (DC bias) affects both the shape and the size of the minor loop that occurs. The shape of the loop (more oval or more rectangular) depends mainly on the magnetic properties of a material, while the size is related to the change in flux density ΔB and to the speed of change of flux density $\frac{dB}{dt}$.

Figure2.11bshows minor loops and their corresponding bounded regions for $\Delta B = 30$ mT, $\frac{dB}{dt} = 0.12$ T/ms, and various B_{bias} values. They are plotted along with the normal magnetization curve obtained with a 1 Hz fundamental power supply AC. All B_{bias} points of the minor loops, i.e., the points around which minor loops orbit, lie on the normal magnetization curve. The minor loop with the largest area lies slightly behind the knee point of the $B - H$ curve, which in this case is at $B_{\text{bias}} = 1.4$ T. The slope of the bisector of the minor loop, the shape and the area of the minor loop differ as a function of the B_{bias} values, as shown in detail in figures2.11cand2.11dwith $B_{\text{bias}} \approx 0.45$ T and $B_{\text{bias}} \approx 1.4$ T, respectively.

The change in flux density from peak to peak ΔB is proportional to the flux ripple, which in turn is indirectly related to the value U_{DC}. Because of losses in the core, U_{DC} must be adjusted with the change in DC voltage value to keep ΔB constant. Otherwise, ΔB is decreased with the increase of DC bias of the magnetic flux density and vice versa. For a given ΔB at a given value of DC bias, ΔH is defined by the $B - H$ curve of the material. In other words, for the same ΔB, ΔH will be higher in the saturated region than in the linear region. Figure2.11ashows the rate of change of ΔH with the B_{bias}, while ΔB is kept constant at 30 mT.

Increasing ΔB to relatively high values leads to a more pronounced change in the

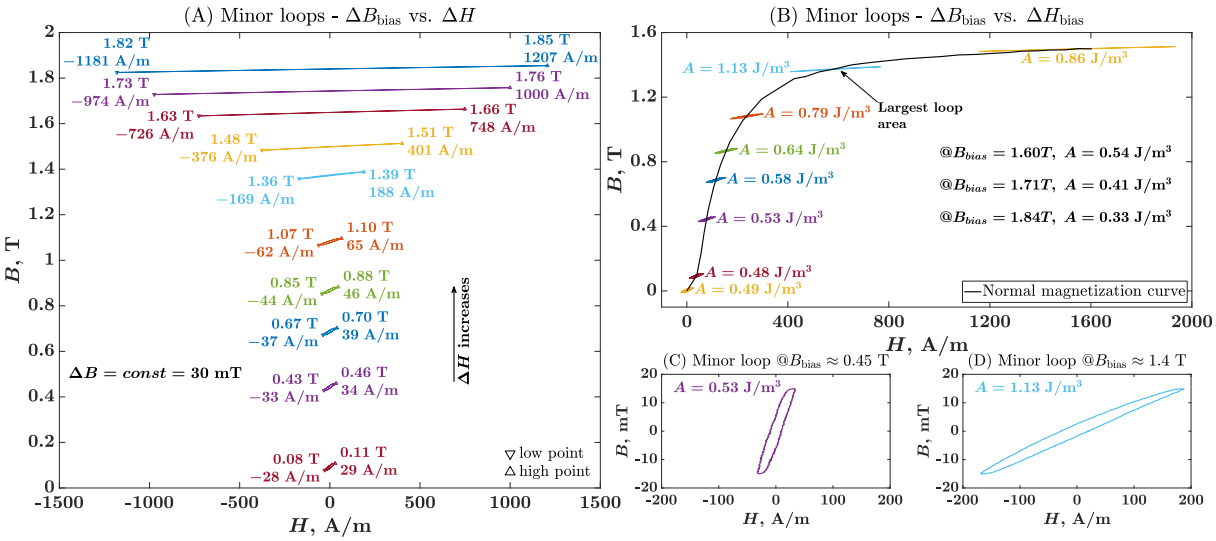

FIGURE 2.11: Minor loops at $\Delta B = 30$ mT and $\frac{dB}{dt} = 0.12$ T/ms for different values of B_{bias}: (A) with H_{bias} subtracted and (B) plotted along the normal magnetization curve. Subfigures (C) and (D) show a detailed view of a single minor loop at $B_{\text{bias}} \approx 0.45$ T and $B_{\text{bias}} \approx 1.4$ T, respectively [27].

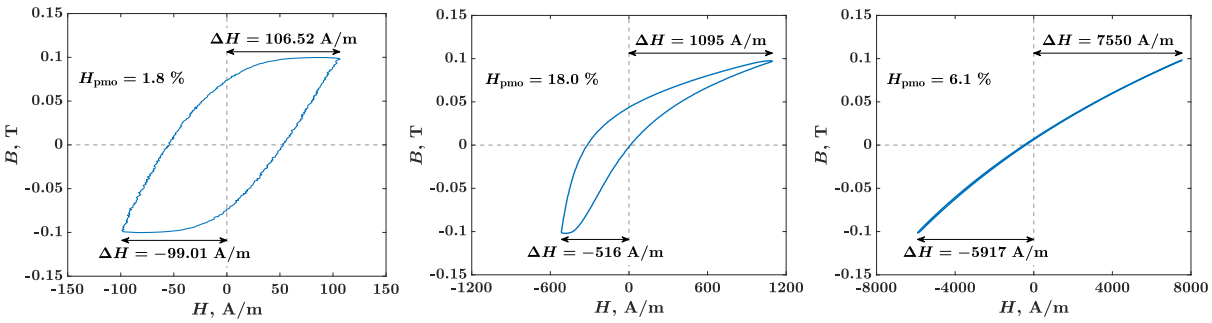

(A) $B_{\text{bias}} \approx 30$ mT (B) $B_{\text{bias}} \approx 1.4$ T (C) $B_{\text{bias}} \approx 1.75$ T

FIGURE 2.12: The effect of a large value of ΔB on the deformation of minor loops and the *peak mean offset* of H as a function of B_{bias}. Minor loops are shown for $\Delta B = 200$ mT, $\frac{dB}{dt} = 0.8$ T/ms, and $f_{\text{sw}} = 2$ kHz.

shape of the minor loops (Figure2.12). This is due to the fact that magnetic flux density B changes significantly and beyond the locally linear range of the $B - H$ curve during the formation of the minor loop. Naturally, this effect is more pronounced at and around the knee point of the $B - H$ curve, where the dependence of B and H is strongly nonlinear (Subfigure2.12b).

As saturation increases, the current waveform generally becomes distorted from sinusoidal, and its peak to RMS value (crest factor) is increased. Furthermore, if the core is magnetically biased, magnetic flux variations around this biased point will cause the value of B to change differently depending on the direction of the applied field. In other words, the ΔB between the peak value of the minor loop and the B_{bias} value of the minor loop is different from the value of ΔB value between the minimum value of the minor loop and the B_{bias}. This means that although the average value of the AC component of the magnetizing current is zero, the average value between its positive and negative peaks is different from zero. Figure2.12shows the difference between the maximum and minimum peaks for $\Delta B = 200$ mT and three different points of B_{bias}. The effect is quantified by the following parameter:

$$H_{\text{pmo}} = \frac{H_{\text{pk}} + H_{\text{min}}}{2 \cdot (H_{\text{pk}} - H_{\text{min}})} \cdot 100\% = \frac{H_{\text{mean}}}{\Delta H} \cdot 100\% \tag{2.5}$$

where H_{pmo} stands for *peak mean offset* of H. The larger the ΔB and the nonlinearity of the B-H curve around this point of B_{bias}, the larger the effect (Subfigure2.12b). However, this effect can also be observed at much lower ΔB values, such as at 30 mT in subfigure 2.12a.

2.3 Calculation of losses in ferromagnetic materials

This section gives a basic overview of the methods for calculating losses in ferromagnetic materials. The methods are divided into three groups based on the fundamental principle of losses calculation: methods based on the Steinmetz equation, methods based on loss separation and methods based on mathematical models of hysteresis.

Due to the complex physical origin of the remagnetization losses in ferromagnetic materials and the lack of an exact model, there are a large number of methods for calculating the AC magnetization losses of laminated cores. The existing methods differ in their complexity, accuracy and applicability to specific cases. In addition, each method requires knowledge of certain core sheet parameters, and the number and type of parameters depends on the used method [35].

2.3.1 Methods based on the Steinmetz equation

A large number of methods for calculating losses in ferromagnetic materials are based on Steinmetz's empirical equation [35], which was later extended to include the dependence on frequency [36]:

$$p_{\mathrm{v}} = C_{\mathrm{m}}\, f^{\alpha}\, B_{\mathrm{pk}}^{\beta}, \tag{2.6}$$

where p_{v} is the material losses per unit core volume, f is the power supply frequency, B_{pk} is the peak flux density, C_{m} is the material constant, and α and β are the empirical parameters - Steinmetz coefficients. Although the Steinmetz coefficients can almost always be determined from the curves provided by the metal sheet manufacturers and the method can be useful in certain cases, the main disadvantage of this method is that it is only applicable for sinusoidal excitation [20], [35].

The modified Steinmetz method (*MSE*) was developed to extend the validity of the Steinmetz method to non-sinusoidal waveforms without having to use additional material coefficients. The approach of the *MSE* method is based on the assumption that the losses in ferromagnetic materials depend on the change of the derivative of the flux density $(\mathrm{d}B/\mathrm{d}t)/\mathrm{d}t$ [20]. The mean value of the change in flux density over the entire remagnetization cycle is defined as:

$$\dot{B} = \frac{1}{\Delta B} \int_0^T \left(\frac{\mathrm{d}B}{\mathrm{d}t}\right)^2 \mathrm{d}t, \qquad \Delta B = B_{\max} - B_{\min}. \tag{2.7}$$

By introducing a normalization coefficient with respect to the sinusoidal waveform of the flux density, the equivalent frequency is defined as follows:

$$f_{\mathrm{eq}} = \frac{2}{\Delta B^2\, \pi^2} \int_0^T \left(\frac{\mathrm{d}B}{\mathrm{d}t}\right)^2 \mathrm{d}t. \tag{2.8}$$

Finally, combining2.8with2.6leads to the definition of material losses according to the *MSE* method [20]:

$$p_{\mathrm{v}} = \left(C_{\mathrm{m}}\, f_{\mathrm{eq}}^{\alpha-1} B_{\mathrm{pk}}^{\beta}\right) f_{\mathrm{r}}, \tag{2.9}$$

where f_{r} is the frequency of the remagnetization cycle.

According to [36], however, the *MSE* method has considerable disadvantages: Dependence of the results on the choice of the base integration period, underestimation of the losses when the amplitude of the fundamental harmonic is small relative to the amplitudes of the other harmonics, and the calculation is limited to the cases with flux density waveforms with a single peak.

The authors in [36] therefore extend the definition of the core losses with $B(t)$:

$$P_{\mathrm{v}}(t) = P_{\mathrm{d}}(\frac{\mathrm{d}B}{\mathrm{d}t}, B(t)). \tag{2.10}$$

By adjusting the exponents to the original Steinmetz equation, an expression is derived that agrees with the Steinmetz method and sinusoidal excitation:

$$P_{\mathrm{v}}(t) = k_1 \left|\frac{\mathrm{d}B}{\mathrm{d}t}\right|^{\alpha} B(t)^{\beta-\alpha}. \tag{2.11}$$

The authors in [36] extended the method to be applicable to excitation signals other than sinusoidal, and named the method the generalized Steinmetz method (*GSE*). The final expression for the calculation of the losses is defined as:

$$\overline{P_{\mathrm{v}}} = \frac{1}{T} \int_0^T k_1 \left|\frac{\mathrm{d}B}{\mathrm{d}t}\right|^{\alpha} B(t)^{\beta-\alpha} \mathrm{d}t. \tag{2.12}$$

Compared to the *MSE* method, the *GSE* method gives more accurate results and is applicable to a wider range of conditions. However, under certain conditions, remagnetization cycle may cause the formation of minor loops within the main hysteresis loop, which are not taken into account in the *GSE* method, as the integration is based on the main cycle period. This leads to a significant underestimation of the total losses in the material when using this calculation method [35], [36].

The equation2.12can be modified so that the term $B(t)$ is replaced by the parameter ΔB (positive to negative peak of the flux density) and still remain compatible with the basic Steinmetz method [37]:

$$\overline{P_{\mathrm{v}}} = \frac{1}{T}\int_0^T k_1 \left|\frac{\mathrm{d}B}{\mathrm{d}t}\right|^{\alpha} \Delta B^{\beta-\alpha}\mathrm{d}t \tag{2.13}$$

In order to take into account both the losses of the minor loops and the losses of the main cycle loop in the material, each remagnetization cycle is calculated separately with an individually determined value of the ΔB parameter and the equation2.13. The authors in [37] have developed a recursive algorithm for such a calculation, which is applicable to cases with an indefinite number of consecutive minor loops or remagnetization cycles:

$$P_{\mathrm{tot}} = \sum_i P_{\mathrm{i}} \frac{T_{\mathrm{i}}}{T}. \tag{2.14}$$

Therefore, total losses are calculated as the weighted sum of all individual loop losses with a weighting factor that depends on the duration of the remagnetization cycle compared to the duration of the main cycle. This method of calculating losses is called the improved generalized Steinmetz method (*i*GSE).

Every method described so far assumes that there are no losses in the material when the flux density has a constant value. However, this is not entirely accurate due to the losses caused by magnetic relaxation and cannot be ignored, especially when high frequency excitation is applied. For this reason, [38] presents an improved[2] generalized Steinmetz method, i^2GSE, where the equation2.13is further extended:

$$P_{\mathrm{v}} = \frac{1}{T}\int_0^T k_{\mathrm{i}} \left|\frac{\mathrm{d}B}{\mathrm{d}t}\right|^{\alpha} (\Delta B)^{\beta-\alpha}\,\mathrm{d}t + \sum_{\ell=1}^{n} Q_{\mathrm{r}_\ell} P_{\mathrm{r}_\ell}. \tag{2.15}$$

The term P_{r_ℓ} represents the losses caused by the ℓ^{th} of the total n voltage transients to zero (change of flux density from variable to constant) and is defined as:

$$P_{\mathrm{r_l}} = \frac{1}{T} k_{\mathrm{r}} \left|\frac{\mathrm{d}}{\mathrm{d}t} B(t)\right|^{\alpha_{\mathrm{r}}} (\Delta B)^{\beta_{\mathrm{r}}} \left(1 - e^{-\frac{t_1}{\tau}}\right), \tag{2.16}$$

where k_{r}, α_{r} and β_{r} are the relaxation parameters of the material, which must be determined empirically by measurements. The exponential term describes the natural physical process of relaxation of the material [38]. In cases where the flux density is

not trapezoidal, measurements in [38] have shown that there are still relaxation effects whose expression depends on the intensity of the change in flux density. For this reason, a correction factor Q_{r_ℓ} is added to the term of the sum, which describes the natural relaxation process of the material due to the change of the flux density from one value to another:

$$Q_{r_\ell} = e^{-q_r \left| \frac{dB(t_+)/dt}{dB(t_-)/dt} \right|}, \tag{2.17}$$

where $dB(t_-)/dt$ is the derivative of the flux density before the change and $dB(t_+)/dt$ is the derivative of the flux density after the change. The parameter q_r is a relaxation parameter which must be determined empirically.

A major drawback of this method is the fact that in addition to the well-known three Steinmetz coefficients k_i, α and β, five empirical parameters k_r, α_r, β_r, τ and q_r have to be determined by measurements.

There are several other variants and improvements of the above methods that can be found in the literature, but this concludes the basic overview. Methods based on the Steinmetz equation and Steinmetz coefficients provide a relatively simple way to calculate losses in a ferromagnetic material without requiring prior measurements on the material (with the exception of the i^2GSE method) [35]. Steinmetz coefficients can almost always be determined from curves provided by the manufacturer, but they depend strongly on the magnetization frequency and are therefore very difficult to determine to be suitable for calculation in devices with a wide range of excitation frequencies. This is a major drawback of all methods that base the loss calculation on Steinmetz coefficients [35].

2.3.2 Methods based on loss separation

The first known conventional approach in the practise of calculating losses in ferromagnetic materials was presented by Jordan, H., and is based on the separation of losses into two components: Hysteresis losses and eddy current losses [20]. Such separation of losses is based on an empirical approach to the problem rather than an explanation of the physical phenomenon underlying the losses and is mainly used in the analysis of electrical machines [35] due to its simplicity and speed in loss calculation.

As already shown in the previous section, the energy converted into losses during a remagnetization cycle is proportional to the core volume and the area of the hysteresis loop. To obtain the average power consumed on account of the hysteresis loss, the energy of a single cycle is multiplied by a frequency of the remagnetization, i.e. excitation

frequency:

$$P_{\text{hys}} = C_{\text{hys}} f B_{\text{pk}}^2, \tag{2.18}$$

where C_{hys} is a material constant that depends on the core geometry and magnetic properties of the material.

In general, any electrical current flow through medium produces heat, i.e. losses in that medium. The losses that are produced are proportional to the resistance of this medium and the current RMS value squared:

$$P_{\text{g}} = I^2 R \tag{2.19}$$

According to Faraday's law, the voltage per turn induced by the sinusoidal change of the magnetic flux in the core is defined as:

$$U = \frac{\mathrm{d}\phi}{\mathrm{d}t} = S\frac{\mathrm{d}B}{\mathrm{d}t} = S(2\pi f) B_{\text{pk}} \cos(2\pi f t), \tag{2.20}$$

where ϕ is the magnetic flux, B is the flux density and S is the cross-sectional area of the material. From (2.20) it follows that the induced voltage is proportional to the peak value of the flux density and the frequency. Assuming that the current is directly proportional to the voltage and considering (2.19), the losses in the material caused by eddy currents can be expressed as follows

$$P_{\text{ec}} = C_{\text{ec}} f^2 B_{\text{pk}}^2, \tag{2.21}$$

where C_{ec} is a material constant that depends on the geometry, resistivity and density of the material.

Finally, the total specific losses are equal to the sum of the hysteresis losses (2.18) and the eddy current losses (2.21)

$$P_{\text{tot}} = C_{\text{hys}} f B_{\text{pk}}^2 + C_{\text{ec}} f^2 B_{\text{pk}}^2. \tag{2.22}$$

The classical model assumes that the material magnetization process is completely homogeneous in space [39], which is a considerable simplification of the problem. It is shown that in certain cases the classical model can lead to significant errors in the calculations [20]. Therefore, Pry, R. and Bean, C. propose the introduction of an empirical correction factor η_{exc} which transforms the equation (2.22) into the following

expression:

$$P_{\text{tot}} = C_{\text{hys}} f B_{\text{pk}}^2 + \eta_{\text{exc}} C_{\text{ec}} f^2 B_{\text{pk}}^2, \tag{2.23}$$

where

$$\eta_{\text{exc}} = \frac{p_{\text{ec}_{\text{meas}}}}{p_{\text{ec}_{\text{calc}}}} > 1. \tag{2.24}$$

Another approach to the same problem is to introduce an additional loss term p_{exc} in (2.22) and then divide the total losses in the material into three components: static hysteresis losses, dynamic losses caused by eddy currents and excess losses [35,39].

$$P_{\text{tot}} = C_{\text{hys}} f B_{\text{pk}}^2 + C_{\text{ec}} f^2 B_{\text{pk}}^2 + C_{\text{exc}} f^{1.5} B_{\text{pk}}^{1.5}, \tag{2.25}$$

where C_{exc} is the empirical factor.

A separation of losses into static and dynamic losses is also proposed in [39,40], where it is stated that the measured dynamic losses are almost always greater than the losses calculated according to the classical model. For this reason, the theory of distribution of losses according to (2.25) is advocated here. In [39,40] a theory is presented according to which the physical basis of the additional losses lies in the constant confrontation of a homogeneous external field with extremely inhomogeneous opposing local fields caused by eddy currents and microstructural interactions. By introducing the concept of magnetic objects and statistical theory to determine the distribution of local fields, an expression to determine the parameter C_{exc} in (2.25) was proposed:

$$C_{\text{exc}} = \sqrt{S V_0 \sigma G}. \tag{2.26}$$

where S is the cross-sectional area of the core, σ is the conductivity of the material, G is the dimensionless constant, and V_0 is the statistical parameter of the distribution of the local fields.

Methods based on loss separation offer a good insight into the dependence of the various loss contributions on frequency and flux density. Such a consideration of the electrical machine offers the possibility to analyse the influence of a power supply with harmonic distortion on the losses, which is particularly interesting for drives with voltage and frequency converters. However, as with the methods based on the Steinmetz equation, these methods also depend on the Steinmetz coefficients.

2.3.3 Methods based on mathematical models of hysteresis

There are a large number of methods that base the calculation of losses on the mathematical models of hysteresis, in particular methods that use computer simulations and FEA analysis to perform calculations. These methods can be roughly divided into two different groups, depending on the model on which they are based: the Jiles-Atherton model and the Preisach model [20].

The Jiles-Atherton model is based on a physical model that uses a differential equation to describe the static behaviour of a ferromagnetic material [41]. Four empirical parameters must be determined using an iterative procedure and a known referential hysteresis loop. The basic Preisach model proposes a statistical approach to describe the temporal and spatial distribution of the domain wall motion in the material [20]. It uses a specially defined weight function to describe the properties of the material.

The two classical models mentioned above describe losses caused exclusively by quasi-static magnetization. Therefore, most models based on them deal with the extension to dynamic magnetization. Such extensions further complicate the already complex models and require the determination of additional empirical parameters.

Computational methods using finite element analysis (FEA) and various computer software tools are also based on the above models. With the development of computer processing power, this approach to solving the problem of losses in materials has improved considerably. However, these calculations are often very time-consuming.

The methods of mathematical hysteresis models provide the most accurate results when calculating losses in ferromagnetic materials. However, their application in practise is limited because a very large number of empirical parameters must be known, which are determined through a very complex and sensitive experimental process [42].

2.4 Iron flux density determination

The results of iron loss measurements and calculations are usually presented in relation to flux density, since this parameter represents the link between the magnetic flux generated in the material and its geometrical proportions, and is therefore crucial for loss analysis. Both the material build factors and the measurement principle affect the accuracy of determining the equivalent cross-sectional area of the material sample, and thus indirectly affect the determined flux density value. The following subsections describe the measures taken to address these challenges in determining flux density.

2.4.1 Laminated cores and stacking factor

To reduce eddy current losses, cores are usually assembled of laminated sheets of ferromagnetic material. The sheets are assembled parallel to the direction of magnetic flux, and each sheet is coated with a layer of electrical insulation residue. This restricts the flow of eddy currents only to the thickness of each sheet, reducing the associated losses. However, imperfections in the laminated sheets that may occur during the manufacturing and cutting process, the thickness of the insulating layer, and the core assembly process result in an increased volume of the stacked laminations core. The final dimension of the core, which is axial to the direction of the main magnetic flux, is therefore greater than the sum of all the sheet thicknesses from which it is assembled. In this way, the flux-carrying part of the core is reduced compared to a solid core with the same dimensions and this must be compensated for in further calculations and analysis. This is taken into account with a stacking factor k_{sf}, which is the ratio of the sum of all sheets thicknesses to the actual axial length of the assembled iron core.

The cross-section of a laminated core can be observed as if it consists of ferromagnetic material occupying k_{sf} fraction of the total area, and air gap and insulating layer occupying $(1 - k_{sf})$ fraction of the total area. Thus, the equivalent magnetic resistance of the core can be divided into two parallel magnetic resistances (Figure2.13a), that of the iron and that of the air, with different permeability values and cross-sectional areas (Equation2.27).

$$\frac{1}{R_{eq}} = \frac{1}{R_{iron}} + \frac{1}{R_{air}} \tag{2.27}$$

Iron and air magnetic resistances are defined as

$$R_{iron} = \frac{1}{\mu_{iron}} \cdot \frac{\ell}{k_{sf} \cdot S_g} \tag{2.28}$$

$$R_{air} = \frac{1}{\mu_0} \cdot \frac{\ell}{(1 - k_{sf}) \cdot S_g} \tag{2.29}$$

where ℓ is the length of the magnetic path, S_g geometrical cross section area of the core and μ permeability of the material. The equations2.27-2.29can be used to derive the expression for the equivalent magnetic permeability of the laminated core, which is

$$\mu_{eq} = k_{sf} \cdot \mu_{iron} + (1 - k_{sf}) \cdot \mu_0 \tag{2.30}$$

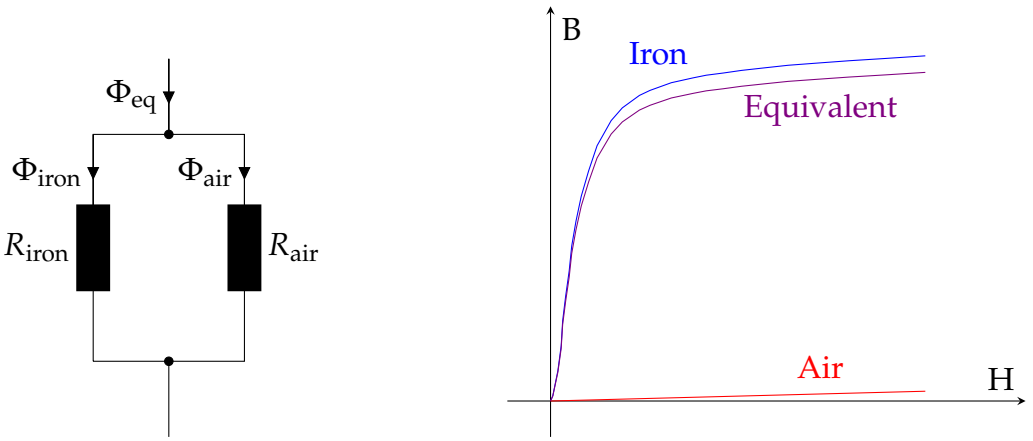

(A) Equivalent magnetic circuit (B) Normal magnetization curves

FIGURE 2.13: Modeling a laminated core as an equivalent homogeneous material

The equivalent permeability is the quantity representing the permeability of the whole core, including the iron and air portions of it. It can be determined from measurements of the magnetic flux Φ in the core and the magnetic field strength H using the following expression.

$$\Phi_{\text{meas}} = \mu_{\text{eq}} \cdot H \cdot S_{\text{g}}. \tag{2.31}$$

However, for the analysis of core losses and the design of electrical machines as a whole, it is essential to determine the corresponding flux densities, especially those in the iron portion of the core. Flux density is defined as the mathematical product of the magnetic permeability of the material and the magnetic field strength. Using this definition and the equation2.30, the iron flux density can be given as follows.

$$B_{\text{iron}} = \mu_{\text{iron}} \cdot H = (\frac{1}{k_{\text{sf}}} \cdot \mu_{\text{eq}} - \frac{1 - k_{\text{sf}}}{k_{\text{sf}}} \cdot \mu_0) \cdot H \tag{2.32}$$

Combining Eq.2.31and2.32provides an expression for the flux density in the iron part of the laminated core

$$B_{\text{iron}} = \frac{\Phi_{\text{meas}}}{k_{\text{sf}} \cdot S_{\text{g}}} - \frac{1 - k_{\text{sf}}}{k_{\text{sf}}} \cdot \mu_0 \cdot H \tag{2.33}$$

Figure2.13bshows how an equivalent normal magnetization curve is decomposed into the normal magnetization curves of iron and air. The flux density of iron is larger than the equivalent flux density due to the correction for the flux-carrying cross-sectional area of the core, which is accounted for by the first term of the equation2.33. The second

term of the equation2.33has a much smaller effect on the final result, but cannot be neglected for precise determination of the flux density at high magnetic field strengths. For example, the expected stacking factor for a 0.1 mm thick lamination is about 90%. This results in a decrease of B by 7 mT at $H = 50$ kA/m, which would be an effect measured in a few parts per thousand, while on the other hand the first term of the equation2.33is increased by about 11%.

2.4.2 Magnetic flux and search winding

The most common and practical procedure of obtaining the signal of magnetic flux is to integrate a voltage signal measured across the search winding. To minimize the magnetic flux in the air enclosed by this winding, it should be wound as close to the core as possible. Depending on the size of the core, the minimum permissible wire bending radius, the winding technique and the maximum values of the magnetic field strength used in the experiments, this may or may not be negligible.

If the average area enclosed by the search winding is represented by $S_{\mathrm{w_s}}$, which is larger than S_{g}, then the obtained flux density defined by equation2.33should be reduced by a term B_{corr} given by the following expression.

$$B_{\mathrm{corr}} = \frac{S_{\mathrm{w_s}} - S_{\mathrm{g}}}{S_{\mathrm{g}}} \cdot \mu_0 \cdot H \tag{2.34}$$

If the wire diameter is kept relatively small and the winding is done by machine, the effect of the air gap on the result is minimized. Using thinner insulating tape without compromising the dielectric strength of the system also reduces the air gap. The larger the core, the smaller the effect of the air gap. The cores used in the experiments of this thesis had cross-sectional areas ranging from 300 mm^2 to 675 mm^2, and the effect of an 0.8 mm air gap on the results was in the range of a few parts per thousand when H was equal to 50 kA.

Chapter 3

Measurement setup

A special measurement setup was designed and built to analyse the influence of the PWM-generated power supply on the total iron losses. The setup can be used both to analyse the individual influence of independent parameters of the single-phase sinusoidal PWM on the total AC losses (AC measurements) and to characterise the material loss as a function of the specific iron loss values for each ΔB, $\frac{dB}{dt}$, and B_{bias} value (DC bias measurements). In the latter case, both DC bias and flux ripple are generated with a single excitation winding and a single-phase inverter source, making this measurement setup novel.

The setup consists of the controllable DC power supply, the single-phase full-bridge inverter, the control board, and the data acquisition system (Figure3.1and3.2). The

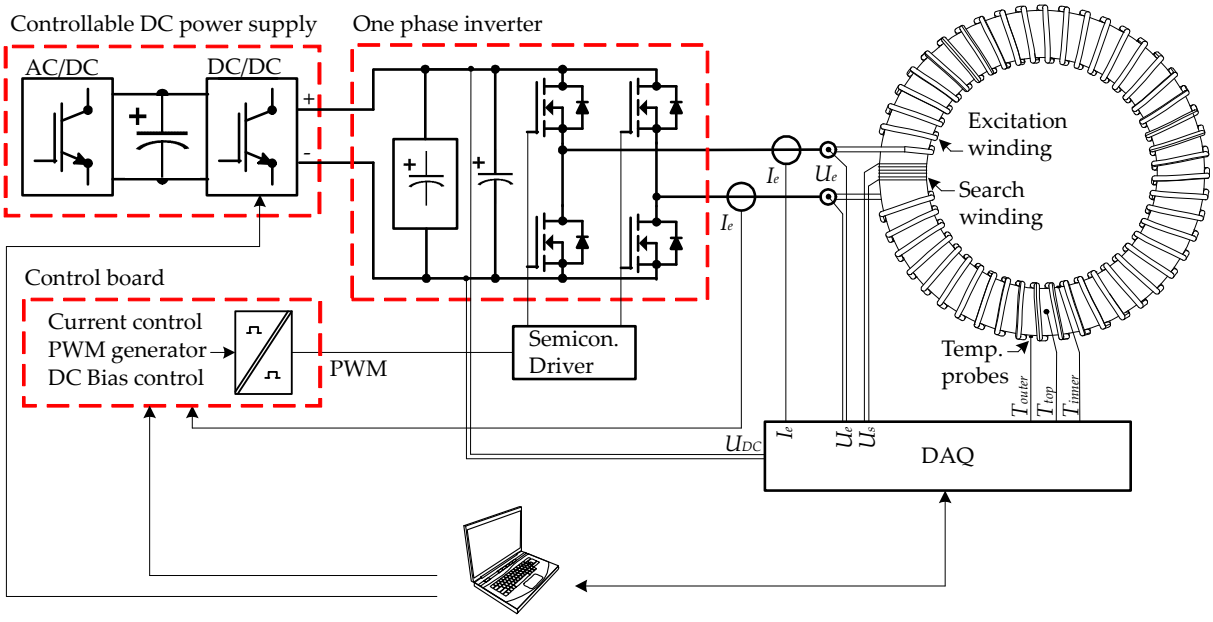

FIGURE 3.1: Block schematics of the measurement setup.

TABLE 3.1: Measurement setup parameters

PART	PARAMETER	VALUE
DC power supply	Type	Delta Elektronika SM15K SM500-CP-90
	Output	15 kW, 0 – 500 V, ±90 A
Inverter	Power modules	Cree CAS300M12BM2
	Switching frequency	2 – 40 kHz
	DC link voltage	0 – 690 V
	DC link capacitance	$C_{main} = 1000\ \mu F$ $C_{bank} = 14$ mF
Measuring equipment	DAQ system	DeweSoft Sirius HS (1MHz)
	Curr. transducer 1	LEM Ultrastab IT205-S, 200A RMS, 283 A pk, 100kHz
	Curr. transducer 2	ABB ES1000F 1 kA, 100 kHz
	Current probe	Tektronix TCP303 DC-15MHz, 150A DC
	Temp. acquisition	WAS5 PRO RTD 1000 + PT1000 (cl. B, 0.12%)

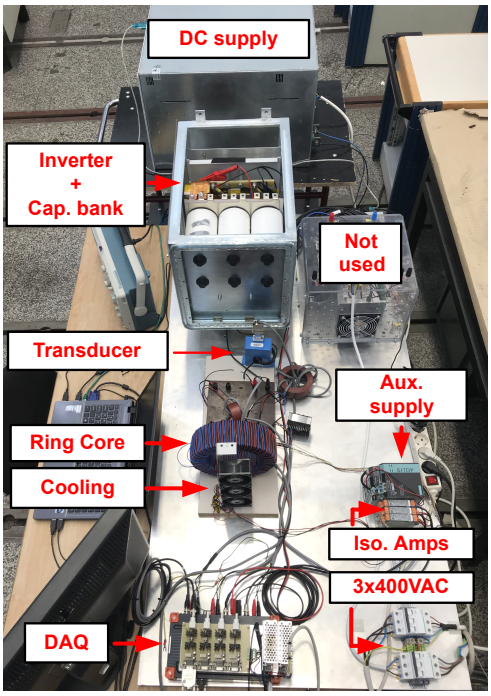

FIGURE 3.2: Photo of the measurement setup built in the laboratory

component parameters of the setup are listed in the table3.1. Instead of a standard Epstein test setup, several laminated ring-core specimens of different sizes were built and wound for the experiments (Table3.2).

3.1 DC power supply

The DC power supply is connected to the AC power grid and is used to provide a stable, arbitrary DC voltage to the DC link of the inverter. The stable, constant DC voltage supply for the DC link is critical for determining the power loss characteristics of the material since a slight change in the voltage value can result in significant changes in the calculated power losses. The use of uncontrolled AC / DC converters is not an option as voltage fluctuations of the AC power supply will affect the results. Also, when the core is highly saturated, a high ripple current is drawn from the DC link, which affects the instantaneous value of the DC link voltage. Increasing the capacitance of the DC link helps to minimise the ripple of the DC link voltage. For this reason, the capacitance bank is added in parallel with the DC link capacitance of the inverter.

TABLE 3.2: Ring core parameters

PARAMETER	CORE C0	CORE C1a	CORE C2a	CORE C3
Inner diameter (m)	0.16	0.450	0.200	0.120
Outer diameter (m)	0.22	0.495	0.220	0.165
Uniformity ratio (d_{outer}/d_{inner})	1.375	1.1	1.1	1.375
Ring width (mm)	30	22.5	10.0	22.5
Core height (mm)	65	31.5	31.5	31.5
Material type	M400-50A	M400-50A	M400-50A	M400-50A
Build process	laser, backlack	laser, backlack	laser, backlack	laser, backlack
Stacking factor	0.977	0.9524	0.9524	0.9524
Mass (kg)	8.7	7.68	1.52	2.32
Equivalent cross sectional area according to IEC 60205 (cm^2)	18.89	6.7422	2.9965	6.6906
Equivalent magnetic length according to IEC 60205 (m)	0.5869	1.4822	0.6587	0.4402

The DC power supply used in the experiments provides high stability of the output DC voltage. As indicated in the datasheet of SM15K model, RMS value of ripple and noise combined, in constant voltage regulation mode, is 10 mV at a maximum current setting of 90 A and 25 mV at a maximum voltage setting of 500 V. This results in 60 ppm and 50 ppm ripple factor value, respectively, where ripple factor RF is defined as:

$$RF = \frac{\sqrt{U_{\mathrm{RMS}}^2 - \overline{U}_{\mathrm{DC}}^2}}{\overline{U}_{\mathrm{DC}}} = \frac{U_{\mathrm{AC}}}{\overline{U}_{\mathrm{DC}}}, \tag{3.1}$$

where U_{RMS} is the RMS value of the complete voltage waveform, $\overline{U}_{\mathrm{DC}}$ is the mean value of voltage waveform and U_{AC} the RMS value of the AC ripple alone. However, this changes when the power supply is loaded with an inverter-fed load and high currents, which occur in both AC and DC measurements. Low switching frequencies and high core saturation points stress the DC power supply source the most in terms of voltage ripple.

Figures3.3and3.4show typical waveforms of the DC link voltage U_{DC} and the excitation current I_{e} during the AC measurement procedure for cores C1a and C3,

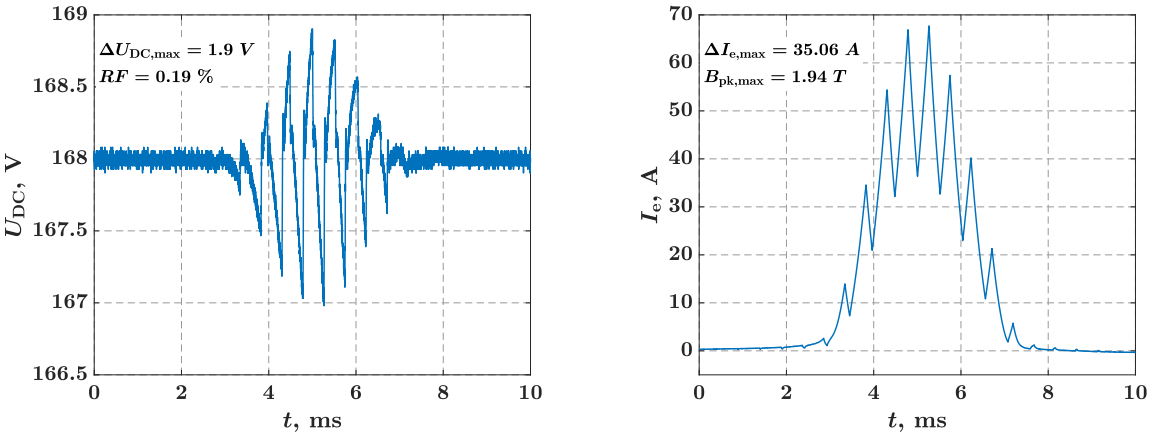

(A) DC link voltage

(B) Excitation current

FIGURE 3.3: The ripple of the DC link voltage and the half-period of the excitation current causing the ripple in the AC measurements experiment on the C1a core and the peak flux density of the fundamental $B_{1hpk} = 1.94$ T. Experiment parameters: $f_{sw} = 2$ kHz, $f_{1h} = 50$ Hz, $U_{DC} = 168$ V, bipolar modulation.

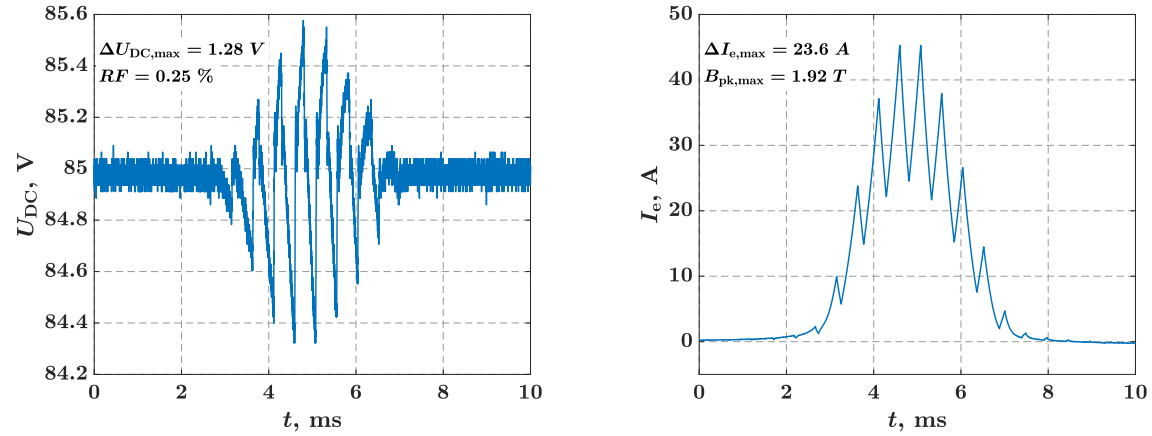

(A) DC link voltage

(B) Excitation current

FIGURE 3.4: The ripple of the DC link voltage and the half-period of the excitation current causing the ripple in the AC measurements experiment on the C3 core and the peak flux density of the fundamental $B_{1hpk} = 1.92$ T. Experiment parameters: $f_{sw} = 2$ kHz, $f_{1h} = 50$ Hz, $U_{DC} = 85$ V, bipolar modulation.

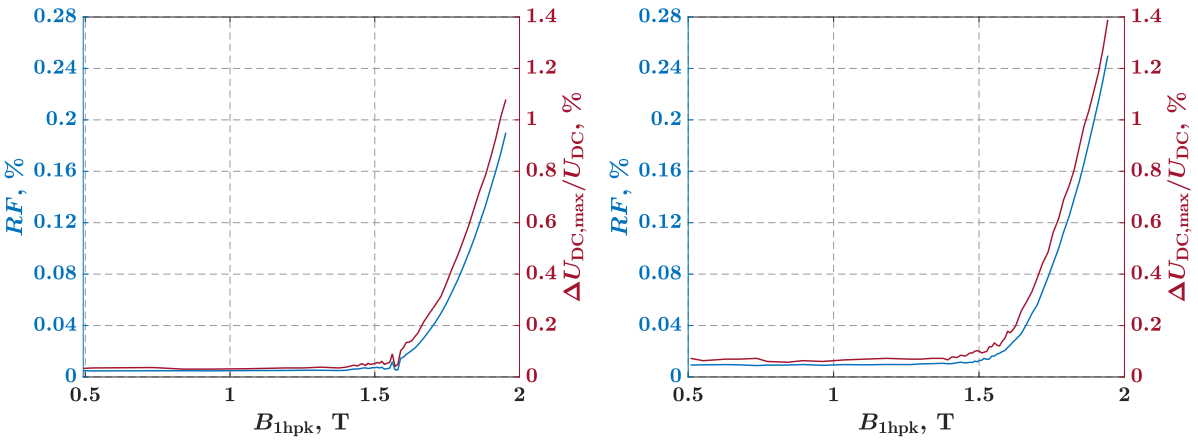

(A) C1a core

(B) C3 core

FIGURE 3.5: Ripple factor (bluecurve) and ratio of peak-to-peak ripple to the mean value (redcurve) with respect to peak flux density B, determined during the AC experiments for cores C1a and C3. Parameters of the AC measurement experiment: $f_{\mathrm{sw}} = 2$ kHz, $f_{1\mathrm{h}} = 50$ Hz, $U_{\mathrm{DC,C1a}} = 168$ V, $U_{\mathrm{DC,C3}} = 85$ V, bipolar modulation.

respectively. These two cores were selected here for comparison due to the significant difference in core volumes. The waveforms are shown for the worst case with respect to the ripple of U_{DC}: low inverter switching frequency of $f_{\mathrm{sw}} = 2$ kHz and relatively high peak flux density of $B_{1\mathrm{hpk}} = 1.94$ T and $B_{1\mathrm{hpk}} = 1.92$ T, respectively.

The determined ripple factor under these conditions is much higher than for the pure DC current load, which in both cases is about $\approx 0.2\%$. However, this is expected and satisfactory in such applications with the highly rippled current load. Figure3.5 shows the dependence of the ripple factor of U_{DC} and $\Delta U_{\mathrm{DC}}/\overline{U}_{\mathrm{DC}}$ ratio on the peak flux density in the cores. It can be seen that the ripple factor practically does not change up to the point where the cores are fairly saturated and is around 50 ppm for core C1a and 90 ppm for core C3. As the saturation progresses, exponential growth can be seen.

Figures3.6and3.7show typical waveforms of U_{DC} and I_{e} during the DC measurement procedure for cores C1a and C3. DC bias measurements are generally more demanding for the DC power supply, resulting in slightly higher values of the ripple factor of U_{DC} than for the AC measurements. Table3.3shows how the ripple factor of the DC link voltage changes with different parameters of the DC bias experiment. The B_{bias} value remains unchanged for all data shown and is the largest B_{bias} obtained. The largest DC bias of magnetic flux density was chosen because the largest current is drawn from the converter at this point, leading to the worst case in terms of DC link

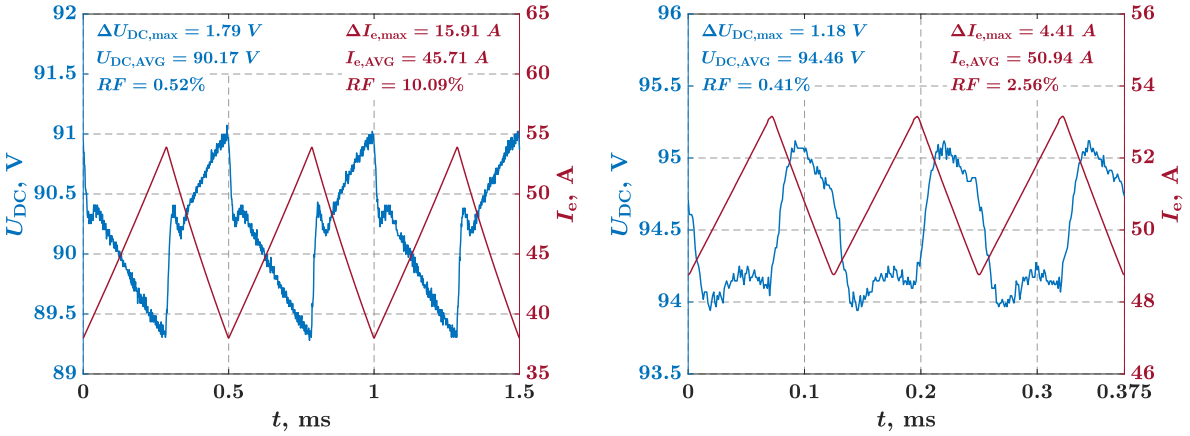

(A) $f_{sw} = 2$ kHz, $\Delta B = 80$ mT, $B_{bias} = 1.85$ T (B) $f_{sw} = 8$ kHz, $\Delta B = 20$ mT, $B_{bias} = 1.87$ T

FIGURE 3.6: DC link voltage U_{DC} (bluesignal) and excitation current I_e (redsignal) waveforms during DC bias experiments with two different parameter sets and C1a core.

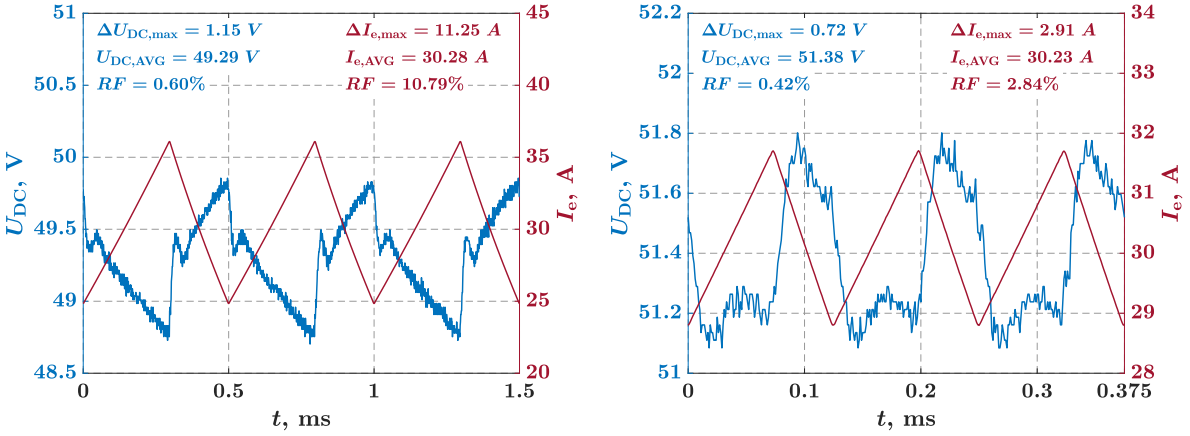

(A) $f_{sw} = 2$ kHz, $\Delta B = 80$ mT, $B_{bias} = 1.83$ T (B) $f_{sw} = 8$ kHz, $\Delta B = 20$ mT, $B_{bias} = 1.83$ T

FIGURE 3.7: DC link voltage U_{DC} (bluesignal) and excitation current I_e (redsignal) waveforms during DC bias experiments with two different parameter sets and C3 core.

voltage ripple for any set of the experiment parameters. However, the ripple factor of U_{DC} changes between experiments with different ΔB and $\frac{dB}{dt}$ due to the change in the ratio $\Delta U_{DC}/\overline{U}_{DC}$. Table3.4shows how these parameters change between the DC bias experiments.

Assuming that the other parameters remain unchanged, ΔB is directly controlled by the value of the DC link voltage. Thus, with an increase in ΔB, $\overline{U}_{DC}$ also increases. And

TABLE 3.3: Ripple factor of the DC link voltage at different parameters of the DC bias experiment and the specific B_{bias} value, shown for the two cores C1a and C3. Same color indicates equal $\frac{\mathrm{d}B}{\mathrm{d}t}$ parameters.

C1a: $RF_{U_{\text{DC}}}$ (%)	ΔB, mT			
$B_{\text{bias}} = 1.85$ T	20	40	80	120
2	/	/0.520.36		
4	0.700.400.21/			
8	0.410.21/	/		
16	0.26/	/	/	

f_{sw}, kHz

C3: $RF_{U_{\text{DC}}}$ (%)	ΔB, mT			
$B_{\text{bias}} = 1.83$ T	20	40	80	120
2	/1.030.600.42			
4	0.750.410.22/			
8	0.420.22/	/		
16	0.29/	/	/	

f_{sw}, kHz

TABLE 3.4: Average DC link voltage and peak-to-peak ripple at different parameters of the DC bias experiment and the specific B_{bias} value, shown for core C3. Same color indicates equal $\frac{\mathrm{d}B}{\mathrm{d}t}$ parameters.

C3: $\overline{U}_{\text{DC}}$, V	ΔB mT			
$B_{\text{bias}} = 1.83$ T	20	40	80	120
2	/27.149.372.5			
4	27.549.997.0/			
8	51.499.4/	/		
16	103.9/	/	/	

f_{sw}, kHz

C3: ΔU_{DC} , V	ΔB mT			
$B_{\text{bias}} = 1.83$ T	20	40	80	120
2	/1.021.061.08			
4	0.670.660.66/			
8	0.650.66/	/		
16	0.83/	/	/	

f_{sw}, kHz

if the parameter ΔB is to remain unchanged, $\overline{U}_{\text{DC}}$ must be increased with an increase in f_{sw} to compensate for an increase in system reactance. Thus, if either of the parameters ΔB or f_{sw} changes independently, resulting in a change in the parameter $\frac{\mathrm{d}B}{\mathrm{d}t}$, $\overline{U}_{\text{DC}}$ also changes. However, if they change in a way that the parameter $\frac{\mathrm{d}B}{\mathrm{d}t}$ remains constant, $\overline{U}_{\text{DC}}$ also remains constant. Table diagonals with the same $\frac{\mathrm{d}B}{\mathrm{d}t}$ parameter are marked with the same text color in the table3.4.

The ΔU_{DC} remains practically unchanged with the change of ΔB parameter, but it changes with the switching frequency. At lower switching frequencies, the duration of the half period is longer which results in the higher change in the current and the DC link voltage. This leads to the highest values of ΔU_{DC} at the lowest switching frequency of $f_{\text{sw}} = 2$ kHz.

Since the mean value of the DC link voltage changes much more than the peak-to-peak of the voltage ripple between experiments, it is mainly the value of the average

DC link voltage that determines the ripple factor. If the $\overline{U}_{\mathrm{DC}}$ remains constant between experiments, the U_{DC} ripple factor is defined solely by the change in ripple of U_{DC}. Thus, generally, the largest ripple factor of the U_{DC} appears at the lowest frequency and lowest $\overline{U}_{\mathrm{DC}}$.

3.2 Inverter

The excitation winding of the ring core under test is supplied with a PWM voltage by the inverter. This results in PWM waveforms with different RMS voltage values, fundamental frequencies, and PWM frequencies when performing AC measurements, while DC measurements use the inverter to generate duty cycle controlled square-wave voltage to obtain the desired values of the DC bias (B_{bias}). The power switches in the inverter are based on Silicon Carbide (SiC) technology, which ensures a wide operating capability in terms of switching frequency, dead-time minimization, absence of knee voltage of the active switch, and conduction of the MOSFET in the third quadrant. All these features of the SiC power module are important for generating a nearly ideal and rigid voltage across the excitation winding. The control board of the inverter is based on the TMS320F28379D digital signal processor (DSP) from Texas Instruments. Its main task is to generate PWM signals for different types of modulation to supply the excitation winding. The excitation current is monitored by DSP using a ABB ES1000F 1 kA, 100 kHz current transducer for control and over-current protection purposes.

3.3 Current transducers and probes

Several current transducers and current probes were used in this research. Several manufacturers and ranges were tested before a final selection was made. The most important current transducer is the one used for measuring the excitation current, since it is directly related to the calculation of the power loss. Another current transducer is used for current control and monitoring by DSP. Finally, a high bandwidth current probe is used for special measurements and analysis.

3.3.1 Zero-flux fluxgate transducers

Precise measurement of the excitation current is one of the essential elements of this research, since this is a quantity used to calculate the power loss in the core. The experiments are designed so that the measured excitation current covers a wide range of amplitudes, RMS values, and frequencies, which places high demands on the current sensor. For this purpose, an isolated zero-flux fluxgate current transducer was chosen, the basic parameters of which are listed in the table3.1. The fluxgate sensing element is a "saturable inductor" integrated into the core [43,44], which is designed so that any change in the external field induced by the measured primary current affects the saturation level and changes the permeability of the core and thus its inductance. In this way, the presence of an external field changes the inductance value of the field-sensing element which is detected by the processing electronics. The closed loop principle is then used to detect and compensate for the inductance variations caused by the primary current I_P by injecting a current into the secondary coil of the transducer I_S to bring the field back to zero and thus the inductance back to a reference case.

This type of transducer exhibits low offset and offset drift because the magnetic core is cycled through its B-H loop, suppressing any magnetic offset in the fluxgate core. This advantage is particularly noticeable in low current measurements where the relative effect of offset is more significant. In addition, they have a wide dynamic range that allows both small and large currents to be measured with the same transducer, very

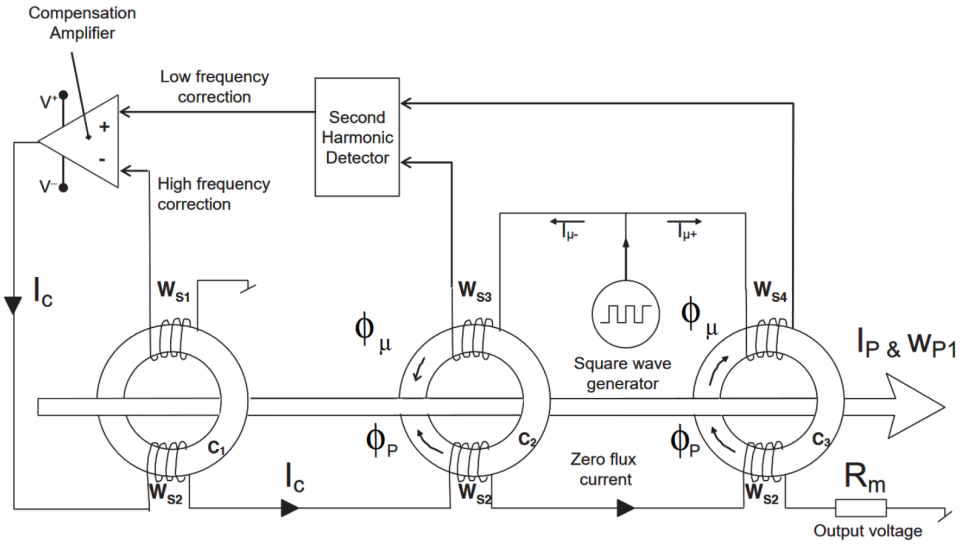

FIGURE 3.8: Block schematics [43] of zero-flux fluxgate transducer used in the measurement setup.

high resolution, and the high bandwidth which is achieved by a separate core for the current transformer effect.

In addition to these advantages, the LEM IT series has been further improved by duplicating the field sensing element, using two toroidal cores with opposing excitation coils, and improving the design of the high-frequency current transformer, allowing higher precision and bandwidth. The block schematic showing the operating principle of the LEM IT series transducers is shown in figure3.8and the photo of the actual sensor is shown in figure3.9. It consists of a current sensing head composed of three magnetic cores, C1, C2, and C3, with primary (w_{P1}) and secondary windings (w_{S1} to w_{S4}), as shown in figure3.8. For the upper frequency range, the secondary current results from a transformer effect in two secondary coils (w_{S1} and w_{S2}). For lower frequencies, including DC, the design functions as a closed-loop fluxgate transducer, with windings w_{S3} and w_{S4} being the fluxgate sensing coils.

The main IT series advantages are:

- Very low initial offset and drift with temperature
- Very high accuracy and stability
- Excellent linearity (< 1 ppm)
- Very good temperature stability (< 0.3 ppm/K)
- Large bandwidth (DC to 100 kHz)
- Very low distortion for AC current measurement
- Very low noise on the output signal

The disadvantages are mainly the complexity of the build, the size, the relatively high power consumption and the price of the transducer, none of which pose as an issue for a laboratory setup. The manufacturer states in [43] that the increased noise level is observed at the excitation frequency and may be coupled into the primary circuit. This

FIGURE 3.9: Photo of zero-flux fluxgate transducer used in the measurement setup.

effect was observed earlier in the research when the LEM IT700-S transducer was used. However, the noise in the primary circuit was indistinguishable later when the IT205-S transducer was used.

3.3.2 Transducer selection

The DC bias experiment was designed to determine the power loss characteristics for a wide range of B_{bias} values, which is achieved with a wide range of excitation current values. In order to utilise the full sensing range of the transducer used in the setup, the supply wire was wound five times through the sensor. This apparently increases the excitation current sensed by the transducer. Figure3.10shows RMS values of the excitation current for typical DC bias measurement experiments. It is plotted with respect to the B_{bias} value for three different values of ΔB, a switching frequency of $f_{\text{sw}} = 2$ kHz, and cores C1a and C2a. The largest core by volume, C1a, also has the lowest ratio of excitation winding turns to core length (N_{exc}/ℓ ratio), which means that the excitation current is the largest for the same H_{bias} compared to the other cores used in the research. In contrast, core C2a is the core with the smallest volume and the largest N_{e}/ℓ ratio, resulting in the smallest values of excitation current for the same H_{bias}. This is clearly visible when comparing the subfigures3.10aand3.10b, where smaller values of current RMS are reached for the C2a core compared to the C1a core. Even so, most of the transducer's nominal range of $I_{\text{N}} = 200$ A is used for C2a core as well.

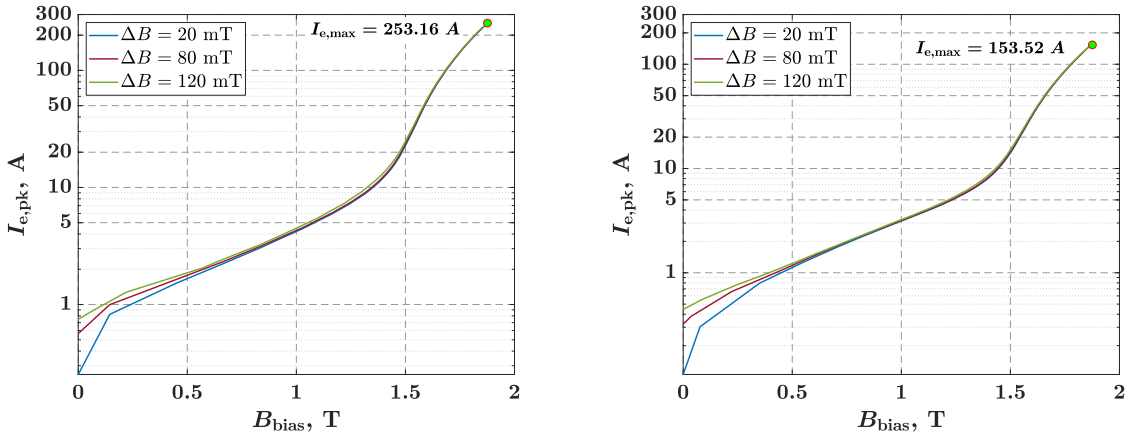

(A) C1a core

(B) C2a core

FIGURE 3.10: Excitation current RMS with respect to the B_{bias} for several values of ΔB.

The DC component of the excitation current contributes most to the total current RMS once the core begins to saturate, so there is almost no difference between the values of the current RMS, regardless of ΔB. For smaller values of $B_{\text{bias}} < 0.5$ T, the AC component of the excitation current becomes more significant compared to the DC component, leading to larger differences in the RMS current value for different ΔB values. Similarly, changing the switching frequency does not significantly affect the DC component of the current during the DC bias experiments, so this plot represents the expected range of the excitation current in this research, which mainly depends on the core under test.

The effect of multiple turns through the sensor on the result was tested before the final measurements were made. Tests were performed for 3 and 5 turns and compared with the results for a single pass of the wire through the sensor. Apart from the existing deviations between measurements due to measurement uncertainty, no additional deviations were observed when the number of turns was changed. Care was taken to distribute the turns evenly around the core to ensure a more even distribution of the magnetic field in the sensor cores.

A transducer with a lower current rating could be used, but the measured current at lower B_{bias} values would be at or near the same percentage of the rated current as the transducer used, since fewer turns would pass through the sensor. In addition, the accuracy of transducers with lower current ratings is often significantly lower. For example, the IT205-S transducer used has an accuracy of 84 ppm, while the same IT60-A series with a rated current of $I_{\text{N}} = 60$ A has an accuracy of 273 ppm.

The author is aware of the reduced accuracy at lower values of excitation current and the problems that may arise. The errors are minimized by using high-precision sensors and multiplying the excitation current by winding 5 turns through the sensor. It is expected that the low B_{bias} points will not have a dominant effect on the total losses when the loss data is applied to the machine at its real operating point.

3.3.3 Phase shift and amplitude attenuation corrections

The active electric power being delivered is defined with the applied voltage and current over one period of time, as is stated in the following expression:

$$P = \frac{1}{T} \int_0^T u(t) i(t) \mathrm{d}t. \tag{3.2}$$

When two AC signals are multiplied, the phase shift between the two signals affects the final result. An error in determining the phase angle of one of the two signals can result in significant errors in the power calculation [45]. The magnitude of the error in the final result depends not only on the magnitude of the error in determining the phase angle, but also on the actual phase shift between the signals. For smaller phase shifts, where the power factor is at or near unity, the phase angle error has little effect on the calculated power. However, as the phase shift increases, and especially as it approaches 90 degrees, even a small error in phase angle determination can significantly change the result.

When the iron core is saturated, the reactive power component used to magnetise the core accounts for most of the apparent power, while the active power component used to cover the iron losses accounts for only a small part. At this point, the power factor approaches zero and the phase angle between the applied voltage and the excitation current approaches 90 degrees. The curves in figure3.16represent the dependence of the correction factor on the phase angle as it approaches 90 degrees, for different values of the phase angle correction.

Current transducers cause a phase shift in the measured AC current signal, delaying the measured current signal relative to the actual current. The phase shift varies with the frequency of the measured AC current and generally increases with frequency. At lower frequencies, the transducer operates with fluxgate sensors and a second harmonic detector. The maximum frequency for this mode of operation is usually 5-10 times lower than the modulation frequency of the CT electronics. At higher frequencies, the CT operates first as an active current transformer and finally, with further increase of excitation frequency, enters a standard current transformer mode (Figure3.11). This design provides excellent bandwidth, but the phase shift to frequency dependence changes between these two modes and a sensitive region can occur at frequencies where the response curves of the two modes overlap.

Amplitude attenuation is introduced into the measured signal as well and also depends on the frequency change. However, its effect on the calculation of power loss for highly inductive loads is not as significant as the phase angle shift.

Determination of correction curves

The phase shift and amplitude attenuation of the current transducer as a function of frequency can be determined, and corrections can be applied to the measured current signal to compensate for errors. The block schematics of the measurement setup used

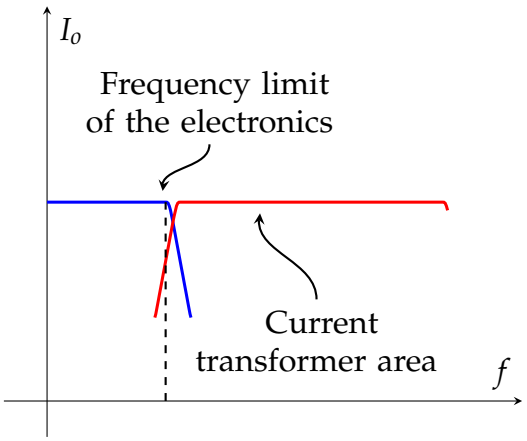

FIGURE 3.11: Current transducer bandwidth for two different modes of operation

for this purpose is shown in figure3.12, and the setup parameters are listed in table3.5. The function generator module is used to generate a sinusoidal reference signal with varying frequency, starting with pure DC up to a frequency of 100 kHz, which is then amplified by the current amplifier. The output of the current amplifier is connected to the series connection of the low inductance shunt and the current transducer, which is the device under test here. All cabling was implemented using coaxial cables and N-type connectors. CT outputs a current signal of $\pm$200 mA, which is converted to a voltage using a current-to-voltage (I-V) converter. Since the phase shift and amplitude attenuation characteristics obtained depend on both the current transducer and the I-V converter, they must be considered as a whole and are to be used in this configuration

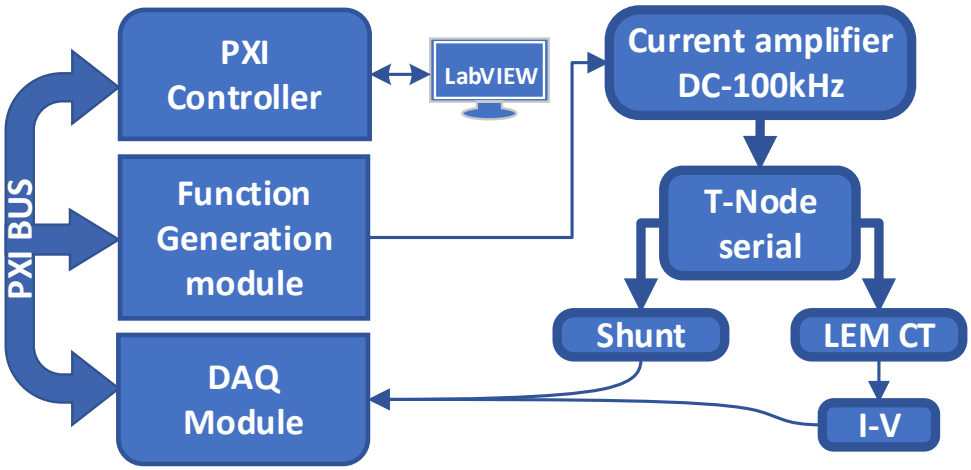

FIGURE 3.12: Block schematics of the measurement setup for current transducer phase and amplitude correction characteristics.

TABLE 3.5: Measurement setup parameters

PART	PARAMETER	VALUE
Current amplifier	Type	Toellner, TOE 7621-6
	Output	240 W, ±6 V, ±40 A, $DC - 100$ kHz
Measuring equipment	DAQ system	National Instruments NI-PXI4461, 2x24-b sigma delta A/D
	Current transducer	LEM Ultrastab IT205-S, 200A RMS, 283 A pk, 100kHz
	Low-Inductance shunt	FER-ZOEM, 10 A, 71.4 mΩ, Cage-type

for all further measurements. The signal cable between CT and the I-V converter and the voltage probes between the I-V and the DAQ module and the shunt and the DAQ module are the same ones that will be used later in the measurements, since their inductive and capacitive properties may also have an influence on the determined characteristics.

The DAQ module is used to obtain voltage measurement signals from both the low inductance shunt and the I-V converter. Post-processing is then used to determine the phase delay between the two voltages obtained for each frequency of the reference signal at the desired resolution. The voltage obtained from the low inductance shunt is

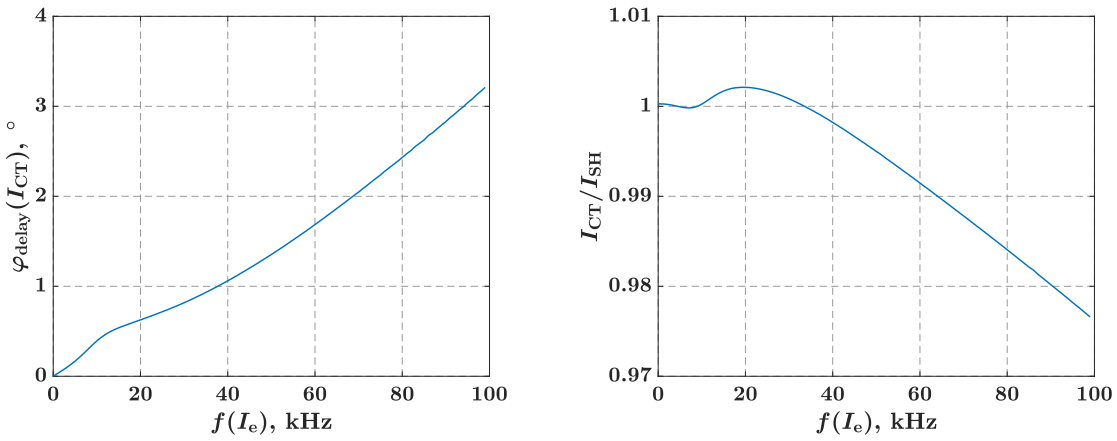

(A) Phase shift

(B) Amplitude attenuation

FIGURE 3.13: Phase shift and amplitude attenuation characteristics in dependence of measured current frequency for LEM IT205-S current transducer used in the measurements (see table3.1)

considered as the reference, and the phase delay and amplitude attenuation found are attributed to the influence of CT, i.e., the CT system as a whole.

Figure3.13shows the phase shift and amplitude attenuation characteristics obtained with the described measurement setup. The characteristics were obtained for an excitation current with an initial RMS value of 10 A at a frequency of 50Hz, which is due to the 10 A limit of the low inductance shunt. The initial current is given here as a reference value because no current control is implemented, so the current naturally decreases as the frequency increases due to the change in the impedance of the system (Figure3.14). The measurements were performed six times and the curves shown in figure3.13are the averaged curves of all six obtained characteristics.

The red shaded area in figure3.15ashows the difference between the six characteristics determined by repeated measurements under presumably the same measurement conditions. It represents the expected error in the determination of the phase shift characteristic as a function of the frequency of the measured current, which is due to measurement uncertainty, a non-ideal current amplifier, temperature variations, and possibly some other unknown factor. There is a relatively large peak in the difference around 17 kHz, which is the frequency close to the modulation frequency of the CT electronics and an area of transition to current transformer operation.

For further investigation, the experiments were repeated with different settings of the initial RMS output value of the current, namely 5 A at a frequency of 50 Hz

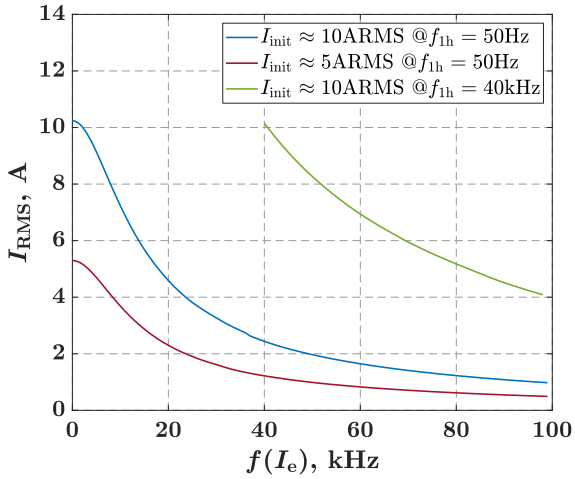

FIGURE 3.14: Dependence of the excitation current RMS on the frequency during the CT calibration experiment, shown for three different cases of initial current setting.

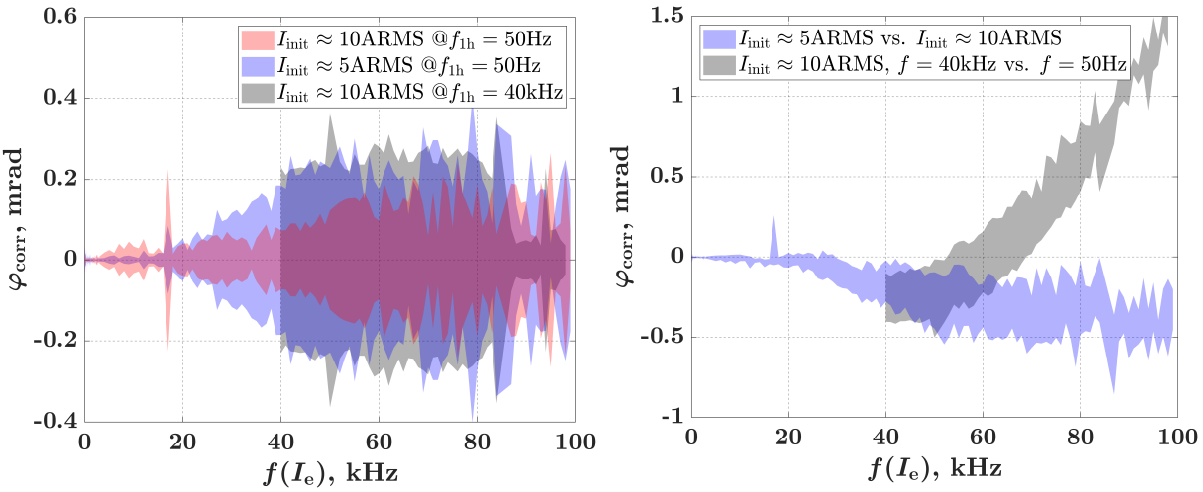

(A) Uncertainty due to the measurement repeatability

(B) Uncertainty due to sensitivity to the current value

FIGURE 3.15: Measurement uncertainty in determining phase shift characteristics using the proposed setup.

and 10 A at a frequency of 40 kHz (Figure3.14). In this way, the RMS value of the current is different over the entire frequency range and any difference in the obtained characteristics would indicate that the phase shift depends on the RMS value of the measured current.

The differences are shown in figure3.15ain blue shading for the initial RMS current value of 5 A at 50 Hz and in grey shading for the initial RMS current value of 10 A at 40 kHz. As for the uncertainty due to the repeatability of the measurements, a slight deterioration of the results compared to the first experiment can be observed. Moreover, a gradual drift of the obtained characteristics is observed compared to the first experiment (Figure3.15b). The phase characteristics obtained with a lower current are somewhat steeper above an excitation current frequency of 20 kHz, resulting in a larger delay in the phase shift. In contrast, characteristics obtained with a higher current are less steep, resulting in a smaller phase shift delay.

This indicates that the effect of signal amplitude on the obtained characteristics needs further investigation, especially for the higher frequencies. In addition, the effect of the harmonic content in the reference signal on the correction curves needs to be investigated. However, this is beyond the scope of this research.

As will be discussed in more detail in the next section, the greatest need for correction occurs when the cores are saturated, i.e., at higher current values. This and the current transducer rating of 200 A RMS are the reasons that the correction curves obtained at

10 A at a frequency of 50 Hz were selected as the correction curves to be used in the later calculations. Although the current values in the experiment with the initial RMS current value of 10 A at 40 kHz are higher, this experiment does not cover the frequency range below 40 kHz, which is of most interest to this research.

Effect of the phase shift correction on power loss calculation

Calculating active power for high inductive loads is challenging, especially at higher excitation frequencies. Any phase shift delay introduced into the measurement system can significantly affect the power calculation. By determining the phase shift characteristics of the current transducer, a correction factor can be implemented in the power loss calculation.

Figure3.16shows the dependence of the correction factor on the current-voltage phase angle for four different cases of phase shift values. The correction factor is defined

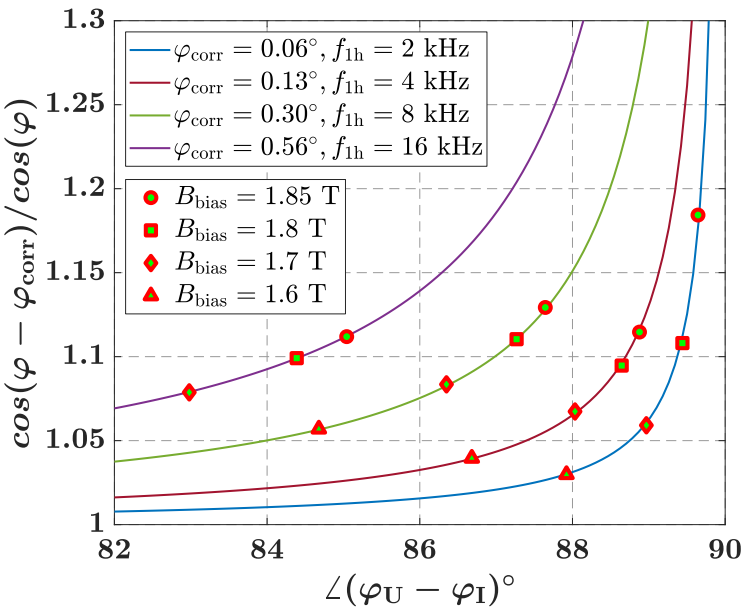

FIGURE 3.16: Effect of the current transducer phase shift on power loss calculation. Curves are shown for several different frequencies of the fundamental current ripple and corresponding phase shift correction of the transducer used in the experiments. Actual determined data points are shown as the results of the DC bias experiment performed on the C1a core with following parameters:[$\Delta B = 80$ mT, ($\frac{dB}{dt} = 0.32$ T/ms)],[$\Delta B = 80$ mT, $\frac{dB}{dt} = 0.64$ T/ms],[$\Delta B = 40$ mT, $\frac{dB}{dt} = 0.64$ T/ms],[$\Delta B = 20$ mT, $\frac{dB}{dt} = 0.64$ T/ms].

as the ratio of the cosine of the corrected phase angle and the measured phase angle, and as such can be used to indicate the difference in calculated power for a given harmonic component with and without the use of the phase shift corrections. The phase shift values were selected from the determined correction curves for the transducer used in the experiments and for typical frequencies used in the DC bias experiments.

Looking at the curves, it can be clearly seen how the influence of the correction factor increases exponentially as the phase angle between current and voltage approaches 90 degrees. In addition, the correction factor increases with increasing frequency, since the phase shift caused by the transducer also increases with frequency.

The markers on the curves represent actual points measured for the C1a core during the DC bias experiments. For example, at a fundamental frequency ripple of 2 kHz, $\Delta B = 80$ mT, and at $B_{\text{bias}} = 1.85$ T, the phase angle between current and voltage was 89.65 $^\circ$ and the correction factor had a value of 1.18. Thus, the power of the fundamental would have been 18% lower if the correction had not been applied.

Although the correction factor is higher at higher frequencies, the phase angle between current and voltage is smaller than at a lower frequency for the same B_{bias} value. This is because the ratio of inductance to resistance decreases with frequency as permeability decreases and wire resistance increases. Therefore, at the highest B_{bias} values the correction factor for the fundamental harmonic is approximately between 5 and 15%, regardless of the DC bias experiment parameters. As the DC bias is reduced below 1.4 T, the effect of the correction nearly diminishes.

Figure3.17shows the distribution of active power loss for C1a core during DC bias experiments with a fundamental frequency ripple of 2 kHz and $\Delta B = 80$ mT. Distribution is shown for several different values of B_{bias} and up to the fifth harmonic component. As the core becomes more saturated, the contribution of the fundamental to the total active power decreases. The same is true for all other odd harmonics, whose contribution even becomes negative at the highest values of B_{bias}. On the other hand, the amplitudes of the even harmonics increase. This is due to the way the DC bias is achieved in the core. The value of the DC bias is controlled by the duty cycle of the inverter switches. For higher DC current values, a greater asymmetry of the duty cycle is required, which leads to a greater asymmetry of the triangular waveform of the excitation current, and the transition from the triangular wave to the sawtooth wave leads to the appearance of the even harmonics.

The contribution of the fundamental harmonic to the total active power at $B_{\text{bias}} = 1.85$ T is about 43%. Although the correction factor for the fundamental harmonic in

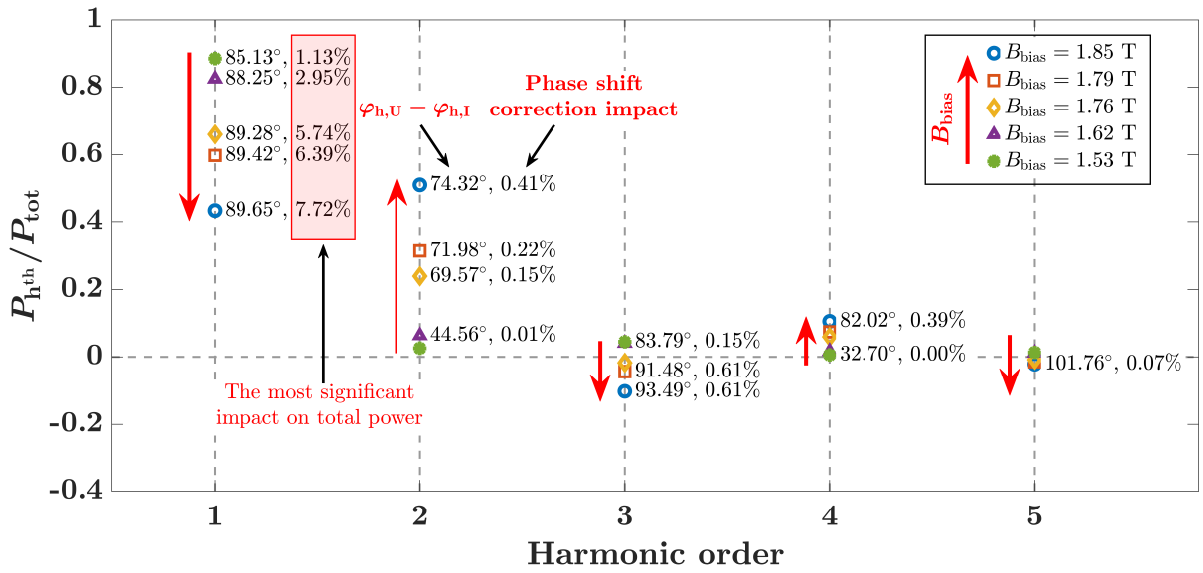

FIGURE 3.17: Effect of the phase shift correction on total power loss calculation shown for each harmonic component up to the fifth order and several B_{bias} values. Actual determined data points are shown as the results of the DC bias experiment performed on the C1a core with following parameters: $f_{\text{sw}} = 2$ kHz, $\Delta B = 80$ mT and ($\frac{\mathrm{d}B}{\mathrm{d}t} = 0.32$ T/ms).

this particular case is 18%, it affects the total active power by only 7.72%. However, this still represents a significant impact on the result. Observing the effects of the other harmonic components on the final result, one can see that the phase shift correction has a much smaller effect on the total active power. In general, about 85% of the correction applied to the calculated power is accounted for by the fundamental.

The fundamental frequency of the current ripple is equal to the switching frequency of the inverter, which means that the maximum fundamental frequency of the ripple in this experimental setup can be $f = 40$ kHz. At present, this is also the maximum switching frequency expected in the power drive applications. Therefore, the phase shift and amplitude attenuation correction characteristics must be determined as accurately as possible, up to the maximum switching frequency at which the DC bias experiments will be performed.

Figure3.18ashows (in blue) the power loss curve obtained during the DC bias experiment performed on the C1a core with experimental parameters $f_{\text{sw}} = 2$ kHz, $\Delta B = 80$ mT, and ($\frac{\mathrm{d}B}{\mathrm{d}t} = 0.32$ T/ms). The red curve shows the power loss curve for the case where the phase shift and amplitude attenuation corrections were included in the power loss calculation. The correction factor for this particular case is shown in figure 3.18b. For B_{bias} values below 1.4 T, the effect of the correction is negligible. However, as

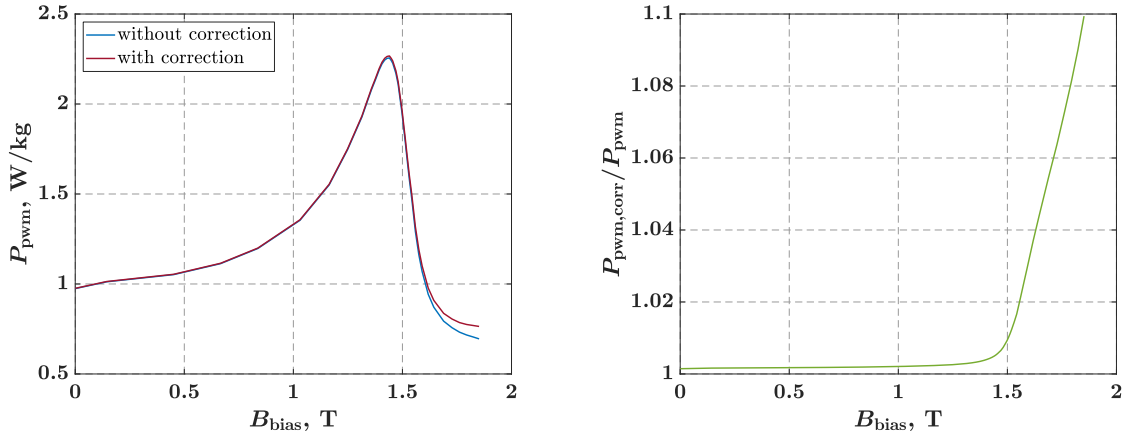

(A) Power loss curves

(B) Phase shift correction effect

FIGURE 3.18: Results of the DC bias experiment performed on the C1a core with and without the use of phase shift correction. The DC bias experiment was performed with the following parameters: $f_{\mathrm{sw}} = 2$ kHz, $\Delta B = 80$ mT and ($\frac{\mathrm{d}B}{\mathrm{d}t} = 0.32$ T/ms).

the core saturates, the correction increases significantly, reaching 10% at $B_{\mathrm{bias}} = 1.85$ T for this particular experiment.

3.4 Windings

To perform the experiments, two different windings are wound around each core: an excitation winding, which is used to generate a magnetic field in the core, and a search (sense) winding, which is used to detect the magnetic field generated.

3.4.1 Excitation winding: design approach

There are generally two different approaches to configure the measurement setup with respect to the excitation circuit: use of separate windings for the AC and DC excitation, and combining the AC and DC excitation into a single winding. The use of separate excitation windings has several drawbacks. Apart from the fact that preparation of sample is technologically more complicated and time consuming, AC ripple induction in the DC winding is inevitable. This reduces the ability to maintain a steady DC bias field. Adding an inductor as a filter to the DC circuit can reduce the occurrence of additional ripple, but it still affects the DC current supplied to the sample. Also, if the setup is used to test at multiple excitation frequencies, several different inductors

should be used to optimize attenuation in specific frequency ranges, which complicates the setup.

Another drawback is the existence of interwinding capacitance between AC and DC excitation windings. To achieve high DC bias fields, the number of turns of the DC winding is usually substantial and it overlaps with the AC winding over the entire length of the core. In this way, the total interwinding capacitance of the excitation system is increased. Because of this capacitance, non-negligible charging currents occur at the PWM switching points, especially at higher excitation frequencies.

Similar observations can be made for single winding excitation systems when a double layer winding is wound. The capacitance of the winding is the result of the capacitive connection of each turn to every other turn, and each turn to every other conductive surface that can hold electric charge. In general, the amount of charge that can accumulate depends on the capacitance, which is defined by the geometric and dielectric parameters and the voltage difference across the capacitor. For the adjacent turns in the single-layer winding, the voltage difference is relatively small and depends on the amplitude of the excitation voltage and the number of turns. For example, if constant DC voltage of 100 V is applied to the core with a single-layer winding with $N_e = 100$ turns, a voltage difference of 1 V per turn is expected. However, if a double-layer winding with $N_e = 100$ turns is used, in addition to the voltage

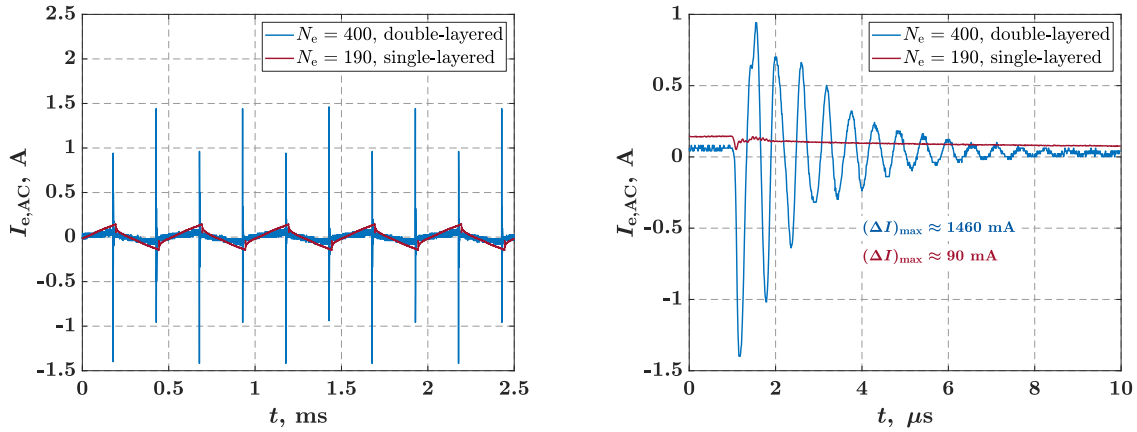

(A) Several periods of excitation current (B) Detail at the point of excitation voltage change

FIGURE 3.19: Excitation current waveform during DC bias experiment performed on the C0 core for two different excitation windings: double-layered with $N_e = 400$ turns of PVC insulated, fine wired conductor and single-layered with $N_e = 190$ turns of enameled wire. Experiment parameters: $U_{DC} = 200$ V, $f_{sw} = 2$ kHz.

difference of 1 V per turn, each turn in the second layer will have a maximum voltage difference of 50 V compared to the turn in the first layer. Thus, more charge can be accumulated in the double-layer winding, resulting in higher charging currents. Figure 3.19shows the waveforms of the AC component of the excitation current when the PWM-generated voltage is applied to the core. The waveforms are shown for cases where two different excitation windings were wound around the core: a double-layer winding with $N_e = 400$ turns of a PVC-insulated fine wire conductor and a single-layer winding with $N_e = 190$ turns of an enameled wire (Figure3.20). Since the double-layer winding can hold more charge, the charge current peaks are clearly visible. If, on the other hand, a single-layer winding is used, a significant reduction in the charge current can be observed. The charge current peaks are even higher when higher U_{DC} or f_{sw} are applied. The TekTronix 15 MHz current probe is used to measure charge current because of its megahertz frequency range. However, this effect is also detected by a 100 kHz transducer with an expected aliasing effect (Figure3.21).

Although these charge currents have no direct effect on the magnetic field in the core or additional iron losses, they are present in the excitation current signal and must be filtered out. Since the excitation current signal is used for loss calculation, this otherwise leads to an apparent increase in PWM-induced losses and to the occurrence of Z-shaped hysteresis loops (Figure3.22).

There are also setups available in the literature [12],[32] which use only a single excitation winding. AC component excitation is superimposed with a DC offset of the power amplifier. Although this approach eliminates the problems associated with

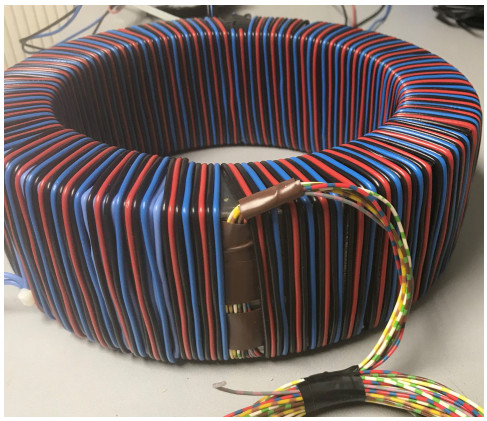

(A) Double-layered, $N_e = 400$ turns PVC insulated fine wire conductor

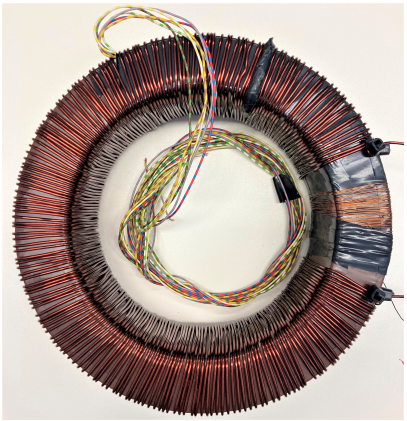

(B) Single-layered, $N_e = 190$ turns enameled wire

FIGURE 3.20: C0 core wound with two different windings.

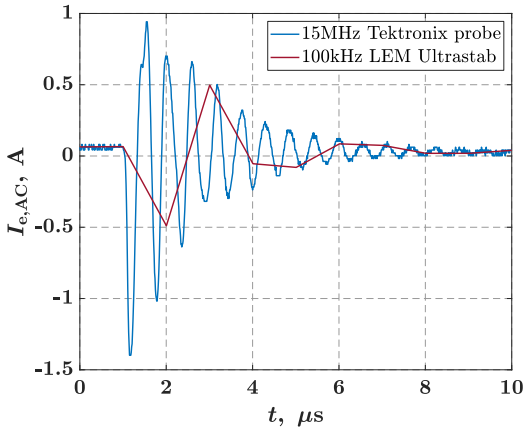

FIGURE 3.21: Capacitance charge current as picked up by the 100 kHz LEM Ultrastab transducer and DeweSoft Sirius DAQ system compared to the current waveform measured using the Tektronix 15 MHz current probe and 350 MHz Tektronix oscilloscope.

the second excitation winding, the use of the signal generator and power amplifier as an excitation system significantly limits the ability to achieve substantial DC bias fields needed to characterize the laminated materials up to the levels used in electrical machines.

The measurement setup constructed for this research is built as a single-winding excitation system with an inverter that serves as both AC and DC power supply. The use of an inverter as the power source in this setup ensures easier replication of the setup since an inverter is a commonly available component in most research laboratories. It also allows a wide range of varying DC bias fields, and with power switches based on silicon carbide technology, the possibility of a wide switching frequency operating range is assured. The novelty of the design of measurement setup presents one of major contributions of this thesis.

3.4.2 Excitation winding: distribution and positioning

The excitation winding must be evenly distributed and tightly packed along the entire length of the core to ensure a uniform magnetic field. Virtually any gap, even the width of a turn, will cause changes in the core flux density in the tangential direction. Such variations are shown in figures3.23and3.24as a result of the FEA simulation performed for the C1a core. The simulation was performed for two different windings: one with a 1° gap and one with a 2° degree gap between the turns. The inverter was used as a DC

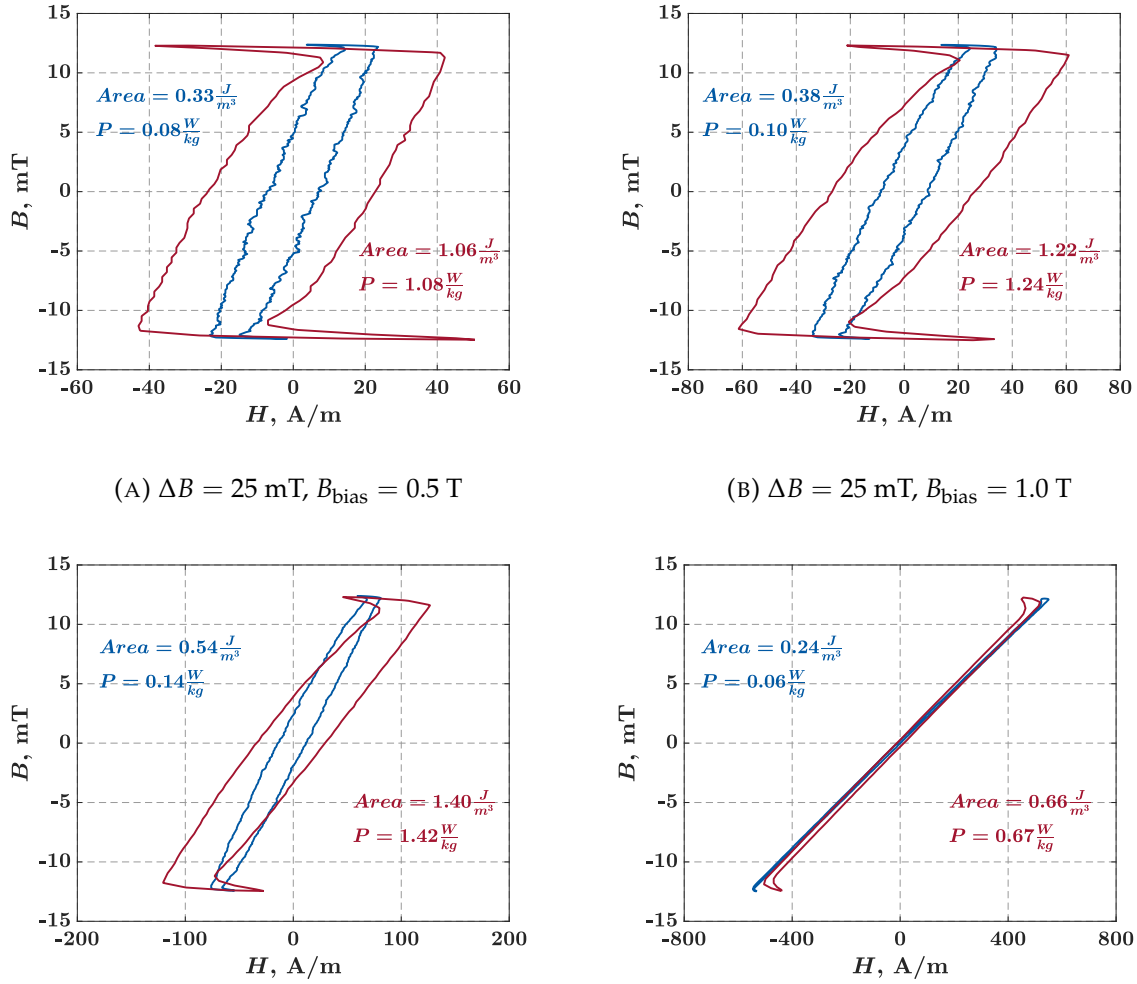

(A) $\Delta B = 25$ mT, $B_{\text{bias}} = 0.5$ T

(B) $\Delta B = 25$ mT, $B_{\text{bias}} = 1.0$ T

(C) $\Delta B = 25$ mT, $B_{\text{bias}} = 1.3$ T

(D) $\Delta B = 25$ mT, $B_{\text{bias}} = 1.7$ T

FIGURE 3.22: Occurrence of the Z-shaped hysteresis loops due to the high interwinding capacitance in the dependence of the B_{bias} and $\frac{\mathrm{d}B}{\mathrm{d}t}$ parameter: $\frac{\mathrm{d}B}{\mathrm{d}t} = 0.1$ T/ms, $\frac{\mathrm{d}B}{\mathrm{d}t} = 0.4$ T/ms.

current source and its parameters were modified accordingly to achieve approximately the same $B_{\text{bias}} \approx 1.65$ T with both windings. Due to the ring shape of the core, the gap between turns of a winding is larger at the outer edge of the core, so the peak-to-peak values of flux density are larger. Depending on the ratio $d_{\text{outer}}/d_{\text{inner}}$, this effect is more or less pronounced. In this case, the peak-to-peak value of flux density is more than 5 times larger at the inner edge and more than 3.5 times larger at the outer edge of the core when a 2° degree gap winding is used compared to a 1° degree gap winding. The limits of the color scale in figure3.24were set according to the minimum and maximum

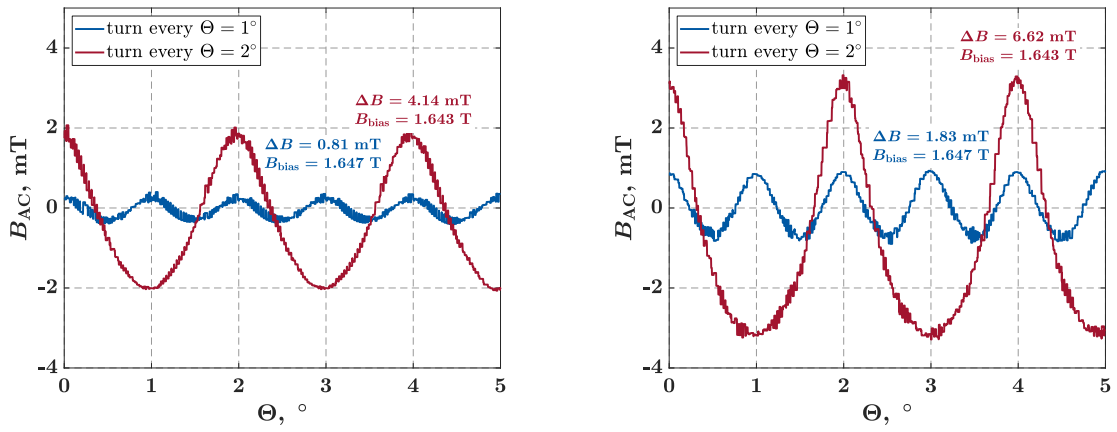

(A) Inner edge of the core, $r = 0.225$ m

(B) Outer edge of the core, $r = 0.2475$ m

FIGURE 3.23: Tangential fluctuations of the flux density in the C1a core with different number of turns of the excitation winding ($N_{e1} = 360$, $N_{e2} = 180$) and approximately equal B_{bias} value.

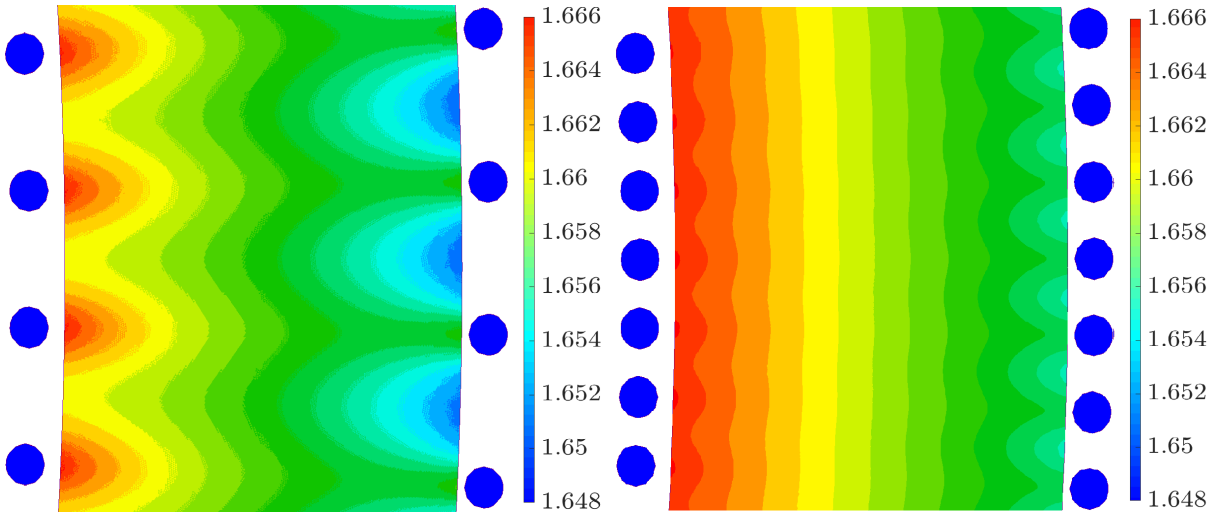

(A) $N_{exc} = 180$, $B_{bias} = 1.643$ T

(B) $N_{exc} = 360$, $B_{bias} = 1.647$ T

FIGURE 3.24: Radial and tangential distribution of the flux density in the C1a core with different number of turns of the excitation winding ($N_{e1} = 360$, $N_{e2} = 180$) and approximately equal B_{bias} value.

values of the flux density in the core. The flux density in the conductors is much lower, but cannot be shown correctly here because it is below the lower limit of the plot.

Leaving a start-to-finish gap in the winding for the purposes of reduction of the winding capacitance is not an option in this case for the same reasons. A significant

drop of ≈ 5% in flux density value can be observed in figure3.25where simulation was performed for the C1a core and a winding with a 10% start-to-finish gap. Further more, an impact of such a gap is visible along almost the entire length of the core.

Evaluating the power loss for the core with a winding that causes relatively large variations in flux density values could lead to significant errors. Apart from the dependence on the width of the gaps, i.e. the magnitude of the flux density fluctuations, the error in such a case would also depend on the DC bias value, with greater impact in nonlinear regions of the power loss characteristics: if the flux density fluctuates significantly then the power loss at the points of maximum and minimum flux densities will also differ significantly.

For geometrically non-uniform cores, the magnetic field strength varies along the radial lines of each cross-section of the core and is therefore not uniformly distributed, regardless of the distribution of the excitation winding. However, a uniformly distributed, tightly packed excitation winding ensures that the total magnetic flux for each cross-section is the same at every point along the entire length of the core. The effects of non-uniformly designed cores on losses in the core is investigated later in this research.

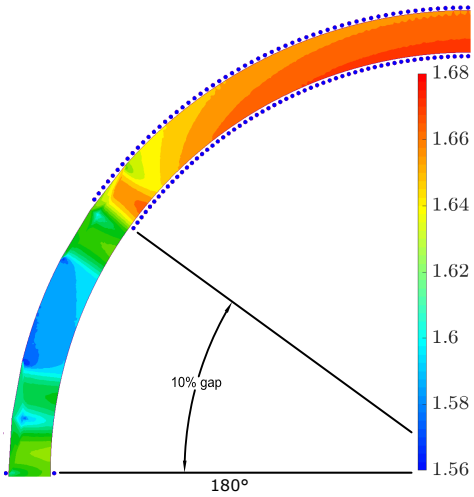

(A) Shaded plot

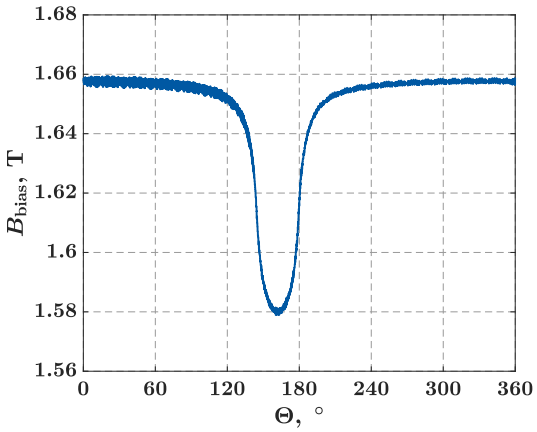

(B) Radial distribution at $r = 0.23625$ m (the centre of the ring lamination width)

FIGURE 3.25: Flux density in the C1a core when the gap of 10% is left between the beginning and the end of the excitation winding. $N_e = 350$, $B_{\text{bias}} \approx 1.65$ T.

3.4.3 Search winding: distribution and positioning

Local imperfections in the material can cause an uneven distribution of the magnetic field at that point, i.e., in the cross section of the core. For this reason, the IEC 60404-6:2018 standard [46] proposes to distribute both the excitation and search windings uniformly along the entire length of the test specimen. The distribution of the search winding over the entire length of the core would then average all fluctuations in the flux density value in the tangential direction, regardless of the cause, and if the fluctuations are small enough, the effect of these fluctuations would be absent. However, this is proposed only for power frequencies, i.e., power system frequencies. The same standard also suggests that, for measurements at frequencies above power system frequencies, care should be taken to avoid complications related to capacitance by separating the excitation and search windings whenever possible. As the overlap length of the windings increases, the capacitance between the windings also increases. Similar to what was mentioned earlier with the separate AC and DC excitation windings and double-layer windings, this also leads to an apparent increase in PWM-induced losses and the appearance of Z-shaped hysteresis loops (Figure3.22). At higher switching frequencies, this can have a significant effect on the result if not compensated for. For this reason, the search winding was wound only in a section of the core that occupies about 30 geometric degrees of the full circle.

3.4.4 Windings: experiment specifics

For the initial AC measurements, the core C0 was used with an excitation winding consisting of four individual windings evenly wound around the core and distributed in two layers. Three of the individual windings were wound with $N = 100$ turns and the fourth was wound to achieve $N = 100$ or $N = 116$ turns. The windings could then be combined in series or parallel circuits, allowing four different combinations of excitation windings with $N = 100,\ 200,\ 316$ or 400 turns (Table3.6). All four windings were wound with wires of the same cross-section, and the connection of each winding in the final excitation winding is done in such a way that the power loss of the winding does not change or changes only minimally (Table3.6). This ensures equal magnetic conditions in the core ($H_{\text{before}} = H_{\text{after}}$) when the amplitude index modulation m_a remains unchanged. In this way, the influence of the modulation depth and the DC link voltage on the PWM-induced loss contribution could be investigated. The search

TABLE 3.6: Table showing the connections of each individual winding to obtain four different combinations of excitation winding with the same power loss at the same values of magnetic field strength. The wire cross-section of each individual winding is equal to 0.5 mm^2 and its resistance is represented in the table as R. Individual winding 4 (IW4) can be easily modified so that its number of turns is equal to $N = 100$ or $N = 116$ turns.

Excitation winding turns	**Individual winding connections**	**Resistance**	**Winding power loss (when $H_1 = H_2 = H_3 = H_4$)**
100	IW1 ‖ IW2 ‖ IW3 ‖ IW4	$\frac{R}{4}$	$I_1^2 \cdot R_1 = I_1^2 \cdot \frac{R}{4}$
200	(IW1 ‖ IW2) + (IW3 ‖ IW4)	R	$I_2^2 \cdot R_2 = (\frac{I_1}{2})^2 \cdot R = I_1^2 \cdot \frac{R}{4}$
316	(IW1 ‖ IW2) + IW3 + IW4	$2.5R$	$I_3^2 \cdot R_3 = (\frac{I_1}{3.16})^2 \cdot 2.5R = I_1^2 \cdot \frac{R}{4}$
400	IW1 + IW2 + IW3 + IW4	$4R$	$I_4^2 \cdot R_4 = (\frac{I_1}{4})^2 \cdot 4R = I_1^2 \cdot \frac{R}{4}$

winding with $N_s = 20$ turns was wound below the excitation winding in a single layer as close as possible to the core.

This winding configuration was soon abandoned due to high winding capacitance which affected the results in the newly performed DC bias experiments. A new single-layer excitation winding was then wound using a enameled wire to maximize the copper-to-insulation ratio, allowing more turns per unit length. The excitation winding was wound uniformly along the entire length of the core, achieving $N_s = 190$ turns, while the search winding was wound only on a relatively short section of the core with $N_s = 40$ turns.

For the final measurements of the research, three new cores were built and wound. The parameters of the windings are listed in the table3.7.

TABLE 3.7: Winding parameters for three different cores used in the research.

CORE	EXCITATION WINDING		SEARCH WINDING		
	Turns	Wire diameter (mm)	Turns	Wire diameter (mm)	Section length (°)
C1a	424	2,2	40	0,6	31,5
C2a	386	1,6	40	0,6	35,5
C3	211	1,75	40	0,6	36,1

3.5 Cores

Regardless of the excitation approach, another disadvantage of the measurement setups available in the literature is that they are all limited to relatively small core samples. This is mainly because signal amplifiers are used to generate the AC excitation, which generally can only provide limited power. Therefore, the magnetic path length of the ring core is relatively short. In addition, to achieve a uniform distribution of the magnetic field in each cross-section of the core, the short length cores must be relatively narrow. For example, the width of the sample core in [10] is only 5.7 mm. With a laser cut depth effect of about 1 mm on both sides of the ring, about 35% of the core cross section is affected by this design factor. The setup proposed in this dissertation allows measurements on cores of larger size, reducing the effects of laser cut and core non-uniformity on measurement error. For the final measurements, three cores are built to verify the methodology and to determine the possible influence of core non-uniformity and laser-cut depth impact on core losses (Figure3.26, Table3.2). All cores were made from the same batch of M400-50A laminated material and stacked using the same method. Thus, the difference in build factor for all of the cores is kept to a minimum. Furthermore, DC bias experiments were performed with the B_{bias} in both directions to evaluate the possible difference in losses related to the orientation of the magnetization of the material.

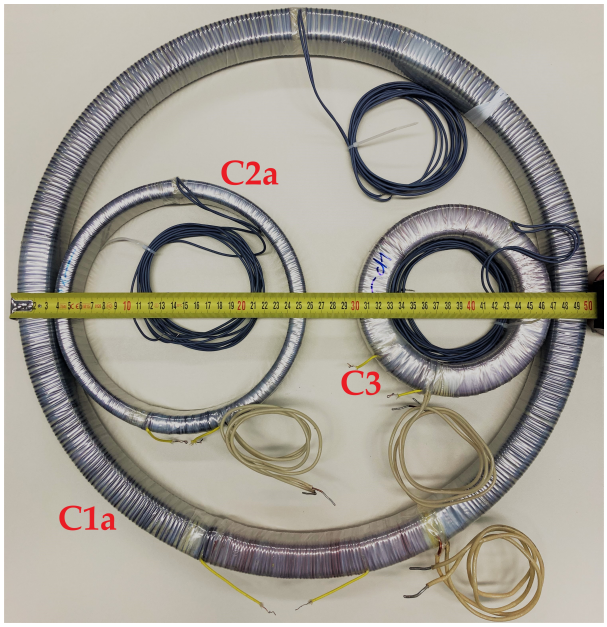

FIGURE 3.26: A photo of the wound cores C1a, C2a, and C3.

Core uniformity is defined in IEC 60404-6 standard [46] as the ratio of outer to inner ring diameter. The core is considered uniform if the uniformity index is less than 1.1. When this condition is met, the ring core can be considered as an infinite diameter core, which means that there is no difference in flux density at the inner edge of the core compared to the outer edge. The FEA simulation results showing the change in flux density as a function of radial position on the ring and B_{bias} are shown in figure3.27. Subfigure3.27ashows the change in flux density across the width of the core ring for a particular excitation case, which turns out to be the least favorable for this phenomenon. In addition, the subfigure3.27bshows how ΔB changes as a function of the B_{bias} in the cores, where ΔB is defined as the difference in flux density between the inner and outer edges of the core.

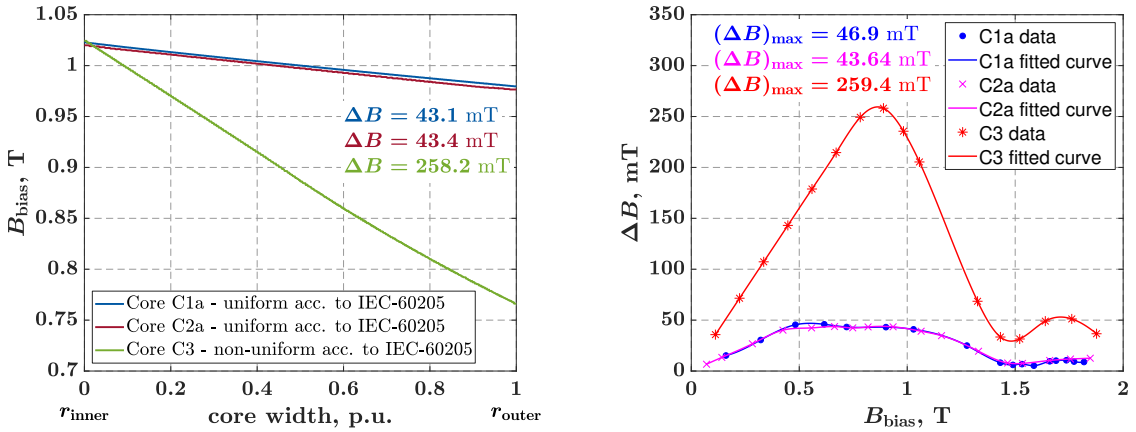

(A) Change of flux density in radial direction for the most unfavorable value of B_{bias}

(B) The difference in the values of B at the outer and inner edges of the ring core as a function of the B_{bias}.

FIGURE 3.27: Change of flux density over the radial cross section of uniform C1a and C2a cores and non-uniform C3 core.

Cores C1a and C2a were built as uniform cores with a uniformity index of 1.1, and with a uniformity index at the boundary line, the flux density still changes as a function of the radial position on the ring. Moreover, regardless of the significant size difference between cores C1a and C2a, the same uniformity index ensures an approximately equal gradient of flux density across the radial cross section (Figure3.27a) and this for any B_{bias} value (Figure3.27b). Cores C1a and C2a were intentionally built with the same uniformity index but different width ($r_{\text{outer}} - r_{\text{inner}}$) of the ring lamination. Therefore, the difference in PWM contribution to losses between the two cores can be attributed to the influence of laser cutting.

Core C3 was built with a uniformity index of 1.375 and is therefore classified as nonuniform. Figure3.27clearly shows that the difference in the gradient of flux density across the width of the ring is much larger for a non-uniform core. The difference in ΔB is more than 6 times larger in the worst case than for uniformly built cores. The C3 core was intentionally built as a non-uniform core, but with the same ring width as the C1a core. Therefore, the difference in PWM contribution to losses between the two cores can be attributed to the effect of the uniformity of the flux density distribution.

Three PT1000 temperature sensors were attached to the surface of the C0 core: one on the inner and outer surfaces of the ring core and one on the top of the ring core. Since the differences in the measured temperatures were negligible and the temperature change at all three locations followed the same slope, the C1a, C2a and C3 cores were later equipped with only one PT1000 temperature sensor, which was placed on the top surface of the ring core.

Chapter 4

Measurement Methodology

The measurement setup proposed and built in this dissertation is used to perform three main types of measurements: determination of the normal magnetization curve, effect of PWM-generated voltage supply parameters on losses, and acquisition of iron loss data for a given B_{bias} value and a flux density ripple waveform.

The first two are classified as AC measurements because both involve applying an AC voltage to the core. The normal magnetization curve must be determined because it provides basic information about the quality of the magnetic material and the connection between magnetic field strength H and flux density B. The bias value of B is essential in the DC bias measurements because it is one of the parameters used to define the minor loop in the relation to the loss data. Since B_{bias} cannot be measured with the proposed setup and samples, it is determined using the normal magnetization curve and the measurable bias value of H. For the evaluation of the iron losses in the core, the AC loss mode has been implemented in the inverter control board and is used to generate the classical bipolar and unipolar PWM output voltage. The evaluation of the results obtained with this measurement mode allows the determination of the individual influence of independent parameters of standard single-phase sinusoidal PWMs on the total AC losses and also serves to validate the setup, since the results can be easily compared with the results of the well-known theoretical expectations and the findings of other research papers.

Finally, the DC bias measurement was implemented. This measurement mode is used for simultaneous generation of both the DC bias of the core magnetization and the flux density ripple. By changing the switching frequency of the inverter, the value of the DC link voltage, and the duty cycle of the SiC MOSFET switches, the value of the DC bias and the peak-to-peak value of the flux density ripple change. In this way, numerous different magnetic states can be achieved in the core, mimicking the conditions of the small remagnetization cycles that occur when the PWM-generated

AC voltage is applied. By performing the DC bias experiments for a wide range of parameters, iron loss data is obtained that can be represented as a multidimensional array of the specific iron loss values for each ΔB, $\frac{\mathrm{d}B}{\mathrm{d}t}$, and B_{bias} value.

Ambient and core temperature were considered in all measurements performed. The ambient temperature was always in the range of $23 \pm 5^{\circ}$ C, as required by the IEC standard [46,47]. Also, as required in [46,47], the surface temperature of the cores was always kept below 50°C during the measurements where the effects of temperature on losses were not evaluated. The surface temperature of the cores was always kept in the range of $\pm 2.5^{\circ}$C, relative to the initial temperature at the beginning of the experiment. The core temperature of 30°C was defined as the initial cold temperature in this research. A temperature slightly above ambient was chosen as the initial temperature of the core for two reasons: It is easier to reproduce the same initial conditions since the system is not set up in a temperature-controlled room, and it is possible to cool the core down to the initial temperature more quickly after the experiment, allowing less time-consuming repetition of measurements on the same core. The core loss phenomenon was used to heat the core to the specific initial temperatures. DC bias bias measurement mode was activated for this purpose because then the condition could be reached where relatively large core losses would be generated compared to the excitation winding losses. This avoided indirect heating via the excitation winding and thus ensured a more uniform temperature distribution over the entire core volume.

Due to the relatively high mass of the cores, thermal time constant is also relatively high and it takes substantial amount of time to uniformly heat the entirety of the core. Thus, measurement of the core temperature on its surface does not give the exact image of core temperature, however, the change in temperature can be monitored and evaluated. Excessive heating of the excitation winding should be avoided since it is located very close to the core, which may result in significant heat transfer, especially if enameled wire is used. This can also lead to the false temperature readings if temperature sensor is not thermally insulated towards the excitation winding.

The excitation winding was forced cooled by means of two fans with a nominal air flow rate of 3.7 $\mathrm{m}^3/\mathrm{min}$ each.

4.1 AC measurements

The AC measurement mode is used to apply a PWM-generated AC voltage to the device under test and allows setting various parameters of such a supply:

- type of modulation: unipolar or bipolar
- switching frequency of the inverter (f_{sw}): from 2 kHz to 40 kHz
- fundamental frequency ($f_{1\mathrm{h}}$)[1]: from 1 Hz to $f_{\mathrm{sw}}/10$
- DC link voltage of the inverter: from 0 V to 500 V DC

After setting the initial parameters of the supply, an automatic measurement procedure can be initiated, which is implemented in the inverter control board. The parameters of the procedure are the start value, the end value and the step resolution of the modulation depth m_{a}. Excitation voltage and current, search winding voltage and DC link voltage are measured for each step in the procedure i.e. different $B_{1\mathrm{hpk}}$ value. Signal samples in the duration of at least 10 periods of the fundamental frequency are used to ensure sufficient frequency resolution in the FFT post-processing.

According to the IEC 60404-6:2018 standard, the device under test must be carefully demagnetized before each measurement starting from a field strength of at least ten times the coercivity by slowly reducing the corresponding magnitude of the magnetizing current to zero. Demagnetization shall be performed at the same or lower frequency as will be used for the measurements [46]. The implemented measurement procedure is used to determine either the normal magnetization curve or the PWM contribution to iron losses for the entire range of values of $B_{1\mathrm{hpk}}$, starting at values well above ten times the coercivity and always ending at or around zero. Thus, the demagnetization process was not performed as an isolated procedure, but was integrated into the actual measurement procedure by following the rules below:

- The measurement always starts with the chosen maximum value of $B_{1\mathrm{hpk}}$, e.g. 1.8 T, and then $B_{1\mathrm{hpk}}$ is reduced towards zero with each step of the procedure
- The maximum chosen value of $B_{1\mathrm{hpk}}$ is always well above the knee point of the magnetization curve of the material
- The core is held at the point of maximum chosen $B_{1\mathrm{hpk}}$ for at least 50 periods before a measurement is performed to achieve a steady state of the core

[1] The measurement setup is capable of operating in this range of fundamental frequencies. Although the first tests were carried out for higher values of $f_{1\mathrm{h}}$, the focus of the research remained on $f_{1\mathrm{h}} = 50$ Hz, and all further measurement results in the thesis are presented for this value of the fundamental frequency.

- The ramp between two adjacent B_{1hpk} values is slow, and after reaching the new value of B_{1hpk} there is enough time left to reach a steady state: the ramp parameters and settling time are adjustable parameters and can be changed according to the fundamental frequency and the difference of B_{1hpk} values between two adjacent steps (Figure4.1)
- The measurement procedure is performed in a single run: no return to the zero value of the flux density at any time during the experiment

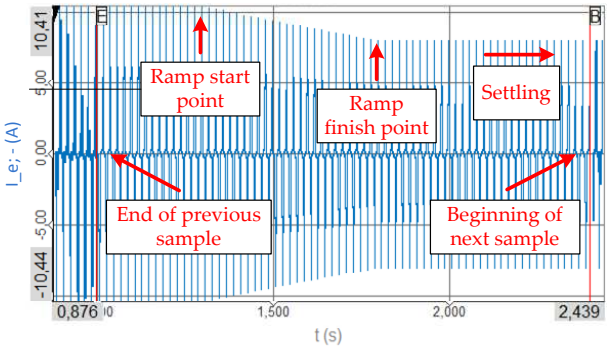

FIGURE 4.1: Transition between two different values of peak flux density during automatic AC measurement procedure.

4.1.1 Determination of the normal magnetization curve

The IEC 60404-4:2008 standard provides a method for the normal magnetization curve determination using the current commutator, flux integrator and a ring core sample. However, due to the complexity of the setup that must provide high power commutable DC current to the core, method is proposed using the measurement setup built in this dissertation. The ideal way to mimic the conditions induced with the current commutator would be to supply the core with a sinusoidal current of relatively low frequency. Since the excitation in the proposed setup is done by a PWM-generated power supply, the excitation voltage and consequently the excitation current are distorted compared to the sinusoidal form. The negative effects of such a power supply were minimized by increasing the switching frequency to the maximum of $f_{sw} = 40$ kHz and using a unipolar modulation switching. In this way, the peak-to-peak ripple of the flux and the core losses are minimized. The corresponding main-cycle hysteresis loop is almost as narrow as for sinusoidal voltage excitation, and small remagnetization cycles have a minimal effect on the determination of the normal magnetization curve. On the other

hand, the excitation current is more distorted at higher switching frequencies due to the system capacitance, mainly the winding capacitance. However, this capacitive charging current does not generate a magnetic field in the core and most of it can be easily filtered out afterwards by low-pass filtering at 100 kHz. All figures presented further in this section, and used as an example to explain the methodology, represent the results of measurements performed on core C1a (see table3.2), for the following experimental parameters: Switching frequency of $f_{sw} = 40$ kHz, fundamental frequency of $f_{1h} = 10$ Hz, and unipolar modulation.

AC source evaluation

The properties of the AC source evaluated here apply to all AC measurements made, including the AC loss mode. However, this subsection is included in the *Determination of the normal magnetization curve* section because a certain quality of AC power supply must be satisfied to meet the standard in determining this basic characteristic of the material. Voltage and frequency variations, form factor, and high harmonic content are observed to determine if the use of this setup and methodology is justified for this type of measurement. AC loss mode, on the other hand, is used to evaluate the effect of the inverter supply on losses, so these standard supply requirements do not apply in that case.

According to the IEC 60404-6:2018 [46] standard, which specializes in magnetic measurements with ring core samples, the AC source must have a voltage and frequency variation at its output that does not exceed $\pm 0.2\%$ of the set value during the measurement. The stability of the AC output voltage generated by the proposed setup mainly depends on the stability of the DC link voltage of the inverter. Figure4.2ashows the dependence of the U_{DC} crest factor with respect to the set value on the peak flux density. It can be seen that this variation does not exceed the threshold values defined by the standard.

Furthermore, to obtain comparable measurements, either the waveform of the induced secondary voltage or the waveform of the magnetizing current must be kept sinusoidal with a form factor of 1.111 and a relative tolerance of $\pm 1\%$. The output voltage is generated by PWM at a high switching frequency and consists of a fundamental and low-frequency harmonics that occur due to the highly nonlinear load, and high-frequency harmonics that occur at and around the switching frequency and its multiples. These high-frequency harmonics add ripple to the output voltage signal, and at lower flux densities, the RMS value caused by this ripple exceeds the RMS value of

the fundamental and low-frequency harmonics combined. For this reason, the total RMS value of the output voltage increases at lower flux densities compared to the output voltage generated without PWM. Since the average value of both signals is practically the same, this leads to an increase in the voltage form factor for the PWM-generated power supply. However, if the high-frequency harmonics are filtered out with a low-pass filter with cutoff frequency set to $f = 1$ kHz, the form factor of the output voltage remains within the limits specified by the standard (Figure4.2b). The justification and validity of filtering out high-frequency harmonics will be discussed in more detail in the following subsection.

In figure4.2ban abrupt change of the U_s form factor is visible at about $B_{1hpk} = 1.75$ T. This is due to the combination of the high value of the modulation depth of 0.85 and above, the high switching frequency, and the unipolar modulation, all of which result in a flattened peak of the search voltage waveform U_s from this point and above. The occurrence of the flat peak in the U_s waveform leads to this significant change in the form factor curve as a function of B_{1hpk}.

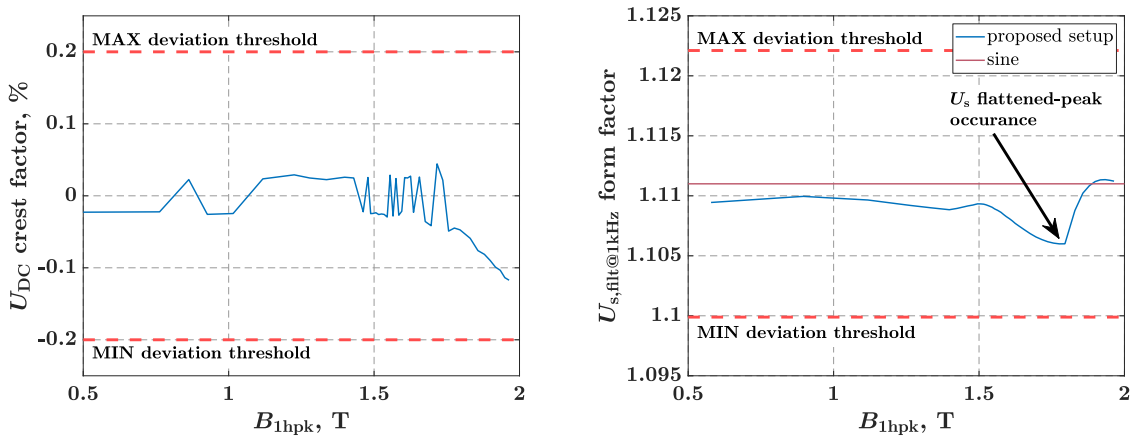

(A) U_{DC} crest factor

(B) Form factor of U_s filtered at 1kHz

FIGURE 4.2: DC link voltage crest factor and search coil flux linkage form factor in dependence on the peak flux density value for C1a core during AC measurement experiment. Parameters of AC measurement experiment: $f_{sw} = 40$ kHz, $f_{1h} = 50$ Hz, $U_{DC} = 172.5$ V, unipolar modulation. Maximum and minimum deviation thresholds are shown according to the IEC 60404-6:2018 standard [46].

Elimination of higher harmonic components

At the switching frequency of 40 kHz and its first multiple of 80 kHz, some harmonic components are still present in the excitation current and magnetic flux. Figure4.3 shows how the amplitudes of the higher harmonics of the current and flux change with respect to the peak flux density of the corresponding cycle. The scale of the Y-axis is logarithmic and set to the per-unit system, with the amplitude of the first harmonic as the reference value.

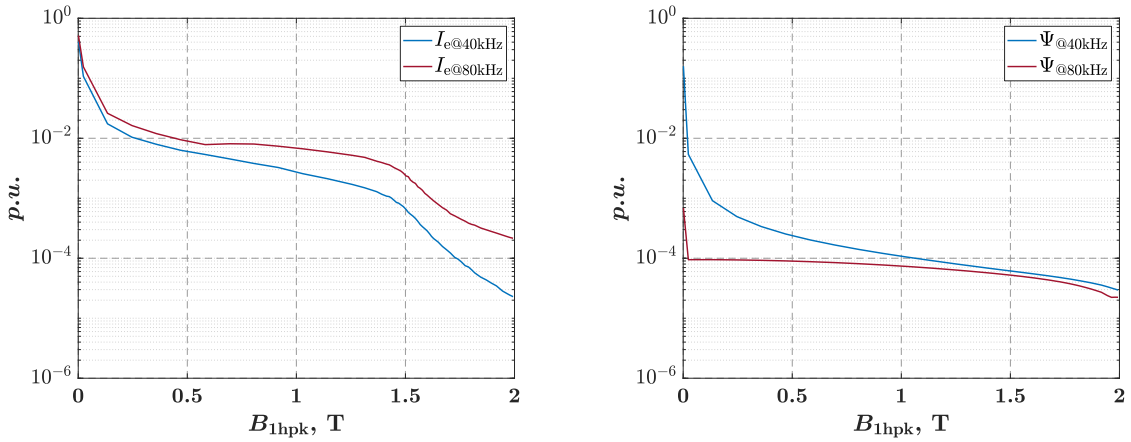

(A) Excitation current

(B) Magnetic flux

FIGURE 4.3: Excitation current and magnetic flux higher harmonic components contribution in relation to the fundamental harmonic amplitude.

First, it is evident that even at the lowest flux density peaks of 1 mT and 5 mT, the 80 kHz harmonic component of the magnetic flux is about a thousand times smaller in amplitude than the 40 kHz component, which is already between ten to a hundred times smaller in amplitude than the fundamental. This indicates that the magnetic flux in this core does not respond, or responds only slightly, to such rapid changes in excitation. Therefore, the 80 kHz harmonic components can be filtered out and are not considered. It is also clear that the contribution of the higher harmonics to the excitation current decreases as the core approaches saturation. For this reason, the difference in the determined normal magnetization curve with and without considering the higher harmonic contributions decreases at higher peak flux density values. However, a more significant difference can occur at lower flux density values (Figure4.4). It is suggested that the reason for this is the increased peak-to-peak ripple of the current compared to its RMS value. This is also confirmed by a larger increase in the ratio of H_{pk} to B_{pk}

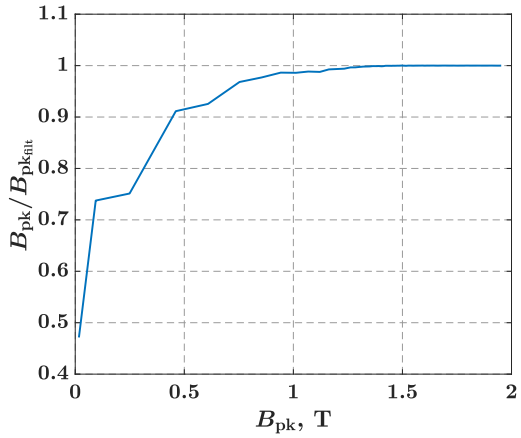

FIGURE 4.4: Quantification of the difference in the determined normal magnetization curves obtained without and with 1 kHz low-pass filtering: the ratio of peak flux densities obtained for both cases.

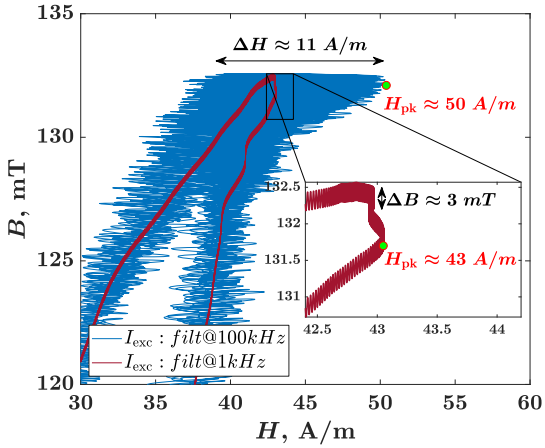

FIGURE 4.5: Detailed view of hysteresis loops obtained without and with 1 kHz low-pass filtering of excitation current. A significant difference in peak magnetic field strength $H_{1\mathrm{hpk}}$ can be observed.

in the Rayleigh region compared to a pure sinusoidal excitation. The same happens with magnetic flux, but the effect is so much smaller that it can be neglected compared to the current. Figure4.5shows a detailed view of a hysteresis loop with a peak flux density value of $B \approx 132$ mT for cases where the current signal is and is not filtered with a low-pass filter whose cutoff frequency is set to $f = 1$ kHz. It is evident why determining the peak point of this hysteresis loop is a problem and why there are large differences in the obtained characteristics at lower flux densities. ΔB of 3 mT is present in both cases, but it is not observable due to the high value of ΔH when the current is not filtered out.

In a sense, this method was developed to determine material properties under DC bias conditions, but using the PWM-generated AC excitation system. The ultimate goal is to determine the DC value of B as accurately as possible under certain DC values of H. Although it is evident from the figure4.5that the excitation current and magnetic flux in the core exhibit ripple at the switching frequency, it is assumed that the switching frequency is too high for the flux density to reach its final maximum value for a given current peak. The peak magnetic field strength lies somewhere between two borderline values, which is 43 A/m $< H <$ 50 A/m for the particular case in figure4.5. However, it is assumed to be closer to the lower boundary, meaning that the error in determining the normal magnetization curve would be smaller if the 40 kHz component is also

filtered out. In this way, the flux ripple is also eliminated, but this results in such small changes in the normal magnetization curve obtained that it can be neglected, especially compared to all the other effects already considered.

Selection of fundamental harmonic frequency

The initial magnetization curve is a property of the magnetic material that is independent of the effects of the alternating magnetic field. Moreover, the normal magnetization curve is referred to as the curve connecting the apparent peak points of the hysteresis loops when the peak value of the cyclic magnetic field is varied, and it coincides almost perfectly with the initial magnetization curve. However, if the normal magnetization curve is determined using the AC power supply instead of the current commutator, the frequency of the applied voltage will affect the result. With an increase in the fundamental frequency of the applied voltage, the hysteresis loop becomes wider, corresponding to the higher AC losses in the core, and the apparent peaks (see section2.1) of the hysteresis loops are shifted: a higher H_{pk} is required to achieve the same B_{pk} when the fundamental frequency $f_{1\mathrm{h}}$ is increased. This naturally leads to the conclusion that the best result is achieved with the lowest possible fundamental frequency. However, the lower the fundamental frequency, the greater the measurement uncertainty in determining the flux density in an alternating magnetic field, for practical reasons. Figure 4.6shows the fluctuation of the determined B_{bias} points around the natural derivative of the normal magnetization curve for several different fundamental frequencies. The

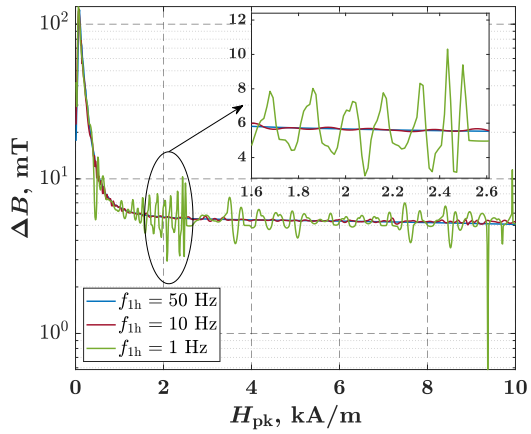

FIGURE 4.6: ΔB for every two adjacent points of the normal magnetization curve determined with AC excitation frequency of 50 Hz, 10 Hz and 1 Hz respectively.

fundamental frequency of $f_{1h} = 10$ Hz was chosen as the lowest frequency at which it was still possible to determine the flux density without significant fluctuations between adjacent points.

Measurement procedure and methodology

AC measurement procedure was used for the determination of the normal magnetization curves. The start value of the modulation depth is set to $m_a = 1$ and the DC link voltage value is adjusted accordingly to reach a desired H_{pk} i.e. the expected B_{pk}. The m_a is then reduced in unequal steps towards zero. The step resolution is set with respect to the H_{pk} value such that the resolution is increased when H_{pk} is expected to be in nonlinear regions of the $B - H$ curve and decreased when quasi-linear regions are reached. Decreasing the resolution in certain regions minimizes the time required to perform the experiment and thus the heating of the core. Because the fundamental frequency is relatively low, down-ramping between two adjacent points, settling, and sampling for at least 10 periods requires a significant amount of time that thermally stresses the setup. Therefore, minimizing sampling in the linear regions can help to significantly reduce the increase in core temperature during testing.

Because of the wide range of excitation current measured in this type of experiment, a set of two measurements was made for each core. The number of turns through the current transducer was adjusted between the two measurements to optimize the current measurement range. The two measurements overlapped at several sampling points to ensure that the results were not affected by the adjustment (Figure4.7). The adjustment was made at the point where there was still significant saturation ($B_{pk} > 1.8$ T), and demagnetization of the sample was performed before both measurements. This justifies the combining of the two measurements made separately.

For each measured 10-period sample of the current signal, a single period with the highest current amplitude was selected and then the peak magnetic field strength H_{pk} was calculated as follows:

$$H_{1hpk} = \frac{N_e}{2 \cdot \ell} \cdot (I_{e,pk+} + I_{e,pk-}), \tag{4.1}$$

where $I_{e,pk+}$ is the positive and $I_{e,pk-}$ is the negative peak of the excitation current, N_e is the number of turns of the excitation winding, and ℓ is the magnetic path length calculated according to IEC 60205. The search voltage signal was integrated to obtain the flux waveform, and then using the period corresponding to the current signal, the

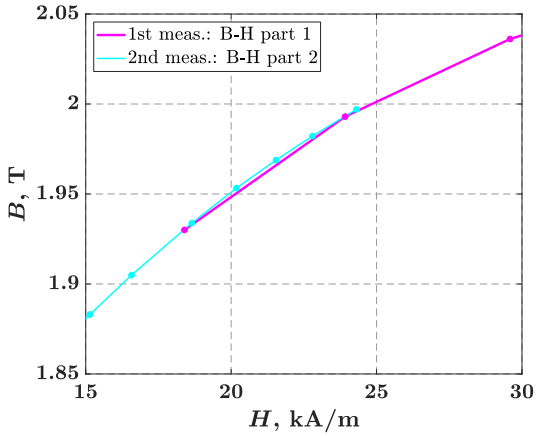

FIGURE 4.7: Overlapping of two separate measurements of the $B-H$ curve performed on the C1a core.

peak flux density B_{pk} was calculated as follows:

$$B_{\mathrm{pk}} = \frac{\Psi_{\mathrm{pk}+} + \Psi_{\mathrm{pk}-}}{2 \cdot S_{\mathrm{eq}} \cdot N_{\mathrm{s}}} - \mu_0 \cdot H_{\mathrm{pk}} \cdot \left(\frac{1 - k_{\mathrm{sf}}}{k_{\mathrm{sf}}} - \frac{S_{\mathrm{w_s}} - S_{\mathrm{g}}}{S_{\mathrm{g}}} \right), \tag{4.2}$$

where $\Psi_{\mathrm{e,pk}+}$ is the positive and $\Psi_{\mathrm{e,pk}-}$ is the negative peak of the flux linkage waveform, S_{eq} is the equivalent core cross-sectional area according to [48], N_{s} is the number of turns of the search winding, k_{sF} is the stacking factor, $S_{\mathrm{w_s}}$ is the area enclosed by the search winding, and S_{g} is geometric cross-sectional area of the core. The peak value of the flux density is slightly out of phase with respect to the peak value of the magnetic field strength, so that the calculated pair of H_{pk} and B_{pk} represents an apparent peak of the hysteresis loop. Because of the probability of different magnetic resistances when magnetised in opposite directions, H_{pk} and B_{pk} are determined as the average of the maximum and minimum peaks along a single main cycle.

4.1.2 AC loss mode

Several experiments were performed in AC loss mode to obtain data for the analysis of DC link voltage, modulation depth, and modulation type on core loss. Each set of experiments is performed for different switching frequencies. The effect of temperature on the core loss is also considered. The iron loss is nonlinear over the entire range of B

values for which measurements were made, so the same step resolution in B is used in both the linear and nonlinear regions of the $B-H$ curve.

To analyse the effects of the inverter supply parameters on core losses, the core must be operated under the same fundamental magnetic conditions with different sets of supply parameters. Comparison of the losses will then show which set of parameters causes more or less losses. To determine the isolated effect of a particular inverter supply parameter on core losses, equal fundamental magnetic conditions must be achieved by changing only one of the parameters, thereby eliminating the effects of the other parameters on losses. This can only be achieved by changing the parameters of the excitation winding. Experiments to determine the effects of U_{DC} and m_{a} parameters on losses were conducted only in the initial phase of this research using a C0 core and a specially designed excitation winding with the parameters listed in the table3.6. The effects of the switching frequency and modulation type are evaluated for the other cores as well.

DC link voltage effect on losses

The DC link voltage U_{DC} and the modulation depth m_{a} are directly related parameters, and changing either parameter independently changes the fundamental magnetic conditions in the core. Changing only the parameter U_{DC} changes the RMS value of the excitation current, and as a consequence, the fundamental magnetic conditions also change. This can be compensated by changing the number of turns and the resistance of the excitation winding so that the same value $H_{1\mathrm{hpk}}$ is obtained as before the change of U_{DC}. To achieve this, the following relationships must be satisfied:

$$H = \frac{I_{\mathrm{e}}}{\ell}\, N_{\mathrm{e}}, \qquad (4.3) \qquad\qquad P_{w_e loss_1} \approx P_{w_e loss_2}. \qquad (4.4)$$

The same $H_{1\mathrm{hpk}}$ is obtained when the multiple of N_{e} and I_{e} remains the same, but the winding losses reduce the amount of energy coming from the source used to magnetize the core. Therefore, there is no combination of excitation winding parameters other than those given in4.3and4.4that results in the same $H_{1\mathrm{hpk}}$ value. If the new modified value of U_{DC} is defined as $U_{\mathrm{DC}_2} = k\, U_{\mathrm{DC}_1}$, the winding parameters must be modified in the following relations:

$$N_{\mathrm{e}_2} = k\, N_{\mathrm{e}_1}, \qquad (4.5) \qquad\qquad R_{\mathrm{e}_2} = k^2\, R_{\mathrm{e}_1}. \qquad (4.6)$$

The quadratic dependence of the resistance on the parameter U_{DC} results from the quadratic dependence of the power loss on the current:

$$P_{\mathrm{w_eloss}} = I^2 \, R. \tag{4.7}$$

Modulation depth effect on losses

Determining the effect of modulation depth on losses is similar to determining the effect of U_{DC}, except that here U_{DC} remains unchanged and the value of m_{a} is the one that changes. Naturally, the excitation winding must also be changed. If the change in the number of turns is defined as $N_{\mathrm{e}_2} = k \, N_{\mathrm{e}_1}$, the resistance must satisfy the relation4.6. As a result of this change, the current will be scaled by the factor of $1/k^2$, leading to different H_{1hpk}, i.e. not equal fundamental magnetic conditions (4.8).

$$H_{\mathrm{pk}_2} = \frac{1}{k^2} \, I_{\mathrm{e}_1} \, k \, N_{\mathrm{e}_1} \frac{1}{\ell} = \frac{1}{k} \, H_{\mathrm{pk}_1} \tag{4.8}$$

The modulation depth must then be increased to compensate for this reduction of H_{1hpk} to such a value that the following relationship is satisfied:

$$I_{\mathrm{e}_2} = \frac{1}{k} \, I_{\mathrm{e}_1}. \tag{4.9}$$

Modulation type effect on losses

The effect of modulation type is determined by repeating the experiment for both unipolar and bipolar modulation types, leaving all other parameters of the inverter and experiment unchanged.

Switching frequency effect on losses

The switching frequency can be changed independently of the other supply parameters without significantly changing the voltage RMS of the output. However, the change in the harmonic content of the output voltage and current has an effect on the load itself. The resistance of the excitation winding increases with the frequency due to the skin and proximity effects, while on the other hand, the core loss decreases due to the reduction of the area bounded with each minor remagnetization cycle.

In general, resistance increases with frequency due to skin and proximity effects. Changing the switching frequency does not change the fundamental frequency of voltage and current, so the resistance remains unchanged for that frequency component. However, since higher harmonic components occur at and around the switching frequency and its multiples, the higher harmonics experience higher resistance when the switching frequency is increased.

This leads to the conclusion that the influence of the switching frequency itself cannot be completely excluded from the other inverter parameters: U_{DC} or m_{a} will be different for the same $B_{1\mathrm{hpk}}$ value at the different switching frequency. Usually, the experiment is performed for a static value of U_{DC}, and m_{a} is the parameter that changes throughout the experiment: equal m_{a} for two different frequencies leads to different $B_{1\mathrm{hpk}}$ values. However, these differences in m_{a} are minor and most of the change in loss can be attributed to the change in switching frequency itself. Therefore, the effect of switching frequency is determined by repeating the experiment for different switching frequencies in the range of $2 - 40$ kHz while keeping all other parameters of the inverter and the experiment unchanged.

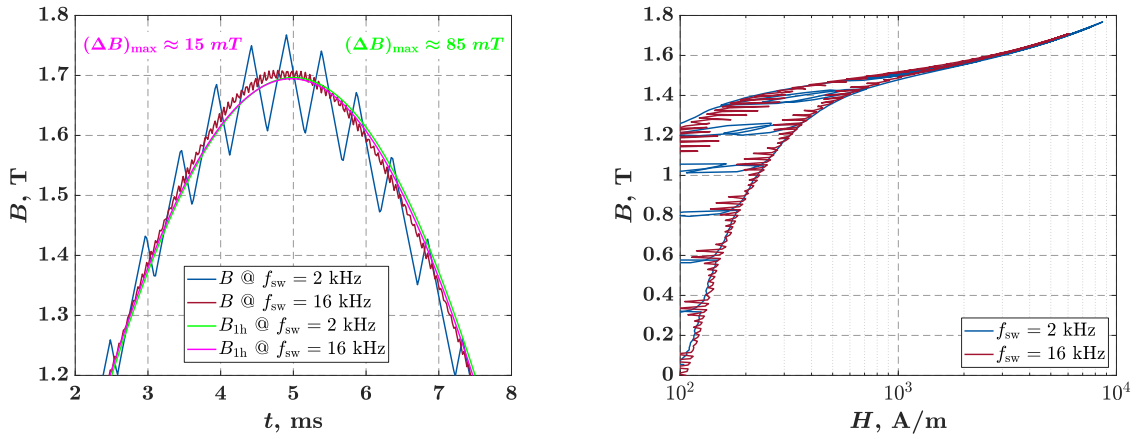

(A) Flux density waveforms

(B) Hysteresis loops

FIGURE 4.8: Relationship between the peak value of the flux density waveform and the amplitude of the fundamental, shown for the AC measurements on the C1a core and two different switching frequencies under bipolar modulation. A section of the corresponding hysteresis loop shows the misalignment of the loop peaks for different switching frequencies.

Comparison of losses

At lower switching frequencies, the current ripple is considerable, as is the ratio of the ripple to the fundamental. This can be seen in the subfigure4.8a, where a significant difference in overall waveform ripple can be observed between waveforms obtained at two different switching frequencies for the virtually identical fundamental components. The peak-to-peak ripple is much larger for the lower value of f_{sw}, resulting in a higher maximum value of B_{pk}. This can also be seen in the subfigure4.8b, where it is clear that the peaks of the hysteresis loop do not coincide with each other.

Since flux ripple is a byproduct of the inverter power supply and does not contribute to the useful work in electromechanical conversion, losses should not be compared using peak flux density, as this could mean comparing losses at two different machine operating points. Therefore, for the purpose of this research, the losses are compared using the peak of the fundamental flux density waveform.

4.2 DC bias measurements

To determine the effect of varying DC bias field on the formation of the minor loops, i.e. PWM-induced losses, the DC bias measurements procedure is implemented. It is designed to set different values of DC core magnetization as well as flux ripple frequency and peak-to-peak values. The DC bias setting is reflected by specifying a particular B_{bias}, while the flux ripple is determined by specifying both $\frac{dB}{dt}$ and ΔB parameters. The unique feature of this setup is that the DC magnetization bias is achieved using a single-phase inverter with a single excitation winding.

Figure4.9shows the typical waveforms of the excitation voltage, current, flux, and flux density for the DC bias measurement performed with the following parameters: $\frac{dB}{dt} = 0.1$ T/ms, $\Delta B = 25$ mT and values of DC bias $B_{bias} = 1.5$ T and $B_{bias} = 1.84$ T, respectively. The inverter supplies the excitation winding with a square-wave voltage shown in Figure4.9a. The amplitude of the square wave voltage corresponds to the value of the DC link voltage of the inverter U_{DC}, and its average value (U_{bias}) is controlled by changing the duty cycle of the MOSFET switches. A duty cycle of $D = 0.5$ results in a mean value of zero because both pairs of MOSFETs conduct for the same amount of time. Although the average is zero, there is a AC current ripple in the winding whose amplitude depends on the DC link voltage, the switching frequency, and the winding and core parameters. When the duty cycle is increased towards $D = 1$,

one of the MOSFET switch pairs conducts longer than the other, and consequently, a non-zero average value occurs at the inverter output.

When the voltage shown in Figure4.9ais applied to the excitation winding, a DC current with triangular ripple begins to flow, and a magnetic flux with non-zero average value and ripple is produced, as shown in subfigures4.9band4.9c. The average value of the current is determined by the average value of the voltage and the winding resistance (U_{bias}/R), while the peak-to-peak value of the ripple depends on the amplitude of the applied square-wave voltage (U_{DC}). Both effects are visible in Figure4.9b. A higher

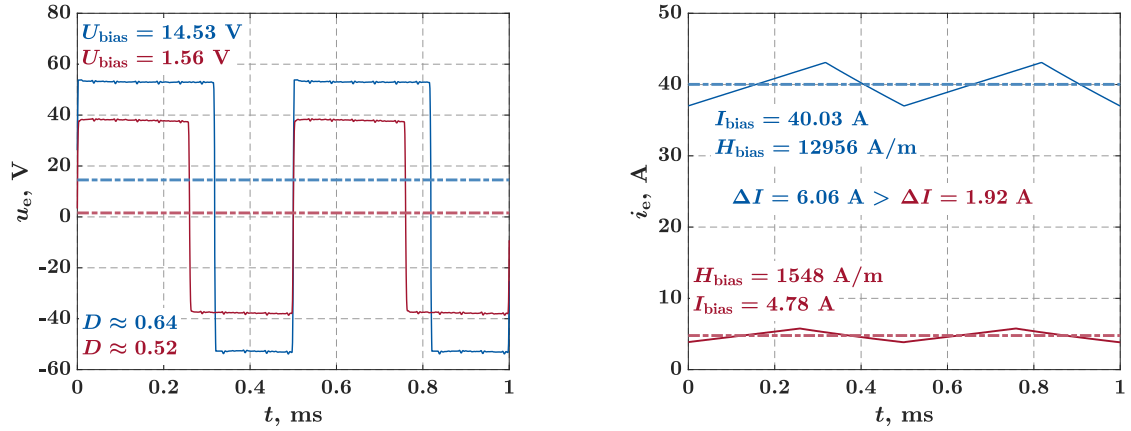

(A) Excitation voltage

(B) Excitation current

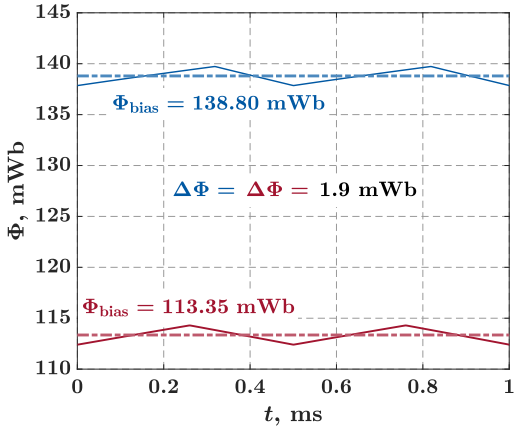

(C) Flux

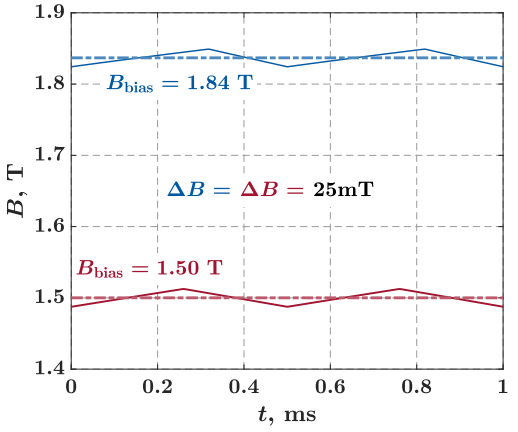

(D) Flux density

FIGURE 4.9: Typical excitation and response waveforms for DC bias measurements at $f_{\text{sw}} = 2$ kHz and $\frac{\text{dB}}{\text{dt}} = 0.1$ T/ms.

value of DC current I_{bias} is obtained with a larger duty cycle of $D = 0.64$, and the peak-to-peak ripple increases due to the increase in the amplitude of the applied square-wave voltage.

Just as with the current, the average value of the flux and the peak-to-peak ripple of the flux are associated with U_{bias} and U_{DC}, respectively. However, the resistance of the excitation winding, the saturation level, and the iron loss determine the final values. Since the average value of flux is related to the average value of voltage U_{bias}, the voltage drop across the winding resistance affects the average value of flux. Thus, if the winding resistance changes for any reason, such as temperature changes or skin and proximity effects, the same bias voltage U_{bias} applied to the terminals of the excitation winding will result in a different Φ_{bias}. The peak-to-peak ripple of the flux depends on U_{DC}, and with no change in Φ_{bias}, an increase in U_{DC} increases the peak-to-peak ripple. The flux is proportional to the flux density, so the peak-to-peak ripple of the flux defines the peak-to-peak ripple of the flux density, i.e., the ΔB of the minor loop (Figure4.9d). For different values of B_{bias}, U_{DC} must be adjusted to obtain the same peak-to-peak ripple. This can be seen by comparing the4.9band4.9dsubfigures, where it is evident that the same values of ΔB were obtained with two different values of U_{DC} at different B_{bias} values. At a higher B_{bias} point of 1.84 T, a larger U_{DC} was required to keep the peak-to-peak ripple of the current, i.e., the magnetic field strength, high enough to achieve the same ΔB of 25 mT. The weight of the U_{DC} adjustments is related to the $B - H$ curve of the material and is more pronounced at higher saturation values (Figure4.10).

The fundamental frequency of I, Φ and B is equal to the switching frequency of the inverter. The switching frequency, in conjunction with a given ΔB, determines the $\frac{\mathrm{d}B}{\mathrm{d}t}$ of the minor loop. The parameter $\frac{\mathrm{d}B}{\mathrm{d}t}$ is thus defined over the entire period of the minor loop, ignoring the asymmetry between the half-periods caused by the change in duty cycle. This parameter was chosen as one of the parameters defining the characteristics of a minor loop, rather than the switching frequency, because it is more physically accurate to define the effects of the minor loop on losses as a function of the rate of change of flux density. In addition, the use of the parameter $\frac{\mathrm{d}B}{\mathrm{d}t}$ allows easier classification of the specific measurement and subsequent comparison of the results: The results can be compared in terms of $\frac{\mathrm{d}B}{\mathrm{d}t}$, but not in terms of f_{sw}, since for the two different values of ΔB the same rate of change of flux density occurs for two different values of switching frequency.

Finally, different values of U_{bias} define the B_{bias} of the core which can be determined

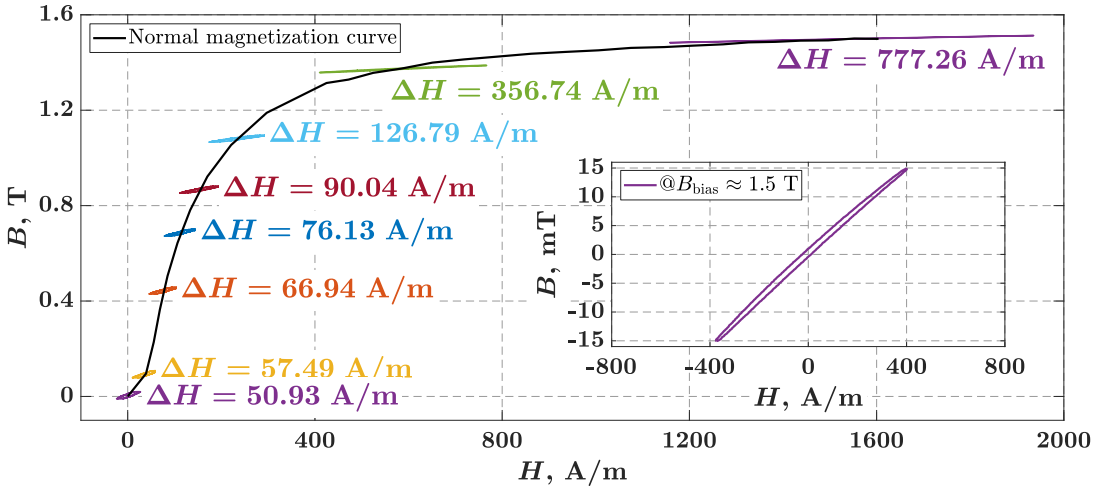

FIGURE 4.10: Minor loops with $\Delta B = 30$ mT at different values of B_{bias}. Different values of the peak-to-peak ripple of the magnetic field strength ΔH are required to keep the ΔB unchanged when the B_{bias} is changed.

using the known $B - H$ curve of the material and the H_{bias} calculated from the average value of the excitation current.

The ripple of AC is generated only by PWM switching, so measurements of power loss under these conditions provide data on the contribution of PWM to losses. The data are collected in terms of the parameters ΔB, $\frac{dB}{dt}$, and B_{bias}.

Experiments were performed on cores C1a, C2a, and C3 for the parameter combinations listed in Table4.1. The ΔB parameter values were chosen to be in the range of expected flux density ripples in electrical machines, and f_{sw} as the expected typical values of inverter switching frequencies. The number in each cell of the table4.1represents a value of the $\frac{dB}{dt}$ parameter for a given pair of ΔB and f_{sw}, and the same background

TABLE 4.1: Combination of parameters ΔB, f_{sw} and $\frac{dB}{dt}$ for which experiments were performed.

$\frac{dB}{dt}$ VALUES (T/ms)				
f_{sw} (kHz)	ΔB			
	20 mT	40 mT	80 mT	120 mT
2		0,16	0,32	0,48
4	0,16	0,32	0,64	
8	0,32	0,64		
16	0,64			

color of the cell indicates the same $\frac{dB}{dt}$ parameter. All measurements were performed in the B_{bias} range of 0 - 1.8 T or higher.

Two modes of operation are implemented for the conduction of DC bias measurements: current control and duty cycle set point mode.

In the current control mode (CC), the desired current value can be set and the implemented PI controller continuously adjusts the duty cycle to achieve the current set point. This mode is used only for the DC bias measurements at B_{bias} values greater than 1.5 T, since the stability of the output is greatly reduced at lower current setpoints. The M400-50A material used in the experiments requires $H_{bias} \approx 180$ A/m to achieve B_{bias} of 1 T. As an example, consider a C1a core where the excitation winding has $N_e = 424$ turns and the equivalent magnetic length of the core is $\ell_{eq} = 1.4822$ m. The full range of B_{bias} from 0 to 1 T is then achieved in the current range of 630 mA. Oscillations of the output current with respect to the set point become more severe as the set point decreases, and for a larger number of excitation winding turns, a relatively small oscillation of I_e can result in significant oscillations of H with respect to H_{bias}.

The Duty Cycle Set Point (DCS) mode allows the user to manually enter the desired duty cycle, which then results in a specific average current value. This control mode results in stable B_{bias} operating points over a relatively wide operating range. However, it becomes unstable in the region of high core saturation because the excitation current has a significant effect on the temperature of the winding and consequently on its resistance. The change in resistance makes it impossible to achieve a stable operating B_{bias} point to take a sufficiently long sample for analysis. Therefore, the application of the duty cycle setpoint mode is limited to B_{bias} values obtained with an excitation current whose RMS value is low enough not to change the winding resistance in the time required to take a sample. The practical limit for the measurement setup used in this research was about $B_{bias} \approx 1.65$ T. This limit could be further extended by optimizing the ratio of winding turns per cross section.

Regardless of the fact that both modes have their limitations, they are found in different ranges of the parameter B_{bias}, and by combining the two modes, stable B_{bias} points can be obtained throughout the whole range of interest.

The DC measurements procedure consists of the following steps:

- **U_{DC}, f_{sw} and PI controller setting**

  The U_{DC} parameter determines the ΔB value and in combination with the switching frequency, it determines $\frac{dB}{dt}$ value. Both parameters affect the response of the current to a step change, so the parameters of the PI controller should be adjusted to achieve a fast but aperiodic response.

- **U_{DC} - I_e pairs mapping**

  Because of losses in the core, the U_{DC} value must be adjusted for each measurement point to keep the ΔB parameter constant. Its value for certain B_{bias} can be predicted but not accurately determined. For higher B_{bias} values, the core heats up relatively quickly and the adjustment of U_{DC} takes some time. Therefore, U_{DC} - I_e pairs for higher B_{bias} ($>\approx 1.5$) must be mapped in advance to avoid excessive heating of the core during the subsequent measurement process.

  In the CC mode and at higher fundamental frequencies ($>=$ 16 kHz), a low-frequency oscillation of B_{bias} can occur, which then leads to somewhat higher measured values of ΔB. This problem was related to the DAQ system specific to this measurement setup, since the time window for determining the ΔB value could not be further reduced. A steady B_{bias} can be achieved by switching to DCS mode and then taking a measurement of ΔB.

- **Measurements**

  Measurements are made primarily in the CC mode and using mapped pairs of U_{DC} - I_e, starting with the highest field density values. When $B_{bias} \approx 1.5$ T is reached, the mode is switched to DCS for lower values of B_{bias}. The duty cycle is then changed in fixed steps with respect to the desired resolution of P_{PWM} - B_{bias} and B_{bias} - H_{bias}. The resolution can be set higher in the regions of greater interest, i.e., in the region of peak PWM loss contribution and in the region near the knee point of the B-H curve of the material.

  The core temperature should always be monitored and kept within a relatively narrow range during the measurement procedure to eliminate the temperature effect on the losses.

4.2.1 Current ripple

In the previous sections, it was mentioned that the ripple of current and flux waveforms has a triangular shape. However, since the measurement setup proposed in this research uses a single excitation winding and source to generate both the DC bias of the flux and the flux ripple in the core, some clarifications are needed to fully understand the ripple shape and its deviations from the ideal triangular waveform.

The DC bias of the flux is controlled by changing the duty cycle of the MOSFET switches. Therefore, the ascending and descending legs of the triangular waveform do not last the same amount of time, except at the point $B_{\text{bias}} = 0$ T, i.e. $D = 0.5$. When the duty cycle is increased to increase the B_{bias} in the core, the duration of the ascending leg of the triangular waveform increases at the expense of the descending leg. This can be seen in figure4.11, where the duty cycle had to be increased to $D = 0.57$ to achieve $B_{\text{bias}} = 1.85$ T (Figure4.11b). The effect of the duty cycle on losses cannot be evaluated with the proposed setup because a single excitation winding is used. However, the authors in [10] have performed such an evaluation with their measurement setup. According to their results, shown in Figure4.12, the duty cycle value affects PWM losses up to about $3 - 4\%$ for duty cycle values between 0.5 and 0.6, which corresponds to the range of values used in this research.

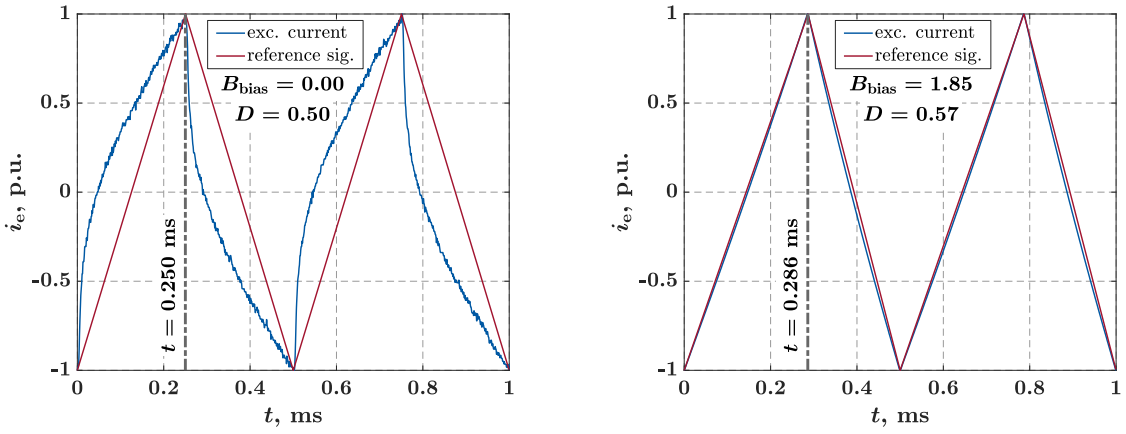

(A) Zero (low) flux density

(B) High flux density

FIGURE 4.11: Normalized ripple of the excitation current during the DC bias measurements performed on C1a core compared to the reference (ideal) triangular waveform with equal duty cycle. The DC value of the excitation current was removed from the waveform and only AC component is compared. Experiment parameters: $f_{\text{sw}} = 2$ kHz, and $U_{\text{DC}} = 91.4$ V.

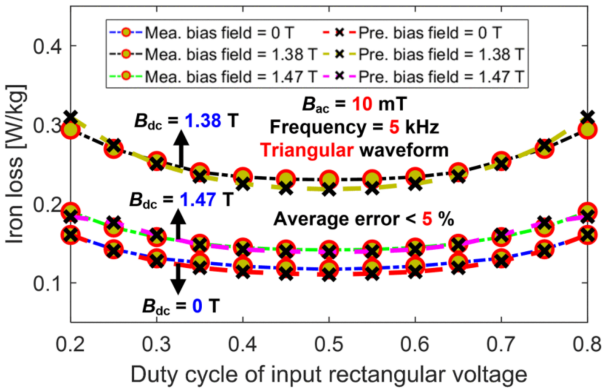

FIGURE 4.12: Effects of duty cycle on PWM losses as presented in [10]. Figure original caption: "Comparison of measured and predicted iron loss of triangular waveforms with different duty cycles for three dc-bias field values".

Apart from the asymmetry, the shape of the ripple can be distorted compared to the triangular shape depending on the value of the B_{bias} (Figure4.11a). The reason for this is the change of the iron losses with the change of the B_{bias} value. The simple equivalent circuit of the core with excitation and search windings is shown in Figure 4.13. At lower B_{bias} values, the iron losses are smaller compared to the losses at higher B_{bias} values, which is reflected in a smaller resistance value R_{i} of the equivalent circuit. For the same voltage applied to the core, a smaller resistance results in a larger current,

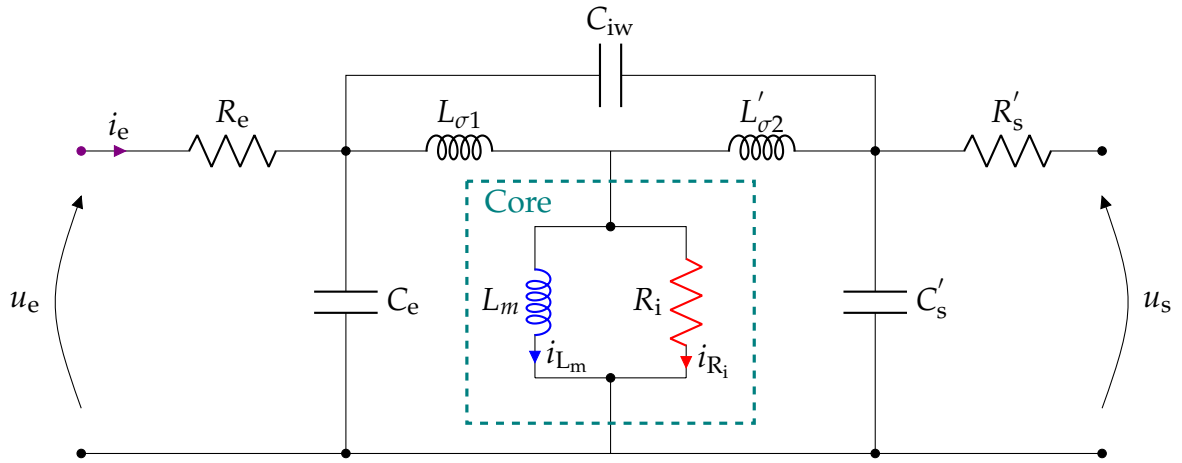

FIGURE 4.13: Equivalent circuit of a core with excitation and search windings, where R_{e} and R'_{s} are resistances, $L_{\sigma 1}$ and $L'_{\sigma 2}$ are leakage inductances, and C_{e} and C_{s} are capacitances of the excitation and search windings, respectively. C_{iw} is the capacitance between the excitation and search windings, L_{m} is the main magnetizing inductance, and R_{i} is the resistance representing the iron losses of the core. The $'$ sign next to the variables indicates that the variable value is based on the primary with a ratio $(\frac{N_{\text{e}}}{N_{\text{s}}})^2$.

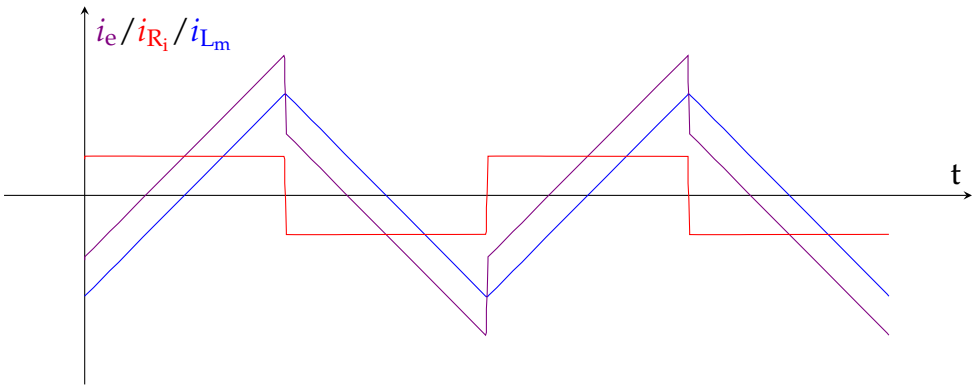

FIGURE 4.14: AC component of the excitation current I_e and the currents through the R_i and L_m elements of the equivalent circuit.

and since the current flow through R_i changes as rapidly as the excitation voltage, which happens almost instantaneously when a square-wave voltage is applied, the effect of this instantaneous change on the waveform of the excitation current is clearly visible (Figure4.14). Considering only the parallel branch of the equivalent circuit for explanatory purposes, at the point where the square-wave voltage changes, the excitation current drops almost instantaneously by a value determined by R_i, and then follows the slope defined by the value of L_m. For larger values of B_{bias}, R_i is also larger, and the current flow through it is negligible compared to the total excitation current.

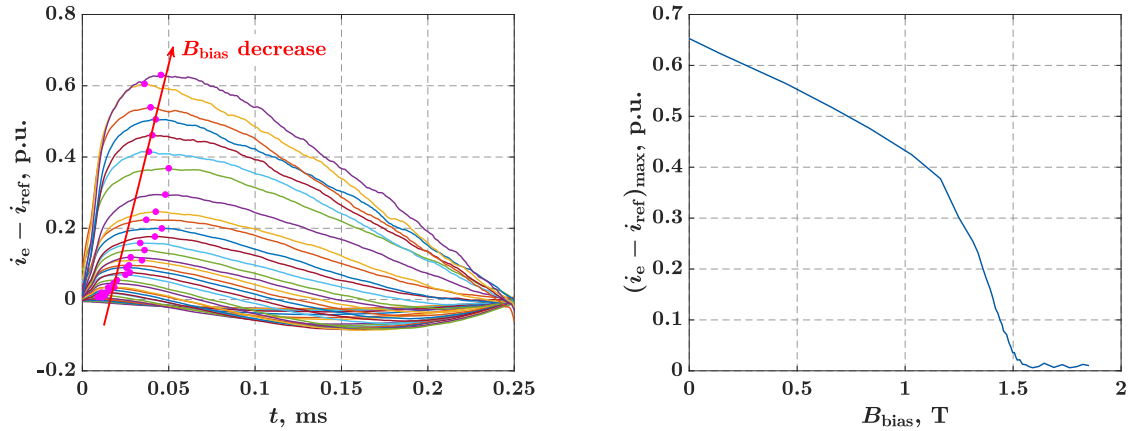

(A) Half of period for each value of B_{bias}

(B) Max. difference in the relation to B_{bias} value

FIGURE 4.15: The difference between the excitation current during the DC bias measurements performed on C1a core and reference (ideal) triangular waveform shown in per unit system. DC bias experiment parameters: $f_{sw} = 2$ kHz, and $U_{DC} = 91.4$ V.

Therefore, at higher B_{bias}, this effect decreases, and the waveform of the excitation current is almost equal to the L_{m} current. This also means that the waveform of the excitation current almost completely matches the ideal triangular shape (Figure4.11b).

The deviation of the excitation current from the ideal triangular waveform with the same duty cycle is shown in Figure4.15. On the left side, for each value of B_{bias}, a half period of the deviation is shown, and the maximum of the deviation is marked with a magenta dot. On the right side, the maximum deviation for each cycle is plotted against the value of B_{bias} to clearly show how this deviation decreases with the increase of the DC bias field and the increase of the iron losses.

4.3 Loss determination methodology

Losses in the core are calculated using the measured signals of the excitation current and search voltage. The power loss is calculated in the frequency domain and each harmonic frequency is analysed separately. In this way, amplitude deviation and phase delay caused by current transducer imperfections can be corrected [45]. The fast Fourier transform (FFT) is used to transform the search winding voltage and excitation current into a series of Fourier harmonics expressed by amplitude and phase. Each harmonic contribution to the power loss is then calculated separately, taking into account phase and amplitude corrections. The total active power is then the sum of all calculated active power contributions at each harmonic frequency:

$$P_{\text{loss}} = k \cdot \sum_{h=1}^{n} 0.5 \cdot \widehat{U}_{\text{s}_\text{h}} \cdot \frac{\widehat{I}_{\text{e}_\text{h}}}{A_{\text{C}_\text{h}}} \cdot \cos(\varphi_{\text{U}_\text{h}} - \varphi_{\text{I}_\text{h}} - \varphi_{\text{C}_\text{h}}), \tag{4.10}$$

$$k = \frac{1}{m} \frac{N_{\text{e}}}{N_{\text{s}}}. \tag{4.11}$$

where $\widehat{U}_{\text{s}_\text{h}}$ and $\widehat{I}_{\text{e}_\text{h}}$ are the voltage and current amplitudes of the h_{th} harmonic, $\varphi_{\text{U}_\text{h}}$ and $\varphi_{\text{I}_\text{h}}$ are the voltage and current phase angles for the h_{th} harmonic. A_{C_h} and $\varphi_{\text{C}_\text{h}}$ are amplitude and phase delay corrections of the h_{th} harmonic for the data acquisition system and transducer used for measurement. Factor k includes the transformation ratio of excitation and search winding and core mass, as stated by equation4.11. By using the search voltage signal and a transformation ratio instead of the excitation voltage, the winding losses are not included in the calculations and the results represent only the core loss.

Other methods of determining losses have been considered, mainly to confirm the calculation method. However, almost all other methods are calorimetric and result in loss data that are merged with excitation winding losses. Extracting these losses from the total losses measured under conditions that involve skin and proximity effects, which are also temperature dependent, is a task that again leads to the same or even greater uncertainty than the proposed calculation method. One could attempt to measure only the heating of the core by placing sensors directly on its surface, but because of its better thermal conductivity and much lower mass, the excitation winding heats much faster than the core. Since the winding and the core are closely bound together, there is no way to prevent heat transfer from the winding to the core. The core temperature is monitored during the experiments, but there is no way to determine the extent to which heating the winding affects the rise in the core temperature. In addition, the experiment set up in this way neglects the energy transferred from the core to the ambient air by convection.

4.4 Presentation of the results of measured losses

Power loss is always presented in relation to the flux density value, whether it is the peak flux density for the AC loss experiment results or the flux density bias value for the DC bias experiment results. However, there are some difficulties in determining the exact value of $B_{1\text{hpk}}$ and B_{bias}, and one should take this into account when analysing and comparing the results. For example, the value of the flux density depends on the area S of the ring core cross- section regardless of the type of experiment:

$$B = \frac{\Phi}{S} \tag{4.12}$$

Due to the curvature of the ring cores, especially cores with lower degrees of non-uniformity, the distribution of the field in the core is not uniform over the entire geometric cross section of the core. The calculation of the equivalent area is proposed in the IEC standard [46], but the effect of the non-uniform field distribution does not vary linearly with $B_{1\text{hpk}}$. Furthermore, specifically for the DC bias experiment, B_{bias} is determined from the measured value of DC current, i.e., DC value of magnetic field strength and $B - H$ curve of the material. The accuracy of the available $B - H$ curve determines how accurately B_{bias} can be determined.

Chapter 5

Discussion and Results of AC and DC Bias Measurements

The experimental results are presented in this chapter in three main sections: Determination of the normal magnetization curve, AC loss measurements, and DC bias measurements. First, the results of the normal magnetization curve measurements are presented and the final curves are determined. In the following section, the measurement results are presented, focusing on the effect of the voltage supply parameters generated by the PWM on the total AC iron losses. Finally, in the section on the DC bias experiment, the results of the minor loop measurements are presented in terms of the different values of the parameters ΔB, $\frac{\mathrm{d}B}{\mathrm{d}t}$ and B_{bias} and their effects on the PWM-induced losses. The results on the geometrical parameters of the cores, laser cutting, and temperature effect on the total losses AC and PWM-induced losses are also presented in the corresponding sections.

A large number of measurements were made in each experiment, in particular for the DC bias experiment. Many measurements were made to obtain loss data for a wide range of inverter supply or minor loop parameters, and most results between two different measurements do not differ phenomenologically. For this reason, not all measurement results are shown in the thesis, but only those that best represent the phenomena currently under discussion.

5.1 Determination of the normal magnetization curve

The normal magnetization curves were obtained using the proposed setup, and the results were compared with those of measurements performed at the Končar Electrical Engineering Institute (IET), where a pure sinusoidal source was used as excitation. In

both experiments, the same measurement methodology was used as described in the chapter4section4.1.1. The comparison of the obtained curves for core C1a is shown in figure5.1. Considering the ratio between the obtained curves, shown in the subfigure 5.1b, it is clear that there is a relatively large error of up to 15 % in determining the normal magnetization curve with the proposed setup for lower values of $B_{1\mathrm{hpk}}$. This is due to the relatively high peak-to-peak value of the ripple compared to the fundamental. As $B_{1\mathrm{hpk}}$ increases, the ratio of ripple to fundamental decreases significantly, and the difference between the two curves falls below 1 % at $B_{1\mathrm{hpk}} = 0.55$ T and below 0.3 % at $B_{1\mathrm{hpk}} = 1.25$ T.

The advantage of the proposed setup is the possibility to achieve much higher values of $B_{1\mathrm{hpk}}$ compared to the only other setup available at the Končar IET. The final normal magnetization curve for each core is determined by combining the results obtained at the Končar IET for lower values of $B_{1\mathrm{hpk}}$ and the results obtained with the proposed setup for $B_{1\mathrm{hpk}}$ values higher than those achievable in the Končar IET laboratory. The final normal magnetization curves for each core are shown in subfigure5.2a.

Subfigure5.2bshows the difference in the obtained normal magnetization curves for cores C2a and C3 compared to the reference core C1a. The difference is shown as the ratio of the B values of the $B - H$ curves for the corresponding cores. The effect of both core non-uniformity and laser cutting can be observed, but laser cutting seems to

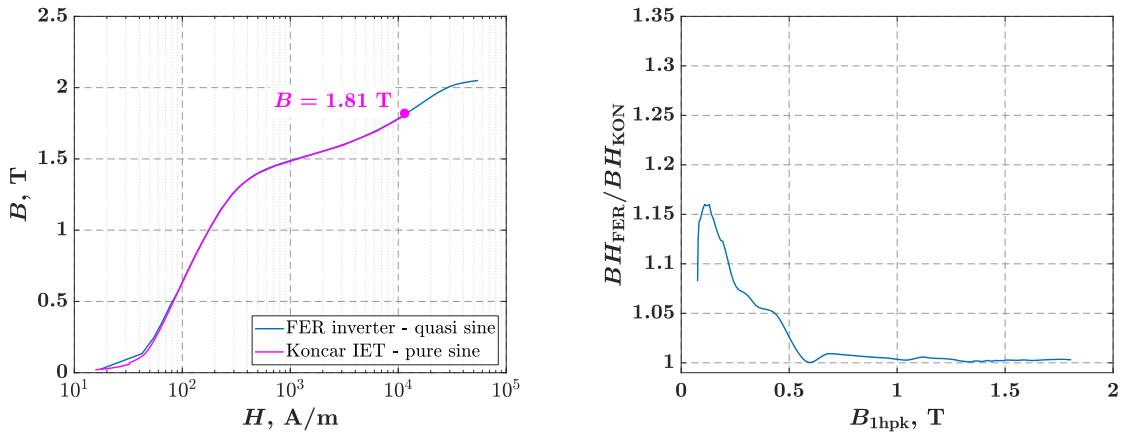

(A) Determined $B - H$ curves

(B) Ratio of the determined curves

FIGURE 5.1: Normal magnetization curve of the C1a core determined for $f_{1\mathrm{h}} = 10$ Hz using the proposed measurement setup compared to the normal magnetization curve determined at the Končar Electrical Engineering Institute (Končar IET). The maximum value of B obtained at the Končar IET was $B = 1.81$ T.

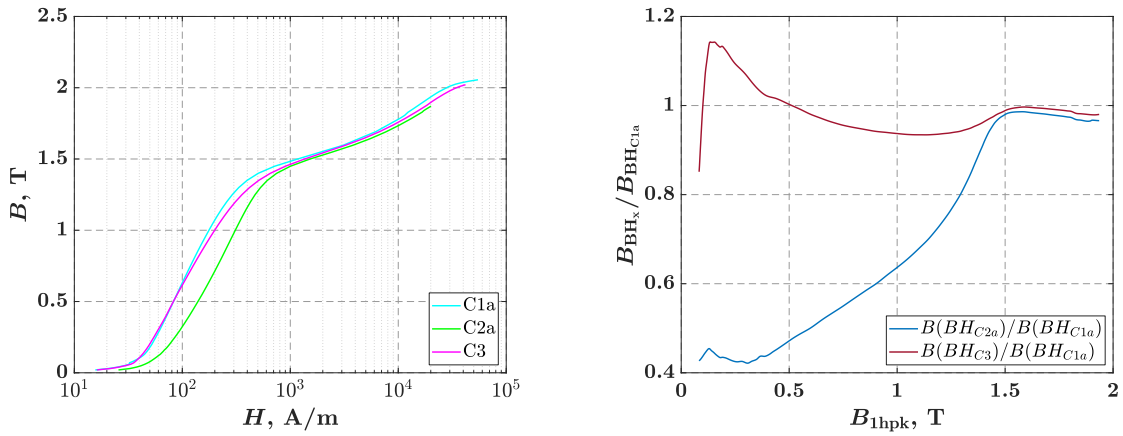

(A) Determined $B - H$ curves

(B) Ratio of the determined curves

FIGURE 5.2: Normal magnetization curves shown for the C1a, C2a and C3 cores obtained by combining measurements at the Končar IET and the proposed measurement setup.

have a much more remarkable effect on the $B - H$ curve, especially for lower values of the peak of the fundamental flux density $B_{1\text{hpk}}$.

5.2 AC loss measurements

The AC loss measurement method was implemented and measurements were performed to determine the influence of the inverter PWM parameters on the total loss and to compare the results with the well known theory and findings from other research papers. Initial measurements were performed on the core C0 to observe the change in losses when the power supply is changed from sinusoidal to PWM-generated. In addition, the effect of the modulation type on the core losses, the modulation depth and the effect of the DC link voltage were also studied, which was made possible by a specially designed excitation winding (Section3.4.4). Later, AC loss measurements and analysis is performed on newly designed, industrially built and wound cores C1a, C2a, and C3. Apart from PWM-generated power supply effect on losses, the effect of core non-uniformity, laser cut, and temperature are also considered.

The figures in the following sections show the calculated (Section4.3) total AC losses under PWM-generated excitation for several different cores and different supply parameters, and where applicable, the results are compared with the AC losses under

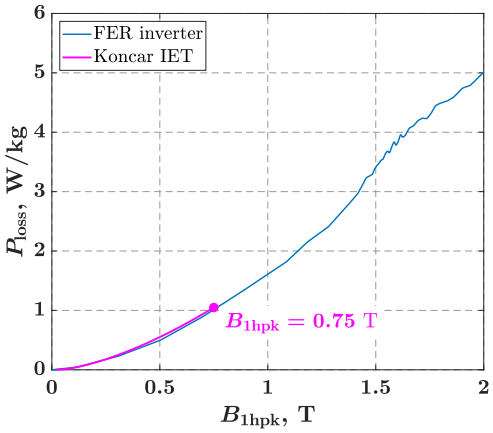

(A) C1a core

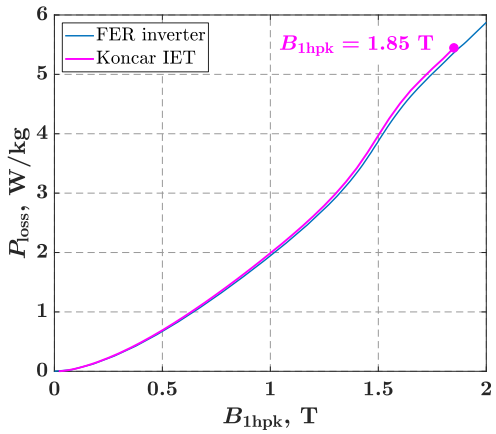

(B) C2a core

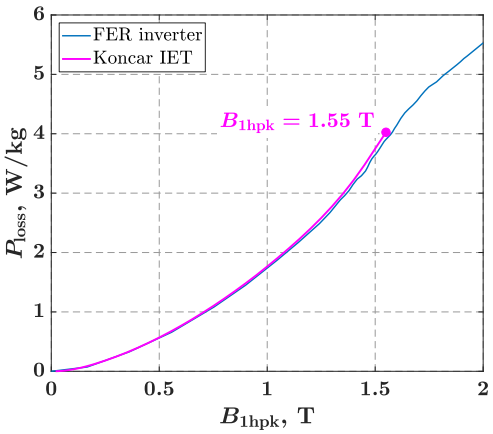

(C) C3 core

FIGURE 5.3: Total AC losses obtained under sinusoidal excitation at the Končar Electrotechnical Engineering Institute (IET) and under quasi-sinusoidal excitation using proposed measurement setup and inverter. Maximum B_{1hpk} value obtainable at the Končar IET is marked with a magenta dot.

the so-called quasi-sinusoidal excitation. This quasi-sinusoidal excitation is also generated with PWM, but with such inverter supply parameters ($f_{sw} = 40$ kHz, unipolar modulation) that the results obtained are similar to those obtained under sinusoidal excitation. Some variation in the results is to be expected, but the lack of a powerful sinusoidal source required to produce high density fields in relatively large cores forced the choice of the inverter as the power supply. The high switching frequency of $f_{sw} = 40$ kHz and the unipolar modulation provided a flux waveform in the core

FIGURE 5.4: Laboratory for Testing of Magnetic Materials at the Končar IET Laboratory Center and ring measuring coil sensor used in this research [49].

that was very similar to the sine wave. Figure5.3shows a comparison of the core losses obtained under pure sinusoidal excitation at the Končar IET using high-quality Brockhuas measuring equipment (Figure5.4and Table5.1) with the losses obtained with inverter and quasi-sinusoidal excitation. Good agreement between the curves is observed for all three tested cores. Themagentadot marks the maximum $B_{1\mathrm{hpk}}$ value achievable at the Končar IET for each core. The values of the maximum achievable $B_{1\mathrm{hpk}}$ of 1.55 T for core C3 and, in particular, $B_{1\mathrm{hpk}}$ of 0.75 T for core C1a are too low to use these results in comparison with those obtained with PWM-generated supply. Although the maximum achievable $B_{1\mathrm{hpk}}$ of 1.85 T would be sufficient for core C2a, quasi-sinusoidal excitation is used for comparison for all three cores. Therefore, when the results are compared between the cores, differences in the type of power supply can be ruled out as a cause.

5.2.1 Measurements on core C0

Contribution of the PWM-generated power supply on iron losses is usually observed in the relation to the peak of the fundamental flux density waveform $B_{1\mathrm{hpk}}$ and inverter switching frequency f_{sw} parameters. In general, losses increase with $B_{1\mathrm{hpk}}$, which is natural to expect. However, the rate at which they increase changes as a function of peak flux density. Regardless of the switching frequency, the most significant change in the loss curve occurs around the same point of $B_{1\mathrm{hpk}} \approx 1.4$ T (Figure5.5). The greatest ripple in flux density with respect to peak-to-peak value occurs at the peak of the fundamental, and if the peak of the fundamental is in the nonlinear region of the $B - H$ curve, minor loops with the largest values of ΔB for that particular case also form in the nonlinear region where they contribute most to the losses. Maximum

TABLE 5.1: Technical data of Brockhaus measurement system used for testing in Končar IET [50].

PARAMETER	VALUE
Model	MPG200D
Sensor	Ring Measuring Coil
Repeatability	0.1 %
Comparability of the measured results	according to IEC 60404 ff.
Setting accuracy of the nominal value	according to IEC 60404 ff.
Maximum current	40 A
Maximum voltage	100 V
Measuring frequency	3 Hz - 20 kHz

PWM contribution to the losses also occurs in this region, which will be discussed in more detail later in relation with the DC bias measurements. Interestingly, the same pronounced point of maximum increase in losses can also be observed for sinusoidal excitation, where small remagnetization cycles do not occur. This suggests that the rate of change of flux through the nonlinear region of the $B - H$ curve has an effect

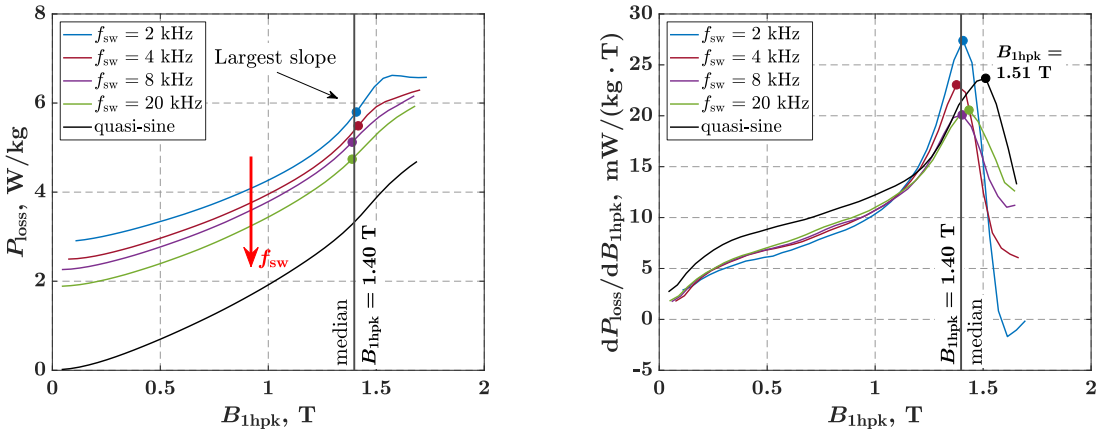

(A) Total AC loss curves

(B) Derivative of total AC loss curves

FIGURE 5.5: Total AC loss curves and their derivative shown for several switching frequencies and sinusoidal excitation. The curves shown are result of the experiment performed on the C0 core with the following supply parameters: $f_{1h} = 50$ Hz, bipolar modulation, $U_{DC} = 400$ V, $N_e = 400$, $m_a \in [0\ 1]$.

on the core losses. The point of maximum loss rise occurs somewhat later than in the PWM-generated excitation case and the difference between the points changes as a function of the core geometry and the build factors.

Figure5.5also shows that the switching frequency f_{sw} has a significant effect on the core losses. Increasing the switching frequency increases the frequency of the current and flux ripples, but decreases the amplitudes of the ripples. At a higher ripple frequency, the number of small remagnetization cycles is larger, but at the same time their contribution to the losses is smaller because the peak-to-peak ripple is smaller. The reduction in losses for fixed B_{1hpk} is more pronounced at lower values of f_{sw}, where losses decrease exponentially with the increase in f_{sw}, than later when this reduction in theory asymptotically approaches a constant value, which would correspond to losses under sinusoidal flux density at a given fundamental frequency (figure5.6).

Surface plots in figure5.7show the dependence of the losses on the peak of the fundamental of flux density B_{1hpk} and the inverter switching frequency f_{sw} for different modulation types and modulation depth ranges. Both surface plots in figure5.7awere obtained with the same $U_{DC} = 400$ V and DC voltage-per-turn ratio of $U_{DC}/N_e = 1$, showing the impact of the modulation type on the losses. Furthermore, subfigures 5.7band5.7cshow the change in the effect of U_{DC}/N_e on the total iron loss for both unipolar and bipolar modulation. Increasing this ratio forces m_a to lower values for the same B_{1hpk}, therefore the total range of m_a values is reduced. With this reduction, the

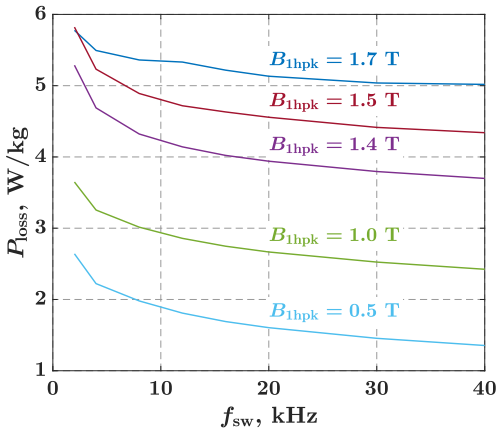

FIGURE 5.6: The effect of the switching frequency on the core losses for a several specific values of B_{1hpk}. The curves shown are result of the experiment performed on the C0 core with following supply parameters: $f_{1h} = 50$ Hz, bipolar modulation, $U_{DC} = 400$ V, $N_e = 400$, $m_a \in [0\ 1]$.

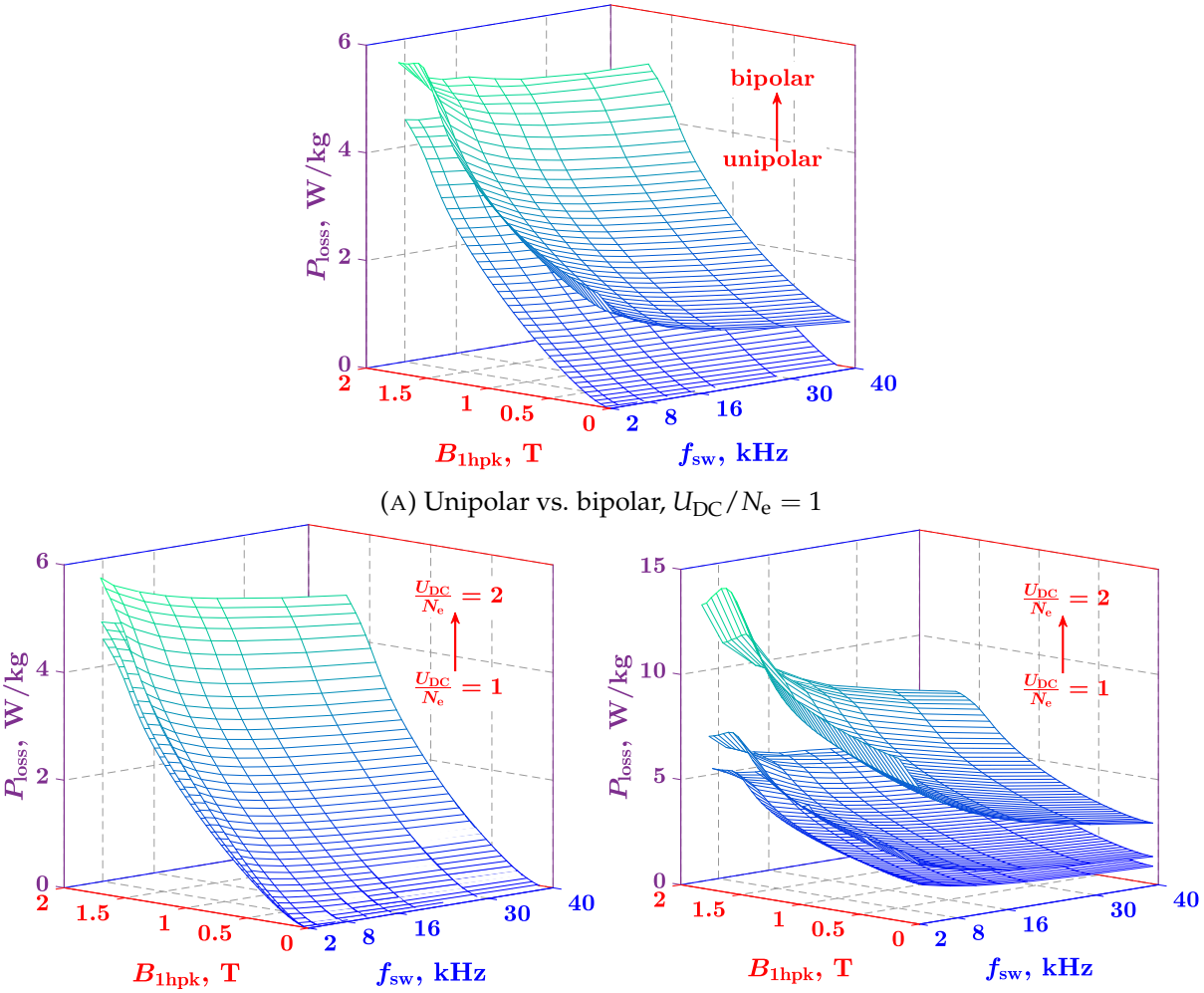

(A) Unipolar vs. bipolar, $U_{\text{DC}}/N_{\text{e}} = 1$

(B) Unipolar, $U_{\text{DC}}/N_{\text{e}} = 1, 1.27, 2$

(C) Bipolar, $U_{\text{DC}}/N_{\text{e}} = 1, 1.27, 2$

FIGURE 5.7: The influence of $B_{1\text{hpk}}$, f_{sw}, modulation type and $U_{\text{DC}}/N_{\text{e}}$ ratio on the total iron losses in the C0 core at $f_{1\text{h}} = 50$ Hz. (A) shows the influence of the modulation type on the loss increase. (B) and (C) show the influence of the ratio $U_{\text{DC}}/N_{\text{e}}$, i.e. a lower m_{a} for the same $B_{1\text{hpk}}$ for unipolar and bipolar modulation, respectively.

total losses increase especially for bipolar modulation where an exponential increase is observed (note the change in the y-axis scale between the subfigures).

The significant influence of the modulation type on the iron loss is due to the different principle of generation of the output voltage. While bipolar modulation uses only two fixed output voltage values $+U_{\text{DC}}$ and $-U_{\text{DC}}$, unipolar modulation also uses zero output voltage. This significantly reduces the ripple of an output signal and does not produce a voltage with opposite polarity along the main loop. In general, the ratio of the current and flux ripple to the fundamental determines how the losses change for virtually the same effective magnetic conditions in the core. Any modulation type and

depth range that reduces the ripple relative to the fundamental also reduces the losses relative to the other case. Here, fundamental was used as a reference, however, there are possibly several harmonic components other than the fundamental that contribute to the effective magnetic flux.

No significant difference was observed in the measured losses with respect to the U_{DC} when the ratio of U_{DC}/N_e is held constant, which is in agreement with the theory. However, for larger values of U_{DC}, dU_e/dt is increased for each switching point, and, since U_{DC}/N_e must be kept constant, N_e is increased accordingly, resulting in a higher capacitance of the excitation winding. This leads to the larger capacitive currents in the excitation winding, which must be filtered out to avoid additional errors in the power loss calculation. The maximum observed increase in losses compared to the case with N_e =100 was 0.8%, 1.5% and 1.8% for N_e =200, 316 and 400 turns, respectively.

5.2.2 Measurements on cores C1a, C2a, C3

The AC loss measurements performed on cores C1a, C2a, and C3 are consistent with those previously presented on core C0. However, improvements were made, especially in the design of the excitation winding, which allowed a more accurate calculation of the iron losses. The excitation winding was industrially wound to ensure uniform distribution and tightness of the turns and to leave a minimal air gap between the winding and the core. Enameled wire was used to maximize the copper-to-insulation ratio, allowing more turns per unit length, which further improves the uniform distribution of the magnetic field in the core. The winding was wound in a single layer and over the entire length of the core.

Figures5.8-5.10show the results of the AC loss measurements performed on cores C1a, C2a, and C3. First subfigure shows the surface plot of the obtained measurements, while other two figures emphasize the effects of the switching frequency and peak flux density on the core losses. Three differently designed cores were used in the measurements to analyze the core geometry and the influence of the laser cut on the losses. Core C1a served as a reference core and cores C2a and C3 were designed differently to observe the effects of the changed parameters on the losses. Comparison of core C1a with core C2a illustrates the effect of laser cut on losses, while comparison of core C1a with core C3 illustrates the effect of uniform to non-uniform geometry of the core on losses.

Cores C1a and C2a are designed as uniform cores, both with the same outer to inner diameter ratio of 1.1. However, core C2a is intentionally designed with a smaller diameter, which in combination with achieving a uniformity ratio of 1.1, results in a reduction in the width of the ring core. Since the laser cut depth does not depend on other core parameters and has an approximately equal value for both cores, the laser cut depth has a larger effect on the core with smaller width. Subfigure5.11ashows the difference in core losses between C1a and C2a cores. It can be seen that the losses of

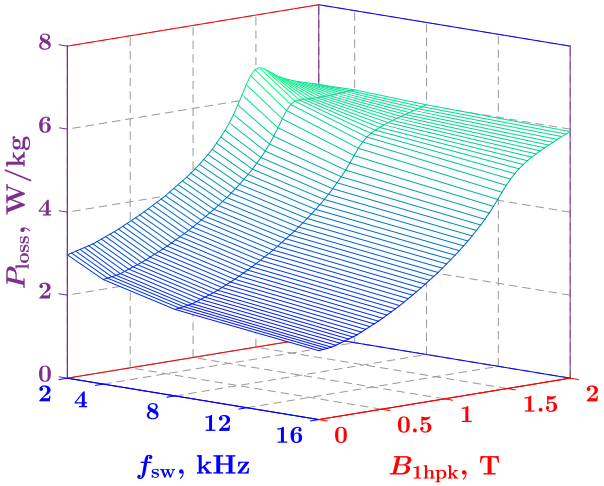

(A) Surface plot of total AC losses

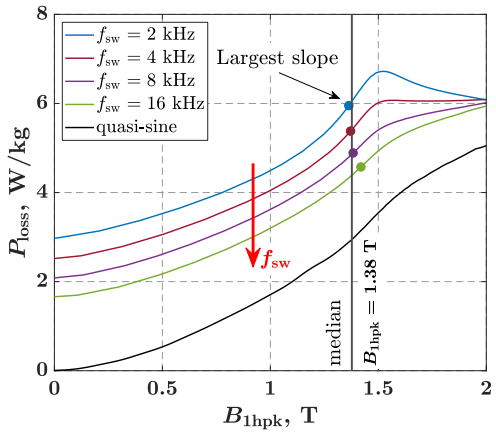

(B) Total AC loss curves

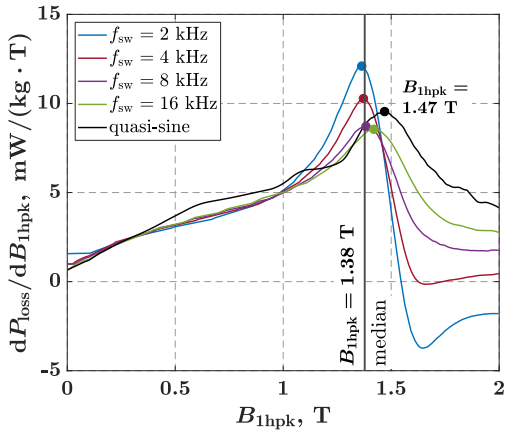

(C) Derivative of total AC loss curves

FIGURE 5.8: Surface plot, total AC loss curves and their derivatives, showing the influence of B_{1hpk} and f_{sw} on the total iron losses in the **C1a** core under PWM-generated and sinusoidal excitation at $f_{\text{1h}} = 50$ Hz. PWM-generated supply parameters: bipolar modulation, $U_{\text{DC}} = 170$ V, $m_{\text{a}} \in [0\ 1]$.

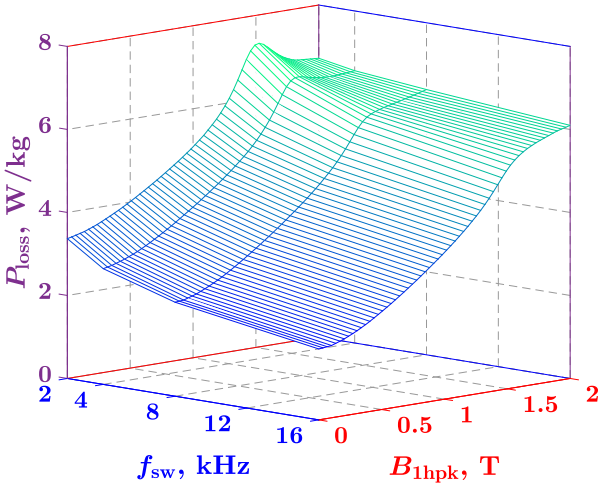

(A) Surface plot of total AC losses

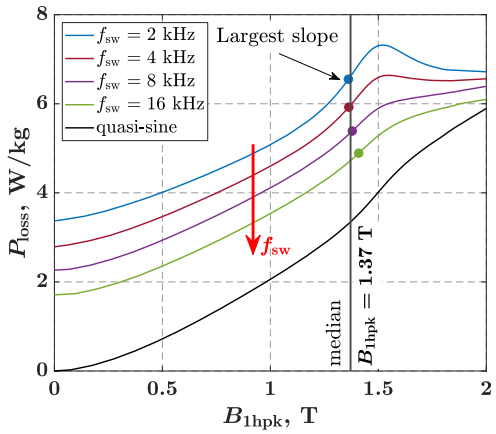

(B) Total AC loss curves

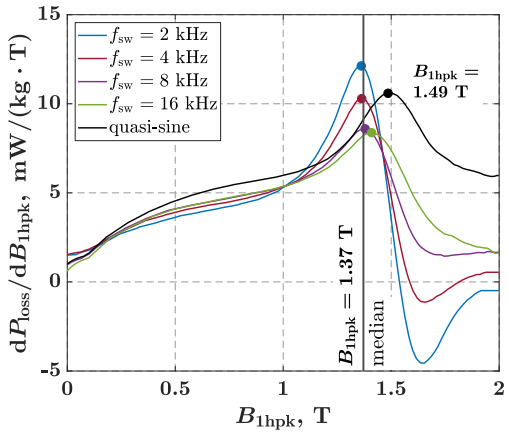

(C) Derivative of total AC loss curves

FIGURE 5.9: Surface plot, total AC loss curves and their derivative, showing the influence of B_{1hpk} and f_{sw} on the total iron losses in the **C2a** core under PWM-generated and sinusoidal excitation at $f_{\text{1h}} = 50$ Hz. PWM-generated supply parameters: bipolar modulation, $U_{\text{DC}} = 70$ V, $m_{\text{a}} \in [0\ 1]$.

the C2a core are larger than those of the C1a core, up to about 0.6 W/kg, depending on the parameters B_{1hpk} and f_{sw}. Presumably, the losses increase at and around the edges of the core laminations, i.e., in the region affected by the laser cut, increasing the total losses of the core. Thus, by reducing the core width, the losses were increased as if a material with slightly worse properties had been used. The loss difference curves agree with the shapes of the PWM-induced loss curves, and the largest difference occurs around $B_{\text{1hpk}} = 1.38$ T regardless of the switching frequency, where the PWM-induced losses also reach their maximum. Moreover, the contribution of PWM-induced losses

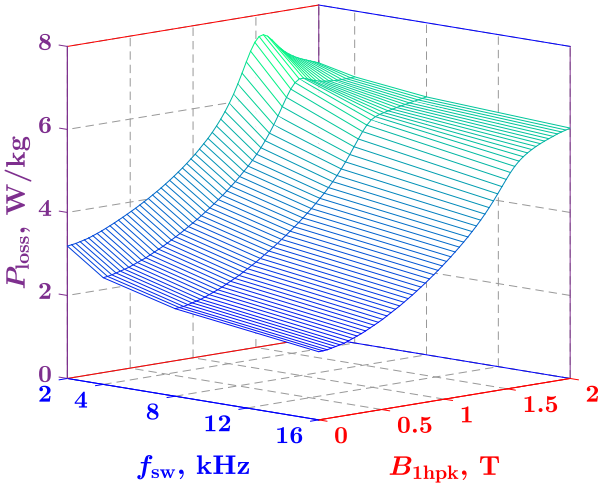

(A) Surface plot of total AC losses

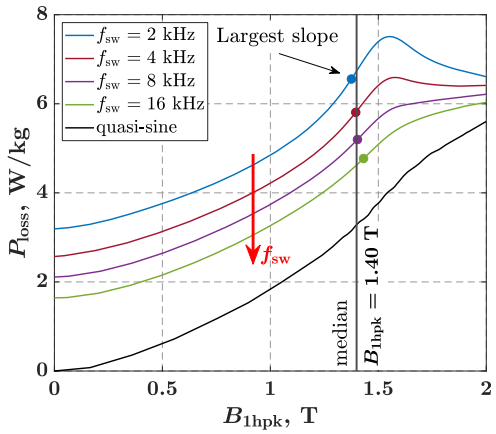

(B) Total AC loss curves

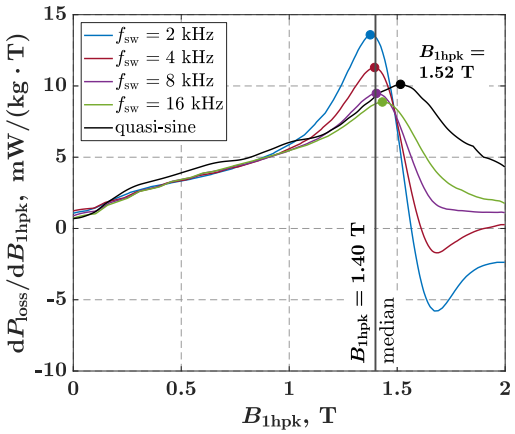

(C) Derivative of total AC loss curves

FIGURE 5.10: Surface plot, total AC loss curves and their derivative, showing the influence of B_{1hpk} and f_{sw} on the total iron losses in the **C3** core under PWM-generated and sinusoidal excitation at $f_{\text{1h}} = 50$ Hz. PWM-generated supply parameters: bipolar modulation, $U_{\text{DC}} = 85$ V, $m_{\text{a}} \in [0\ 1]$.

decreases significantly at saturation, which is also clearly reflected in the loss difference surface plot in subfigure5.11a. Further discussion of the PWM-induced losses and their contribution to the total losses will be presented later in this chapter in connection with the DC bias measurements (see section5.3).

Core C3 is designed as a non-uniform core with a uniformity ratio of 1.375. However, the width of the C3 core is the same as that of the C1a core, so the laser cutting effect in theory remains unchanged. Thus, comparing the losses between the two cores, the influence of the uniformity ratio on the losses can be seen. Subfigure5.11bshows the

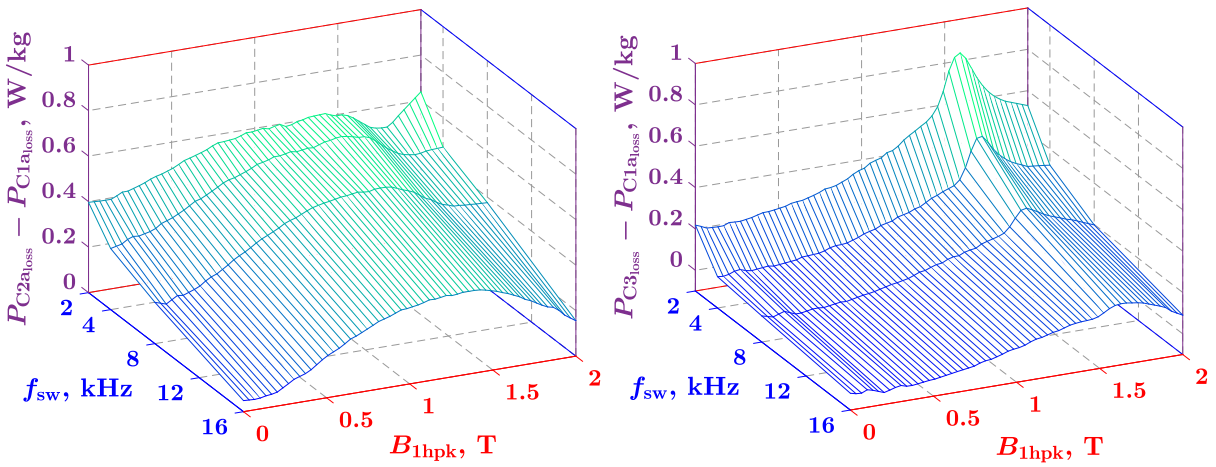

(A) C1a vs C2a

(B) C1a vs C3

FIGURE 5.11: The difference in total AC losses between cores at $f_{1h} = 50$ Hz.

difference in core losses between C1a and C3 cores. It can be seen that the losses of the C3 core are larger than those of the C1a core, up to about 0.8 W/kg, depending on the parameters B_{1hpk} and f_{sw}. Due to the nonuniform distribution of the field in the core, the region of the ring closer to the inner edge is more saturated than the region closer to the outer edge, as explained in chapter3, section3.4.2. Thus, as the degree of non-uniformity increases, the losses also increase, as if there were less core area available than for a core with a lower degree of non-uniformity. The effect of the uniformity ratio on the losses is nonlinear, much stronger than the effect of the laser cut, which is visible in the subfigure5.11b. Comparing the loss curves for each switching frequency between the C1a and C3 cores, it can be seen that the loss curve for the non-uniform core is slightly shifted toward the higher B_{1hpk} values. For this reason, the largest difference between the loss curves occurs slightly later than does the peak of PWM-induced losses, around $B_{1hpk} = 1.6$ T, regardless of the switching frequency. Nevertheless, the loss difference curves agree with the shapes of the PWM-induced loss curves.

5.2.3 Temperature effect on losses

The effect of core temperature on core losses was observed for a PWM-generated power supply, and the results are compared with the case in which a quasi-sinusoidal power supply was used. The experiment was performed at four different temperatures, namely 30°C, 50°C, 80°C, and 100°C. Figure5.12shows the comparison of experimental results for core C1a and a switching frequency of $f_{sw} = 4$ kHz. A single core and a single

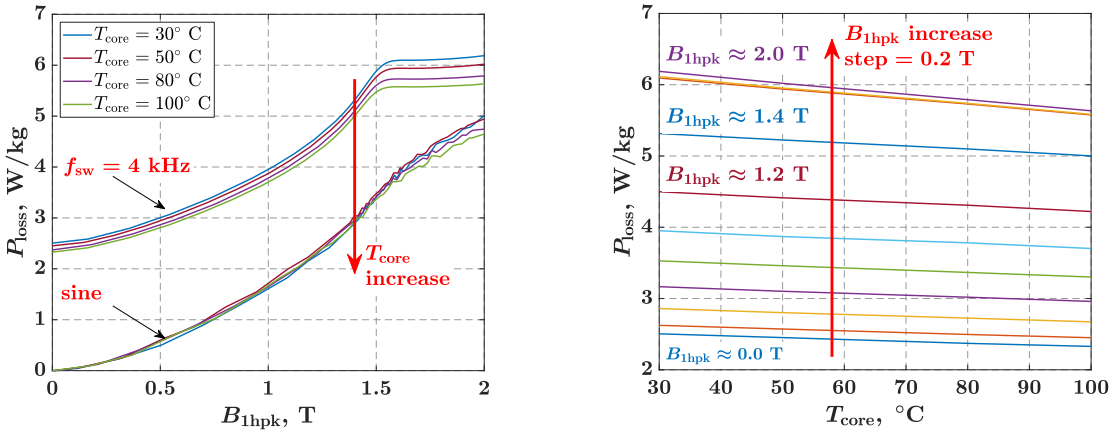

(A) Core temperature effect on total AC loss curves

(B) Core temperature effect on total AC core loss for a given value of B_{1hpk}

FIGURE 5.12: The effect of core temperature on core losses in C1a core under PWM-generated and sinusoidal excitation.

switching frequency were chosen for this analysis because there is no qualitative change from core to core and different values of f_{sw}. The subfigure5.12aclearly shows that core losses decrease with increasing temperature. This is true for both sinusoidal and PWM-generated power supply, but the difference between the loss curves at different temperatures is slightly larger when a PWM-generated power supply is used, which means that the temperature also affects the PWM-induced losses. The subfigure5.12b shows that for any given value of B_{1hpk}, the losses change linearly with temperature, and the slopes of the changes are almost identical except for the case where the core is highly saturated ($B_{1hpk} > 1.6$ T), when the slope increases slightly.

The electric machine is expected to operate in a hot state, i.e. the temperature of the machine is expected to be well above room temperature. The trend for losses to decrease with temperature therefore argues for measurements to be taken at or near the cold state, i.e. at room temperature, as this will result in the highest losses calculated for this particular material and operating point.

5.3 DC bias measurements

The DC bias measurement method was implemented and measurements were performed in order to obtain data of the PWM contribution to the total losses with respect to the parameters ΔB, $\frac{dB}{dt}$ and B_{bias} of the minor loops. Measurements were performed on the cores C1a, C2a, and C3 so that the impact of the core non-uniformity and laser cutting could be analyzed separately. Measured data is later gathered and formed in 3D loss maps which serve as a characterization of the magnetic material.

Table5.2shows the range of each of the parameters for which measurements were made for all three cores. The ΔB parameter range is chosen in the range of expected flux density ripples in electrical machines and f_{sw} as the expected typical values of inverter switching frequencies. The number in each cell of the table represents a value of the $\frac{dB}{dt}$ parameter for a given pair of ΔB and f_{sw}. Therefore, each cell with a value has a background color: same color indicates the same $\frac{dB}{dt}$ parameter. All measurements were performed in the B_{bias} range from $\approx$ 0.2 to 1.95 T.

The lower limit of B_{bias} is imposed by the geometrical and magnetic parameters of the core, excitation winding, inverter switching capacitance and DSP specifications. Take core C1a for example, where N_e =424 and ℓ_{eq} = 1.4822 m: B_{bias} of 0.2 T is achieved with an excitation current of $I_e \approx$ 170 mA. Excitation voltage is adjusted by duty cycle value so that a certain ΔB parameter is achieved, and this changes with the switching frequency f_{sw}. The minimum resolution at which the duty cycle can be changed is limited to 5×10^{-4}, and when the switching frequency is increased, such subtle changes in duty cycle do not produce any difference in the results due to the capacity of the switching circuit. All of this leads to the following: the smallest change

TABLE 5.2: Minor loops parameter for which DC bias measurements were made.

$\frac{dB}{dt}$ VALUES (T/ms)				
f_{sw} (kHz)	ΔB			
	20 mT	40 mT	80 mT	120 mT
2		0,16	0,32	0,48
4	0,16	0,32	0,64	
8	0,32	0,64		
16	0,64			

in duty cycle value that is applicable at the specific f_{sw} and U_{DC} value will define minimum obtainable B_{bias}. This value varies depending on the measurement and the core, but is somewhere between 150 mT at best and 350 mT at worst case scenario. Power loss curves shown in following figures are extrapolated to reach $B_{bias} = 0$ T. The upper limit was imposed mainly by successive core heating at higher B_{bias} values which made impossible to maintain a relatively stable core temperature throughout entire measurements cycle.

Figure5.13shows minor loops measured for several different combinations of the minor loop parameters. Subfigures5.13ato5.13cshow the dependence of the shape of the minor loops, the enclosed area, and the power loss on the change of B_{bias}, all for a constant ΔB value of 20 mT, while subfigures5.13dto5.13fshow the same but for $\Delta B = 40$ mT. The $\frac{dB}{dt}$ parameter varies in each subfigure according to the curve color ($\frac{dB}{dt} = 0.32$ T/ms, $\frac{dB}{dt} = 0.64$ T/ms). From the comparison of subfigures5.13ato5.13c

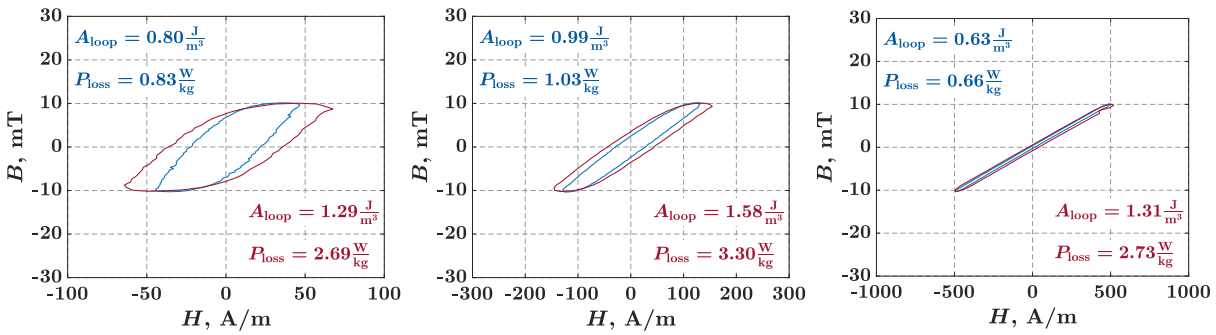

(A) $\Delta B = 20$ mT, $B_{bias} = 1$ T

(B) $\Delta B = 20$ mT, $B_{bias} = 1.45$ T

(C) $\Delta B = 20$ mT, $B_{bias} = 1.8$ T

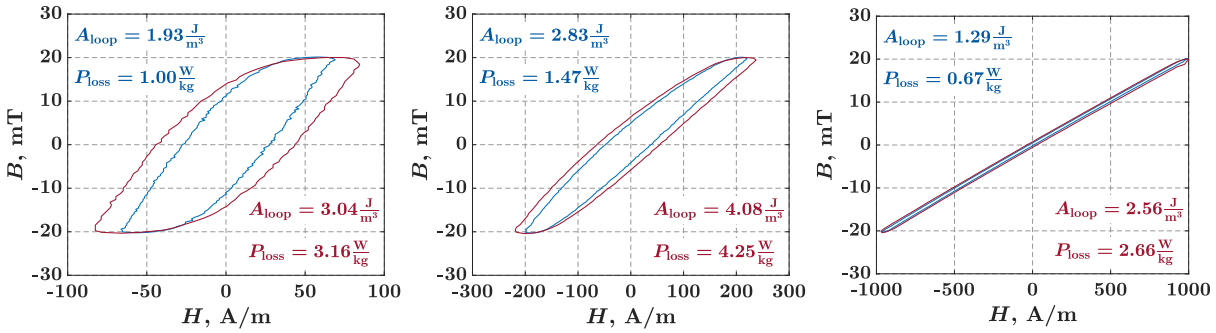

(D) $\Delta B = 40$ mT, $B_{bias} = 1$ T

(E) $\Delta B = 40$ mT, $B_{bias} = 1.45$ T

(F) $\Delta B = 40$ mT, $B_{bias} = 1.8$ T

FIGURE 5.13: Minor loops shape, area and loss comparison in dependency of ΔB, $\frac{dB}{dt}$ and B_{bias} parameters. Every plot contains two curves in regards to the $\frac{dB}{dt}$ T/ms parameter: blueforredfor.

and5.13dto5.13fin figure5.13, it can be seen that there is a relation between power losses and the value of B_{bias}.

Figure5.14shows the nature of this relation. The power losses increase with B_{bias} up to a certain point in the saturation region, after which the losses start to decrease and tend to a constant value, high in saturation even slightly lower than at $B_{\text{bias}} = 0$ T. The peak points of the PWM contribution to the total losses and their corresponding B_{bias} value are marked for each plotted curve. It can be seen that all these points fall within a relatively narrow range from $B_{\text{bias}} = 1.36$ T to $B_{\text{bias}} = 1.4$ T, which averages out at $B_{\text{bias}} \approx 1.38$ T for this particular magnetic material. Similar results are also reported in [10] where the peak point of the losses was reached at the same value of $B_{\text{bias}} \approx 1.38$ T.

Moreover, two curves on each subfigure, obtained with different $\frac{\mathrm{d}B}{\mathrm{d}t}$ show the influence of this parameter on the PWM contribution to the losses. The relation of the power loss to the $\frac{\mathrm{d}B}{\mathrm{d}t}$ has a parabolic character, which is shown in figure5.15. The ΔB parameter, on the other hand, is almost linearly co-dependent with the PWM contribution to the losses, so that for the same B_{bias}, as the parameter ΔB increases, the PWM contribution to the losses increases linearly (figure5.16). However, the slope of this linear co-dependence changes as a function of the B_{bias}. This effect can also be observed by comparing subfigures5.14ato5.14c, where a measurable influence of the ΔB parameter is visible at the points of maximum PWM contribution to the losses, in contrast to the points in saturation, where almost no influence is observable.

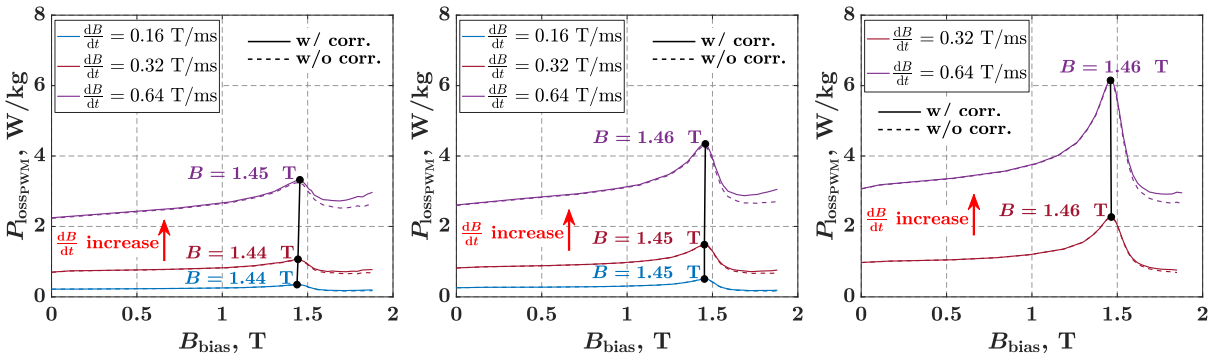

(A) $\Delta B = 20$ mT (B) $\Delta B = 40$ mT (C) $\Delta B = 80$ mT

FIGURE 5.14: PWM losses change in relation to ΔB, $\frac{\mathrm{d}B}{\mathrm{d}t}$ and B_{bias} parameters.Blue ($\frac{\mathrm{d}B}{\mathrm{d}t} = 0.32$ T/ms)andred ($\frac{\mathrm{d}B}{\mathrm{d}t} = 0.64$ T/ms)curves corresponds to the minor loops shown in figure5.13.

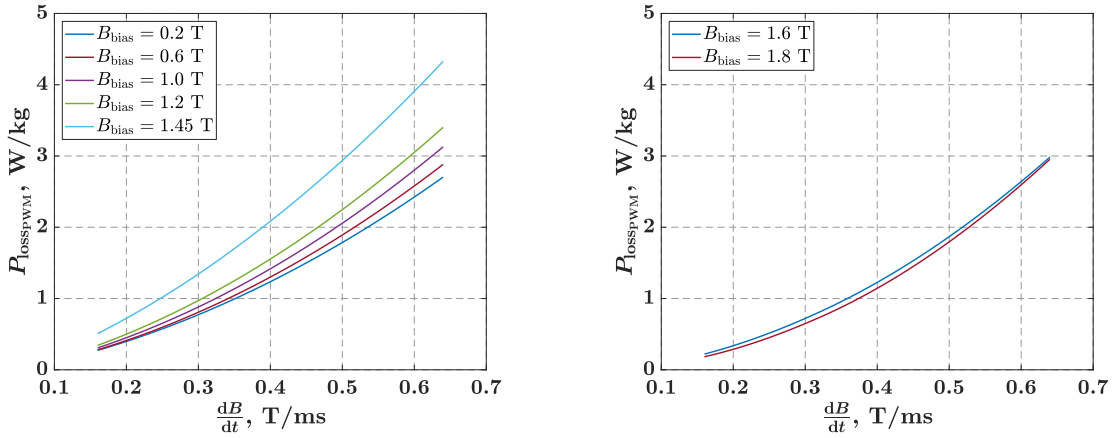

(A) $B_{\text{bias}} = 0.2 - 1.45$ T (B) $B_{\text{bias}} = 1.6 - 1.8$ T

FIGURE 5.15: The effect of $\frac{dB}{dt}$ change on power loss curve for different values of B_{bias}.

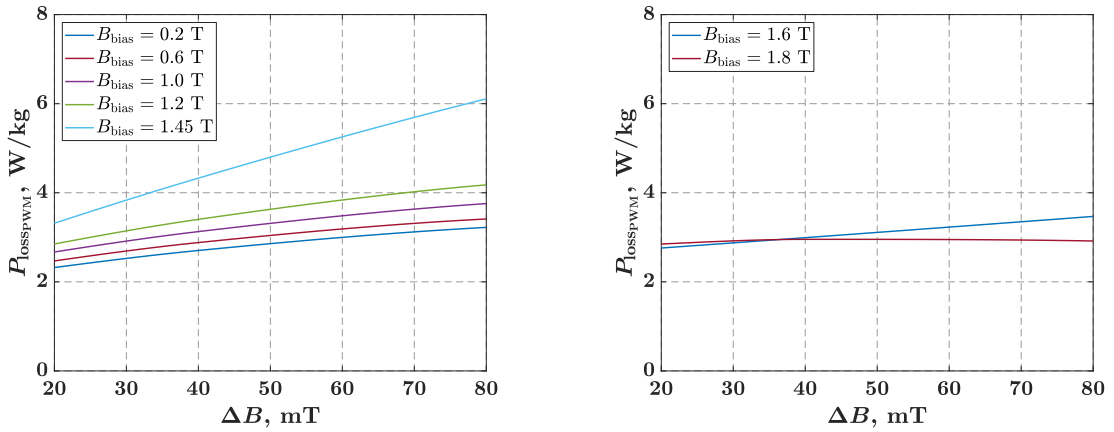

(A) $B_{\text{bias}} = 0.2 - 1.45$ T (B) $B_{\text{bias}} = 1.6 - 1.8$ T

FIGURE 5.16: The effect of ΔB change on power loss curve for different values of B_{bias}.

5.3.1 Temperature and DC bias direction effect on losses and measurement repeatability effect on final results

The effects of temperature and direction of magnetization on the variation of PWM-induced losses are also considered. Therefore, for some combinations of the parameters ΔB, $\frac{dB}{dt}$, and B_{bias}, DC bias measurements were also performed for other direction of the DC bias field and different temperatures. Table5.3gives an overview of the DC bias direction and temperatures at which DC bias measurements were made for each

combination of the minor loop parameters.

To minimize the possibility of measurement error, the repeatability of measurements for each set of minor loop parameters was tested. The test was performed by repeating each measurement cycle three times, and then the differences were analyzed. In case of a larger deviation of the results, the measurement cycle is repeated again. Otherwise, the results are averaged and considered as the final result for a given measurement cycle. An example of power curves obtained with three different measurement cycles and their mutual differences are shown in Figure5.17.

Figure5.18shows comparisons of the averaged power loss curves and their difference for the case when a different direction of the DC bias field was applied during the measurements. It can be seen that the direction of the DC bias has an influence on the iron losses and this should be taken into the account when performing measurements. However, when looking at the difference between the loss curves, it should be noted that apart from the direction of magnetisation, the difference between the two curves is also influenced by errors due to the repeatability of the measurement. Therefore, the difference shown in the subfigure5.18bshould be smaller if only the DC bias magnetisation would influence it. For the cases for which DC bias measurements were made for both directions of DC bias, the final power loss curve was obtained by averaging power loss curves obtained for both directions.

As it was assumed in connection with the temperature effect on AC power loss curves (subsection5.2.3), PWM-induced losses are affected as well by the change of the core temperature: power losses are reduced with an increase of core temperature. Figure5.19shows the power loss curve dependence of the core temperature for the

TABLE 5.3: DC bias direction and temperatures for which DC bias measurements were made.

MEASUREMENTS DIRECTION AND CORE TEMPERATURES										
f_{sw} (kHz)	ΔB									
	20 mT				40 mT	80 mT				120 mT
	30° C	50° C	80° C	100° C	30° C	30° C	50° C	80° C	100° C	30° C
2					D1	D1				D1
4	D1	D1	D1	D1	D1	D1, D2	D1, D2	D1, D2	D1, D2	
8	D1				D1					
16	D1									

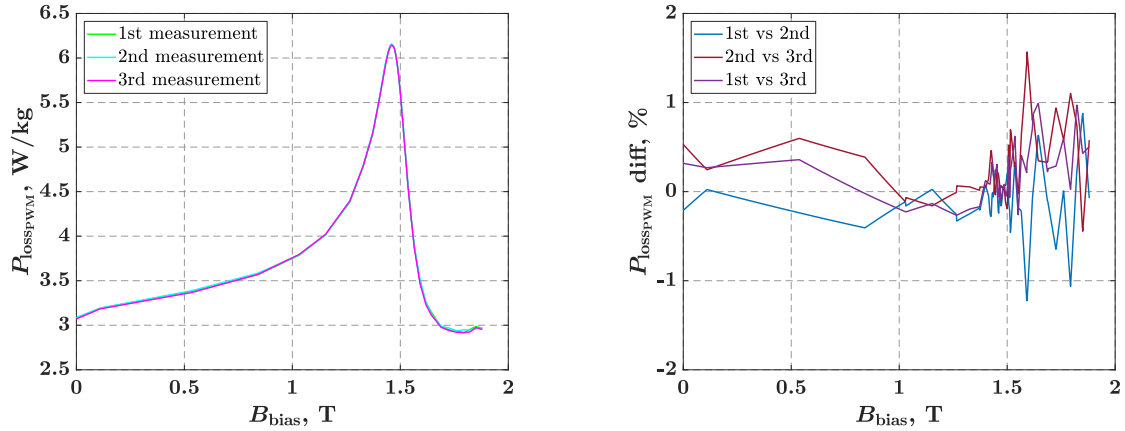

(A) Power loss curves

(B) Power loss curves - mutual difference

FIGURE 5.17: The effect of the measurement repeatability on the final results of the DC bias measurements. Curves are shown for a specific DC bias measurement with the following parameters: $\Delta B = 80$ mT and $\frac{\mathrm{d}B}{\mathrm{d}t}$=0.64 mT/s i.e. $f_{\text{sw}} = 4$ kHz.

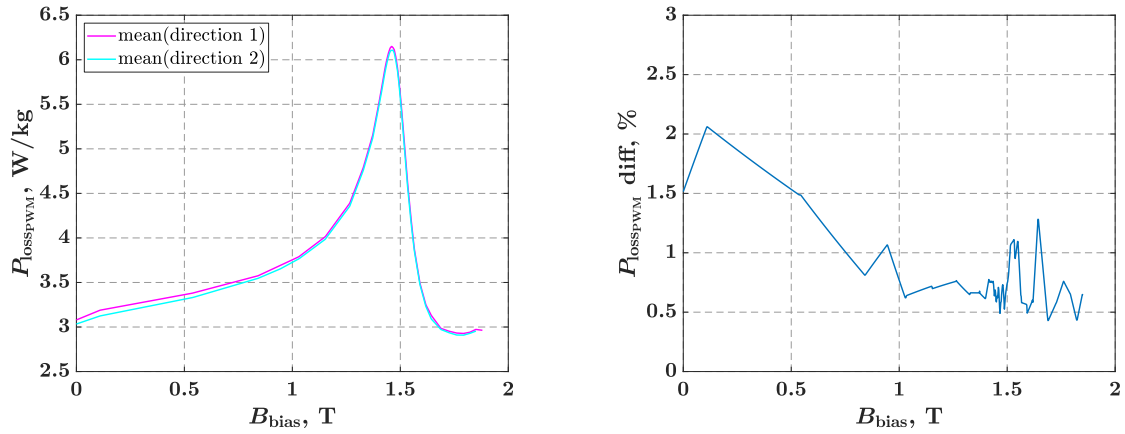

(A) Power loss curves

(B) Power loss curves - difference

FIGURE 5.18: The effect of DC bias direction on the final results of the DC bias measurements. Curves are shown for a specific DC bias measurement with the following parameters: $\Delta B = 80$ mT and $\frac{\mathrm{d}B}{\mathrm{d}t}$=0.64 mT/s i.e. $f_{\text{sw}} = 4$ kHz.

cores C1a and C2a. The most significant difference can be observed at the range where PWM losses are the highest in the relation to the B_{bias} parameter. The difference is more pronounced for the core C1a where the area of maximum PWM contribution to losses is more narrow.

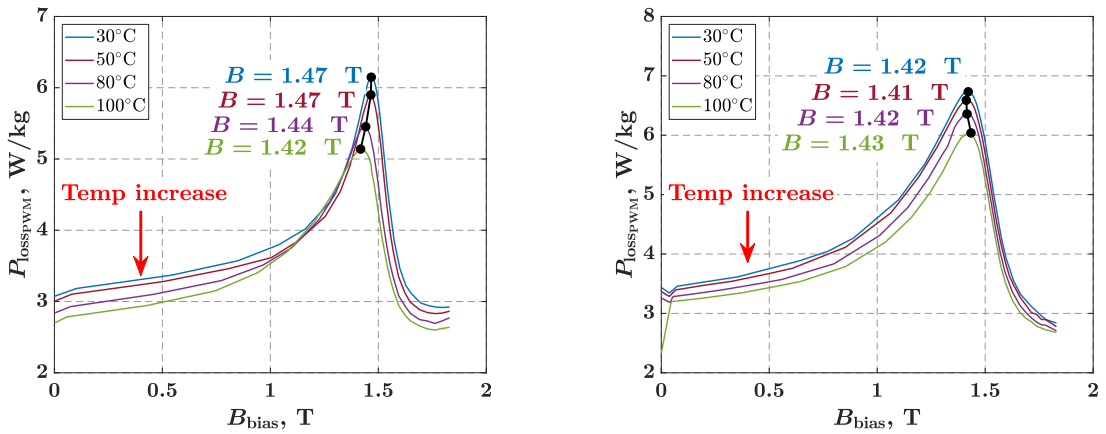

(A) Core C1a

(B) Core C2a

FIGURE 5.19: The effect of core temperature on PWM-induced losses. Curves are shown for a specific DC bias measurement with the following parameters: $\Delta B = 80$ mT and $\frac{dB}{dt}$=0.64 mT/s i.e. $f_{sw} = 4$ kHz.

5.3.2 Comparison between cores C1a, C2a and C3

DC bias measurements were performed on three cores with different geometrical parameters. Core C1a was built as a uniform core and as large as possible to minimize the effect of laser cutting on losses. Thus, core C1a is used as a reference core. Core C2a was also built as uniform but with width of the ring 2.25 time smaller than width of the C1a core. Thus, comparison of two points out the effect of the laser cut on losses. Core C3 was built with the same width of the ring as is C1a core, but much smaller in diameter which made that core non-uniform. So by comparing core C3 to C1a, sample non-uniformity effect on the losses is pointed out.

Figure5.20and5.21shows comparison of obtained power loss curves between the cores C1a and C2a, and C1a and C3 respectively, for different ΔB and $\frac{dB}{dt}$ parameter combinations. Increase in power loss can be observed for all of the comparisons.

Due to the apparent non-linear influence of laser cut on losses, the range of the B_{bias} value with higher loss values is wider than it is for core C1a. The maximum value is also higher. Same non-linear dependence can be observed when comparing C3 to C1a as well. Although, the range of B_{bias} value with higher loss values is not as wide, the maximum value of losses is the greatest between all three cores.

The effects of laser cutting and core non-uniformity are definitely measurable and can make a significant difference in determining power losses. However, quantification

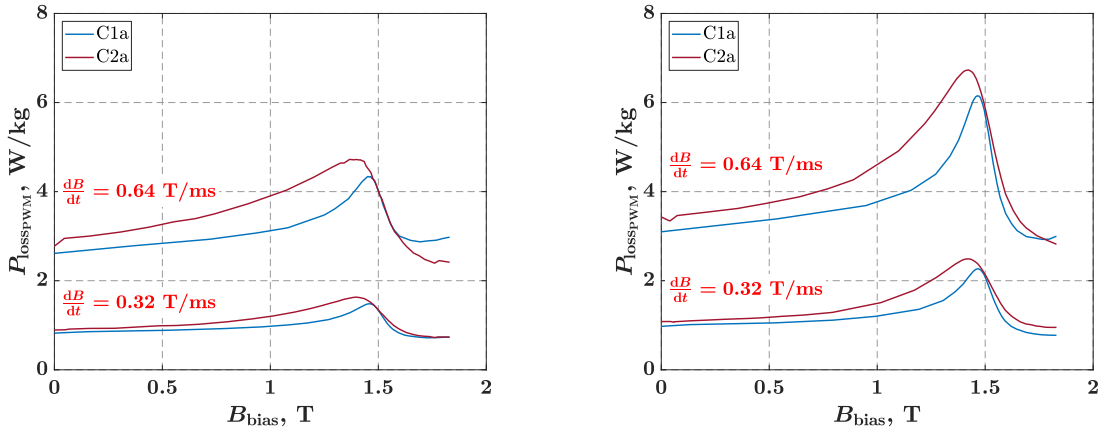

(A) $\Delta B = 40$ mT (B) $\Delta B = 80$ mT

FIGURE 5.20: Comparison between power loss curves obtained for cores C1a and C2a for two different values of ΔB and $\frac{dB}{dt}$ parameter.

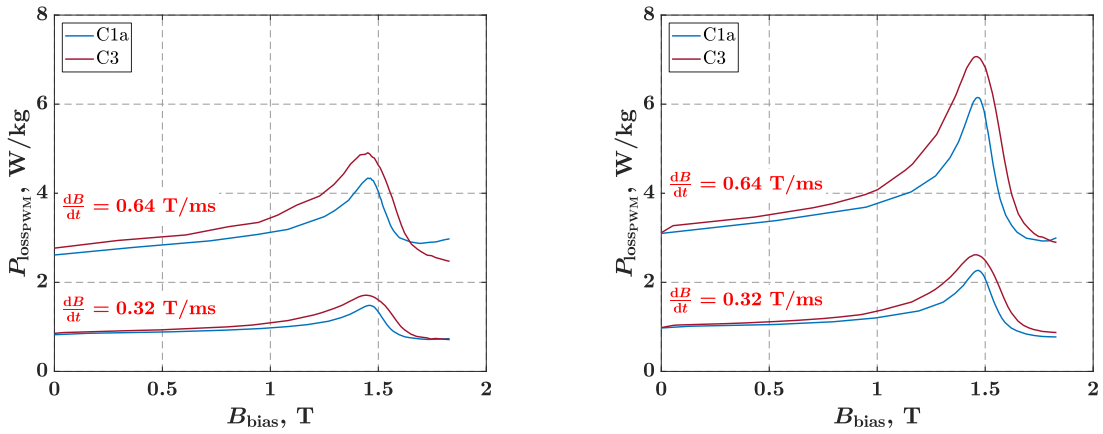

(A) $\Delta B = 40$ mT (B) $\Delta B = 80$ mT

FIGURE 5.21: Comparison between power loss curves obtained for cores C1a and C3 for two different values of ΔB and $\frac{dB}{dt}$ parameter.

of this influence is not possible on the basis of only two samples, and further tests are needed to check the possible physical background of the relationships that could be applied to compensate for such effects.

Chapter 6

Method for calculation of PWM-induced iron losses

The DC bias measurements provided magnetic material data in the form of the parameters ΔB, $\frac{\mathrm{d}B}{\mathrm{d}t}$, and B_{bias}. Combining the results collected with different combinations of these parameters allows the creation of a 3D loss map showing the contribution of the PWM-formed minor loops to the iron losses. By analyzing minor loops formed under AC excitation and classifying each of them with respect to the parameters ΔB, $\frac{\mathrm{d}B}{\mathrm{d}t}$, and B_{bias}, the 3D loss map can be used to retrieve the loss data for each loop separately, and then the contribution of PWM-induced losses can be calculated.

In this chapter, a method for calculating the contribution of PWM-related effects to total AC losses is proposed, and different approaches, problems and limitations of this method are discussed. To make it easier to refer to this method later in the text, an acronym for the method is defined as *3DLMB* (**3D L**oss **M**ap based on the minor loop parameters in relation to the $\boldsymbol{B}$). This method is based on the idea that the minor loops formed under AC excitation are obtained as a result of a simulation on a model of an electrical machine and that this minor loop data can be used in combination with the 3D loss map of the material to calculate the contribution of PWM-induced losses to the total AC losses. In order to classify the minor loop data based on the parameters $\boldsymbol{\Delta B}$, $\boldsymbol{\frac{\mathrm{d}B}{\mathrm{d}t}}$ and $\boldsymbol{B_{\mathrm{bias}}}$, the flux density waveform for each finitely small point or specific region of the electrical machine is needed. At this stage of the thesis, it is assumed that such data can be obtained using simulation platforms commonly used in the design of electrical machines, and the evaluation of this assumption will be assessed later in the section8.4. In this chapter, the results of the AC measurements have been used both as reference and as input data for the proposed method. In this way, the theory of the method and the proposed algorithm alone are put to the test.

All diagrams, curves, and hysteresis loops presented in this chapter are the result of measurements made on core C1a, and therefore this is not indicated separately with each figure, but is mentioned here. All other parameters of interest for a particular figure are listed in the caption.

6.1 3D loss map creation

PWM-generated power supply can cause any number of minor loops having different shapes and sizes depending on the supply parameters themselves, the windings, the sample geometry, etc. Thus, to create a 3D loss map that is generally useful for a given material, one must perform DC bias measurements in a wide range of parameters $\boldsymbol{\Delta B}$, $\frac{\mathbf{d}\boldsymbol{B}}{\mathbf{d}t}$, and $\boldsymbol{B}_{\mathbf{bias}}$ that one would expect to occur in an actual machine fed by an inverter supply. Since the number of possible combinations is quite large, it is not possible to create a loss map that contains the measured loop data for each combination of the minor loop parameters. However, using the mathematical interpolation tool, a mesh with the desired resolution can be created between the loss data points in 3D space determined by measurements. The accuracy of the interpolated loss data naturally increases with the number of measurements made and the uniformity of the distribution of the measured data points in the 3D space of the loss data. Knowing how the minor loop loss changes as a function of each parameter independently, extrapolation can be used to further extend the space of 3D loss data beyond the values of the measured loss data. However, since the change in loss as a function of each of the parameters does not exactly follow a certain function and, in the case of $\boldsymbol{B}_{\mathbf{bias}}$, even changes depending on the range of this parameter, extrapolation can be used only for smaller expansions of the loss data. Otherwise, the accuracy of the extrapolated values deviates significantly from the actual values.

Figure6.1represents an overview of all of the loss data points in 3D space that have been obtained for core C1a in DC bias measurements. At the time when DC bias measurements were performed in this research, the focus was on the evaluation of the effect of a specific parameter on the PWM contribution to the losses. Thus, for each of the DC bias measurements made, the ratio of the parameters $\boldsymbol{\Delta B}$ and $\frac{\mathbf{d}\boldsymbol{B}}{\mathbf{d}t}$ was first defined and kept constant, while the parameter $\boldsymbol{B}_{\mathbf{bias}}$ changed, and for each value of $\boldsymbol{B}_{\mathbf{bias}}$, the power loss was determined. By repeating the measurements for different ratios of the parameters $\boldsymbol{\Delta B}$ and $\frac{\mathbf{d}\boldsymbol{B}}{\mathbf{d}t}$, data were collected that allowed the effect of changing individual parameters on losses to be analyzed separately. This is why loss

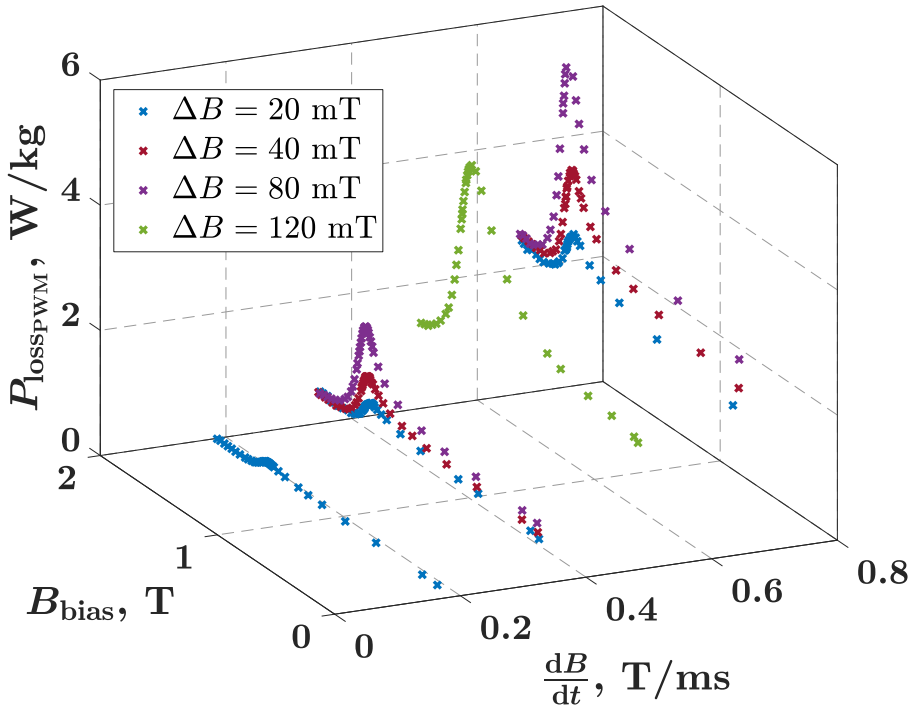

FIGURE 6.1: Overview of all ΔB, $\frac{dB}{dt}$ and B_{bias}points for which DC bias measurements were performed (Table5.2), shown for core C1a and with associated loss values.

data points are so concentrated and can be found lying on one of the four surfaces in the 3D space of loss data (Figure6.1). For the purpose of creation of the 3D loss map, it is not important to keep ΔB and $\frac{dB}{dt}$ in a certain ratio while changing B_{bias}, it is only important to fill the 3D loss space with relatively evenly distributed loss data at the desired resolution.

The most non-linear behaviour of the loss change is the one depending on the B_{bias} parameter and each of the measurements made in this research obtained enough of the loss data points to define those curves correctly. However, due to the relatively large spaces in between loss data points with different values of ΔB and $\frac{dB}{dt}$ parameters, accuracy of the interpolated results are certainly reduced. Performing more measurements with additional values of ΔB and $\frac{dB}{dt}$ would improve the results.

Since the measured loss data are unevenly distributed in space and change in losses follow different functions depending on the minor loop parameters, tools such as 4D or scattered interpolation are not suitable to obtain good results. To overcome this problem, a 3D loss map is created according to the following steps:

- The loss data are organized into 2D arrays, one for each different value of the parameter ΔB for which the DC bias measurement was made (Figure6.2). In this

way, each 2D array contains loss data in relation to the parameters $\frac{dB}{dt}$ and B_{bias}, whose change has a nonlinear effect on the loss change, and what distinguishes two different 2D arrays from each other is the parameter ΔB, whose change has a more linear correlation with the change in losses.

- Each 2D array is then interpolated separately using the gridded data interpolation function and the cubic spline interpolation method, which was found to be most suited for the nonlinear dependence of the $\frac{dB}{dt}$ and B_{bias} parameters on losses.
- These interpolated 2D arrays, representing loss data surfaces in the 3D space of the loss data, were then used to fill in the loss data in the third dimension as a function of the ΔB parameter. Interpolation was performed separately for each cell of the 2D arrays using a 1D interpolation function and a linear interpolation method, which was found to be best suited for the mostly linear dependence of the ΔB parameter on the losses.

The basic layout of the 3D loss map created for the purposes of this research is shown in Figure6.2. The DC bias measurement results obtained for the parameter combinations listed in table4.1were used as the structure for creating the loss map. The final range of parameters ΔB, $\frac{dB}{dt}$, and B_{bias} obtained with extrapolation and uniform step resolution with interpolation is given in table6.1for each of the parameters.

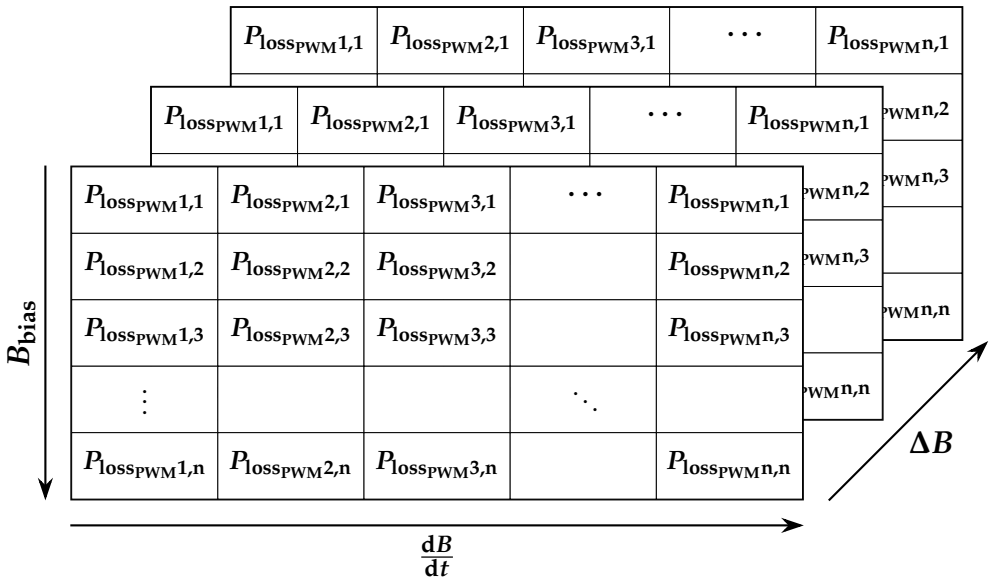

FIGURE 6.2: Overview of the 3D loss map layout

TABLE 6.1: Minor loops parameters range and step resolution used for the creation of the 3D loss map

PARAMETER	START VALUE	END VALUE	STEP
ΔB (mT)	0	120	0.12
$\frac{dB}{dt}$ (T/ms)	0	0.8	0.8e-3
B_{bias} (T)	0	2	2.0e-3

Figure6.3illustrates the created 3D loss map for the core C1a in the form of several slices through the 3D space of the loss data. The color represents the value of the loss data at that specific point in space defined with all three parameters of the minor loops. For better illustration, the slices are shown transparently, so the colors appear slightly different from the colors of the color bar.

The same method for creating a 3D loss map can be used to create a 3D map of any other parameter of interest as a function of the parameters ΔB, $\frac{dB}{dt}$, and B_{bias} that have been measured during the experiments and is related to the above parameters. For example, the same method was later used to create a 3D map of the ΔH parameter to relate the ΔB-ΔH values of the minor loops.

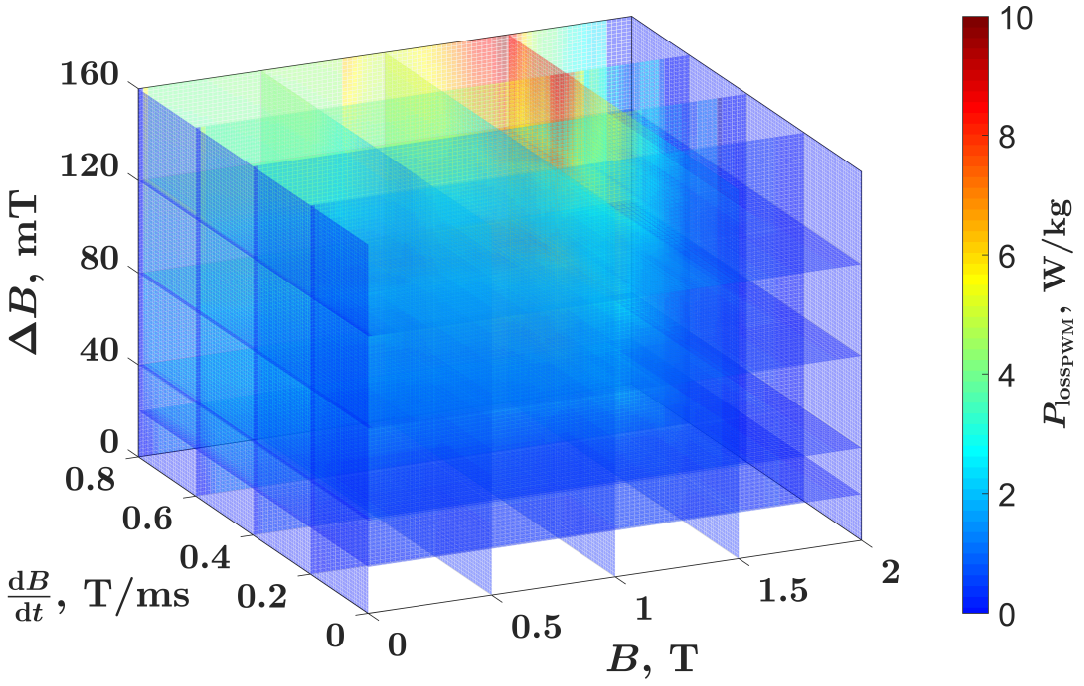

FIGURE 6.3: Visualization of the created 3D loss map

6.2 PWM effects on hysteresis loop in relation with the proposed method

The area of the hysteresis loop is proportional to the iron losses, so observing the change in the shape and size of the hysteresis loop can provide information about the effects of different power supply parameters on iron losses. This is, of course, assuming that the sample under test remains unchanged.

Looking at the effects of the PWM power supply on iron losses based on the appearance of the hysteresis loop, several separate effects can be identified. First, small remagnetization cycles are observed along the main cycle loop, and when the PWM is generated with bipolar modulation, minor loops also occur (Figure6.4). The number of small remagnetization cycles is proportional to the switching frequency of the PWM power supply, and the area they enclose adds to the area of the main cycle loop and thus the iron losses increase.

The second effect that can be observed is the deformation of the main loop of the cycle. After the completion of the minor loop, i.e. when the value of the flux density is equal to the flux density at the time of the voltage switching that triggered this minor loop, the magnetic field strength does not have the same value as it had at the beginning of the remagnetization cycle (Figure6.4). For this reason, it looks like some parts of the

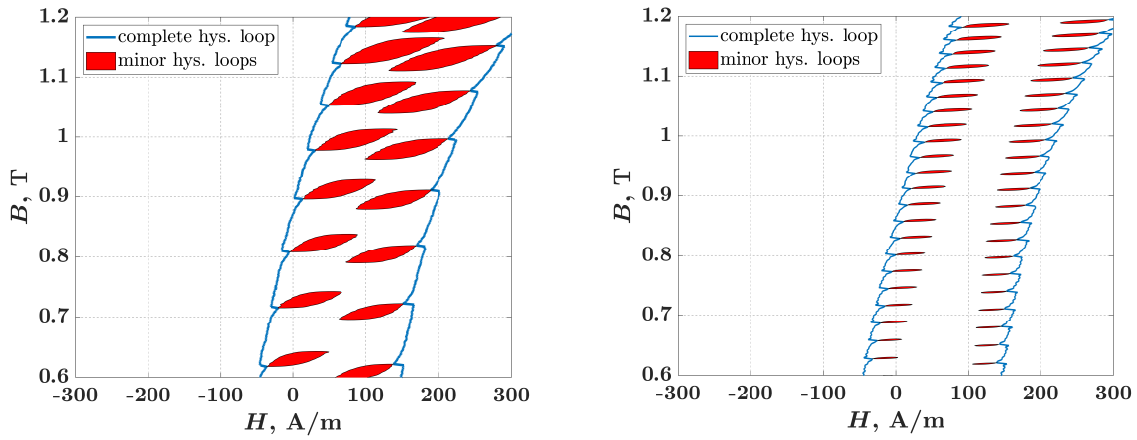

(A) $f_{sw} = 4$ kHz (B) $f_{sw} = 16$ kHz

FIGURE 6.4: Occurrence of the minor hysteresis loops along the main cycle hysteresis loop due to the PWM generated power supply shown for two different inverter switching frequencies and equal B_{1hpk} value of 1.6 T.

main cycle loop have been cut out and regions have been subtracted from the apparent hysteresis loop that would envelope the measured hysteresis loop (Figure6.5a).

The third effect cannot be observed without comparing the hysteresis loop obtained with a PWM power supply with that obtained with a sinusoidal supply. The comparison in figure6.5bshows that the main cycle loop widens with PWM excitation and additional area is added to the area of the main cycle loop produced with quasi-sinusoidal power supply. This widening effect is the reason and explanation why iron losses increase even when a unipolar switching PWM supply is used as excitation (Figure2.8). In this case, since no minor loops are induced and parts of the main cycle loop are cut out, it seems as if the losses should be lower. However, the additional area created by widening the main loop outweighs the areas apparently subtracted from the main loop (Figure6.5b).

The PWM-induced losses can be divided into the minor loops losses and the additional losses, which include all other effects of the PWM-generated supply on iron loss. Figure6.6shows how the contribution of each PWM loss component varies as a function of the peak value of the fundamental $\boldsymbol{B_{1hpk}}$. Adding the quasi-sinusoidal loss component to the additional loss component of the PWM-induced losses gives

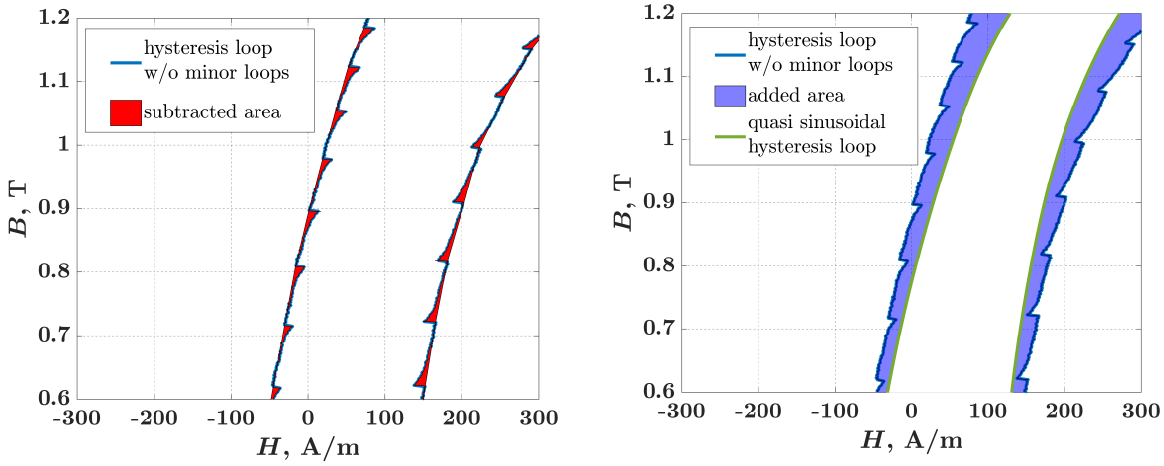

(A) Apparent subtracted area

(B) Added area

FIGURE 6.5: The PWM-generated hysteresis loops with minor loops removed. Subfigure (A) highlights what seems to be the area subtracted from the hysteresis loop that would envelop the measured loop, and subfigure (B) shows how the main hysteresis loop increases in size as the power supply changes from quasi-sinusoidal to PWM-generated. Both subfigures are shown for the $f_{sw} = 4$ kHz and $B_{1hpk} \approx 1.6$ T.

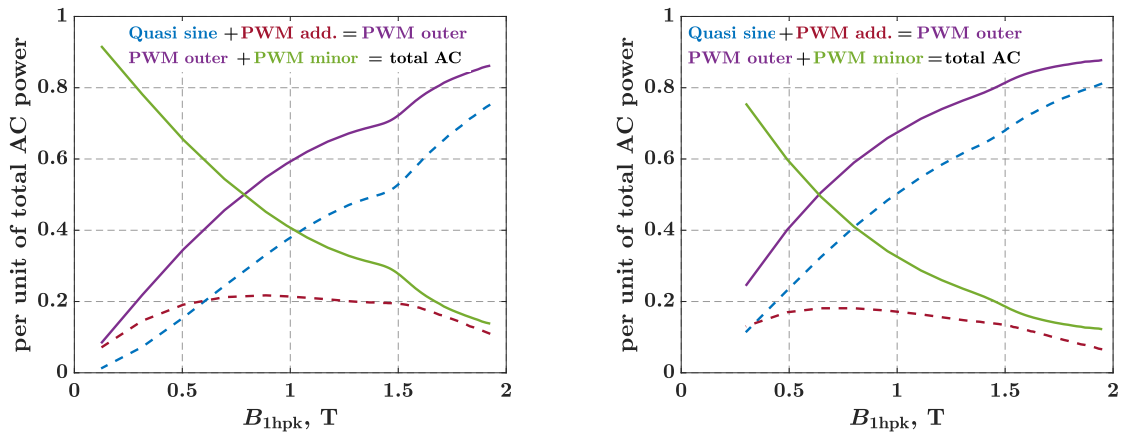

(A) $f_{sw} = 4$ kHz (B) $f_{sw} = 16$ kHz

FIGURE 6.6: Total AC losses distribution in relation to the B_{1hpk} value of the fundamental.

the losses that would have been induced in the material if the minor loops had not been considered. The $B - H$ loop that would correspond to this case is the hysteresis loop without minor loops shown in subfigure6.5aand is referred to here as the outer hysteresis loop. If the losses of the minor loops are added to the losses of the outer hysteresis loop, the total losses AC are obtained. The percentages and curve shapes differ slightly between $f_{sw} = 4$ kHz and $f_{sw} = 16$ kHz, but it can be seen that the same laws of physics apply in both cases.

The additional PWM losses contribute to the total AC losses up to about **20 %** and do not change significantly over the entire measured range of B_{1hpk}. A slightly larger variation is observed at the relatively low and relatively high flux density values where the additional losses contribute up to about **10 %**. This is due to the fact that the additional losses are associated with the losses of the main cycle loop. When the flux density is reduced, the contribution of the main cycle losses to the total losses tends to zero, and so do the additional losses. Further on, the widening of the main cycle loop contributes to the total AC losses, mainly in the region up to or slightly above the knee point of the magnetization curve. Further increasing B_{1hpk} leads to more total AC losses, but almost no more PWM additional losses. Thus, one can also observe some reduction in the contribution of the additional losses above $B_{1hpk} \approx 1.5$ T.

The losses of the minor loops dominate in the range of low flux density values, because the size of the minor loops is then comparable to that of the main cycle loop and there are many minor loops and only one main cycle loop. As B_{1hpk} increases, the main

cycle loop increases in area and begins to contribute more to the total AC losses, so the relative contribution of the minor loops to the total losses reduces. Also, the modulation depth changes for each different $\boldsymbol{B_{1hpk}}$, causing most of the minor loops to become smaller as $\boldsymbol{B_{1hpk}}$ increases. This effect goes to the extent that, as the $\boldsymbol{B_{1hpk}}$ increases far in saturation region (above 1.65 T for core C1a), some of the minor loops are lost, and remagnetization cycle leaves only deformation of the main cycle loop (Subigure6.7a). Subfigure6.7bshows duty cycle values of the inverter switches that correspond to the hysteresis loop shown in subfigure6.7a. The number of data points of the constructed waveform depends on the number of the minor loops formed along a single main cycle. For this reason, the index of the minor loop is shown in the x-axis of the6.7bsubfigure, where the index represents the ordinal number of the minor loop within a single main cycle. Finally, the number of small remagnetization cycles over a cycle of the main loop remains the same regardless of $\boldsymbol{B_{1hpk}}$, so that as $\boldsymbol{B_{1hpk}}$ increases more and more above saturation, more of the minor loops appear above the saturation region. There, the contribution of the minor loops to the losses is smaller because a large ripple in the magnetic field strength value is required to enclose any significant area.

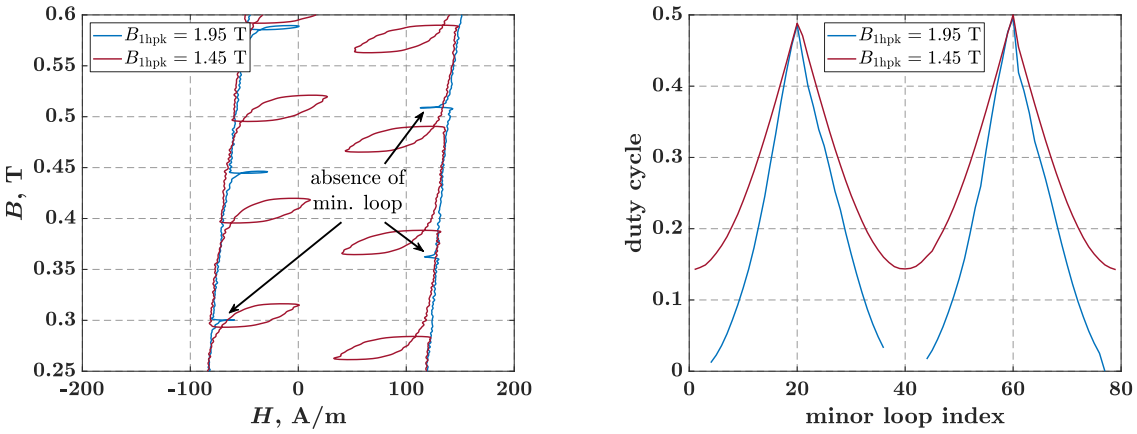

(A) Size and occurrence

(B) Duty cycle of inverter switches

FIGURE 6.7: Comparison of minor loops size and occurrence and corresponding duty cycle values shown for core C1a for two different values of $\boldsymbol{B_{1hpk}}$ and $\boldsymbol{f_{sw}} = \mathbf{4}$ kHz.

6.3 Comparison between minor loops obtained with AC and DC bias measurements

During the DC bias measurements, the flux density of the core is biased to a specific point and due to the switching nature of the PWM supply, only a minor hysteresis loop forms around this DC bias point. The same DC bias value can be achieved with different values of the PWM supply parameters, which will affect the shape and size of the hysteresis loop that forms. Thus, by changing the DC bias of the core and the parameters of the PWM supply, hysteresis loops with different parameters will form at different points of the DC bias value. By calculating the power dissipation for each of these cases, a loss map can be created in terms of the parameters of the hysteresis loops. For this purpose, $\boldsymbol{\Delta B}$, $\frac{\mathbf{d}B}{\mathbf{d}t}$, and $\boldsymbol{B}_{\mathbf{bias}}$ are used to define each of the loops formed.

Thus, if the magnetic field strength and flux density signals are known, either from the AC measurements performed or as a result of simulating the FEA model, $\boldsymbol{\Delta B}$, $\frac{\mathbf{d}B}{\mathbf{d}t}$, and $\boldsymbol{B}_{\mathbf{bias}}$ can be determined for each of the formed minor loop. By finding the most similar loop parameters in the loss map, a power loss value can be retrieved that specifies how much the power loss is increased by that single PWM-induced minor loop. Adding the power loss data of each loop formed along the main cycle gives the total power dissipation increased by the formation of the minor loops. However, there is an issue with connecting the parameters determining the minor loops formed during AC power supply to the parameters determining the minor loops formed during the procedure of the DC bias measurements.

For every combination of the DC bias value and PWM supply parameters, only a single hysteresis loop is formed per cycle when DC bias measurements are performed. This loop oscillates around the DC bias point at a frequency equal to the inverter switching frequency. Therefore, this loop can be considered as the main cycle loop with the fundamental frequency equal to the switching frequency of the inverter. In contrast, the conditions under which loops form when the PWM-generated AC voltage is applied to the core are not so ideal. Here, minor loops can be observed in two different ways: First, they can be considered as part of the main cycle loop, and second, they can be considered as separate minor loops that occur independently of the main cycle. The acronyms for the two specified approaches are defined as *MLL* (**M**inor **L**oop **L**osses) and *TACL* (**T**otal **AC** **L**osses) respectively. Depending on the approach, a different part of the PWM loss contribution to losses is analyzed: only the loss contribution of the PWM minor loops or the total PWM contribution to the AC losses. Regardless of the

approach, however, the minor loops form under conditions of a varying DC magnetic field which affects the ability to match the loop shape, size and parameters between AC and DC measurements.

As will become clear in the following subsection, the complete $\boldsymbol{B} - \boldsymbol{H}$ loop, including the main cycle loop and the minor loops, must be known for each operating point in order to apply the method according to the *MLL* approach. This means that the complete waveform of $\boldsymbol{B}$ including main cycle and superimposed ripple must be known in exact correspondence with the waveform of $\boldsymbol{H}$. As mentioned at the beginning of this chapter, this is not yet known to be possible for complex excitation signals. If this were the case, the losses could simply be calculated by integrating the product of $\boldsymbol{H}$ and $\boldsymbol{B}$. Nevertheless, this approach was initially followed to validate the basis of the method and the possibility of obtaining loss data from the created 3D loss map based on the minor loop parameters.

Each approach brings its own challenges when comparing minor loops. The main difference between the approaches that affects the comparison is the influence of the fundamental on the minor loops. When the minor loops are considered as part of the main cycle loop, the fundamental wave of the magnetic field strength and the flux density play a role in the shape and size of the minor loops. However, when the minor loops are considered separately, the change in the fundamental wave only determines the DC bias at which the minor loop forms. Furthermore, if the fundamental is eliminated from the waveform, only the ripple remains, which causes additional problems when comparing loops.

In order to discuss the matter further, it is first necessary to establish some basic definitions concerning minor loops, which will be presented in the following subsection.

6.3.1 Defining the parameters of the minor loops

Figure6.8shows part of the flux density waveform and the corresponding minor loop from the results of AC measurements performed on core C1a at $\boldsymbol{f_{sw}} = \mathbf{4}$ kHz. The small remagnetization cycle shown occurred at a $\boldsymbol{B_{bias}}$ value of 0.69 T, but represents a typical small remagnetization cycle that occurs due to the PWM-generated voltage supply. This particular switching frequency and bias value were chosen only because they are in a range where it is easier to distinguish the representation of all characteristic points of a small remagnetization cycle. The following characteristic points are indicated:

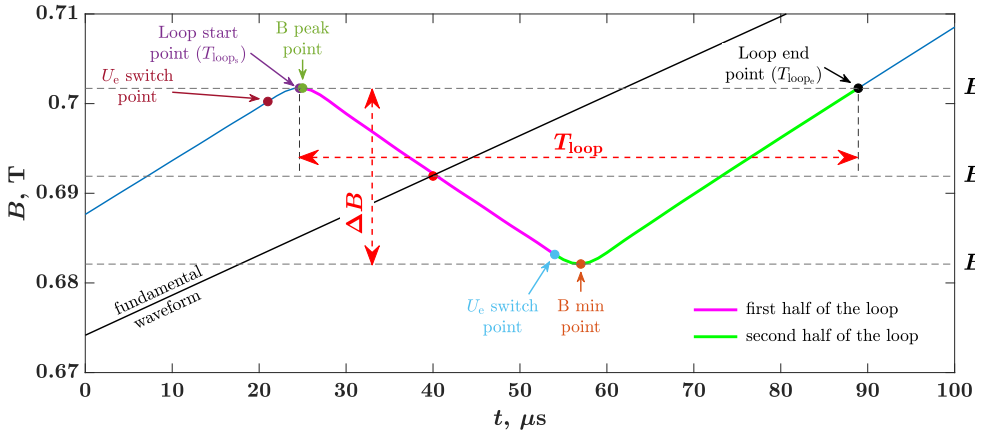

(A) Flux density waveform

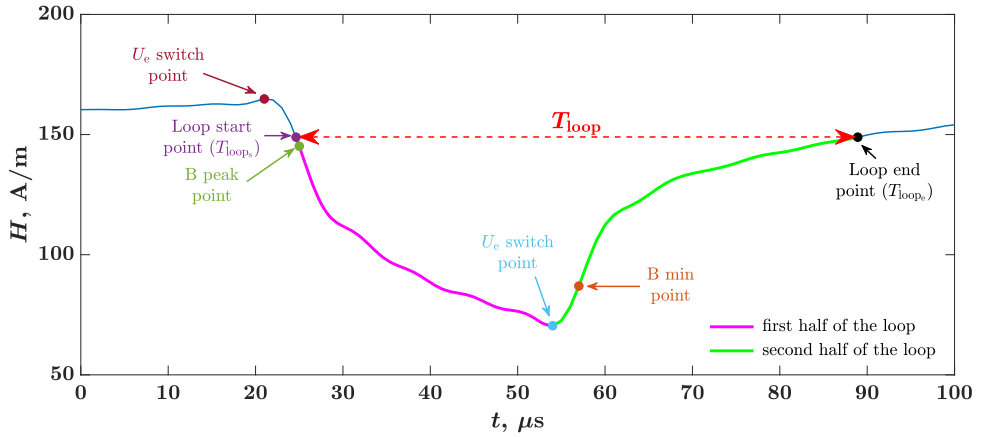

(B) Magnetic field strength waveform

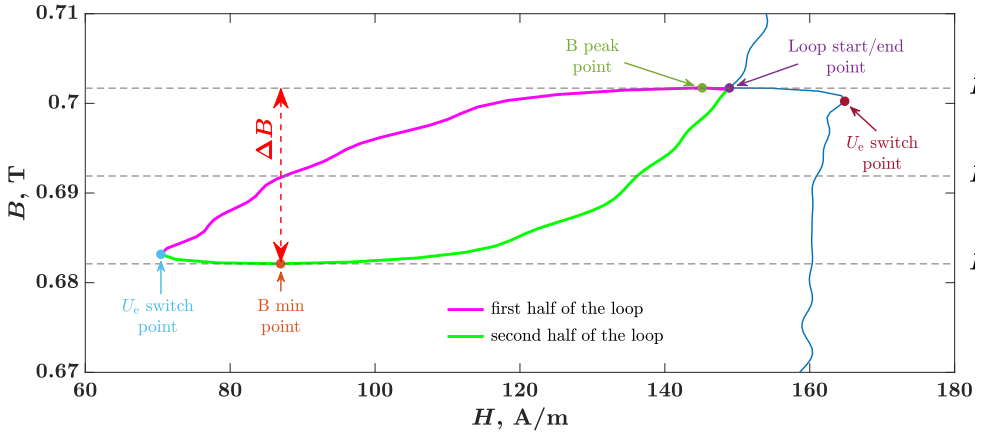

(C) Minor hysteresis loop

FIGURE 6.8: Characteristic points of the small remagnetization cycle on the flux density and magnetic field strength waveform and corresponding minor hysteresis loop shown for core C1a, $f_{sw} = 4$ kHz and $B_{bias} = 0.69$ T.

- "$\boldsymbol{U_e}$ switch point": this is the point in time at which the excitation voltage undergoes a step change due to PWM switching. There are two such points for every small remagnetization cycle that occurs.
- "B peak point" and "B min point": these are the points of maximum and minimum flux density values, respectively, which are reached during a small remagnetization cycle.
- "Loop start point" and "Loop end point": these are the points where the hysteresis loop of the main cycle intersects with itself, creating a minor hysteresis loop. In the $\boldsymbol{B-H}$ plane, these points have the same coordinates, but they are spaced apart in time, which can be seen by observing their position on the corresponding $\boldsymbol{B}$ waveform.
- "Loop half": each minor loop can be divided into two halves, where a dividing point is defined as the switching point $\boldsymbol{U_e}$. The first half of the loop is the half between the loop start point and second switching point $\boldsymbol{U_e}$ in the "middle" of the loop, and the other half is the half between the second switching point $\boldsymbol{U_e}$ and the end of the loop.

At the moment of the voltage step, the change in magnetic field strength follows instantaneously. However, since the flux density lags the magnetic field strength in phase, the maximum and minimum points of $\boldsymbol{B}$ appear somewhat later and their values are somewhat higher, or lower, than they were at the moment of the initial voltage step.

The difference between the maximum and minimum values of $\boldsymbol{B}$ is defined as the minor loop parameter $\boldsymbol{\Delta B}$, and the average of the two as the parameter $\boldsymbol{B_{bias}}$. If the $\boldsymbol{B_{bias}}$ point is positioned halfway between the points of the maximum and minimum values of $\boldsymbol{B}$, it lies almost perfectly on the fundamental waveform of $\boldsymbol{B}$ (Figure6.8a).

For the purposes of this method, minor loops are considered as a whole, not as a group of points forming that loop. Therefore, the parameters associated with the minor loop describe it in its entirety. In this context, the parameter $\frac{\mathbf{d}\boldsymbol{B}}{\mathbf{d}\boldsymbol{t}}$ of the minor loop is calculated as the quotient of $\boldsymbol{\Delta B}$ of the minor loop and the time required for such a change of $\boldsymbol{B}$. For the example shown in Figure6.8, the parameter $\frac{\mathbf{d}\boldsymbol{B}}{\mathbf{d}\boldsymbol{t}}$ would be calculated as follows:

$$\frac{\mathbf{d}\boldsymbol{B}}{\mathbf{d}\boldsymbol{t}} = \frac{\boldsymbol{\Delta B}}{\boldsymbol{\Delta T}} = \frac{\boldsymbol{B_{pk}} - \boldsymbol{B_{min}}}{\boldsymbol{T_{B_{min}}} - \boldsymbol{T_{B_{pk}}}}, \tag{6.1}$$

where $\boldsymbol{T_{B_{min}}}$ and $\boldsymbol{T_{B_{pk}}}$ are times at which $\boldsymbol{B_{pk}}$ and $\boldsymbol{B_{min}}$ values are reached. However, since the start and end points of the loops do not coincide with the initial $\boldsymbol{U_e}$ switching points, minor loops occurring in the core during AC measurements are asymmetric: the

time difference between the starting point of the loop and the point $\boldsymbol{B_{min}}$ is not equal to the time between $\boldsymbol{B_{min}}$ and the end point of the loop. Therefore, not only is the $\frac{\mathbf{d}\boldsymbol{B}}{\mathbf{d}\boldsymbol{t}}$ not equal along the entire closed curve of the minor loop, but it is even not equal for the first and second halves of the minor loop. Since the minor loop must be considered as a whole, the equivalent value of $\frac{\mathbf{d}\boldsymbol{B}}{\mathbf{d}\boldsymbol{t}}$ parameter is calculated by defining the time required to reach a given $\boldsymbol{\Delta B}$ as half the time required to complete the entire minor loop (Figure 6.8a):

$$\left(\frac{\mathbf{d}\boldsymbol{B}}{\mathbf{d}\boldsymbol{t}}\right)_{\mathbf{eq_1}} = \frac{\boldsymbol{B_{pk}} - \boldsymbol{B_{min}}}{(\boldsymbol{T_{loop_e}} - \boldsymbol{T_{loop_s}})/\mathbf{2}}\,, \tag{6.2}$$

where $\boldsymbol{T_{loop_e}}$ is time of the loop end point and $\boldsymbol{T_{loop_s}}$ time of the loop start point. This way of calculating the equivalent $\frac{\mathbf{d}\boldsymbol{B}}{\mathbf{d}\boldsymbol{t}}$ is simple and sufficient for *MLL* approach since the asymmetry of the minor loops is negligible.

Minor loops as independent of the main cycle - exceptions

The most of the characteristic points of the minor loops and the parameters are defined in the same way for *TACL* approach as they were for the *MLL* approach. However, because of the possibility of the occurrence of minor loops with much greater asymmetry and of loops that are not closed, there are some peculiarities in this context.

The definition of the start and end points of the minor loop for the approach *MLL* is simple: the minor loop starts and ends at the point where it intersects itself. However, if the *TACL* approach is used, the intersections do not always exist. Figure6.9shows some of the specific loops and their characteristic points that occur when the *TACL* approach algorithm is used. Of all the minor loops shown, only the minor loop in the 6.9asubfigure intersects itself. The start point of the minor loop is therefore not longer defined at a point of intersection, since often there is none, but at the PWM switching point that causes the formation of minor loop in question. The endpoint of the loop is defined based on one of two conditions: Either the value of $\boldsymbol{B}$ or $\boldsymbol{H}$ is reached that matches its initial value at the beginning of the loop.

If the initial value of $\boldsymbol{H}$ for the subsequent minor loop is not significantly different from the initial value of $\boldsymbol{H}$ for the loop just observed, the endpoint of the loop is defined as the point at which the value of $\boldsymbol{B}$ reaches its initial value at the starting point of the loop. This is the case for the minor loops shown in the subfigures6.9a-6.9c. In contrast, the end of the loop is defined as the point where the value of $\boldsymbol{H}$ reaches its initial value at the start point of the loop (Subfigures6.9d-6.9f). Otherwise, the parameter $\frac{\mathbf{d}\boldsymbol{B}}{\mathbf{d}\boldsymbol{t}}$ at the time of reaching the initial value $\boldsymbol{B}$ would be so small that the calculated contribution to

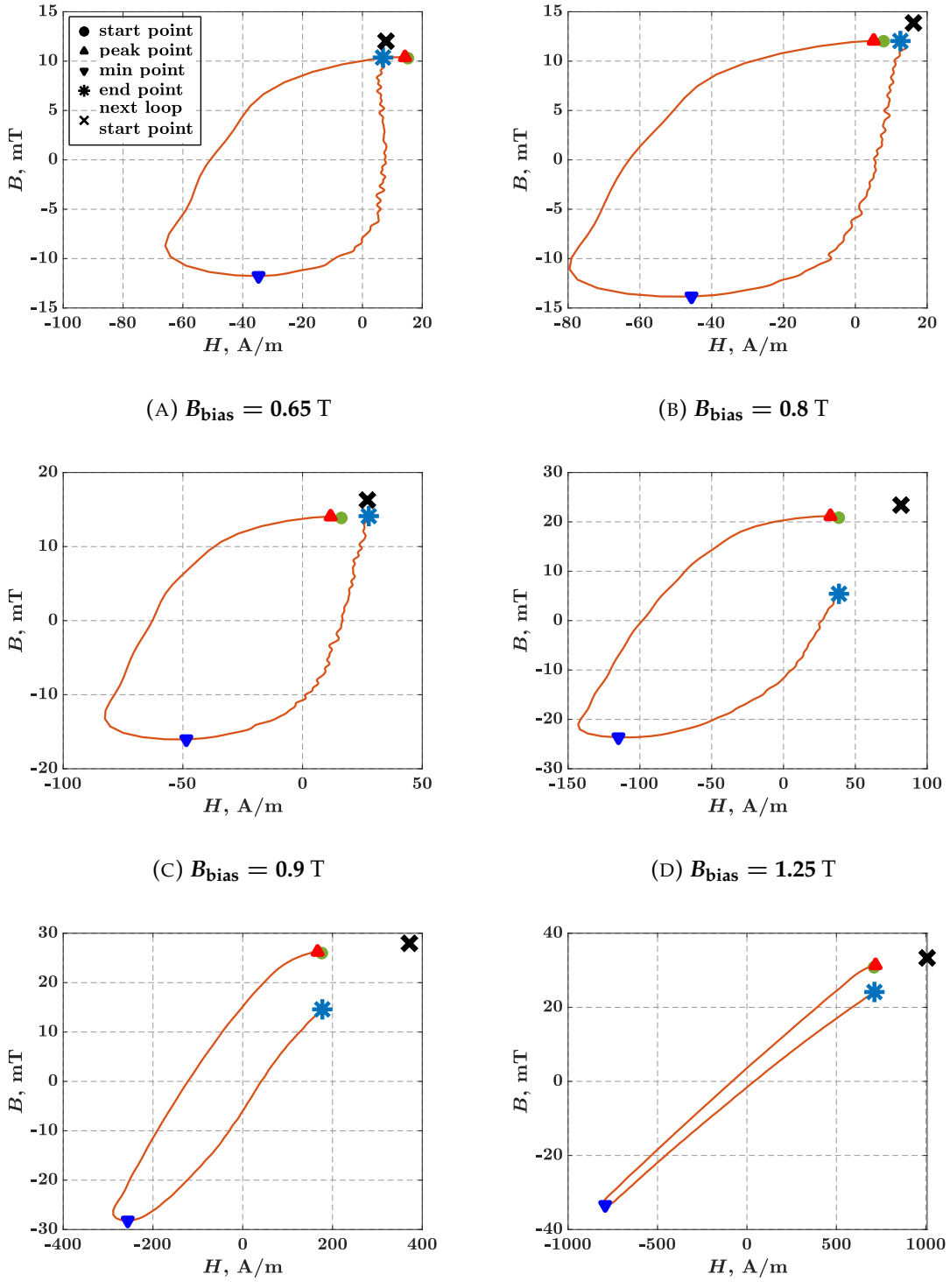

(A) $B_{\text{bias}} = 0.65$ T

(B) $B_{\text{bias}} = 0.8$ T

(C) $B_{\text{bias}} = 0.9$ T

(D) $B_{\text{bias}} = 1.25$ T

(E) $B_{\text{bias}} = 1.425$ T

(F) $B_{\text{bias}} = 1.55$ T

FIGURE 6.9: Some of the minor loops with a specific shape and loop parameters obtained from AC measurements with $f_{\text{sw}} = 4$ kHz.

the losses of the loop in question would be insignificant, and this would not correctly reflect the actual impact of this loop on the losses. In some cases, i.e. for some of the loops, this initial value $\boldsymbol{B}$ would not be reached at all before the start of the next loop, which would have the same negative impact on the calculation of the loop loss contribution.

Consequently, the definition of the loop half must also be slightly changed: The first half of the loop is the part of the loop in between the two switching points $\boldsymbol{U_e}$, one of which triggered the formation of the loop and the other of which is in the "middle" of the loop, and the other half is the part of the loop between the second switching point $\boldsymbol{U_e}$ and the end of the loop.

In a case of highly asymmetric minor loop, the value of the parameter $\frac{\mathbf{d}B}{\mathbf{d}t}$ of the first half of the minor loop differs significantly from the value of the other half. Figure 6.10ashows how the values of the parameter $\frac{\mathbf{d}B}{\mathbf{d}t}$ change for both the first and second halves of the typical minor loops. The curves are shown with respect to each minor loop occurring for a given peak value of the fundamental $\boldsymbol{B_{1hpk}} = \mathbf{1.5}$ T and $\boldsymbol{f_{sw}} = \mathbf{4}$ kHz. The degree of difference between the curves of the two halves indicates the degree of asymmetry of the minor loop that occurred. Thus, the minor loops with the highest asymmetry occur at lower values of $\boldsymbol{B_{bias}}$ and the opposite is true for the minor loops with the lowest asymmetry or no asymmetry at all. The cause of such formation of the loops can be seen in the shape of the ripple of the $\boldsymbol{H}$ waveform, which is shown in figure 6.10b. Loops with high asymmetry are formed when the ripple of the $\boldsymbol{H}$ waveform is rather saw-shaped (see left side of figure6.10b), and low asymmetry is obtained when it is rather triangular (see right side of figure6.10b).

There are three additional curves shown in figure6.10arepresenting equivalent values of $\frac{\mathbf{d}B}{\mathbf{d}t}$ parameter obtained in different ways. The first one (shown inviolet) is determined as it was for the *MLL* approach and is stated in equation6.2, and the second one (shown ingreen) is defined as:

$$\left(\frac{\mathbf{d}B}{\mathbf{d}t}\right)_{\mathbf{eq_2}} = \frac{B_{\mathbf{pk}} - B_{\mathbf{min}}}{T_{\mathrm{U_{e,sp2}}} - T_{\mathrm{U_{e,sp1}}}} \cdot \frac{A_{\mathrm{loop_{1/2}}}}{A_{\mathrm{loop_{tot}}}} + \frac{B_{\mathbf{pk}} - B_{\mathbf{min}}}{T_{\mathrm{loop_e}} - T_{\mathrm{U_{e,sp2}}}} \cdot \left(\mathbf{1} - \frac{A_{\mathrm{loop_{1/2}}}}{A_{\mathrm{loop_{tot}}}}\right), \tag{6.3}$$

where $\boldsymbol{B_{pk}}$ and $\boldsymbol{B_{min}}$ are the peak and minimum values of flux density of the minor loop, $\boldsymbol{T_{\mathrm{U_{e,sp1}}}}$ and $\boldsymbol{T_{\mathrm{U_{e,sp2}}}}$ are the time instances of the first and second $\boldsymbol{U_e}$ switching point, $\boldsymbol{T_{\mathrm{loop_e}}}$ is the end time of the loop, $\boldsymbol{A_{\mathrm{loop_{1/2}}}}$ is the area enclosed by the first half of the

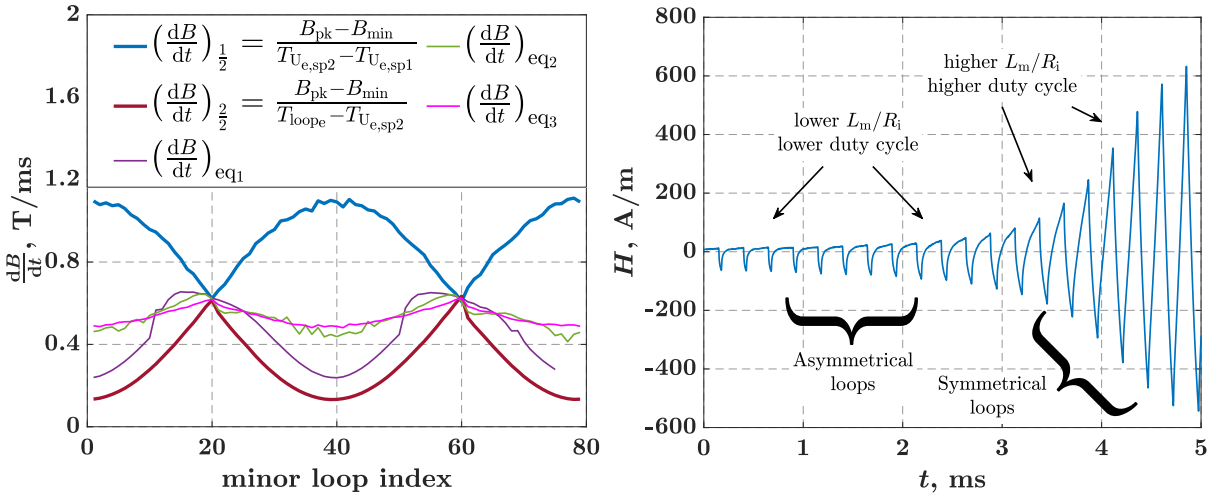

(A) $\frac{dB}{dt}$ parameter (B) Quater of H waveform

FIGURE 6.10: Subfigure (A) shows values of the $\frac{dB}{dt}$ parameter for the first (bluecurve) and the second (redcurve) half of the minor loop with respect to the loop index, specific value of fundamental $B_{1hpk} = 1.5$ T, and $f_{sw} = 4$ kHz. Theviolet,greenandmagentacurves represent three differently determined equivalent values of the $\frac{dB}{dt}$ parameter. Subfigure (B) shows quarter of a period of corresponding magnetic field strength waveform H.

minor loop and $A_{loop_{tot}}$ is the total area enclosed by the minor loop. So, the equivalent $\frac{dB}{dt}$ is calculated as the weighted sum of the $\frac{dB}{dt}$ values of both first and second halves of the loop. The weighing factor is determined as the ratio of the area enclosed by the each half of the minor loop, i.e., the ratio of losses contribution.

Apart from some exceptions, the calculation of $\frac{dB}{dt}$ using equation6.3gives an excellent approximation of the equivalent $\frac{dB}{dt}$ value. However, in order to calculate $\left(\frac{dB}{dt}\right)_{eq_2}$ this way, one must be able to calculate the area of the minor loop, i.e. one half of the minor loop, which requires knowing the time dependent waveform of the flux density $B(t)$. This would require solving in FEA software using a dynamic hysteresis loop model, which to the author's knowledge doesn't give useful results for PWM-generated sinusoidal excitation: One can solve for each minor loop separately by determining the parameters of the dynamic loop model for each loop using the results of the DC bias measurements [10], but this is a completely different approach to loss determination [1]. If both waveforms $B(t)$ and $H(t)$ could be determined as the result of a known PWM-generated current $I_e(t)$ or voltage $U_e(t)$ excitation, one could easily calculate the losses without the need for a special method.

[1] A discussion of the advantages and comparison between the methods is found later in the chapter8.

Using the results of the AC measurements made in this research, $\left(\frac{dB}{dt}\right)_{eq_2}$ is calculated and used as a reference for later comparison of the total determined AC losses. It will be shown later that the calculated losses obtained with $\left(\frac{dB}{dt}\right)_{eq_2}$ as the minor loop parameter best match the measured AC losses. This leads to the conclusion that the calculation of the equivalent parameter $\frac{dB}{dt}$ using weighting factors is a correct approach. However, none other than the loop area has been shown to be a good weighting factor, so further research on this topic is required.

Another equivalent $\frac{dB}{dt}$ parameter is defined as:

$$\left(\frac{dB}{dt}\right)_{eq_3} = \frac{B_{pk} - B_{min}}{T_{U_{e,sp2}} - T_{U_{e,sp1}}} \cdot k_e + \frac{B_{pk} - B_{min}}{T_{loop_e} - T_{U_{e,sp2}}} \cdot (1 - k_e)\,,\ k_e \in [0.335, 0.375] \tag{6.4}$$

where k_e is an empirically determined weighting factor, whose single value k_e is used for $\left(\frac{dB}{dt}\right)_{eq_3}$ calculation of each minor loop of the experiment. Based on the figure 6.10, a good agreement can be observed between the values of $\left(\frac{dB}{dt}\right)_{eq_2}$ and $\left(\frac{dB}{dt}\right)_{eq_3}$. The weighting factor k_e is determined from curves constructed from data on the ratio of $A_{loop_{1/2}}/A_{loop_{tot}}$ that are obtained from the AC measurements. For each value of B_{1hpk}, this ratio can be determined for each minor loop formed along the main cycle. If a median of the values of this ratio is then calculated for each curve with different values of B_{1hpk}, the optimal value of k_e as a function of B_{1hpk} is determined (Figure6.11). By averaging this curve, a single value for k_e can be determined for each specific switching frequency (Figure6.11).

6.3.2 Minor loops as part of the main cycle - MLL approach

The hysteresis loop of the main cycle is defined by the fundamental of the AC supply, or by the fundamental and several other harmonic components near the fundamental, all of which are in the relatively low frequency range. Low frequency here stands as a relative term to the frequency of the inverter circuit; the ratio f_{sw}/f_{1h} is expected to be at least 20. Thus, the ripple causing the minor loops occurs at much higher frequency than does the fundamental causing the main hysteresis loop. Nevertheless, both magnetic field strength and flux density fundamental changes during the process of the minor loop formation, and that with more significance as the switching frequency of the inverter decreases. As a result, the shape of each minor loop is slightly deformed compared to

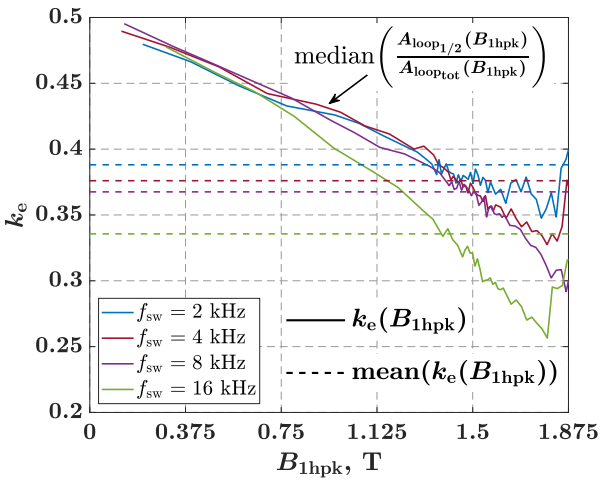

FIGURE 6.11: The weighting factor k_e as a function of B_{1hpk} and its single determined values depending on the switching frequency shown for the core C1a.

the loop formed without the presence of the changing fundamental (Figure6.12), which also affects the parameters ΔB, $\frac{dB}{dt}$, and B_{bias}. If the ΔB of the minor loop obtained from the AC measurements is matched with the ΔB of the minor loop obtained form DC measurements, the ΔH value of loops will differ (Figure6.12). The same would be true if one would match the minor loops according to the ΔH parameter, in which case the parameter ΔB of the loops would differ. In another words there is no such ΔB-ΔH pair that is equal for the minor loops obtained from the AC and DC bias measurements respectively.

This actual minor loop, i.e., the loop created by the combination of both high-frequency ripple and the change in low-frequency components, is the loop of interest when only minor loops contribution to the losses are to be determined. This is the loop that has enclosed an additional area that is to be added to the area of the main loop and thus has affected the increase in core power loss. So, the parameters of the actual minor loops have to be used for retrieval of power loss values out of the 3D loss map. If the parameters of the actual minor loop are within a range of available loops in the 3D loss map, there is no problem finding a loop with those parameters. However, regardless of the same parameters ΔB, $\frac{dB}{dt}$ and B_{bias}, the ΔH of both loops will not match and the area of the loop will not match either. Since the area of the loop is proportional to the losses, a determined value for the power loss will differ slightly from the actual value. This built-in flaw of this method must be accepted and taken into account in the analysis.

The figure6.12shows the comparison between the minor loops obtained from the measurements of AC and DC bias with respect to the different values of the parameter

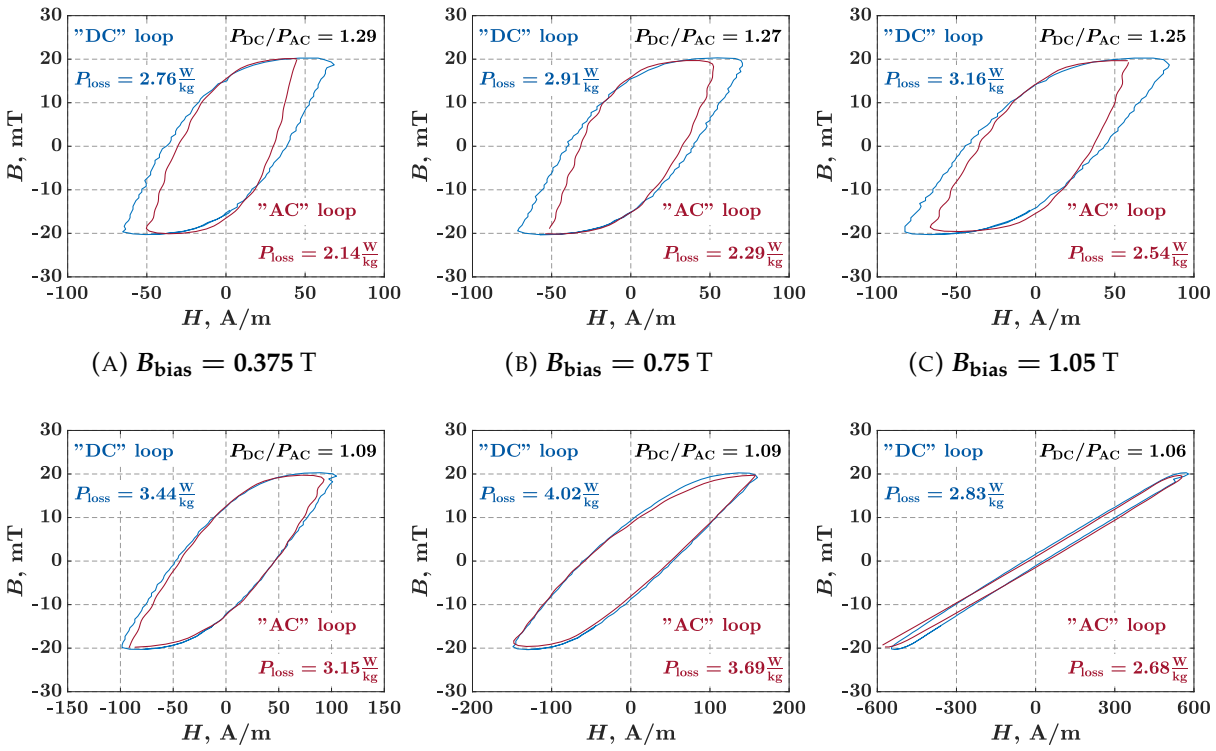

(A) $B_{bias} = 0.375$ T (B) $B_{bias} = 0.75$ T (C) $B_{bias} = 1.05$ T

(D) $B_{bias} = 1.25$ T (E) $B_{bias} = 1.4$ T (F) $B_{bias} = 1.6$ T

FIGURE 6.12: The difference in the minor loops obtained from the DC bias and AC measurements respectively, shown for different values of B_{bias}. Minor loops obtained in the AC measurements are shown for the case when minor loops are considered as a part of the main cycle loop.

B_{bias}. Both minor loops in each subfigure are defined with the same ΔB, $\frac{dB}{dt}$ and B_{bias} parameter. However, it can be clearly seen that the area bounded by the minor loops from the DC bias measurements is larger than the area of those from the AC measurements. Consequently, the loss value determined from the 3D loss map is larger than it should be, which leads to an overestimation of the losses.

In order to be able to present the comparison shown in the figure6.12, loops from AC and DC bias measurements had to be found that had the same loop parameters and were formed under the same conditions. The DC minor loops were formed under controlled conditions and for specific loop parameters, while AC formed minor loops are the result of a natural process of minor loop formation under PWM-generated excitation. Therefore, some of the parameters of the AC minor loops do not exactly match the parameters of the DC minor loops and the conditions under which AC minor loops are formed differ slightly from subfigure to subfigure. With this in mind, the values of the ratio of P_{DC} to P_{AC} should be evaluated relatively between subfigures, i.e.

as a function of $\boldsymbol{B_{bias}}$ and not as correct absolute values of this ratio.

All the AC minor loops shown in the figure6.12are formed under the conditions of the same change in the fundamental, i.e. the slope of the fundamental at the $\boldsymbol{B_{bias}}$ point of the loops is practically the same. This means that the amplitude of the fundamental is varied between subfigures in order to obtain the same derivative of the fundamental function at the time instant when a certain value of $\boldsymbol{B_{bias}}$ was reached. Depending on the $\boldsymbol{B_{bias}}$ and starting from a lower to a higher $\boldsymbol{B_{bias}}$ value, the electrical angle of the fundamental at which the loop was formed changed from 22.5° to 60°. Moreover, the value of the duty cycle of the excitation voltage that caused the AC minor loops is practically the same and is somewhere between 0.51 and 0.52, which means that the loops are almost completely symmetrical and in this sense completely comparable to the minor loops formed in the DC bias measurements. Looking at the ratio of $\boldsymbol{P_{DC}}$ to $\boldsymbol{P_{AC}}$, it is clear that this ratio depends on the $\boldsymbol{B_{bias}}$ value and decreases when $\boldsymbol{B_{bias}}$ is increased. The difference between the calculated and measured losses is about 30 % for a relatively low value of $\boldsymbol{B_{bias}} = \mathbf{0.375}$ T, while for a relatively high value of $\boldsymbol{B_{bias}} = \mathbf{1.6}$ T a difference of about 5 % is determined.

It should be noted that this difference in losses only affects a single minor loop formed at a given $\boldsymbol{B_{bias}}$ value. The total difference between the calculated and the actual losses depends on the difference of all the minor loops that occur in a single main cycle at a given peak flux density value. More on this topic is given later in the chapter8on the results of the loss calculation with the proposed method.

6.3.3 Minor loops as independent of the main cycle - TACL approach

When the FFT is used to separate the low frequency harmonics responsible for the formation of the main cycle loop, the ripple in the magnetic field strength and flux density that causes the formation of the minor loops can be observed independently. This means that the minor loops can also be observed independently of the time varying fundamental, in the sense that the fundamental does not directly affect the shape of the loop, i.e., the parameters $\boldsymbol{\Delta B}$ and $\frac{\mathbf{d}\boldsymbol{B}}{\mathbf{d}\boldsymbol{t}}$. However, the time variation of the fundamental still affects the DC bias at which a particular minor loop is formed, which is the third parameter defining the minor loop. Furthermore, the value of the DC bias slightly changes even during the formation of a single minor loop which will have a significant effect for the minor loops formed with larger duty cycle and at $\boldsymbol{B_{bias}}$ values located at

or near non linear-regions of the $\boldsymbol{B} - \boldsymbol{H}$ curve of the material. In these cases this also indirectly affects the $\boldsymbol{\Delta B}$ and $\frac{\mathbf{d}\boldsymbol{B}}{\mathbf{d}t}$ parameters.

In this approach, the fundamental and the components near the fundamental are excluded from observation, and only the remaining part of the waveforms of $\boldsymbol{H}$ and $\boldsymbol{B}$, representing the ripple otherwise superimposed on the fundamental, is observed. Thus, the fundamental has no direct influence on the shape and size of the minor loop, as evidenced by, among other things, a larger $\boldsymbol{\Delta B}$ and $\frac{\mathbf{d}\boldsymbol{B}}{\mathbf{d}t}$ compared to the *MLL* approach (Figure6.13). These minor loops that are obtained in the *TACL* approach, that is solely from the ripple of the waveforms of $\boldsymbol{B}$ and $\boldsymbol{H}$, contain the information of the total PWM losses induced by specific remagnetization cycle. That means that the area of the minor loop obtained in this way contains both the area of the minor loop obtained with *MLL* approach and the area that is added to the main cycle loop due to the PWM generated supply. This area added to the main cycle loop is manifested as widening of the main cycle loop. Therefore, using these loop parameters to obtain loss data from the 3D loss map results in calculated losses that represent the total PWM contribution to the AC losses. Although the fundamental in *TACL* approach has no direct effect on the forming of the minor loop in the terms of its shape and size, the link between these loops and the fundamental cannot be broken, as it is controlled by the parameter $\boldsymbol{B}_{\mathbf{bias}}$ of the loop.

The comparison between minor loops obtained from DC bias and AC measurements in relation to several different values of $\boldsymbol{B}_{\mathbf{bias}}$ is shown in figure6.14. Same as it was for the case when minor loops were considered as a part of the main cycle, a difference

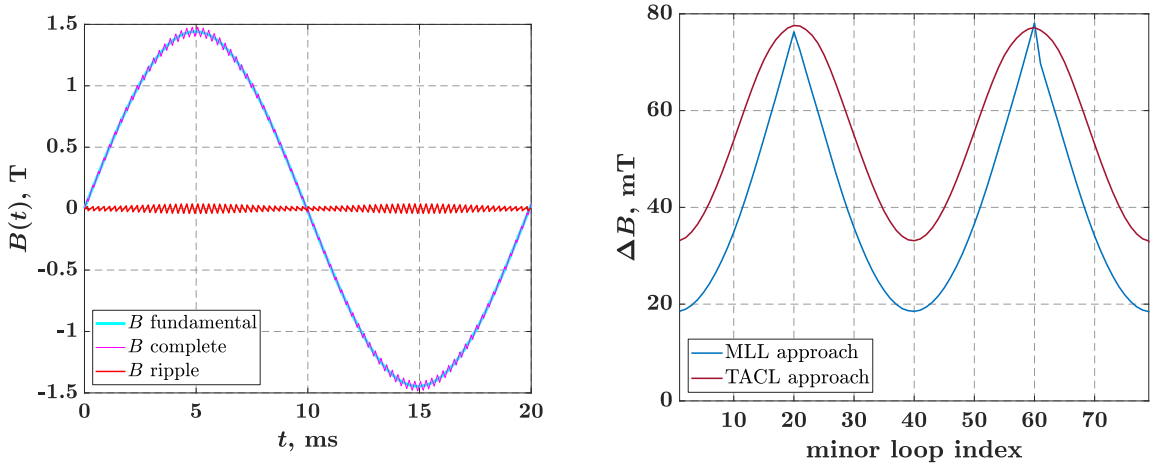

(A) Waveforms of $\boldsymbol{B}$

(B) $\boldsymbol{\Delta B}$ values

FIGURE 6.13: The waveform of $\boldsymbol{B}$ together with the fundamental and the ripple filtered out as well as the values of $\boldsymbol{\Delta B}$ determined with the MLL and TACL approach respectively.

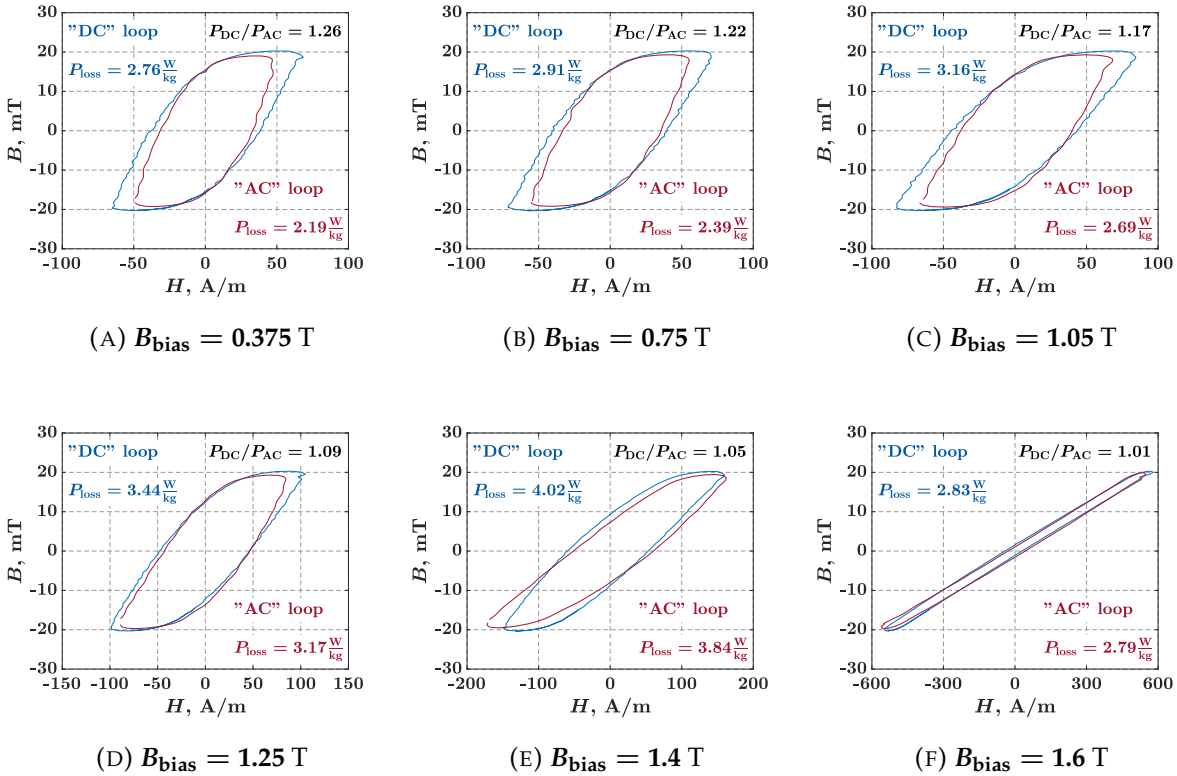

(A) $B_{bias} = 0.375$ T (B) $B_{bias} = 0.75$ T (C) $B_{bias} = 1.05$ T

(D) $B_{bias} = 1.25$ T (E) $B_{bias} = 1.4$ T (F) $B_{bias} = 1.6$ T

FIGURE 6.14: The difference in the minor loops obtained from the DC and AC measurements respectively, shown for different values of B_{bias} and $f_{sw} = 4$ kHz. AC measurements loops are shown for the case when minor loops are considered as independent of the main cycle loop.

in ΔH_{AC} to ΔH_{DC} can be observed here as well, resulting in same issues with loop comparison. However, apart from discrepancy in ΔH values, few additional comparing problems arise when loops are observed independently of the main cycle.

The combination of relatively low values of the duty cycle and the L_m/R_i constant (Figure6.10b) of the equivalent circuit of the core (Figure4.13) leads to the formation of highly asymmetric minor loops, i.e., the time required to form the first half of the loop is significantly different from the time required to form the other half. As a result of highly asymmetric minor loops, the value of the parameter $\frac{dB}{dt}$ of the first half of the minor loop differs significantly from the value of the other half. The comparison between highly asymmetric AC minor loops and DC minor loops is shown in figure 6.15. The comparison is based on the same parameters ΔB and B_{bias} and the $\frac{dB}{dt}$ of AC minor loop equals $\left(\frac{dB}{dt}\right)_{eq_1}$. Using this value of $\frac{dB}{dt}$ for given loop parameters in figure 6.15leads to an underestimation of the PWM-induced losses, which can be clearly seen

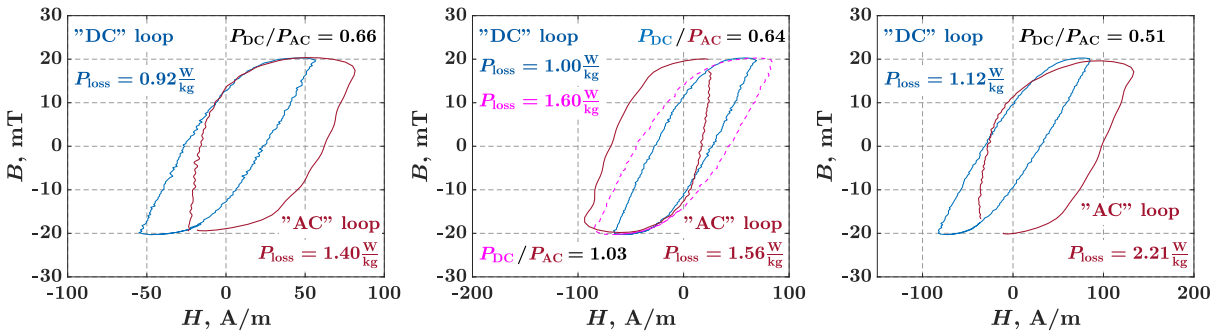

(A) $B_{bias} = 0.75$ T (B) $B_{bias} = 1$ T (C) $B_{bias} = 1.3$ T

FIGURE 6.15: The difference in the minor loops obtained from the DC and AC measurements respectively, shown for different values of B_{bias} and $f_{sw} = 4$ kHz. AC measurements loops are shown for the case when minor loops are considered as independent of the main cycle loop.

by comparing the areas enclosed by AC and DC minor loops respectively. All of the AC minor loops shown enclose a larger area due to the significantly larger $\frac{dB}{dt}$ value of the first half of the minor loop. In the subfigures6.15aand6.15c, this is the right half of the loop while in the subfigure6.15b, it is the left half of the loop, which only depends on the quadrant of the main hysteresis loop in which the specific minor loop occurred.

The minor loops in figure6.15are shown with subtracted mean values of B and H. The abrupt current drop that causes the first half of the loop is of much shorter duration than the other part of the current waveform that causes the other half of the loop. For this reason, and because of the relatively low L_m/R_i constant that allows the current value before the drop to be quickly recovered, the mean value of H is closer to the value before the drop than to the value after the drop. This is manifested in the figure6.15by an apparent shift of the loop body to the left or right.

To compensate for a significant difference in enclosed loop area, $\left(\frac{dB}{dt}\right)_{eq_2}$ or $\left(\frac{dB}{dt}\right)_{eq_3}$ can be used as an equivalent $\frac{dB}{dt}$ parameter of the AC minor loop. Since the value of this parameter is larger than $\left(\frac{dB}{dt}\right)_{eq_1}$ for asymmetric loops, the DC minor loop, with which the AC loop is being compared, has a larger enclosed area compared to the previous case. The dashedmagentaloop in the subfigure6.15brepresents a DC minor loop, with which AC minor loop is compared to when the $\left(\frac{dB}{dt}\right)_{eq_2}$ parameter of the AC loop is used. The original difference of **36%** between the areas enclosed by DC and AC minor loop is now reduced to **3%**.

Another comparing problem occurs when the loops from the AC measurements form under conditions of significant change in the $\boldsymbol{B_{bias}}$ value (the $\boldsymbol{B_{bias}}$ value slides with the time varying fundamental). This effect is all the more pronounced as the switching frequency lowers, since the duration of the minor loops is then higher, and as the $\boldsymbol{B_{bias}}$ values approaches the knee point of the magnetization curve. Under these conditions, the minor loops can be significantly distorted and some of the remagnetization cycles do not form a closed loop (Figure6.16).

If the entire $\boldsymbol{B}$ and $\boldsymbol{H}$ waveforms are used for the analyses, i.e., including the fundamental, a clear separation can be made between the main cycle loop and the minor loops. If only the ripple of the $\boldsymbol{B}$ and $\boldsymbol{H}$ waveforms are considered, there is no main cycle loop, but only a continuous $\boldsymbol{B-H}$ relation curve consisting of the successive remagnetization cycles. Figure6.16shows part of a such $\boldsymbol{B-H}$ curve, plotted as a thick greenline, including three consecutive remagnetization cycles occurring at $\boldsymbol{B_{bias}}$ values near the knee point of the normal magnetization curve. Observing the shown $\boldsymbol{B-H}$ curve, it can be seen that none of the remagnetization cycles form a closed minor loop. Corresponding minor "loops" are plotted over the continuous loop with dashed lines with start and end points marked, which were determined in accordance with section 6.3.1. The term loop is in quotation marks here because loops aren't closed, but are a part of the $\boldsymbol{B-H}$ curve between certain starting and ending points. These points are defined to provide an equivalent loop parameter of the remagnetization cycles that can

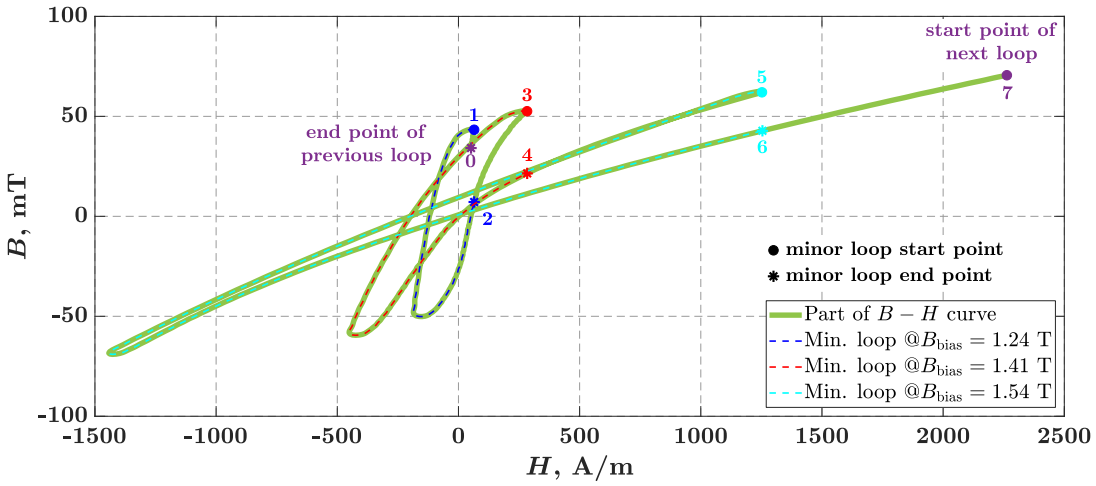

FIGURE 6.16: Three consecutive remagnetization cycles in the nonlinear region of the $\boldsymbol{B-H}$ curve of the material, starting at the point **0** and ending at the point **7**. Three opened minor loops are identified, starting at points **1**, **3** and **5** and ending at points **2**, **4** and **6** respectively. The switching frequency is equal to $f_{sw} = 2$ kHz.

be compared to the minor loops from the DC bias measurements. It can be seen that small portions of the $\boldsymbol{B} - \boldsymbol{H}$ curve between points 0-1, 2-3, 4-5, and 6-7 are not part of any minor loop.

For the minor "loops" defined in this way, the $\boldsymbol{\Delta B}$, $\boldsymbol{\Delta T}$, and $\frac{\mathbf{d}\boldsymbol{B}}{\mathbf{d}\boldsymbol{t}}$ parameters differ significantly between the loop halves, further emphasizing the importance of determining the equivalent $\frac{\mathbf{d}\boldsymbol{B}}{\mathbf{d}\boldsymbol{t}}$ parameter. Although the use of the equivalent parameter can be a good tool to overcome an issue of comparing minor loops formed under significantly different excitation and magnetic circuit conditions, it is not a perfect substitute. Errors in loss calculations are expected to be higher when the AC remagnetization cycles deviate significantly from the ideal teardrop-shaped loops or do not even form a closed loop.

It should be noted that each minor loop is analyzed separately, so relatively large errors in determining the losses of individual loops along the main cycle do not necessarily mean that the error in calculating the total AC losses for a given point $\boldsymbol{B_{1hpk}}$ is equally large. The overall error will depend on the error of all of the minor loops that were formed along cycle for each different $\boldsymbol{B_{1hpk}}$ value. The results of the loss calculation using this method are shown in chapter8.

6.4 Algorithm for determining PWM contribution to iron losses

The proposed method requires determination of all minor loops formed over a single main cycle for each $\boldsymbol{B_{1hpk}}$. Loop parameters are then to be determined and compared with the loop loss data organized in the previously determined 3D loss map. For this purpose, an algorithm was developed to extract the required data from the minor loops and determine the loss values for each measurement with a different peak value of the fundamental, resulting in a curves of power losses in relation to the $\boldsymbol{B_{1hpk}}$.

As previously mentioned, the results of the AC measurements were used as input data for the method. For this reason, some steps of the following algorithm for determining the PWM contribution to iron losses are only applicable to this case. The algorithm block schematics is shown in figure6.17and it consists of the following steps:

1. The waveforms of the sense coil voltage $\boldsymbol{U_s}$ and the excitation current $\boldsymbol{I_e}$ are taken from the measured data for each different peak point of the fundamental flux density $\boldsymbol{B_{1hpk}}$, and then the waveforms of the flux density $\boldsymbol{B}$ and the magnetic field strength $\boldsymbol{H}$ are obtained

2. A single period of each waveform is then extracted and shifted according to the position of the waveform of $\boldsymbol{B}$ positioned to start at zero ($\boldsymbol{B(0) = 0}$ T)

   Otherwise, there is a risk that one or even two of the minor loops will be overlooked, at least to some degree. For example, if one period of the analyzed $\boldsymbol{B}$ waveform were to begin during the formation of the minor loop, the parameters of that loop would be incorrectly determined, and there is a risk that the same would happen for the final minor loop as well. At lower switching frequencies, this could have a measurable impact on the loss calculation: at $f_{sw} = 2$ kHz, the maximum number of minor loops along a single cycle is 39, so the absence of one loop would affect the result by up to $\approx$ **2.5%**.

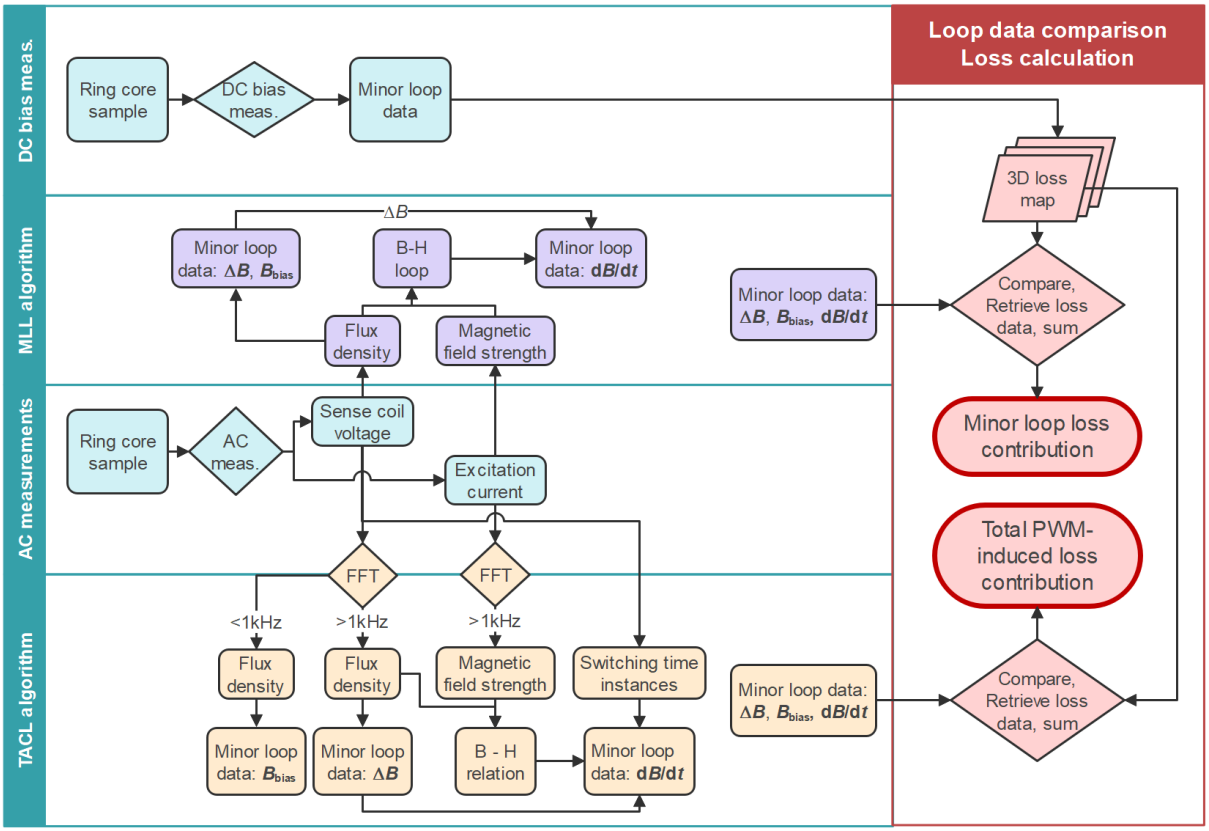

FIGURE 6.17: *MLL* and *TACL* approach algorithms for calculation of the contribution of the PWM-induced losses to the total AC losses.

3. The waveform of $\boldsymbol{U_s}$ is analyzed to determine the position of the points at which the excitation voltage undergoes a step change due to PWM switching

4. The waveform of $\boldsymbol{B}$ is analyzed to determine the positions and values of the points $\boldsymbol{B_{pk}}$ and $\boldsymbol{B_{min}}$ (Figure6.18)

   Based on these data, the values of the parameters $\boldsymbol{\Delta B}$ and $\boldsymbol{B_{bias}}$ are determined for each minor loop. For the minor loops located in the first and fourth quadrants of the one period of the waveform of $\boldsymbol{B}$, the value of the point $\boldsymbol{B_{pk}}$ of the minor loop is greater than the value of the point $\boldsymbol{B_{min}}$ of the minor loop. The opposite is true for the minor loops in the second and third quadrants. This transition is visible in the detailed view in figure6.18. For this reason, for each peak of the fundamental waveform, one leg of the ripple waveform is not used as part of any minor loop. Therefore, the maximum number of minor loops that occur in one period of the main cycle is defined as $(\boldsymbol{f_{sw}/f_{1h}-1})$. The algorithm for detecting the characteristic points of the minor loops must take this into account. This also applies to the detection of the loop starting points from the waveform of $\boldsymbol{U_s}$, but is presented here using the waveform of $\boldsymbol{B}$ for simplicity of presentation.

5. The complete $\boldsymbol{B-H}$ loop is analyzed to determine the endpoints of the minor loops i.e. the intersections of the minor loop with itself

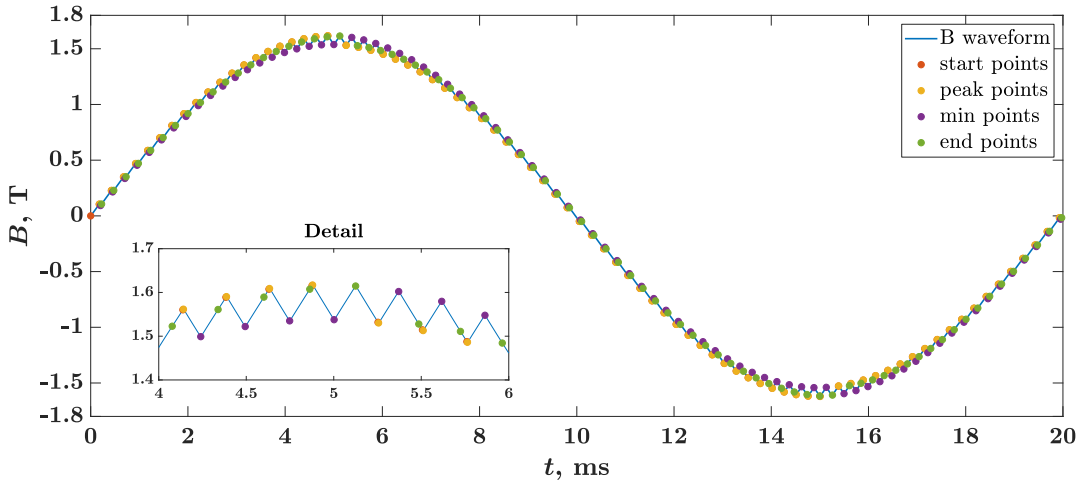

FIGURE 6.18: Waveform of $\boldsymbol{B}$ with all characteristic minor loop points, shown for $\boldsymbol{B_{1hpk}} = \mathbf{1.55}$ T, and $\boldsymbol{f_{sw}} = \mathbf{4}$ kHz. The detailed view illustrates the change in the arrangement of the characteristic loop points when the fundamental reaches the maximum value.

These data are used to determine the duration of each minor loop, which is, in the combination with the parameter $\mathbf{\Delta}\boldsymbol{B}$, needed to determine the parameter $\frac{\mathbf{d}\boldsymbol{B}}{\mathbf{d}\boldsymbol{t}}$ of the minor loop.

6. The closest values of all of the three parameters of the minor loops are looked for in the 3D loss map, and the loss value for the each loop is retrieved

7.The retrieved losses are scaled and summed

The loss data in the 3D loss map are stored in units of W/kg. Since the minor loop is the only loop of the cycle in the DC bias measurements, it actually represents the main loop of the cycle whose fundamental frequency is equal to $\boldsymbol{f_{sw}}$. Therefore, when the loss value is retrieved, it must first be converted to joules ($\boldsymbol{J}$) by multiplying it by the $\mathbf{\Delta}\boldsymbol{T}$ parameter, i.e. the duration of the minor loop in the AC measurements. To transform the data back into the units of W/kg, but in a different fundamental frequency frame, the retrieved value is then multiplied by the value $\boldsymbol{f_{1h}}$. The loop loss data for each specific value of $\boldsymbol{B_{1hpk}}$ are then summed so that the final results are in the form of power loss values in W/kg versus peak flux density in Tesla.

The basics of the algorithm do not change regardless of the approach, but there are some differences in algorithm when minor loops are observed independent of the main cycle, which are listed below:

- After the first step, and before continuing further, the low harmonic components have to be removed from the analyzed waveforms of $\boldsymbol{B}$ and that up to the frequency value of $\boldsymbol{f = 1}$ kHz
- Regarding the step 3. of the algorithm, values of $\boldsymbol{H}$ and $\boldsymbol{B}$ are also determined at the time of the PWM switching points. Start point of the loop is defined by these values, and further more, those values are later used in the step 5. for the determination of the end point of the loop.
- Regarding the step 5. of the algorithm, a continuous $\boldsymbol{B - H}$ curve is analyzed, but no search is made for intersections. Instead, the minimum difference between the $\boldsymbol{B}$ or $\boldsymbol{H}$ waveforms and the $\boldsymbol{B_{start}}$ or $\boldsymbol{H_{start}}$ values of the minor loop is sought. Whether $\boldsymbol{B}$ or $\boldsymbol{H}$ is used for comparison depends on the difference between $\boldsymbol{H_{start}}$ of the current and the subsequent loop: for smaller differences $\boldsymbol{B}$ is used for comparison, otherwise $\boldsymbol{H}$.

- Three different values of $\frac{dB}{dt}$ are determined, and three different loss values are retrieved for each minor loop based on $\frac{dB}{dt}$ parameters

6.5 Validation of results

The results of the application of this method are validated by comparison with the results of the AC measurements performed on the core. AC measurement results are used both as input data for the algorithm of the method and later as reference data for comparison with the results of the method. In this way, the theory of the proposed method and the algorithm alone are put to the test, since practically all other influencing factors are eliminated.

Regardless of the two different approaches, the results of the proposed method represent the contribution of the PWM-generated supply to iron losses. The *MLL* approach gives a result representing only the contribution of the minor loops, while the *TACL* approach gives the total contribution of the PWM to the iron losses. So, in order to compare the results of the method with the measured results, the measured total AC losses must be decomposed into their components: the contribution of the sinusoid to the losses and the contribution of the PWM to the losses, which in turn is decomposed into the losses caused by the minor loops and other losses that include all other PWM effects on the deformation of the main cycle loop.

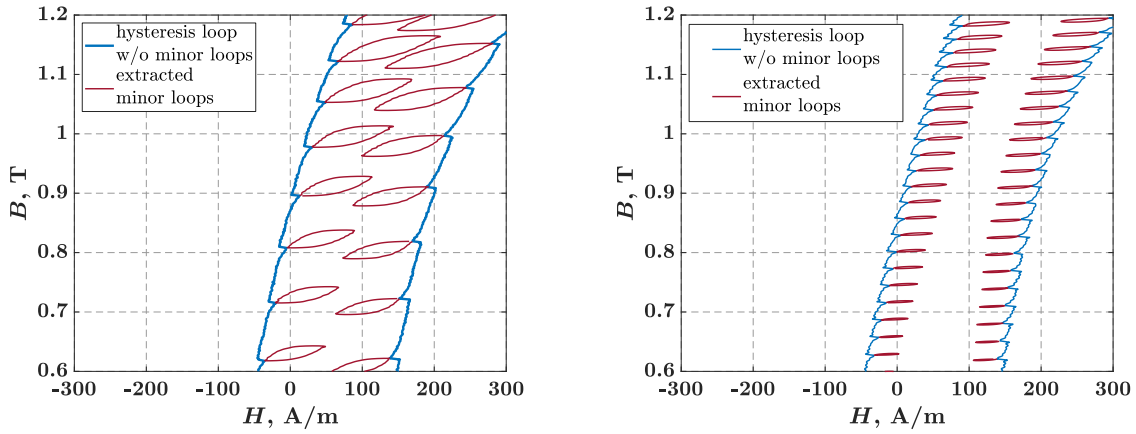

(A) $f_{sw} = 4$ kHz (B) $f_{sw} = 16$ kHz

FIGURE 6.19: The algorithm detects and extracts minor loops from the hysteresis loop of the main cycle.

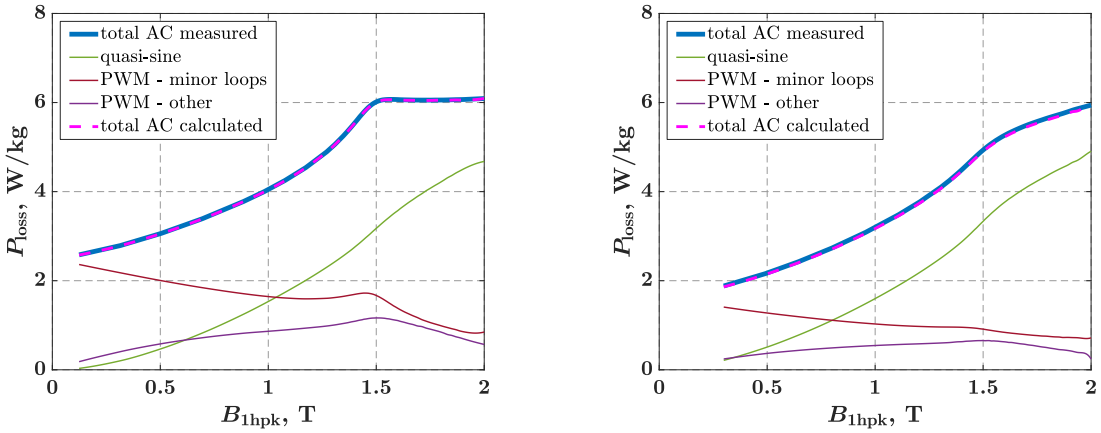

(A) $f_{sw} = 4$ kHz (B) $f_{sw} = 16$ kHz

FIGURE 6.20: Validation of the concept of decomposing total AC losses into components.

The sinusoidal losses are measured using the quasi-sinusoidal power supply already described and validated in Section5.2and are considered known. The contribution of the PWM minor loop losses to the total losses AC is calculated using an algorithm that extracts each minor loop formed in the main cycle (Figure6.19), calculates the area of each loop, and sums them. Finally, the other PWM losses are calculated as the difference between the areas of the hysteresis loop left when the minor loops are extracted and the hysteresis loop formed during quasi-sine excitation. The validation of the decomposition of the losses in this way is shown in figure6.20for two different switching frequencies. There it can be seen that the calculated AC total losses, which are composed of the PWM minor loop losses, the other PWM losses, and the quasi-sine losses, match the measured losses almost perfectly.

All the results of the *MLL* approach are compared only with the curves of the contribution of the minor loops to the losses, but not with the total AC losses. To obtain the total losses, other PWM losses must be added to the losses of the minor loops. However, these cannot be measured, but only calculated from the curves of the total AC losses, and these calculations cannot be performed at the time when the proposed method is to be applied, i.e. in the design phase, when the total AC losses are not yet known. In contrast, the results of the *TACL* approach of the proposed method are compared with the measured total AC losses, since still only the sinusoidal losses need to be known to obtain the total AC losses, and it is expected that these could be known, at least with a certain level of accuracy, at the time of the application of the method.

Chapter 7

Method for calculation of PWM-induced iron losses using waveform of H

The *3DLMB* method described in the previous chapter requires knowledge of the flux density waveform $\boldsymbol{B}$ for each finitely small point or region of the electrical machine in order to calculate the contribution of PWM-induced losses to the total AC losses. Since there may be some difficulties in obtaining the waveform of $\boldsymbol{B}$, which will be evaluated later in the section8.4, the possibility of using other data for the loss calculation is investigated here. A method is therefore proposed that uses the data on waveform of magnetic field strength $\boldsymbol{H}$ to calculate the PWM-induced losses. To facilitate reference to this method in the rest of the text, an acronym for the method is defined as *3DLMH* (**3D L**oss **M**ap based on the minor loop parameters in relation to the $\boldsymbol{H}$).

Similar assumption applies here as with the *3DLMB* method: at this stage of the thesis it is assumed that the waveform of $\boldsymbol{H}$ can be obtained using simulation platforms commonly used in the design of electrical machines, and the evaluation of this assumption will be assessed later in the section8.4. In this chapter, the results of the AC measurements have been used as both reference and input data for the proposed method. In this way, the theory of the method and the algorithm of the method alone are put to the test.

All diagrams, curves, and hysteresis loops presented in this chapter are the result of measurements made on core C1a, and therefore this is not indicated separately with each figure, but is mentioned here. All other parameters of interest for a particular figure are listed in the caption.

7.1 3D loss map based on the waveform of H

The first attempt on the realization of this method was to create a 3D loss map from the performed DC bias measurements but to use $\boldsymbol{\Delta H}$, $\boldsymbol{H_{bias}}$, and $\frac{\mathbf{d}H}{\mathbf{d}t}$ as loop parameters instead of $\boldsymbol{\Delta B}$, $\boldsymbol{B_{bias}}$, and $\frac{\mathbf{d}B}{\mathbf{d}t}$. The problem with this approach was the way in which the DC bias measurements were made: For each measurement set, which consisted of points with different values of the parameter $\boldsymbol{B_{bias}}$, the parameters $\boldsymbol{\Delta B}$ and $\frac{\mathbf{d}B}{\mathbf{d}t}$ were held constant. In this way, the loss results could be organized in the form of a 3D map such that when moving in any axis direction in 3D space, only one parameter changed while the other two remained unchanged. This was crucial for later interpolation and extrapolation of the loss results, and for the creation of 3D loss map in general. However, these results of the DC bias measurements could not then be used to create the 3D loss map in terms of $\boldsymbol{\Delta H}$, $\boldsymbol{H_{bias}}$, and $\frac{\mathbf{d}H}{\mathbf{d}t}$. The reason is that each loss data point in each measurement series has a different value for all three parameters, so they cannot be organized into maps but are scattered in 3D space. If there were enough such loss data points distributed relatively uniformly in space at relatively high resolution, scattered interpolation could be performed to obtain a 3D loss map relative to these parameters. However, this may not be the best solution because the loss data points are non linearly correlated with the two parameters $\boldsymbol{H_{bias}}$ and $\frac{\mathbf{d}H}{\mathbf{d}t}$ and it may be difficult to obtain the measurement results in such a way that the creation of a 3D loss map using scattered interpolation gives a good result. A better way, in the author's opinion, would be to perform the DC bias measurements as they are for the purpose of constructing the 3D loss map in terms of $\boldsymbol{\Delta B}$, $\boldsymbol{B_{bias}}$, and $\frac{\mathbf{d}B}{\mathbf{d}t}$, but with the exception that the parameters $\boldsymbol{\Delta H}$ and $\frac{\mathbf{d}H}{\mathbf{d}t}$ are kept constant for each measurement series consisting of points with different values of the parameter $\boldsymbol{H_{bias}}$.

At this stage of the research, it was not possible to re-run the set of DC bias measurements in relation to the minor loop parameters based on the waveform of $\boldsymbol{H}$. Furthermore, as mentioned above, the existing measurement data could not have been used to create the 3D loss map in terms of the $\boldsymbol{\Delta H}$, $\boldsymbol{H_{bias}}$ and $\frac{\mathbf{d}H}{\mathbf{d}t}$ parameters. For this reason, a mapping algorithm was developed to obtain minor loop parameters $\boldsymbol{\Delta B}$, $\boldsymbol{B_{bias}}$ and $\frac{\mathbf{d}B}{\mathbf{d}t}$ that correspond to the loop parameters based on $\boldsymbol{H}$ which are assumed to be known. From this point, when the minor loop data is obtained in reference to the waveform of $\boldsymbol{B}$, the existing 3D loss map could have been used to obtain the loss data in the same way as in the *3DLMB* method.

7.2 Mapping of the minor loop data

For the purpose of mapping, a 3D map of the values of ΔH relative to ΔB, B_{bias} and $\frac{dB}{dt}$ was created. The values of ΔH were obtained from the DC bias measurements made, and the same principle was used to create the 3D map of ΔH as was used to create the 3D loss map. The preview of the created map is shown in figure7.1. Just as in the 3D loss map, each position in the 3D map of ΔH values is defined by three indices: ΔB value defines the index of the sheet, B_{bias} defines the index of a column and $\frac{dB}{dt}$ defines the index of a row where the data is located. The mapping of the minor loop data based

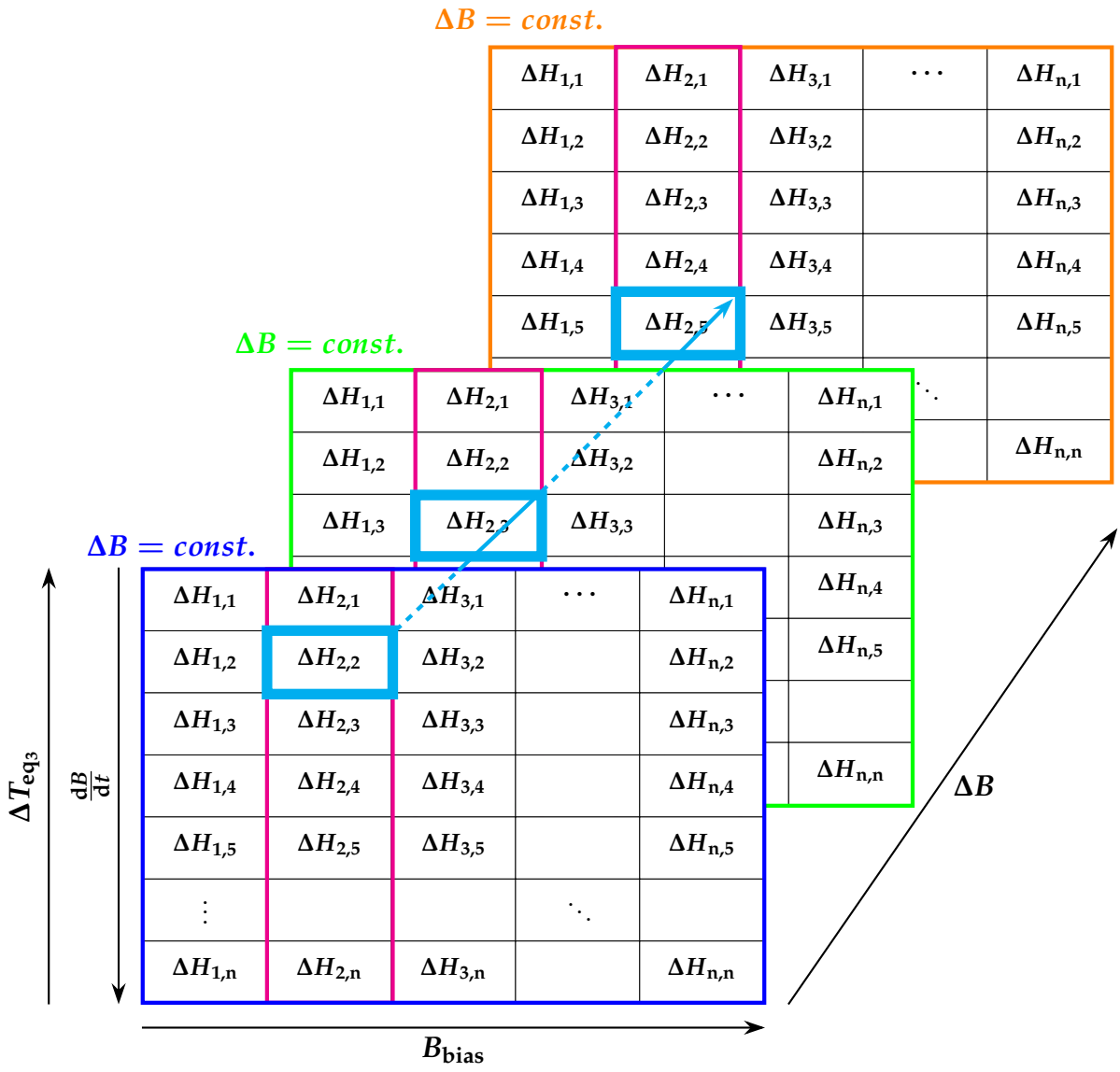

FIGURE 7.1: Overview of the 3D map of the ΔH values.

on $\boldsymbol{H}$ to the minor loop data based on $\boldsymbol{B}$ is performed in several steps to obtain all three indices of the position in the 3D map of the $\boldsymbol{\Delta H}$ parameter of the minor loop. This determined position in the 3D map of $\boldsymbol{\Delta H}$ matches the position that would otherwise be determined using the $\boldsymbol{B}$ based minor loop parameters. Therefore, these indices can then be used to retrieve loss data from the 3D loss map based on the minor loop parameters $\boldsymbol{\Delta B}$, $\boldsymbol{B_{bias}}$ and $\frac{\mathbf{d}\boldsymbol{B}}{\mathbf{d}\boldsymbol{t}}$.

First, the parameter $\boldsymbol{H_{bias}}$ is mapped using a family of $\boldsymbol{B-H}$ loops obtained under sinusoidal excitation and for different values of the peak value of the fundamental $\boldsymbol{B_{1hpk}}$. The frequency of the sinusoidal excitation used to determine the family of $\boldsymbol{B-H}$ loops must correspond to the fundamental frequency of the PWM-generated power supply. Part of the family of $\boldsymbol{B-H}$ loops used for mapping was obtained at the IET Institute in Končar and is shown in the subfigure7.2a. For higher values of $\boldsymbol{B_{1hpk}}$, $\boldsymbol{B-H}$ loops were obtained with a quasi-sinusoidal inverter power supply. The mapping of the minor loop parameter $\boldsymbol{H_{bias}}$ to the minor loop parameter $\boldsymbol{B_{bias}}$ is performed as follows:

1. The $\boldsymbol{H_{bias}}$ waveform is constructed from all $\boldsymbol{H_{bias}}$ values of the minor loops for each set of measurements. Then the maximum value of the $\boldsymbol{H_{bias}}$ waveform is determined, and the $\boldsymbol{B-H}$ loop with the nearest largest peak of the fundamental $\boldsymbol{H_{1hpk}}$ is selected from the family of curves for mapping,

2. The $\boldsymbol{H_{bias}}$ values from each quadrant of the $\boldsymbol{H_{bias}}$ waveform are mapped using a corresponding quadrant of the selected $\boldsymbol{B-H}$ loop.

3. For the higher values of $\boldsymbol{H_{1hpk}}$, when quasi-sinusoidal $\boldsymbol{B-H}$ loops are used for mapping, the mapped values of $\boldsymbol{B_{bias}}$ must be circularly shifted by one or two points to better match the $\boldsymbol{B_{bias}}$ values obtained by measurements. The reason for

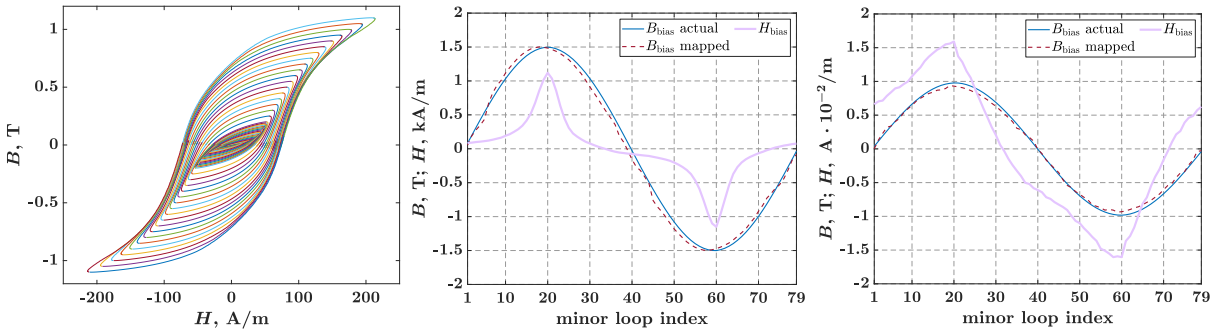

(A) Family of $\boldsymbol{B-H}$ curves (B) Mapping @$\boldsymbol{B_{1hpk}} = \mathbf{1.5}$ T (C) Mapping @$\boldsymbol{B_{1hpk}} = \mathbf{1}$ T

FIGURE 7.2: Mapping of $\boldsymbol{H_{bias}}$ to $\boldsymbol{B_{bias}}$ values.

this is that the $\boldsymbol{B-H}$ loop obtained with quasi-sinusoidal excitation is slightly wider than the loop obtained with pure sinusoidal excitation.

Subfigures7.2band7.2cshow the comparison between the constructed waveform of the $\boldsymbol{B_{bias}}$ values of the minor loops obtained from the AC measurements and the constructed waveform of the $\boldsymbol{B_{bias}}$ values mapped from the $\boldsymbol{H_{bias}}$ values of the minor loops. The number of data points of the constructed waveform depends on the number of the minor loops formed along a single main cycle. For this reason, the index of the minor loop is shown in the x-axis of the7.2band7.2csubfigures, where the index represents the ordinal number of the minor loop within a single main cycle. Each subfigure shows the comparison for a different value of $\boldsymbol{B_{1hpk}}$. The mapped values agree well with the values obtained by measurements, and the differences are mainly due to the use of $\boldsymbol{B-H}$ loops obtained with quasi-sinusoidal excitation for mapping. The analysis of the impact of using mapped $\boldsymbol{B_{bias}}$ values on the loss calculation results is presented later in this chapter.

After mapping the minor loop data from $\boldsymbol{H_{bias}}$ to $\boldsymbol{B_{bias}}$ values, $\boldsymbol{\Delta H}$ and $\frac{\mathbf{d}\boldsymbol{H}}{\mathbf{d}\boldsymbol{t}}$ values of the minor loops are mapped to $\boldsymbol{\Delta B}$ and $\frac{\mathbf{d}\boldsymbol{B}}{\mathbf{d}\boldsymbol{t}}$ values of the minor loops using the created 3D map of $\boldsymbol{\Delta H}$ values. For each AC remagnetization cycle where the value of $\boldsymbol{\Delta H}$ and $\boldsymbol{\Delta T}$ is known, this 3D map can be used to determine the corresponding parameters $\boldsymbol{\Delta B}$ and $\frac{\mathbf{d}\boldsymbol{B}}{\mathbf{d}\boldsymbol{t}}$, which can then be used to retrieve loss data from the 3D loss map as previously in the *3DLMB* method. The problem in defining the parameter $\boldsymbol{\Delta T}$ of asymmetric remagnetization cycles is the same as previously in defining the parameter $\frac{\mathbf{d}\boldsymbol{B}}{\mathbf{d}\boldsymbol{t}}$, and there is a need to determine an equivalent parameter $\boldsymbol{\Delta T}$. Analogous to the definitions of the equivalent $\frac{\mathbf{d}\boldsymbol{B}}{\mathbf{d}\boldsymbol{t}}$ parameters, $\boldsymbol{\Delta T_{eq_1}}$, $\boldsymbol{\Delta T_{eq_2}}$ and $\boldsymbol{\Delta T_{eq_3}}$ are introduced and defined as follows:

$$\boldsymbol{\Delta T_{eq_1} = (T_{loop_e} - T_{loop_s})/2\,,} \tag{7.1}$$

where $\boldsymbol{T_{loop_e}}$ is time of the loop end point and $\boldsymbol{T_{loop_s}}$ time of the loop start point,

$$\boldsymbol{\Delta T_{eq_2} = \frac{\Delta T_{1/2} \cdot \Delta T_{2/2}}{\Delta T_{2/2} \cdot \frac{A_{loop_{1/2}}}{A_{loop_{tot}}} + \Delta T_{1/2} \cdot \left(1 - \frac{A_{loop_{1/2}}}{A_{loop_{tot}}}\right)}} \tag{7.2}$$

where $\boldsymbol{\Delta T_{1/2}}$ and $\boldsymbol{\Delta T_{2/2}}$ are times needed for the completion of the first, i.e., second half of the loop respectively, $\boldsymbol{A_{loop_{1/2}}}$ is the area enclosed by the first half and $\boldsymbol{A_{loop_{tot}}}$ is the total area enclosed by the minor loop,

$$\Delta T_{eq_3} = \frac{\Delta T_{1/2} \cdot \Delta T_{2/2}}{\Delta T_{2/2} \cdot k_e + \Delta T_{1/2} \cdot (1 - k_e)},\ k_e \in [0.35, 0.4] \tag{7.3}$$

where k_e is an empirically determined weighting factor. Using the parameter ΔT_{eq_1} leads to a slight underestimation of the total AC losses, similar to the previous method where the parameter $\left(\frac{dB}{dt}\right)_{eq_1}$ was used as a minor loop parameter. The use of ΔT_{eq_2} is not useful for this method, not even for the reference purpose, as it requires knowledge of the waveform of B, which is in direct contradiction to the basis of this method and will therefore not be considered further. Using the parameter ΔT_{eq_3} gives the best results and the total AC losses calculated with this parameter are shown in the results.

The following steps are performed to complete the mapping process and to calculate the contribution of PWM-induced losses to the total AC losses:

1. Search for the mapped B_{bias} value of the minor loop in the 3D map of ΔH values

   The mapped value of B_{bias} of the minor loop is used to find the closest B_{bias} value available in the 3D map of the ΔH values.Each column in the 3D map of the ΔH values represents a constant value of B_{bias}. Therefore, the index of the found B_{bias} value indicates a column of the 3D loss map (shown inmagentain Figure7.1). This index is the same regardless of the ΔB value, i.e. the sheet of the 3D map.

2.Search for the ΔT_{eq_3} of the minor loop in the 3D map of ΔH values

   The value of ΔB is constant for each sheet of the 3D map of ΔH values. However, the value of $\frac{dB}{dt}$ increases with each row. Since the value of ΔB is constant and the range and resolution of variation of the parameter $\frac{dB}{dt}$ are known, the ΔT parameter of the minor loop can be calculated for each row in the 3D map. Thus, for the particular column defined by the B_{bias}, the ΔT_{eq_3} of the AC minor loop closest to the ΔT of the DC minor loop is searched. The index of the ΔT_{eq_3} value found gives a row of the 3D map of ΔH values, where ΔH value is found that correspond to the specific B_{bias} and $\frac{dB}{dt}$ values of the minor loop. This is done for each sheet, i.e. for each ΔB value available in the 3D map, so that a single ΔH value is found for each sheet in the 3D map (shown incyanin Figure7.1).

3.An array of ΔH values is created

Using the found indices of the columns and rows, the ΔH value is retrieved for each sheet of the 3D map from the locations determined by found indices and a 1D array of the ΔH values is created (shown ascyanvector in Figure7.1).

4.Search for ΔH of the minor loop

The ΔH value of the AC minor loop is searched in the created 1D array of ΔH values and the index of the closest found value indicates the sheet of the 3D map on which this ΔH value is located. Now finally, all three indices of the ΔH position in the 3D map are found.

5.Retrieval of loss data, scaling and summation

The determined position of the ΔH value of the minor loop in the 3D map of the ΔH values matches the position that would otherwise be determined using the the minor loop parameters based on the waveform of B. Therefore, these indices are used to retrieve loss data from the 3D loss map based on the minor loop parameters ΔB, B_{bias} and $\frac{dB}{dt}$. Scaling and summation is performed as for the method *3DLMB*.

7.3 Correspondence between ΔH_{AC} and ΔH_{DC}

In chapter6, the section6.3discusses the problem of comparing minor loops between AC and DC bias measurements. One of the problems is related to the differences in the ΔH values of the minor loops with the same parameters ΔB, $\frac{dB}{dt}$ and B_{bias}.

The method using the H waveform to obtain minor loop data is also affected by this, in two ways. First, when ΔB and $\frac{dB}{dt}$ are retrieved from the 3D map of the ΔH values, and second, when the losses are retrieved from the 3D loss map. The latter is the same as for the previous method, which uses the waveform of B to obtain the minor loop data. The ratio between the ΔH value of the minor loop obtained in the DC bias measurements, ΔH_{DC}, and the ΔH value of the minor loop determined in the AC measurements, ΔH_{AC}, for equal ΔB, $\frac{dB}{dt}$ and B_{bias} parameters of the minor loops, is shown in figure7.3. The ratio is shown for each minor loop and every B_{1hpk} value available from measurements and a switching frequency equal to $f_{sw} = 4$ kHz. The grey area represents the range where $\Delta H_{DC}/\Delta H_{AC}$ of all minor loops is found. As discussed in chapter6, section6.3, the difference in ΔH values between the minor loops

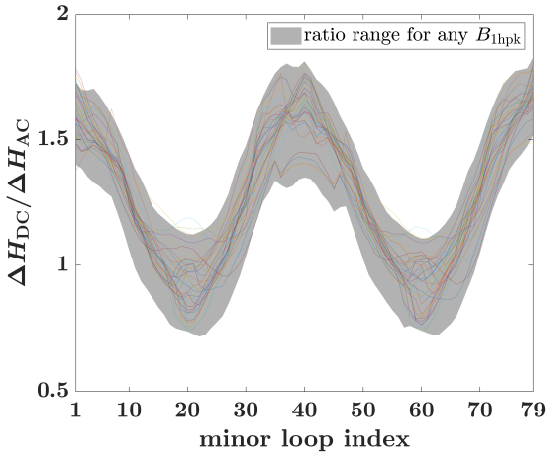

FIGURE 7.3: Ratio between the ΔH values of the remagnetization cycles obtained from AC and DC bias measurements, respectively, plotted for each minor loop of each B_{1hpk} value and a switching frequency of $f_{sw} = 4$ kHz.

from the AC measurements and DC bias is larger for lower values of B_{bias} and almost negligible for higher values of B_{bias}. Since ΔH_{AC} is usually smaller than ΔH_{DC}, the values of ΔB and consequently, and more importantly, $\frac{dB}{dt}$ obtained from the 3D map of ΔH values are underestimated. As a result, the losses obtained from the 3D loss map are underestimated as well.

The subfigure7.4ashows several curves of PWM-induced losses in relation to the B_{1hpk} value. Thebluecurve was obtained using the previous method and is used here as a reference. Theredcurve is the direct result of the loss calculation with this method, without any corrections being made. It is clear to see how much the losses are underestimated. Since the ratio between ΔH_{AC} and ΔH_{DC} is known for each minor loop, corrections can be made to show that it is this difference that leads most to the underestimation of losses. The result is shown as avioletcurve. To show how much the mapping of $H_{bias} - B_{bias}$ affects the final result, the loss calculations were further corrected by using the measured values of B_{bias} instead of the mapped values, which is shown asgreencurve in the subfigure7.4a.

The ratio between ΔH_{AC} and ΔH_{DC} is known, as both AC and DC bias measurements were performed for the purpose of this research. However, this ratio would not have been known otherwise. For this reason, the calculation results obtained using this correction can only serve as a reference and confirmation of the theory of the method. However, based on the known ratio for each minor loop, a correction factor can be

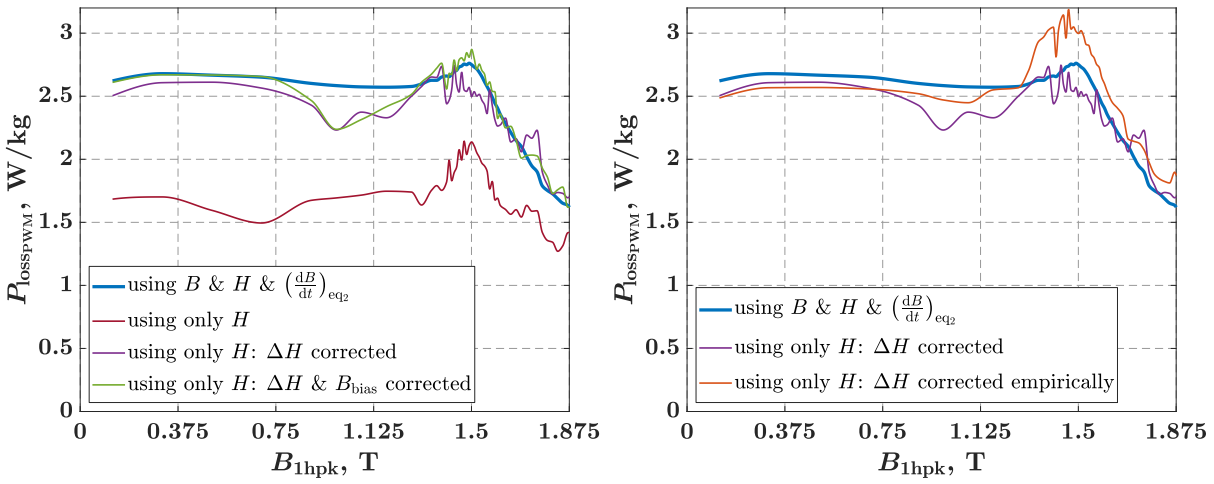

(A) (B)

FIGURE 7.4: Comparison of calculated PWM-induced loss curves.

determined empirically and used to compensate for ΔH differences between AC and DC bias measurements. The subfigure7.4bshows the results of the loss calculation using the empirically determined factor $n = 1.3$ for the compensation of ΔH differences.

It has been shown that the factor $n = 1.3$ is valid for all tested switching frequencies between 2 and 16 kHz and for all cores used in this research. However, since all cores were made of the same laminated ferromagnetic material M400-50A, further investigation of the relationship between this factor and the material type is required.

Chapter 8

Discussion and Results of the Proposed Methods

In this chapter, the results of the proposed methods and approaches are presented and evaluated. The advantages and shortcomings as well as possible future improvements are also discussed. The chapter is divided into five sections, with the first two sections referring to the *3DLMB* method with *MLL* and *TACL* approach respectively, the third section to the *3DLMH* method and the fourth section to a general evaluation of the proposed methods. The fifth section gives a short reference to the possible issues with the further application of the proposed methods to the electrical machines.

8.1 Results of PWM-induced losses calculation using 3DLMB method and MLL approach

This section presents the results of the loss calculations using the *3DLMB* method and the *MLL* approach, which means that minor loops were considered as part of the main cycle. The flux density waveform $\boldsymbol{B}$ used for the calculations was obtained from the AC measurements. Figure8.1shows the comparison between calculated and measured PWM-induced minor loop losses. The calculated curve of the minor loop losses is the result of the proposed method, while the measured curve of the minor loop losses comes from the AC measurements, from which the quasi-sinusoidal losses were subtracted. The loss curves are plotted as a function of the $\boldsymbol{B_{1hpk}}$ value and for different switching frequencies.

By looking at the curves comparisons, overall conclusion can be made that the calculated losses always slightly overshoot the measured losses, regardless of the switching frequency. Another general conclusion can be made about the change in

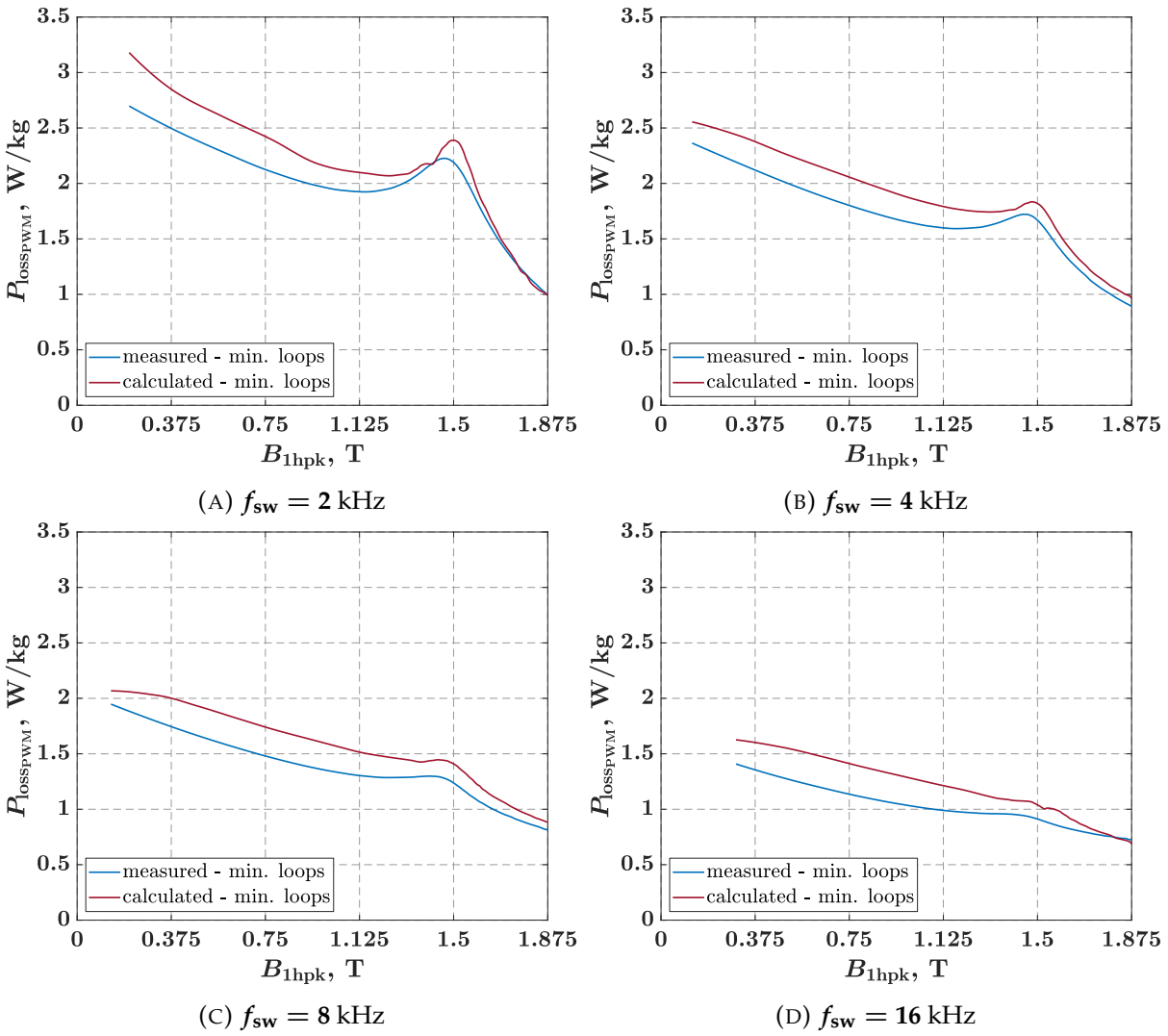

(A) $f_{\mathbf{sw}} = \mathbf{2}$ kHz

(B) $f_{\mathbf{sw}} = \mathbf{4}$ kHz

(C) $f_{\mathbf{sw}} = \mathbf{8}$ kHz

(D) $f_{\mathbf{sw}} = \mathbf{16}$ kHz

FIGURE 8.1: Comparison of the calculation results with measurements of the losses of the minor loops with respect to the $\boldsymbol{B_{1\text{hpk}}}$, shown for different switching frequencies.

difference in the relation to the $\boldsymbol{B_{1\text{hpk}}}$ value: losses generally differ less at higher $\boldsymbol{B_{1\text{hpk}}}$ values. This can be also observed in figure8.2where ratio and difference between calculated and measured curves is shown.

The main cause for the difference in calculated losses is the discrepancy between the $\boldsymbol{\Delta H}$ values of the minor loops obtained from AC and DC bias measurements, respectively. As shown in chapter6, section6.3, the impact of the discrepancy between $\boldsymbol{\Delta H_{\text{AC}}}$ and $\boldsymbol{\Delta H_{\text{DC}}}$ decreases with the increase of $\boldsymbol{B_{\text{bias}}}$. The number of minor loops with higher values of the parameter $\boldsymbol{B_{\text{bias}}}$ increases with the peak value of the fundamental $\boldsymbol{B_{1\text{hpk}}}$. For example, the number of minor loops formed at $\boldsymbol{B_{\text{bias}}}$ values greater than

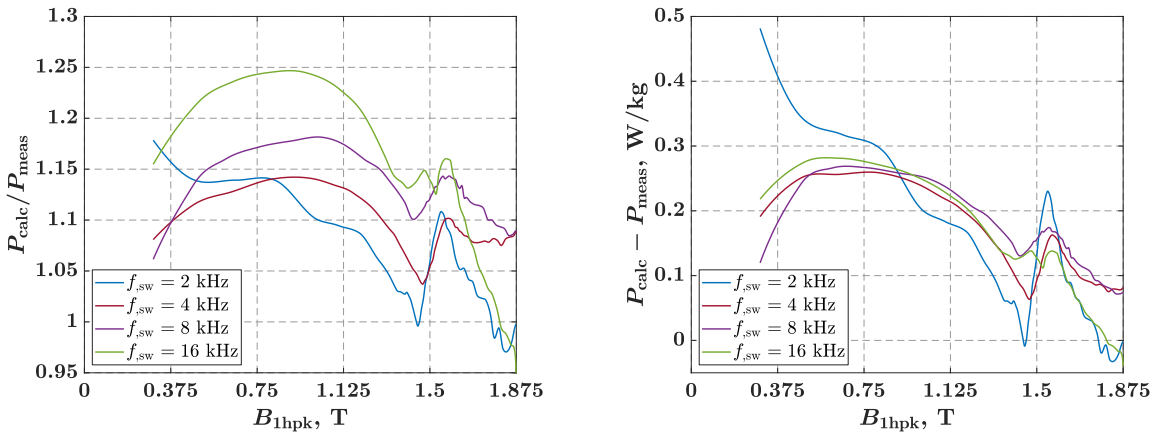

(A) Losses ratio

(B) Losses difference

FIGURE 8.2: Ratio and difference between calculated results and measurements of minor loop losses with respect to $\boldsymbol{B_{1hpk}}$, shown for different switching frequencies. Note the difference in the scaling of the Y-axis between subfigures.

1 T is about 60 % for $\boldsymbol{B_{1hpk}} = \mathbf{1.7}$ T, about 50 % for $\boldsymbol{B_{1hpk}} = \mathbf{1.4}$ T, about 40 % for $\boldsymbol{B_{1hpk}} = \mathbf{1.2}$ T and about 8 % for $\boldsymbol{B_{1hpk}} = \mathbf{1.05}$ T. Therefore, the errors in the loss calculation are slightly lower for higher values of $\boldsymbol{B_{1hpk}}$, as more of the total number of minor loops are then formed at higher values of $\boldsymbol{B_{bias}}$, where the errors due to the discrepancy of $\boldsymbol{\Delta H}$ are lower. Part of the difference between calculated and measured losses is attributed to the inadequate parameter $\frac{\mathbf{d}B}{\mathbf{d}t}$ of the minor loop, but to a much lesser extent.

The effect of the switching frequency on the losses can be assessed in figure8.2by means of two subfigures: one shows the ratio and the other the difference between calculated and measured losses. When assessing the influence of the switching frequency on the loss calculation, it must be taken into account that the total PWM-induced losses decrease with an increase of $\boldsymbol{f_{sw}}$. For this reason, the same difference between the loss curves leads to a higher ratio between them. This can be seen in subfigure8.2a, where in general the ratio between calculated and measured losses increases with $\boldsymbol{f_{sw}}$, while in subfigure8.2b, with some exceptions, no significant difference between the curves can be observed.

As already mentioned, the *MLL* approach of the method *3DLMB* has no practical application in the calculation of PWM-induced losses in the design phase of the electrical machine. However, it served here as a confirmation of the basis of the proposed method.

The results presented show that it is valid to determine the minor loops in terms of the parameters ΔB, $\frac{dB}{dt}$ and B_{bias} and that the use of a 3D look-up map of the losses obtained from DC bias measurements is justified for retrieving loss data.

8.2 Results of PWM-induced losses calculation using 3DLMB method and TACL approach

This section presents the results of the loss calculations using the *3DLMB* method and the *TACL* approach. The flux density waveform B used for the calculations were obtained from the AC measurements. The calculations were performed using the *TACL* approach, which means that the minor loops were considered independently from the main cycle. Three different values of the equivalent parameter $\frac{dB}{dt}$ were used for the calculations and their results are shown as separate loss curves in the figures. Total AC losses were calculated as a sum of total PWM-induced losses, which are result of the method calculations, and sine induced losses, that are determined using quasi-sinusoidal excitation. All power loss curves determined by calculations are compared with the measured power loss curve, which serves as a reference for the actual losses in the core.

The results of the calculations are shown for the cores C1a, C2a and C3 used in the research. 3D loss maps were created for each of the cores and, depending on the core, the corresponding 3D map was used to perform the calculations.

Figure8.3shows the power loss curves as a result of the *3DLMB* method for several switching frequencies. The use of equation6.2to calculate the equivalent parameter $\frac{dB}{dt}$, i.e. $\left(\frac{dB}{dt}\right)_{eq_1}$, leads to an overestimation of $\frac{dB}{dt}$ values for lower values of B_{1hpk} and to an underestimation of $\frac{dB}{dt}$ values for higher values of B_{1hpk}. Consequently, the calculated PWM-induced losses are overestimated for lower B_{1hpk} and underestimated for higher B_{1hpk}, and this is true regardless of the switching frequency. Therefore, the overall trend of the loss curve calculated in this way is somewhat less steep than for the measured loss curve. This can also be observed in subfigure8.4a, which shows the ratio between calculated and measured losses for all four switching frequencies. The general downward trend of all ratio curves can be seen.

The parameter $\left(\frac{dB}{dt}\right)_{eq_2}$, obtained using the equation6.3, is the best representation of the equivalent parameter $\frac{dB}{dt}$. This can be seen in figure8.3, where the best agreement

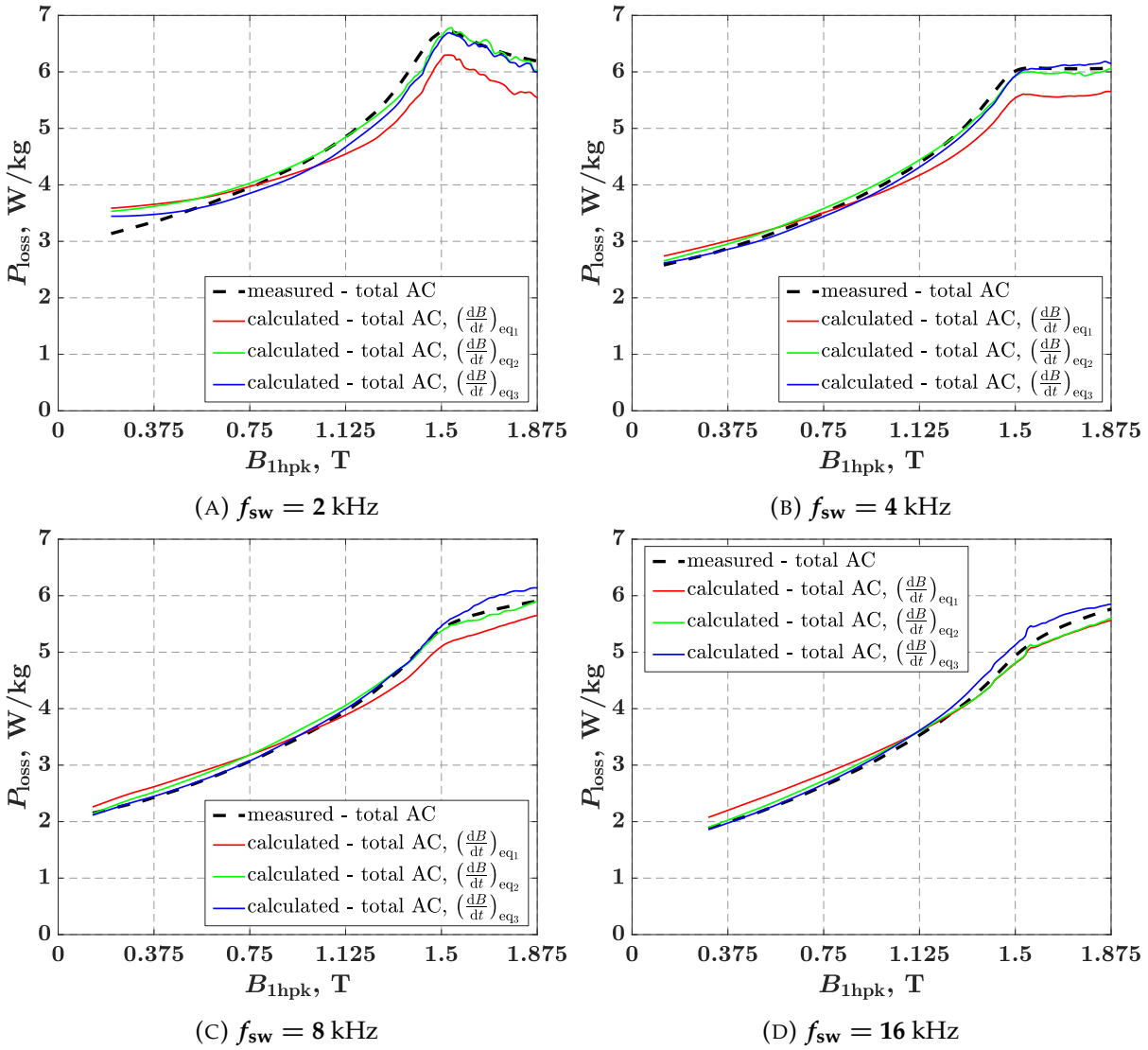

(A) $f_{sw} = 2$ kHz (B) $f_{sw} = 4$ kHz

(C) $f_{sw} = 8$ kHz (D) $f_{sw} = 16$ kHz

FIGURE 8.3: Comparison between the calculation results of the *3DLMB* method and measurements of the total AC losses with respect to B_{1hpk}, shown for core C1a and different switching frequencies.

between calculated and measured loss curve is obtained when the parameter $\left(\frac{dB}{dt}\right)_{eq_2}$ was used to calculate the losses. The best agreement is also confirmed with the smallest ratio values between calculated and measured losses, shown in subfigure8.4b. However, as explained in chapter6, section6.3, the calculation with this equivalent parameter is for reference only, as the actual waveform of B would need to be known to determine this parameter. Instead, $\left(\frac{dB}{dt}\right)_{eq_3}$ is defined, which is calculated with an empirically determined factor based on the data of $\left(\frac{dB}{dt}\right)_{eq_2}$, using equation6.4. The power losses

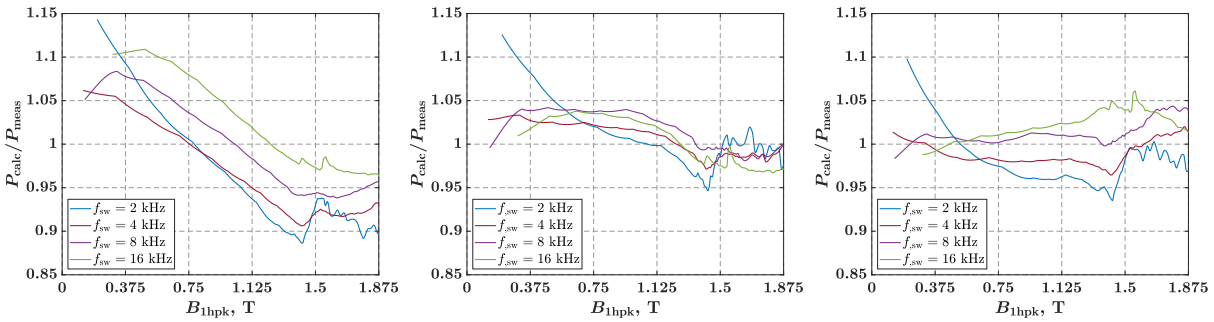

(A) $\frac{dB}{dt} = \left(\frac{dB}{dt}\right)_{eq_1}$ (B) $\frac{dB}{dt} = \left(\frac{dB}{dt}\right)_{eq_2}$ (C) $\frac{dB}{dt} = \left(\frac{dB}{dt}\right)_{eq_3}$

FIGURE 8.4: Ratio between calculated results of the *3DLMB* method and measurements of total AC losses with respect to B_{1hpk}, shown for the core C1a, different switching frequencies and three differently calculated equivalent values of $\frac{dB}{dt}$ parameter.

calculated with this equivalent parameter show good agreement with the measured losses. A single value of the empirically determined factor is used to calculate the PWM-induced losses regardless of B_{1hpk} and f_{sw} values, resulting in a discrepancy between the curves, given by $\left(\frac{dB}{dt}\right)_{eq_2}$ and $\left(\frac{dB}{dt}\right)_{eq_3}$, at certain ranges of B_{1hpk} or at a certain switching frequency f_{sw}. Adjusting the empirical factor k_e with respect to B_{1hpk} and f_{sw} would give better results, but there was no basis for how to define this dynamic value of k_e. Further investigation of the relationship between these parameters and possible quantification of this relation is needed. Nevertheless, it is shown here that even with use of single value of factor k_e, satisfactory results can be obtained.

Figure8.4was already mentioned in the relation to the observing different values of ratio of calculated to measured losses depending on the different equivalent parameters of $\frac{dB}{dt}$. However, this figure also presents how switching frequency effects this ratio, i.e. how does error in calculation of the losses depend on the f_{sw}.

Although difference between power loss curves for different switching frequencies obviously exists, it does not have a significant effect on the results nor can a certain pattern be determined. By observing these curves of calculated to measured ratio it may seem at first that for some of the switching frequencies the calculated losses deviate more i.e. less respectively. However, apart from some exceptions, only the range at which this ratio is found changes between different switching frequencies.

Looking at the ratio curves in the subfigure8.4b, one can conclude that apart from the obvious exception for the $f_{sw} = 2$ kHz curve at lower B_{1hpk}, no pattern can be detected to describe the change in the curves as a function of f_{sw}, and it appears that this difference between the curves is random. This is not to be understood as a statement

that changing the switching frequency has no effect on the loss origin, but that all effects change in such a way that the final result is not affected. Since using the parameter $\left(\frac{\mathbf{d}B}{\mathbf{d}t}\right)_{\mathbf{eq_2}}$ in the loss calculation gives the most accurate results, these curves can be used as a reference. Larger differences in the ratio curves for the other two cases are therefore not due to the direct influence of the switching frequency, but to the dependence of equivalent parameter values on the switching frequency.

In general, it can be noticed that in all cases, regardless of the equivalent $\frac{\mathbf{d}B}{\mathbf{d}t}$ and $f_{\mathbf{sw}}$, the most sensitive region is around the value of $B_{\mathbf{1hpk}}$ between 1.4 and 1.6 T, where, as shown earlier, the PWM-induced losses contribute most to the losses. However, it should be noted that this range is not around this value of $B_{\mathbf{1hpk}}$ because of the PWM-induced voltage, but because of the properties of this particular ferromagnetic material. Near this range, tiny deviations of any of the minor loop parameters from the actual loop parameters can lead to a relatively large difference in the calculation of iron losses. In addition, the loss values interpolated to create the 3D loss map may vary more in this range, which can also affect the calculation of the final loss values, especially if the loop parameters are searched for in the space of the 3D loss map, where the values are largely determined by interpolation. Finally, this is also the area where one finds highly distorted and unclosed minor loops, as shown in the figure6.16, especially at the lower switching frequencies.

The power loss curve for a switching frequency of 2 kHz is somewhat worse in terms of errors in loss calculation, especially at lower values of $B_{\mathbf{1hpk}}$ and in a range of $B_{\mathbf{1hpk}}$ values where PWM-induced losses contribute most to the total losses. In general, the lower the switching frequency, the longer the duration of the minor loops, provided the frequency of the fundamental remains unchanged. This means that the minor loop is more affected by slide of the $B_{\mathbf{bias}}$ value during its creation. Furthermore, and for the same reason, the ΔB values of the minor loops are higher at lower $f_{\mathbf{sw}}$. Thus, when $B_{\mathbf{bias}}$ is found in the non-linear region of the normal magnetization curve, this leads to a greater deformation of the shape of the minor loops compared to the loops with lower ΔB values. Finally, and this refers only to the results of this research, the values of ΔB obtained from the AC measurements are in the range of the extrapolated values of ΔB in the created 3D loss map. The maximum ΔB value for which DC bias measurements were made is 120 mT, and the ΔB values from the AC measurements at $f_{\mathbf{sw}} = \mathbf{2}$ kHz are up to 155 mT. This has the greatest effect on the calculation of losses at low values of $B_{\mathbf{1hpk}}$, where all the minor loops formed over a single main cycle have virtually the same duty cycle value near $D = \mathbf{0.5}$, at which the minor loops have the highest ΔB

values. For example, all 39 minor loops formed over the main cycle with $\boldsymbol{B_{1hpk}} \approx \mathbf{0.2}$ T have a $\boldsymbol{\Delta B}$ value of $\approx \mathbf{150}$ mT.

The mentioned effects are reduced as the switching frequency increases, i.e. $\boldsymbol{f_{sw}/f_{1h}}$ ratio increases. However, a different problem arises. The $\frac{\mathbf{d}\boldsymbol{B}}{\mathbf{d}\boldsymbol{t}}$ have a great influence on the loss calculation. Slight changes in this parameter can lead to significant changes in the loss calculation. The $\boldsymbol{\Delta T}$ of the minor loops is measured in microseconds, which is also the smallest time quantum determined by measurements. Therefore, if the switching frequency increases and the duration of the minor loops decreases, a single microsecond difference will have larger impact on the loss calculation at a higher switching frequency.

When considering the relationship between calculated and measured losses, one must also take into account that as the switching frequency increases, the total AC losses decrease. With the same difference between the calculated and the measured loss curve, the ratio is therefore higher at higher switching frequencies.

As for core C1a, figures8.5and8.7show the power loss curves as a result of the *3DLMB* method at different switching frequencies and for cores C2a and C3, respectively. The ratios between calculated and measured losses for three different values of the equivalent parameter $\frac{\mathbf{d}\boldsymbol{B}}{\mathbf{d}\boldsymbol{t}}$ and different switching frequencies are shown in figures8.6 and8.8for cores C2a and C3, respectively.

The results in these figures are not analysed in detail here, as all the effects mentioned for core C1a also apply to cores C2a and C3. In general, the results presented show good agreement between the calculated and measured power loss curves. However, it can be observed that the errors in determining the loss curves for core C3 are higher for lower values of $\boldsymbol{B_{1hpk}}$ and $\boldsymbol{f_{sw}}$. This is partly due to the larger difference between the values of $\boldsymbol{\Delta H_{AC}}$ and $\boldsymbol{\Delta H_{DC}}$ and partly due to the larger error in extrapolating the DC bias measurement results. The same would be expected for core C2a, but for the same reasons of error in extrapolation, the loss values in the 3D loss map for such loop parameters were initially negative. This was later corrected to zero values.

Problems with extrapolation arose here with cores that were much smaller in volume and mass than core C1a, for which smaller values for excitation current and search voltage had to be measured. The total losses were greater per unit mass, but the absolute values of the measured losses were smaller. This resulted in a larger measurement uncertainty, especially for smaller values of $\boldsymbol{B_{bias}}$. Combined with the relatively large difference between the maximum $\boldsymbol{\Delta B}$ (120 mT) for which measurements were made

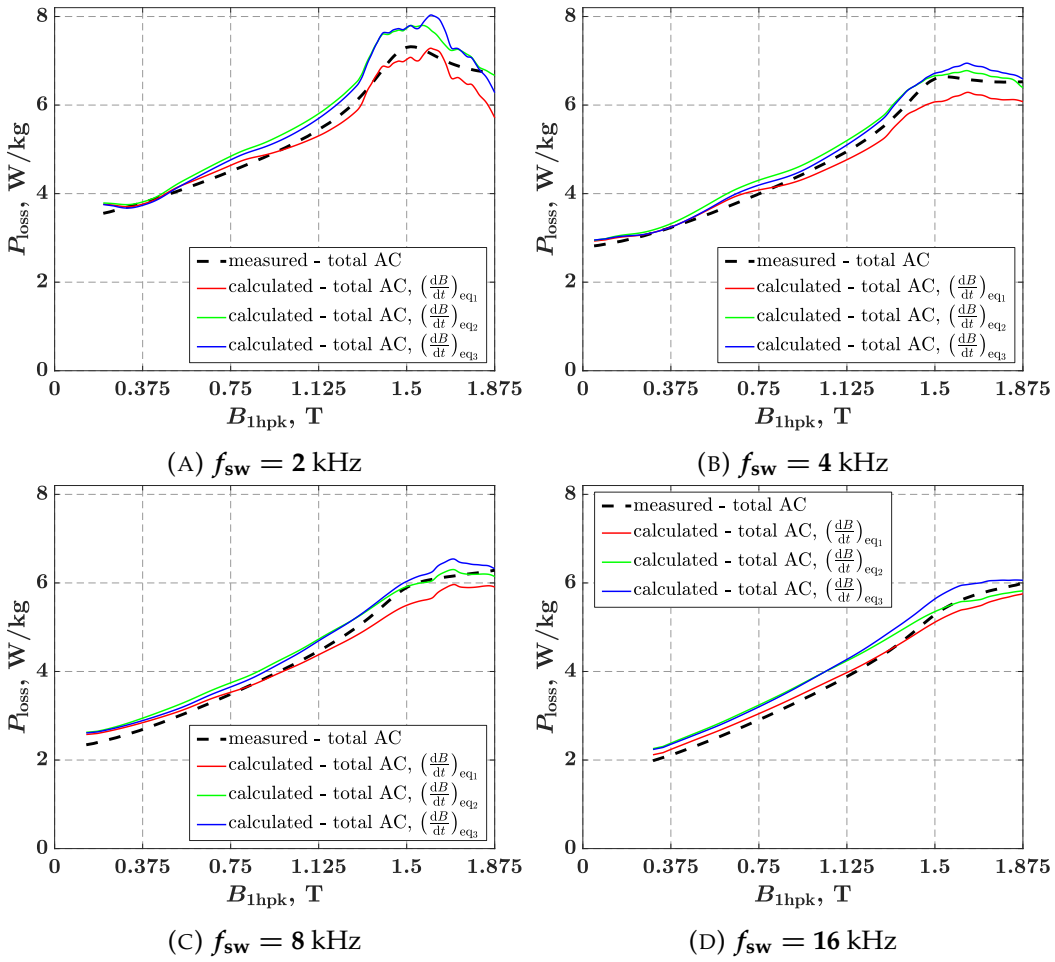

(A) $f_{\mathbf{sw}} = \mathbf{2}$ kHz (B) $f_{\mathbf{sw}} = \mathbf{4}$ kHz

(C) $f_{\mathbf{sw}} = \mathbf{8}$ kHz (D) $f_{\mathbf{sw}} = \mathbf{16}$ kHz

FIGURE 8.5: Comparison between the calculation results of the *3DLMB* method and measurements of the total AC losses with respect to $\boldsymbol{B_{1\mathrm{hpk}}}$, shown for the core C2a and different switching frequencies.

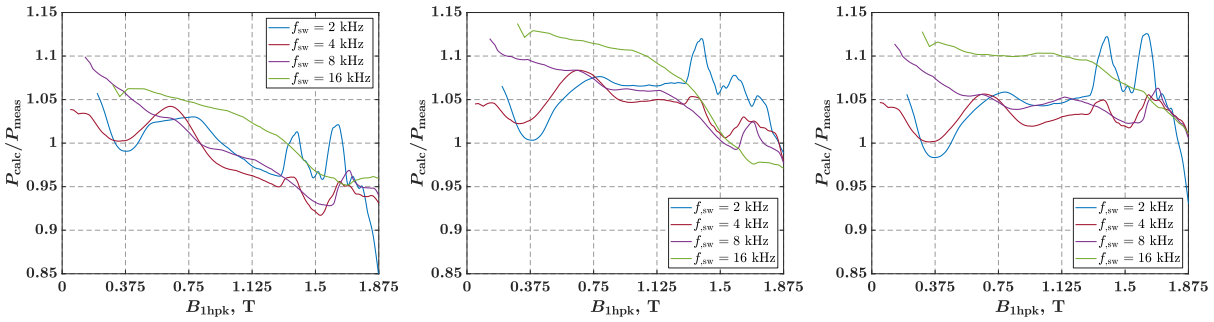

(A) $\frac{\mathbf{d}B}{\mathbf{d}t} = \left(\frac{\mathbf{d}B}{\mathbf{d}t}\right)_{\mathbf{eq_1}}$ (B) $\frac{\mathbf{d}B}{\mathbf{d}t} = \left(\frac{\mathbf{d}B}{\mathbf{d}t}\right)_{\mathbf{eq_2}}$ (C) $\frac{\mathbf{d}B}{\mathbf{d}t} = \left(\frac{\mathbf{d}B}{\mathbf{d}t}\right)_{\mathbf{eq_3}}$

FIGURE 8.6: Ratio between calculated results of the *3DLMB* method and measurements of total AC losses with respect to $\boldsymbol{B_{1\mathrm{hpk}}}$, shown for the core C2a, different switching frequencies and three differently calculated equivalent values of $\frac{\mathbf{d}B}{\mathbf{d}t}$ parameter.

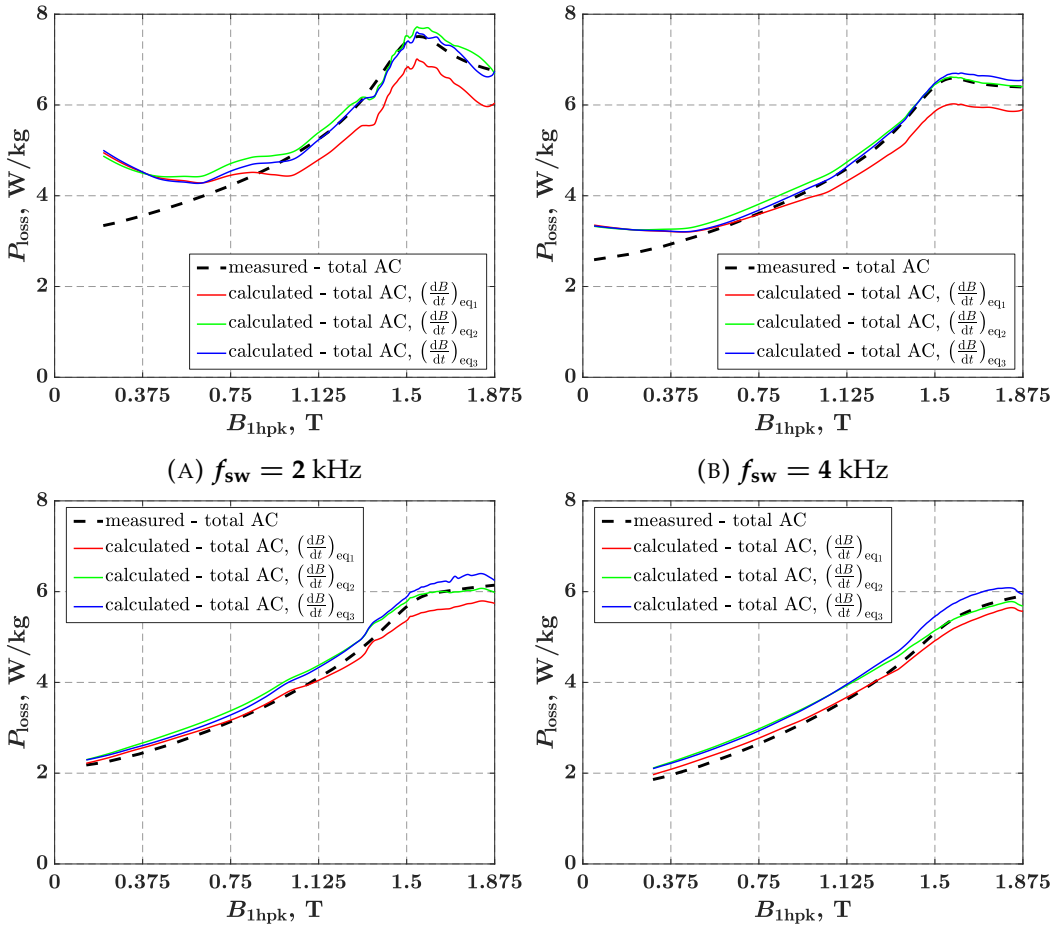

(A) $f_{\text{sw}} = 2$ kHz (B) $f_{\text{sw}} = 4$ kHz

(C) $f_{\text{sw}} = 8$ kHz (D) $f_{\text{sw}} = 16$ kHz

FIGURE 8.7: Comparison between the calculation results of the *3DLMB* method and measurements of the total AC losses with respect to B_{1hpk}, shown for the core C3 and different switching frequencies.

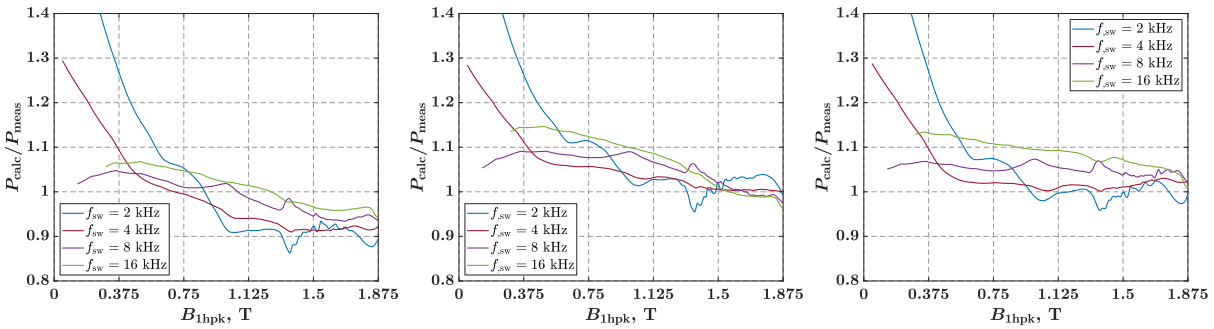

(A) $\frac{dB}{dt} = \left(\frac{dB}{dt}\right)_{\text{eq}_1}$ (B) $\frac{dB}{dt} = \left(\frac{dB}{dt}\right)_{\text{eq}_2}$ (C) $\frac{dB}{dt} = \left(\frac{dB}{dt}\right)_{\text{eq}_3}$

FIGURE 8.8: Ratio between calculated results of the *3DLMB* method and measurements of total AC losses with respect to B_{1hpk}, shown for the core C3, different switching frequencies and three differently calculated equivalent values of $\frac{dB}{dt}$ parameter.

and the maximum $\boldsymbol{\Delta B}$ (155 mT) determined from the AC measurements, this led to larger errors in the extrapolated loss values.

The effects of core non-uniformity and laser cutting on PWM-induced losses and losses in general need further investigation. However, the results presented show that the proposed method and algorithm can be applied to three different cores for which separate measurements have been made and separate 3D loss maps created. This is further evidence of the basis of this method, the results of the measurements performed and the applicability of the algorithm to different sets of input data.

There are several critical parts of this method where one can find the causes for the difference between the measured and calculated losses:

1.DC bias measurements
2.Measurement data resolution, range and interpolation
3. Comparison between minor loops obtained from AC and DC bias measurements

As for the DC bias measurements, the measurement errors and uncertainties could lead to slight errors in the loss calculations of the minor loops formed under DC bias field. The measurement equipment, minor temperature variations, the direction of DC bias, etc., could easily affect the final result. Moreover, the basic principle of the proposed setup is the use of a single excitation winding: both the DC bias voltage and the ripple causing the minor loops are generated with a single winding. The AC waveforms generated in this way deviate slightly from the ideal triangular shape and tend toward the saw shape as the $\boldsymbol{B_{bias}}$ increases. This also affects the calculated losses.

Regarding the second point, the data collected by performing DC bias measurements are crucial for creation of the 3D loss map and consequently for calculating PWM-induced losses. Issues such as low resolution of the collected data or differences in the ranges of the minor loop parameters available in the 3D loss map compared to the actual measured minor loop can have a significant impact on the loss calculations. Finally, the measured data should be collected in such a way that the interpolation method have minimal impact on the loss values that lie between two values actually determined by measurements. Nevertheless, the effects of interpolation and extrapolation will always remain a potential error factor.

Regarding the third point, because of the different magnetic conditions in the core, a comparison of the parameters of the minor loops between the AC and DC measurements is not fully possible. The minor loop in the DC bias measurements is basically the main cycle loop orbiting around the fixed $\boldsymbol{B_{bias}}$ with a frequency equal to the inverter

switching frequency. The inverter switch duty cycle is also fixed and nearly symmetric; it does become asymmetric at higher $\boldsymbol{B_{bias}}$ values, however to a much lesser extent than some of the loops that occur under AC excitation. On the other hand, minor loops formed under AC excitation form in the presence of constantly time varying low-frequency harmonic components, resulting in deformation compared to ideal conditions. In addition, low duty cycle values combined with a low $\boldsymbol{L_m/R_i}$ constant of the core equivalent model lead to strongly asymmetric minor loops. All this means that not all parameters of the compared minor loop are the same and therefore some error in the loss calculation is to be expected when this comparison is used as the basis of the method. The two main discrepancies that lead to errors in the calculation of losses in the means of the strength of an impact on the final result can be stated as follows: discrepancy in the $\boldsymbol{\Delta H}$ values between the minor loops obtained from AC and DC bias measurements, and the discrepancy between the $\frac{\mathbf{d}\boldsymbol{B}}{\mathbf{d}\boldsymbol{t}}$ parameter of the DC bias minor loop and the equivalent $\frac{\mathbf{d}\boldsymbol{B}}{\mathbf{d}\boldsymbol{t}}$ parameter of a AC minor loop.

8.3 Results of PWM-induced losses calculation using 3DLMH method and TACL approach

This section presents the results of the loss calculations using the *3DLMH* method and the *TACL* approach. The waveform of the magnetic field strength $\boldsymbol{H}$, obtained from the AC measurements, is used for the loss calculations. The calculations were performed using the *TACL* approach, which means that the minor loops were considered independently of the main cycle. As a result of this method, a single power loss curve is presented, which is the sum of the total PWM-induced losses resulting from the calculations of the method and the sinusoidally induced losses determined with a quasi-sinusoidal excitation. The PWM-induced losses were determined with the empirical factor $\boldsymbol{n = 1.3}$ for the compensation of the $\boldsymbol{\Delta H}$ differences between AC and DC bias measurements. Other results of the method obtained without correction of the $\boldsymbol{\Delta H}$ value or with corrections of $\boldsymbol{\Delta H}$ using the known ratio of $\boldsymbol{\Delta H_{AC}}$ to $\boldsymbol{\Delta H_{DC}}$ are not presented here as they are not relevant for the evaluation of this method.

The calculated power loss curves are shown in the figure8.9for core the C1a and several different switching frequencies. The loss curves are compared with the measured loss curve, which serves as a reference for the actual losses in the core, and the ratio between the calculated and measured loss curves is shown in figure8.10. The calculated

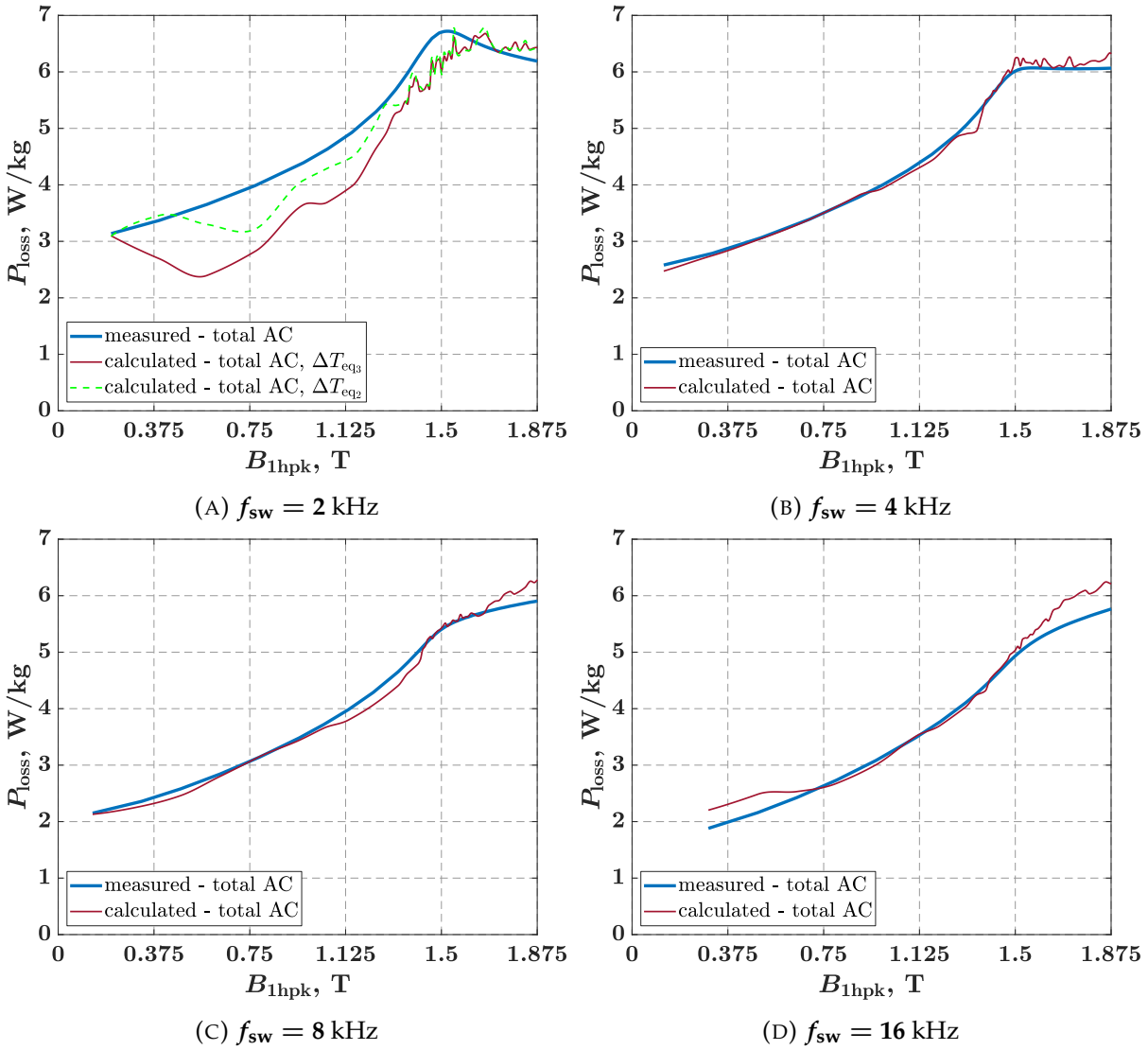

(A) $f_{sw} = 2$ kHz (B) $f_{sw} = 4$ kHz

(C) $f_{sw} = 8$ kHz (D) $f_{sw} = 16$ kHz

FIGURE 8.9: Comparison between the calculation results of the *3DLMH* method and measurements of the total AC losses with respect to B_{1hpk}, shown for the core C1a and different switching frequencies.

loss curves agree well with the measured loss curves, except for the switching frequency of $f_{sw} = 2$ kHz, where the calculated losses are significantly underestimated, especially for smaller values of B_{1hpk}. One of the main reasons for this is the wrong value of the equivalent parameter ΔT of the loop, which was determined with the equation7.3and the empirical factor value of $k_e = 0.35$. In the subfigure8.9a, a significant improvement can be seen when the power loss curve was calculated with the parameter ΔT_{eq_2} (see equation7.2). The rest of the difference is partly due to the underestimated ΔH values, i.e. the value of the empirical factor n, which should be set to a higher value for a

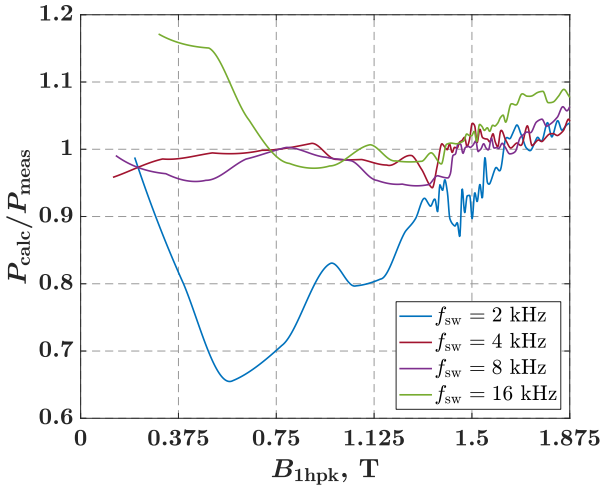

FIGURE 8.10: Ratio between the calculated results of the *3DLMH* method and the measurements of total AC losses with respect to $\boldsymbol{B_{1hpk}}$, shown for the core C1a and different switching frequencies. The results were calculated with corrected values of $\boldsymbol{\Delta H}$ using the empirically determined factor $\boldsymbol{k}$.

$\boldsymbol{f_{sw} = 2}$ kHz excitation. Finally, the remapped value of $\boldsymbol{B_{bias}}$ have some effect on the calculated loss curve as well.

The equivalent $\boldsymbol{\Delta T}$ parameter, the $\boldsymbol{\Delta H}$ correction and the remapped values of $\boldsymbol{B_{bias}}$ also affect the loss calculations at higher values of the switching frequencies, but with much less impact on the final results. Apart from these effects on the losses, as with the *3DLMB* method, errors in the measurement of DC bias and errors related to the resolution of the measurement data, range and interpolation also have an impact on the final results. For the purpose of this research only, two 3D maps had to be created to apply this method, which further increases the uncertainty in the calculation of the losses. Considering all this, the results of the loss calculations using the *3DLMH* method are more than satisfactory.

The results are only presented for core C1a, as it has already been shown that the *3DLMB* method can also be applied to the other cores and how it affects the results. The basic principle of both methods is the same, the difference lies only in the available input data. Therefore, only the validity of using the $\boldsymbol{H}$ waveform as input data is tested here, while the rest has already been evaluated for the *3DLMB* method.

8.4 Evaluation of the proposed methods and final observations

The calculation of PWM-induced losses is nowadays recognized as a research area of growing interest, and several research groups are working intensively on the possible methods and solutions. There are no reports in the literature that it has been possible to obtain a useful model for the calculation of PWM-induced losses using FEA simulations and a dynamic hysteresis loop model that can be applied to the current and flux waveforms as a whole. Instead, based on the measurements performed on the simple core, dynamic Jiles-Atherton (J-A) model parameters for minor loops are determined as a function of the $\boldsymbol{B}_{\mathbf{bias}}$, $\boldsymbol{f}_{\mathbf{sw}}$, and $\boldsymbol{\Delta B}$ parameters of the loop [9,10]. Determined J-A models are then used to calculate the contribution of each minor loop separately using FEA simulation.

The two methods proposed in this research, the *3DLMB* and *3DLMH* methods, are based on a different principle: comparing the parameters of the minor loops formed under AC excitation with the parameters of the minor loops obtained by DC bias measurements. The idea behind the methods is that the data on the AC formed minor loops should be obtained by simulations on the machine model, while the data on the DC minor loops should be obtained by DC bias measurements on the ring core sample made of ferromagnetic material intended for the build of the machine. Then, by comparing the loop parameters, the loss data can be retrieved from the 3D loss map and the contribution of the PWM-induced losses to the total AC losses can be calculated at the design stage. The difference between the methods lies in the parameters of the minor loops that are being compared: in the *3DLMB* method, the parameters $\boldsymbol{\Delta B}$, $\frac{\mathbf{d}\boldsymbol{B}}{\mathbf{d}t}$ and $\boldsymbol{B}_{\mathbf{bias}}$ are compared, while the *3DLMH* method compares the parameters $\boldsymbol{\Delta H}$, $\frac{\mathbf{d}\boldsymbol{H}}{\mathbf{d}t}$ and $\boldsymbol{H}_{\mathbf{bias}}$. Thus, in order to classify minor loops based on these parameters, one needs to know either the flux density waveform $\boldsymbol{B}$ or the magnetic field strength $\boldsymbol{H}$ for each finitely small point or region of the machine, depending on which method one wants to use. The driving force for developing two methods is explained in detail in following paragraphs.

Assuming that the supply parameters of the inverter are known for a given operating point of the machine, the current waveform including ripple can be determined using a non-linear dynamic machine model based on flux-current maps [51,52]. This current can then be used as an excitation waveform in current-driven FEA simluations. In the initial stages of the research, it was assumed that the current-driven FEA simulation

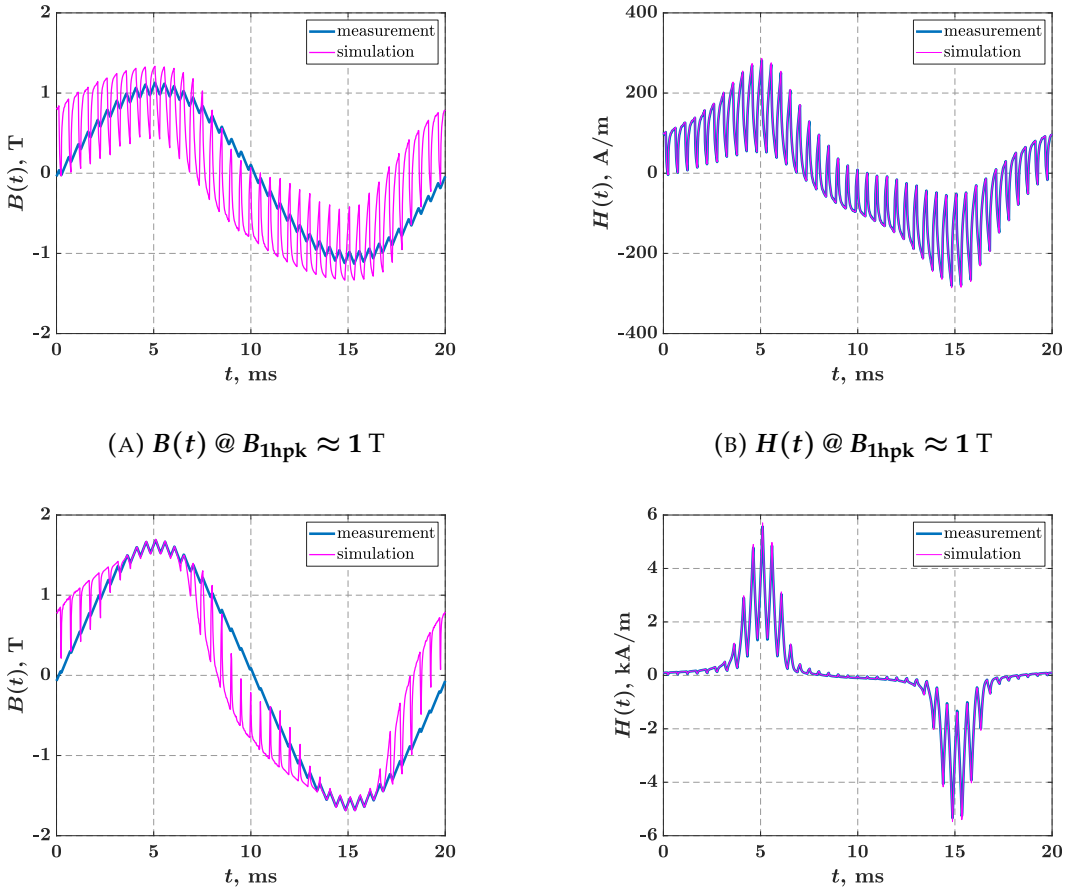

(A) $B(t)$ @ $B_{1hpk} \approx 1$ T

(B) $H(t)$ @ $B_{1hpk} \approx 1$ T

(C) $B(t)$ @ $B_{1hpk} \approx 1.6$ T

(D) $H(t)$ @ $B_{1hpk} \approx 1.6$ T

FIGURE 8.11: Comparison of the waveforms of $\boldsymbol{B}$ and $\boldsymbol{H}$ obtained from AC measurements with the simulation results of the current-driven FEA simulation, shown for the C1a core, $f_{sw} = 2$ kHz and two different B_{1hpk} values.

would result in a flux density waveform necessary for obtaining minor loop data and calculating PWM-induced losses using the proposed *3DLMB* method and its algorithm. However, initial attempts to confirm this assumption on the FEA model of core C1a showed that the ripple of the flux density waveform $\boldsymbol{B}$ largely did not match the measured ripple when the current obtained form AC measurements was used as an excitation. Figures8.11and8.12show the comparison of the flux density $\boldsymbol{B}$ and magnetic field strength $\boldsymbol{H}$ waveforms obtained from the AC measurements with the results of the current-driven FEA simulations. The comparison is shown for two different values of the peak of the fundamental waveform of the flux density B_{1hpk} and two different values of the switching frequency f_{sw}. From these figures, it can be seen that the

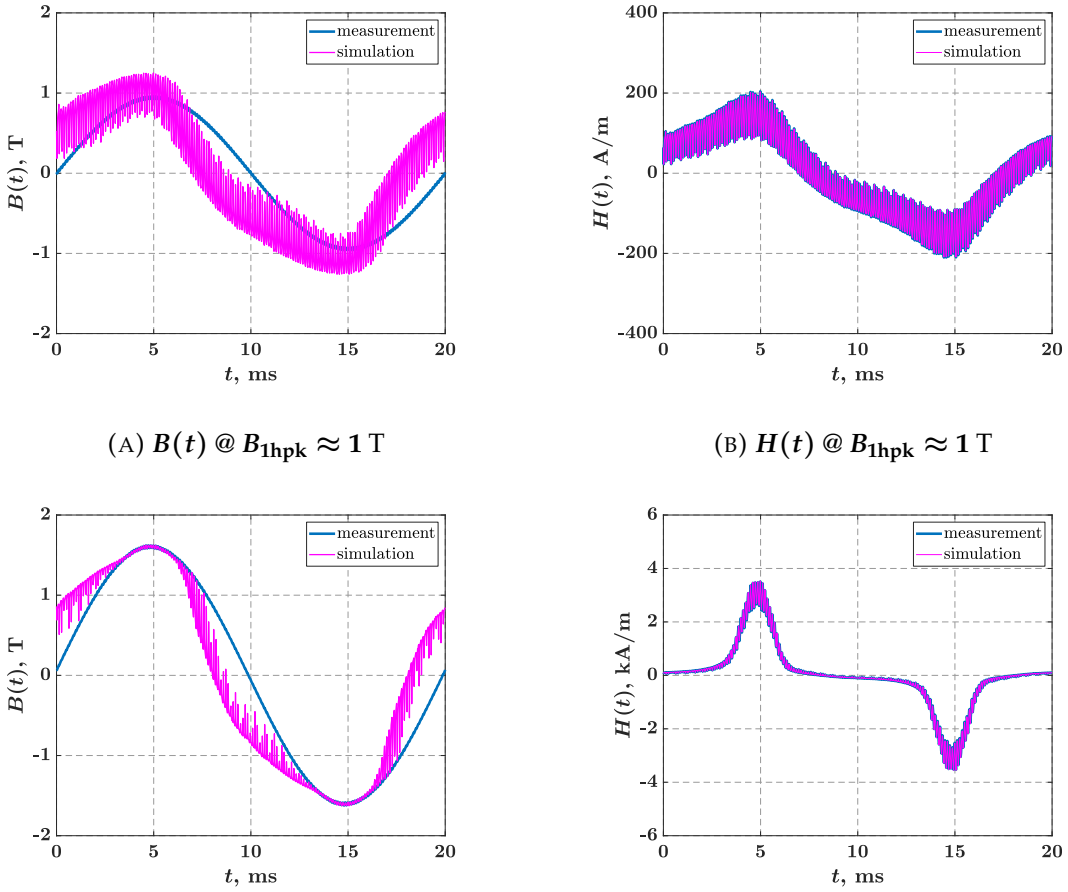

(A) $B(t)$ @ $B_{1hpk} \approx 1$ T

(B) $H(t)$ @ $B_{1hpk} \approx 1$ T

(C) $B(t)$ @ $B_{1hpk} \approx 1.6$ T

(D) $H(t)$ @ $B_{1hpk} \approx 1.6$ T

FIGURE 8.12: Comparison of the waveforms of $\boldsymbol{B}$ and $\boldsymbol{H}$ obtained from AC measurements with the simulation results of the current-driven FEA simulation, shown for the C1a core, $f_{sw} = 8$ kHz and two different B_{1hpk} values.

waveform of $\boldsymbol{B}$ as a result of the simulation does not match the waveform of $\boldsymbol{B}$ derived from measurement results except when the core is highly saturated. On the other hand, it can also be determined that the waveforms of $\boldsymbol{H}$ match quite well for all cases.

The reason for this discrepancy in the relation between the waveforms of $\boldsymbol{B}$ and $\boldsymbol{H}$ is recognized to be in the use of the normal magnetization curve of the material to define the relation between $\boldsymbol{B}$ and $\boldsymbol{H}$ values. It can be confirmed that this is the case by mapping the values of the waveform of $\boldsymbol{H}$ derived from the AC measurements to the values of $\boldsymbol{B}$ using the determined normal magnetization curve. The results of this mapping, shown in figure8.13, confirm that the waveform of $\boldsymbol{B}$ obtained in this way matches the simulation results almost perfectly. Relatively high in saturation, where

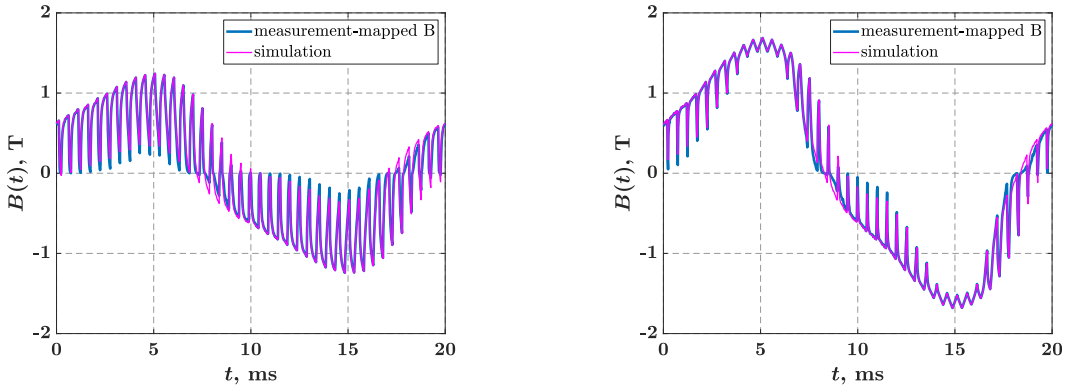

(A) $B_{1hpk} \approx 1$ T (B) $B_{1hpk} \approx 1.6$ T

FIGURE 8.13: Waveform of B obtained from AC measurements by $H - B$ mapping compared to the simulation results of the current-driven FEA simulation, shown for the C1a core, $f_{sw} = 2$ kHz and two different B_{1hpk} values.

ascending and descending branches of the hysteresis loop are substantially overlapped, the difference between the $B - H$ pairs obtained from the hysteresis loop and the normal magnetization curve tends to zero. For this reason, the simulation results also show a correct ripple of the waveform of B when core is highly saturated.

The relation between B and H is much more complicated when PWM-generated voltage is applied to the core compared to sinusoidal supply, and this relation cannot be described by a simple normal magnetization curve of the material. Defining the hysteresis loop instead does not help either, because minor loops that occur follow their own $B - H$ curve and this happens around a biased value of B. Only if a new hysteresis loop would be defined for the material each time a minor loop occurs, in relation to the parameters ΔB, $\frac{dB}{dt}$ and B_{bias}, then one could expect a fairly good match between B and H. However, this information is not available during the design stage of the machine and can only be determined by measurements when it has already lost its purpose in terms of determining the waveform of B as a result of the current-driven FEA simulation.

The correct data on the waveform of B could be obtained by a voltage-driven FEA simulation. This was proven with the simulation performed on the core C1a. The results of the obtained waveform of B at a point in the centre of the core ring compared to the waveform of B obtained by AC measurements are shown in figure8.14. However, performing voltage-driven simulations is highly impractical due to the extremely time-consuming simulations required to reach a steady state in the machine or ring core.

Considering that the applied voltage is PWM-generated, the minimum number of points to describe such a rectangular voltage waveform correlates with the switching frequency of the inverter. For the lowest expected $f_{\mathbf{sw}}$ of 2 kHz, this is at least 160 points per period, disregarding all frequency components in the waveform except the one corresponding to the switching frequency. If one also considers that it takes tens of seconds to reach a steady state, it becomes clear that this procedure is not useful in practice. Similar to the current-driven FEA simulations, where the waveform of $\boldsymbol{B}$ as the result of the simulation did not match the waveform of $\boldsymbol{B}$ determined from AC measurements, voltage-driven simulations result in the waveform of $\boldsymbol{H}$ that does not match the waveform of $\boldsymbol{H}$ determined from AC measurements.

Due to the aforementioned problems in determining the waveform of $\boldsymbol{B}$, the motivation arose to develop a method using the minor loop data based on the waveform of $\boldsymbol{H}$, which can be determined using current-driven FEA simulations. Since the obtained DC bias measurement data was in the form of the minor loop parameters based on the waveform of $\boldsymbol{B}$, an algorithm had to be developed to map the minor loop data in the form of the parameters based on $\boldsymbol{H}$ into the minor loop data in the form of the parameters $\boldsymbol{\Delta B}$, $\frac{\mathbf{d}\boldsymbol{B}}{\mathbf{d}t}$ and $\boldsymbol{B}_{\mathbf{bias}}$. However, it is assumed that it would also be possible to create a 3D loss map based on the minor loops defined by the parameters $\boldsymbol{\Delta H}$, $\frac{\mathbf{d}\boldsymbol{H}}{\mathbf{d}t}$ and $\boldsymbol{H}_{\mathbf{bias}}$, which would eliminate the need for the remapping process and presumably simplify the method. However, a more complicated measurement procedure is anticipated.

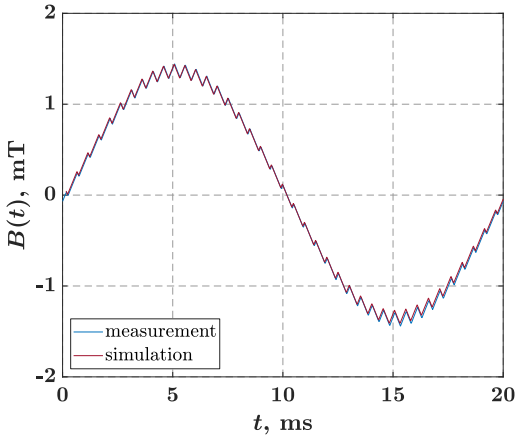

FIGURE 8.14: Flux density waveform $\boldsymbol{B}$ obtained from AC measurements compared to the simulation results of the voltage-driven FEA simulation, shown for the C1a core, $f_{\mathbf{sw}} = \mathbf{2}$ kHz and $\boldsymbol{B}_{\mathbf{1hpk}} \approx 1.45$T.

In the last phase of the research, it has become clear that the non-linear dynamic machine model based on the flux-current maps of the core C1a leads to a current waveform which ripple does not match the current ripple obtained from the AC measurements, but is rather smaller in terms of peak-to-peak values. This is especially so for the cases with lower values of $\boldsymbol{B_{1hpk}}$. Thus, if such a current were used in a current-driven FEA simulation, namely the current with the smaller peak-to-peak values of ripple, this would lead to the solution of a waveform of $\boldsymbol{H}$ that would have smaller peak-to-peak values. If such a waveform of $\boldsymbol{H}$ were then used to calculate the contribution of the PWM-induced losses, the calculated losses would be underestimated. With this in mind, the proposed *3DLMH* method is not applicable for losses calculation if there is no correct waveform of current available for use as excitation in current-driven FEA simulations.

Although the current-driven FEA simulation using an incorrect waveform of the simulated current as excitation results in an incorrect waveform of $\boldsymbol{H}$, it was also found to give the correct waveform and ripple of the flux density $\boldsymbol{B}$. The subigure8.15a shows the comparison between the current obtained from the non-linear dynamic machine model based on the flux-current maps and the current obtained from the AC measurements for the same DC link voltage $\boldsymbol{U_{DC}}$, modulation depth value and modulation type. It is clear that the simulated current waveform does not match the measured current waveform. The results of the current-driven FEA simulation using the simulated current waveform as the excitation signal are shown in subfigures8.15b and8.15c, and the resulting waveforms of $\boldsymbol{H}$ and $\boldsymbol{B}$ are compared with the waveforms of $\boldsymbol{H}$ and $\boldsymbol{B}$ obtained from the AC measurements. It is obvious that the waveform of

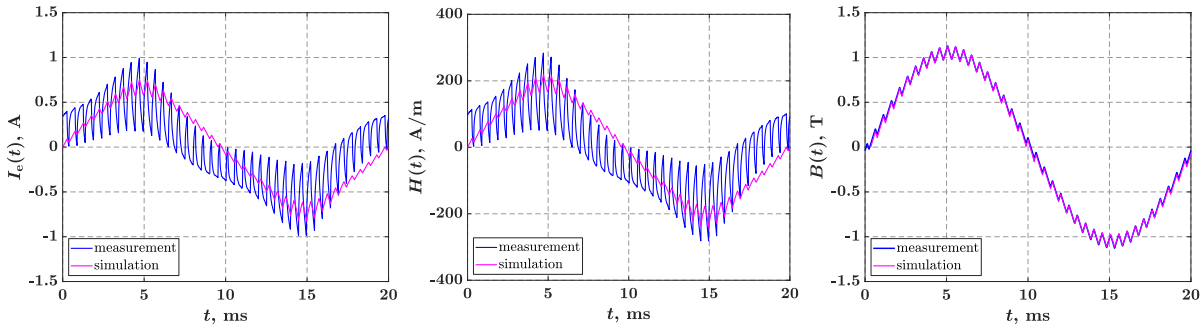

(A) $\boldsymbol{I_e(t)}$ (B) $\boldsymbol{H(t)}$ (C) $\boldsymbol{B(t)}$

FIGURE 8.15: Current waveform as a result of simulation using the non-linear dynamic machine model and results of current-driven FEA simulation using the simulated current waveform compared to waveforms obtained from the AC measurements. The waveforms are shown for $\boldsymbol{B_{1hpk}} \approx \mathbf{1}$ T and $\boldsymbol{f_{sw}} = \mathbf{2}$ kHz.

$\boldsymbol{H}$ as a result of the simulation does not match the waveform of $\boldsymbol{H}$ obtained from the measurements. This result was to be expected as it was previously shown that the correct current waveform leads to a correct solution for $\boldsymbol{H}$ in current-driven simulations (Subfigures8.11band8.12b). It is therefore undeniable that the incorrect waveform of the excitation current leads to an incorrect waveform of $\boldsymbol{H}$. However, in the subfigure 8.15cit is also evident that the solution of the waveform of $\boldsymbol{B}$ almost perfectly matches the waveform of $\boldsymbol{B}$ obtained from the measurements.

After all the above, the final sequence of steps defining the procedure for determining the PWM-induced loss contribution to the total AC losses in electrical machine is shown in figure8.16and consists of the following steps:

1. Ring core sample shall be prepared using laminated ferromagnetic material intended for use in the construction of the electrical machine

2. The DC bias measurements shall be performed on the ring core sample and the 3D loss map shall be created

3. Static current-driven FEA simulations shall be performed on the ring core model to obtain current-flux linkage maps

4. Simulations shall be performed with a non-linear dynamic machine model based on the flux-current maps to obtain current waveforms for the different operating points of the electrical machine

5. The current-driven transient FEA simulation shall be performed for each current waveform obtained from the non-linear dynamic machine model. Each current-driven transient FEA simulation provides the waveform of flux density $\boldsymbol{B}$, including its ripple, for each triangle of the model mesh

6. From the results of the FEA simulations, for each triangle of the model mesh and for each operating point of the machine, the data of the minor loops formed under AC excitation shall be collected in the form of the parameters $\boldsymbol{\Delta B}$, $\frac{\mathbf{dB}}{\mathbf{dt}}$ and $\boldsymbol{B}_{\mathbf{bias}}$ (*3DLMB* method)

7. This minor loop data shall be used to retrieve loss values from the created 3D loss map (*3DLMB* method)

8. For each operating point of the machine, the PWM-induced losses in each triangle of the model mesh shall be summed up, giving the total contribution of the PWM-induced losses to the total AC losses for that particular operating point of the machine (*3DLMB* method)

The shortcoming of the proposed methods is the dependence of the loss data on the geometrical and structural parameters of the ring core. Different laser cut impact and non-uniform distribution of the field in the magnetic material affect the results of the method. Therefore, for the time being, a 3D loss map has to be created individually for each given core geometry. This means that the possibility of generalising the method should be further investigated.

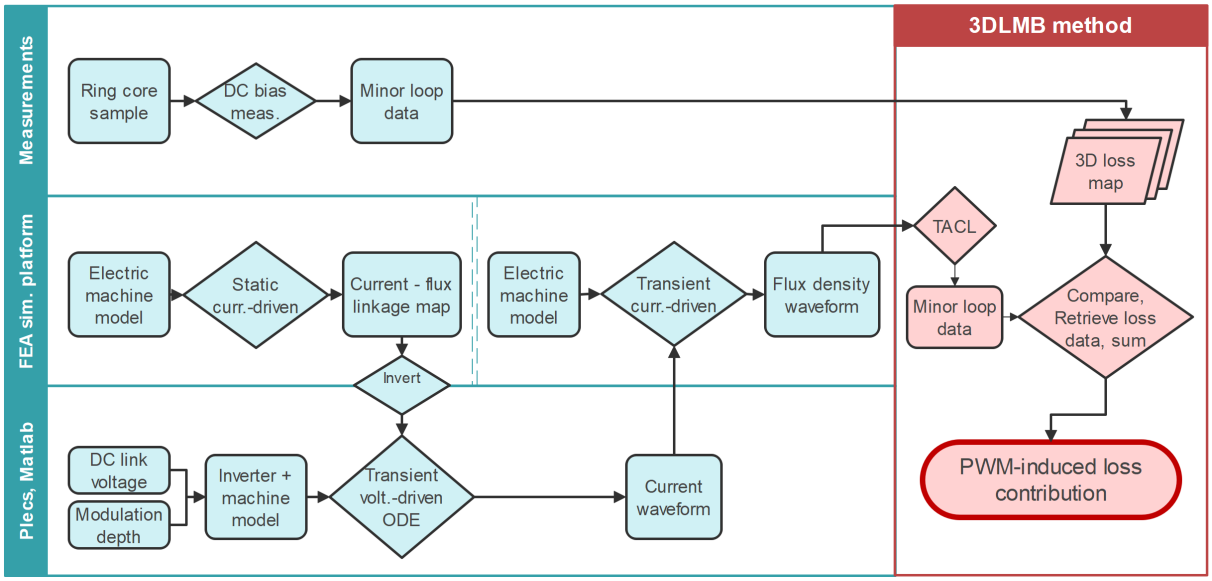

FIGURE 8.16: Step chart for calculation of the contribution of the PWM-induced losses to the total AC losses in electrical machine using the proposed method *3DLMB* and *TACL* approach.

8.5 On the applicability of the proposed methods to electrical machines

The aim of this research was to develop a method for calculating the PWM-induced contribution to the total AC losses of an electrical machine. The author is aware that the total losses in the machine also consist of losses caused by a fundamental and lower level harmonics, and that there are some peculiarities related to electrical machines that may cause difficulties in applying the proposed methods to real machine geometries. The application of the proposed loss model remains a task for future research to follow.

The flux density waveforms in certain sections of the magnetic circuit of the electric machine deviate from the pure sinusoidal form, even though the current waveform in the windings is sinusoidal. These waveforms also contain lower order harmonics, resulting in a trapezoidal shape of the flux density. Provided that the inverter switching frequency to the lower level harmonic frequency ratio is relatively high, it is assumed that this does not affect the applicability of the proposed methods, but merely defines different levels of $\boldsymbol{B}_{\mathbf{bias}}$ at which specific minor loop is formed. However, this was not tested in this research and has yet to be confirmed experimentally.

Furthermore, the magnetic field in the stator yoke of electrical machines does not only pulsate in a single direction, as was the case with the ring core used in the experiments of this research. Rather, the flux density vector rotates and describes curves with different elliptical shapes depending on the geometric position in the yoke. However, the pulsations in the magnetic field caused by the PWM-generated power supply occur asynchronously to the rotation of the flux density vector, and that at a much higher speed. For this reason, this phenomenon is not expected to have a significant impact on the applications of the proposed methods. Nevertheless, this was not tested in this research and has yet to be confirmed experimentally.

Chapter 9

Conclusion

The PWM-generated power supply has a great impact on the increase of iron losses in electrical machines, so an accurate prediction of these losses in the design phase is of great importance. For this purpose, an accurate characterization of soft magnetic materials is required, which so far is available only under conditions of sinusoidal excitation. There is no standardized, generally accepted method to account for such effects in soft magnetic materials.

In this research, a measurement setup is proposed and built to perform measurements on soft magnetic materials. This setup would first allow the analysis of different PWM effects on losses and later provide data for material characterization in terms of magnetization and losses. Setup was built as a single winding excitation system with an inverter serving as both AC and DC power supply and as capable for achieving wide operating range of excitation frequencies and varying DC bias fields, all of which makes this setup novel. The proposed setup was validated by comparing the initial measurements with the well known theory and results of other research papers.

Two measurement modes were implemented in DSP: AC and DC bias. The AC measurement mode was used to obtain power loss curves for various inverter parameters that served as reference data for later analysis, comparison and loss calculation. The DC bias measurement mode was used to obtain loss data under conditions of DC bias for various combinations of the minor loop parameters $\boldsymbol{\Delta B}$, $\frac{\mathbf{d}B}{\mathbf{d}t}$, and $\boldsymbol{B}_{\mathbf{bias}}$. These data were later used to create the interpolated 3D loss maps, which were used as characterisation of the magnetic material.

Two methods for calculating the contribution of PWM-induced losses to the total losses AC have been proposed, both based on the 3D lookup maps and the comparison of the minor loop parameters between the minor loops formed under AC excitation and minor loops obtained through the DC bias measurements. Method *3DLMB* uses waveform of $\boldsymbol{B}$ to define the minor loop data, while method *3DLMH* uses waveform of

$\boldsymbol{H}$ to do the same. The methods were evaluated by comparing the losses calculation obtained directly from the performed AC measurements with the losses calculated using the proposed methods. The loss calculations obtained using the methods agree well with the losses calculated using measurements. The difference between the calculations and the measurements varies depending on the method, switching frequency of the inverter and values of the parameter $\boldsymbol{B_{1hpk}}$, but the error is generally in the range of $\pm$**5%** for the reference core C1a and in the range of $\pm$**10%** for the cores C2a and C3, which is considered satisfactory with respect to the calculation of the losses.

Although the results of AC measurements were used in this research to evaluate the proposed methods, the use of these methods is intended for calculation of contribution of PWM-induced losses to the total AC losses in electrical machine design stage. Therefore, data on the minor loops that form under AC excitation are to be obtained using electric machine model and simulation tools, while only the DC bias measurements are to be performed on the ring core sample of the ferromagnetic material that is intended for the build of the machine. Preliminary simulation experiments were performed on the model of the core C1a in order to confirm that the minor loop data can be obtained using current-driven static and transient FEA simulations along with a non-linear dynamic machine model based on the flux-current maps. However, the applicability of the proposed methods to more complex core geometries and magnetic circuits, such as those found in electrical machines, still needs to be experimentally tested and evaluated.

Further investigation is needed on some topics that were outside the time frame of this research but directly related to the results and could lead to a better understanding of PWM-induced loss phenomena and possibly general material characterisation in terms of PWM-induced losses:

1. The relationships between the geometrical and build parameters of the core and the losses, i.e. the material characterisation data, and analysis of a possible quantification of these relationships

2. Other possible definitions and calculations of the equivalent parameter $\frac{\mathbf{d}\boldsymbol{B}}{\mathbf{d}\boldsymbol{t}}$ of asymmetric and non-closed minor loops, as well as the analysis of the relationship between the determined empirical parameters to different types of ferromagnetic materials and core geometries

3. Ability to create a 3D loss map in terms of the parameters $\boldsymbol{\Delta H}$, $\frac{\mathbf{d}\boldsymbol{H}}{\mathbf{d}\boldsymbol{t}}$ and $\boldsymbol{H_{bias}}$ and use it for loss calculation with the *3DLMH* method

Bibliography

[1] F. Tinazzi et al. “Energy efficiency assessment for inverter-fed induction motors”. In: *8th IET International Conference on Power Electronics, Machines and Drives (PEMD 2016)*. Apr. 2016, pp. 1–6. DOI: 10.1049/cp.2016.0356.

[2] Julio R. Gómez et al. “Identification of Technoeconomic Opportunities with the Use of Premium Efficiency Motors as Alternative for Developing Countries”. In: *Energies* 13.20 (Oct. 2020), p. 5411. ISSN: 1996-1073. DOI: 10.3390/en13205411.

[3] Daniel Glose. “Modulation Strategies for Symmetrical Six-Phase Drives”. PhD thesis. Technische Universitat Munchen, Mar. 2016.

[4] L. Chang and T. M. Jahns. “Prediction and Evaluation of PWM-Induced Current Ripple in IPM Machines Incorporating Slotting, Saturation, and Cross-Coupling Effects”. In: *IEEE Transactions on Industry Applications* 54.6 (2018), pp. 6015–6026. DOI: 10.1109/TIA.2018.2846718.

[5] A. Boglietti et al. “Influence of the inverter characteristics on the iron losses in PWM inverter-fed induction motors”. In: *IEEE Transactions on Industry Applications* 32.5 (Sept. 1996), pp. 1190–1194. ISSN: 1939-9367. DOI: 10.1109/28.536882.

[6] A. Boglietti et al. “Energetic behavior of soft magnetic materials fed by inverter supply”. In: *Conference Record of the 1992 IEEE Industry Applications Society Annual Meeting*. Oct. 1992, 54–59 vol.1. DOI: 10.1109/IAS.1992.244465.

[7] Andreas Krings. “Iron Losses in Electrical Machines - Influence of Material Properties, Manufacturing Processes, and Inverter Operation”. PhD thesis. KTH, School of Electrical Engineering (EES), 2014.

[8] A. Boglietti et al. “Core loss estimation method for PWM inverter fed induction motors”. In: *IECON 2010 - 36th Annual Conference on IEEE Industrial Electronics Society*. Nov. 2010, pp. 811–816. DOI: 10.1109/IECON.2010.5675180.

[9] L. Chang, T. M. Jahns, and R. Blissenbach. "Estimation of PWM-Induced Iron Loss in IPM Machines Incorporating the Impact of Flux Ripple Waveshape and Nonlinear Magnetic Characteristics". In: *IEEE Transactions on Industry Applications* 56.2 (Mar. 2020), pp. 1332–1345. ISSN: 1939-9367. DOI: 10.1109/TIA.2019.2961074.

[10] L. Chang, T. M. Jahns, and R. Blissenbach. "Characterization and Modeling of Soft Magnetic Materials for Improved Estimation of PWM-Induced Iron Loss". In: *IEEE Transactions on Industry Applications* 56.1 (Jan. 2020), pp. 287–300. ISSN: 1939-9367. DOI: 10.1109/TIA.2019.2955055.

[11] Z. Zhu et al. "Evaluation of Iron Loss Models in Electrical Machines". In: *IEEE Transactions on Industry Applications* 55.2 (Mar. 2019), pp. 1461–1472. ISSN: 1939-9367. DOI: 10.1109/TIA.2018.2880674.

[12] S. Zhu et al. "Core Loss Analysis and Calculation of Stator Permanent-Magnet Machine Considering DC-Biased Magnetic Induction". In: *IEEE Transactions on Industrial Electronics* 61.10 (Oct. 2014), pp. 5203–5212. ISSN: 1557-9948. DOI: 10.1109/TIE.2014.2300062.

[13] G. E. Fish. "Soft magnetic materials". In: *Proceedings of the IEEE* 78.6 (1990), pp. 947–972. DOI: 10.1109/5.56909.

[14] The Electric Motor Education and Research Foundation. *Lamination Steels Third Edition - A Compendium of Lamination Steel Alloys Commonly Used in Electric Motors*. ISBN 0-9714391-3-3. 2007.

[15] Fausto Fiorillo. "Chapter 1 - Basic Phenomenology in Magnetic Materials". In: *Characterization and Measurement of Magnetic Materials*. Ed. by Fausto Fiorillo. Elsevier Series in Electromagnetism. San Diego: Academic Press, 2004, pp. 3–24. DOI: https://doi.org/10.1016/B978-012257251-7/50003-4.

[16] S. Tumanski. *Handbook of Magnetic Measurements*. Series in Sensors. CRC Press, 2016. ISBN: 9781439829523.

[17] C. D. Graham Jr. "Physical Origin of Losses in Conducting Ferromagnetic Materials". In: *Journal of Applied Physics* 53 (1982), pp. 8276–8280.

[18] E.C. Snelling. *Soft ferrites: properties and applications*. Soft Ferrites: Properties and Applications. Iliffe, 1969.

[19] G. F. Nataf, Guennou M., and J.M. et al Gregg. "Domain-wall engineering and topological defects in ferroelectric and ferroelastic materials". In: *Nature Reviews Physics* 2 (2020).

[20] J. Reinert, A. Brockmeyer, and R. W. A. A. De Doncker. "Calculation of losses in ferro- and ferrimagnetic materials based on the modified Steinmetz equation". In: *IEEE Transactions on Industry Applications* 37.4 (2001), pp. 1055–1061. DOI: 10.1109/28.936396.

[21] M.S. Lancarotte and A. de A. Penteado. "Estimation of core losses under sinusoidal or nonsinusoidal induction by analysis of magnetization rate". In: *IEEE Transactions on Energy Conversion* 16.2 (2001), pp. 174–179. DOI: 10.1109/60.921469.

[22] D.W. Hart. *Power Electronics*. McGraw-Hill education. McGraw-Hill, 2011. ISBN: 9780071289306.

[23] A. Boglietti et al. "Change of the iron losses with the switching supply frequency in soft magnetic materials supplied by PWM inverter". In: *IEEE Transactions on Magnetics* 31.6 (1995), pp. 4250–4252. DOI: 10.1109/20.489942.

[24] A. Boglietti et al. "Influence of the inverter characteristics on the iron losses in PWM inverter-fed induction motors". In: *IEEE Transactions on Industry Applications* 32.5 (1996), pp. 1190–1194. DOI: 10.1109/28.536882.

[25] Nicolas Denis, Shunya Odawara, and Keisuke Fujisaki. "Attempt to Evaluate the Building Factor of a Stator Core in Inverter-Fed Permanent Magnet Synchronous Motor". In: *IEEE Transactions on Industrial Electronics* 64.3 (2017), pp. 2424–2432. DOI: 10.1109/TIE.2016.2573267.

[26] Nicolas Denis et al. "Core loss increase due to inverter carrier frequency in an interior permanent magnet synchronous motor". In: *2015 18th International Conference on Electrical Machines and Systems (ICEMS)*. 2015, pp. 795–800. DOI: 10.1109/ICEMS.2015.7385142.

[27] Igor Sirotić, Marinko Kovačić, and Stjepan Stipetić. "Methodology and Measurement Setup for Determining PWM Contribution to Iron Loss in Laminated Ferromagnetic Materials". In: *IEEE Transactions on Industry Applications* 57.5 (2021), pp. 4796–4804. DOI: 10.1109/TIA.2021.3094501.

[28] A. Krings et al. "Comparison of PWM and Sinusoidal excitations conditions of Induction Machines". In: *Proceedings of 5th International Conference Magnetism and Metallurgy WMM 2012, Ghent, Belgium*. 2012.

[29] Nicolas Denis, Yenyi Wu, and Keisuke Fujisaki. "Impact of the inverter DC bus voltage on the core losses of a permanent magnet synchronous motor at constant speed". In: *2016 19th International Conference on Electrical Machines and Systems (ICEMS)*. 2016, pp. 1–6.

[30] C. A. Baguley, B. Carsten, and U. K. Madawala. "The Effect of DC Bias Conditions on Ferrite Core Losses". In: *IEEE Transactions on Magnetics* 44.2 (2008), pp. 246–252.

[31] S. Xue et al. "Iron Loss Model Under DC Bias Flux Density Considering Temperature Influence". In: *IEEE Transactions on Magnetics* 53.11 (2017), pp. 1–4.

[32] M. S. Lancarotte, C. Goldemberg, and A. d. A. Penteado. "Estimation of FeSi Core Losses Under PWM or DC Bias Ripple Voltage Excitations". In: *IEEE Transactions on Energy Conversion* 20.2 (2005), pp. 367–372. DOI: 10.1109/TEC.2005.847971.

[33] P. Papamanolis et al. "Minimum Loss Operation and Optimal Design of High-Frequency Inductors for Defined Core and Litz Wire". In: *IEEE Open Journal of Power Electronics* 1 (2020), pp. 469–487. DOI: 10.1109/OJPEL.2020.3027452.

[34] D. Menzi et al. "Novel iGSE-C Loss Modeling of X7R Ceramic Capacitors". In: *IEEE Transactions on Power Electronics* 35.12 (2020), pp. 13367–13383. DOI: 10.1109/TPEL.2020.2996010.

[35] Andreas Krings and Juliette Soulard. "Overview and Comparison of Iron Loss Models for Electrical Machines". In: *Journal of Electrical Engineering* 10 (May 2010), pp. 162–169.

[36] Jieli Li, T. Abdallah, and C.R. Sullivan. "Improved calculation of core loss with nonsinusoidal waveforms". In: *Conference Record of the 2001 IEEE Industry Applications Conference. 36th IAS Annual Meeting (Cat. No.01CH37248)*. Vol. 4. 2001, 2203–2210 vol.4. DOI: 10.1109/IAS.2001.955931.

[37] K. Venkatachalam et al. "Accurate prediction of ferrite core loss with nonsinusoidal waveforms using only Steinmetz parameters". In: *2002 IEEE Workshop on Computers in Power Electronics, 2002. Proceedings.* 2002, pp. 36–41. DOI: 10.1109/CIPE.2002.1196712.

[38] Jonas Muhlethaler et al. "Improved Core-Loss Calculation for Magnetic Components Employed in Power Electronic Systems". In: *IEEE Transactions on Power Electronics* 27.2 (2012), pp. 964–973. DOI: 10.1109/TPEL.2011.2162252.

[39] G. Bertotti. "General properties of power losses in soft ferromagnetic materials". In: *IEEE Transactions on Magnetics* 24.1 (1988), pp. 621–630. DOI: 10.1109/20.43994.

[40] G. Bertotti et al. "An improved estimation of iron losses in rotating electrical machines". In: *IEEE Transactions on Magnetics* 27.6 (1991), pp. 5007–5009. DOI: 10.1109/20.278722.

[41] M. Albach, T. Durbaum, and A. Brockmeyer. "Calculating core losses in transformers for arbitrary magnetizing currents a comparison of different approaches". In: *PESC Record. 27th Annual IEEE Power Electronics Specialists Conference*. Vol. 2. 1996, 1463–1468 vol.2. DOI: 10.1109/PESC.1996.548774.

[42] Davide Aguglia and Michel Neuhaus. "Laminated magnetic materials losses analysis under non-sinusoidal flux waveforms in power electronics systems". In: *2013 15th European Conference on Power Electronics and Applications (EPE)*. 2013, pp. 1–8. DOI: 10.1109/EPE.2013.6631889.

[43] *Isolated current and voltage transducers: Characteristics - Applications - Calculations*. LEM components. URL: https://www.lem.com/en/file/3139/download.

[44] *High Precision Current Transducers*. LEM components. URL: https://www.lem.com/en/file/1860/download.

[45] I. Sirotić, M. Kovačić, and S. Stipetić. "Methodology and measurement setup for determination of PWM influence on iron losses". In: *2020 International Conference on Electrical Machines (ICEM)*. Vol. 1. 2020, pp. 932–939. DOI: 10.1109/ICEM49940.2020.9271048.

[46] *Methods of measurement of the magnetic properties of magnetically soft metallic and powder materials at frequencies in the range 20Hz to 200kHz by the use of ring specimens*. International Electrotechnical Commission, Standard IEC 60404-6:2018. 2018.

[47] *Methods of measurement of d.c. magnetic properties of magnetically soft materials*. International Electrotechnical Commission, Standard IEC 60404-4:2008. 2008.

[48] *Calculation of the effective parameters of magnetic piece parts*. International Electrotechnical Commission, Standard IEC 60205:2016. 2016.

[49] *Testing of Magnetic Materials*. Končar Electrical Engineering Institute - Laboratory Center, Testing of Magnetic Materials Brochure. URL: https://www.koncar-institut.hr/wp-content/uploads/2019/05/KONCAR-Institute-Testing-of-magnetic-materials-20-1904.pdf.

[50] Brockhaus Masurements. *MPG-Expert 3 - Manual: Manual for software operation of the MPG 200 D*. 2015.

[51] Xiao Chen et al. "A High-Fidelity and Computationally Efficient Model for Interior Permanent-Magnet Machines Considering the Magnetic Saturation, Spatial Harmonics, and Iron Loss Effect". In: *IEEE Transactions on Industrial Electronics* 62.7 (2015), pp. 4044–4055. DOI: 10.1109/TIE.2014.2388200.

[52] Klemen Drobnič, Lovrenc Gašparin, and Rastko Fišer. "Fast and Accurate Model of Interior Permanent-Magnet Machine for Dynamic Characterization". In: *Energies* 12 (Feb. 2019), p. 783. DOI: 10.3390/en12050783.

List of Figures

List of Tables

List of Abbreviations

PWM	**P**ulse **W**idth **M**odulation
SiC	**Si**licon **C**arbide
DSP	**D**igital **S**ignal **P**rocessor
RMS	**R**oot **M**ean **S**quare
ppm	**p**arts **p**er **m**ilion
CT	**C**urrent **T**ransducer

List of Symbols

u, U	voltage	V
i, I	current	A
Φ	magnetic flux	Wb
Ψ	magnetic flux linkage	Wb
B	magnetic flux density	T
H	magnetic field strength	A/m
P	electric power	W
f	frequency	Hz
φ	electrical angle	rad
R	electrical resistance	Ω
C	electrical capacitance	F
L	inductance	H
S	area	m^2
V	volume	m^3
ℓ	length	m
d	diameter	m
r	radius	m
N	number of turns of a winding	
m	index of modulation	
D	duty cycle	
RF	ripple factor	

List of Suffixes

s	search (voltage, winding)
e	excitation (voltage, winding, current
w	winding
sw	switching (frequency)
pk	peak (value of signal)
h	harmonic (value of specific harmonic component)
1h	$\mathbf{1}^{st}$ harmonic (value of fundamental harmonic component)
1hpk	peak of $\mathbf{1}^{st}$ harmonic (peak value of fundamental harmonic component)
max	maximum (maximum value of parameter, signal)
bias	DC, average value (voltage, flux density, magnetic field strength etc.)
eq	equivalent (area, length)
g	geometrical (area,length)
meas	measured (value)
sf	stacking factor (core)
σ	leakage (inductance, capacitance)
tot	total
a	amplitude (modulation)

Biography

Igor Sirotić is a senior researcher at the Faculty of Electrical Engineering and Computing, University of Zagreb, in the Department of Electrical Machines, Drives and Automation. He graduated from the same faculty and department in 2011 under the supervision of Prof. Zlatko Maljković, Ph.D.. In the period from 2011 to 2014, he worked professionally in the private sector and from 2014 to 2020 as an assistant at FER. From 2020 to present he is a Senior Researcher in the project Development of Submerged Generator for Small Hydropower Plants with Low Head. In 2019, he started doctoral studies at the Faculty of Electrical Engineering and Computing under the supervision of full professor Stjepan Stipetić Ph.D.. He participates in teaching courses in the field of electrical machines and design in electrical engineering. His scientific interest is in the design of electrical machines, and his research area is closely related to the characterization of ferromagnetic materials and the analysis of losses in the iron of electrical machines.

List of Publications

1. I. Sirotić, M. Kovačić and S. Stipetić, "Methodology and Measurement Setup for Determining PWM Contribution to Iron Loss in Laminated Ferromagnetic Materials," in IEEE Transactions on Industry Applications, vol. 57, no. 5, pp. 4796-4804, Sept.-Oct. 2021, doi: 10.1109/TIA.2021.3094501

2. I. Sirotić, M. Kovačić and S. Stipetić, "Methodology and measurement setup for determination of PWM influence on iron losses," 2020 International Conference on Electrical Machines (ICEM), Gothenburg, Sweden, 2020, pp. 932-939, doi: 10.1109/ICEM49940.2020.9271048

3. S. Tusun, I. Erceg and I. Sirotić, "Laboratory model for design and verification of synchronous generator excitation control algorithms," 2016 39th International Convention on Information and Communication Technology, Electronics and Microelectronics (MIPRO), Opatija, Croatia, 2016, pp. 146-151, doi: 10.1109 / MIPRO. 2016.7522128

4. I. Sirotić, V. Šunde and Ž. Ban, "Algorithm for fast determination of LiFePO4 battery nominal current," 2014 37th International Convention on Information and Communication Technology, Electronics and Microelectronics (MIPRO), Opatija, Croatia, 2014, pp. 121-124, doi: 10.1109/MIPRO.2014.6859545

Životopis

Igor Sirotić zaposlen je kao iskusni istraživač na Fakultetu elektrotehnike i računarstva Sveučilišta u Zagrebu, na Zavodu za elektrostrojarstvo i automatizaciju. Na istom zavodu diplomirao je 2011. godine pod mentorstvom prof.dr.sc. Zlatka Maljkovića. U razdoblju od 2011. do 2014. godine radi u struci u privatnom sektoru, a od 2014. do 2020. godine kao asistent na FER-u. Od 2020- godine do danas zaposlen je na mjestu iskusnog istraživača na projektu Razvoj potopljenog agregata za male hidroelektrane s niskim padom vode. Doktorski studij na Fakultetu elektrotehnike i računarstva upisao je 2019. godine pod mentorstvom redovitog profesora dr. sc. Stjepana Stipetića. Sudjeluje u izvođenju nastave iz područja električnih strojeva i projektiranja u elektrotehnici. Njegov znanstveni interes obuhvaća projektiranje u elektrostrojarstvu, a područje istraživanja je usko vezano uz karakterizaciju feromagnetskih materijala i analizu gubitaka u željezu električnih strojeva.